A Wave Propagation Approach for Prediction of Tire-Pavement Interaction Noise

Sterling M. McBride Granda

Dissertation submitted to the faculty of the Virginia Polytechnic Institute and State University in partial fulfillment of the requirements for the degree of

Doctor of Philosophy
In
Mechanical Engineering

Ricardo A. Burdisso, Chair
Corina Sandu, Co-Chair
Pablo A. Tarazaga
Michael J. Roan
Kevin T. Lowe

August 16, 2019

Blacksburg, Virginia

Keywords: Tire Vibrations, Tire-Pavement Interaction Noise

A Wave Propagation Approach for Prediction of Tire Pavement Interaction Noise

Sterling M. McBride Granda

ABSTRACT

Induced vibrations due to tire-pavement interaction are one of the main sources of vehicle exterior noise, especially near highways and main roads where traveling speeds are above 50 kph. Its dominant spectral content is approximately within 500-1500 Hz. However, accurate prediction tools within this frequency range are not available. Current methods rely on structural modeling of the complete tire using finite elements and modal expansion approaches that are accurate only at low frequencies. Therefore, alternative physically-based models need to be developed. This work proposes a new approach that incorporates wave behavior along the tire's circumferential direction, while modes are assumed along its transversal direction. The formulation for new infinite plate and cylindrical shell structural models of a tire is presented. These are capable of accounting for orthotropic material properties, different structural parameters between the belt and sidewalls, inflation pressure, and rotation of the tire. In addition, a new contact model between the pavement and the tire is developed presented. The excitation of the tire due to the impact of the tread-pattern blocks in the contact patch region is characterized and coupled to the structure of the tire. Finally, a Boundary Element Method is implemented in order to compute the vibration-induced noise produced by the tire. All the modeling components are combined in a single prediction tool named *Wave Pro Tire*. Lastly, simulated responses and validation cases are presented in terms of harmonic responses, Frequency Response Functions (FRF), and produced noise.

A Wave Propagation Approach for Prediction of Tire-Pavement Interaction Noise

Sterling M. McBride Granda

GENERAL AUDIENCE ABSTRACT

Induced vibrations due to tire-pavement interaction are one of the main sources of vehicle exterior noise, especially near highways and main roads where traveling speeds are above 50 kph. Accurate prediction tools are not currently available. Therefore, new physically-based models need to be developed. This work proposes a new approach to model the tire's structure with a formulation that accounts for multiple physical phenomena. In addition, a model that simulates the contact between the pavement and the tire's tread is presented. Finally, the vibrations are coupled to the produced noise in a single prediction tool named *Wave Pro Tire*. This work also includes simulated responses and validation cases.

Acknowledgments

I would like to thank my advisor Dr. Ricardo Burdisso, Professor at the Department of Mechanical Engineering at Virginia Tech. His continuous advice and support during my graduate studies have encouraged my self-determination and pursuit of excellence as a researcher and a professional. This work would not have been possible without his guidance. I would also like to express my gratitude to Dr. Corina Sandu, Professor at the Department of Mechanical Engineering at Virginia Tech for providing valuable advice and broadening my area of expertise by allowing me to collaborate in international investigation efforts. In addition, I would like to thank the members of my committee Dr. Pablo Tarazaga, Dr. Michael Roan, and Dr. Todd Lowe whose input and collaboration in this research project are greatly appreciated. I would like to acknowledge Dr. Mohammad Albakri and Mr. Mostafa Motahari for their assistance in collecting tire vibrations data. Finally, I would also like to express my appreciation to all my graduate student colleagues, including Mark Hurtado and Lucas Spies and Tan Li from the Vibrations and Acoustics Laboratory at Virginia Tech. Collaborating with them has been a great privilege.

I would like to thank God for helping me successfully reach my educational and professional goals. I am thankful to my family for their continuous and unconditional support. Without their tireless efforts, this accomplishment would not be possible. Andrea, thank you for your support during this journey.

Table of Contents

List of Figures

List of Tables

1. Introduction

Tire-Pavement Interaction Noise (TPIN) is one of the predominant noise sources contributing to pollution in urban areas. Its impact is higher in the vicinity of freeways and main roads, where vehicle speeds are high. As shown in Figure 1.1, TPIN is the largest source of noise produced by typical passenger vehicles traveling at speeds between 50 kph and 130 kph (Donavan et al., 2007). Tire noise is dominant over power train noise and aerodynamic noise. Since power train noise is typically produced by the engine, transmission, intake, and exhaust, it is only significant at low speeds. On the other hand, aerodynamic noise becomes important only at very high speeds, above 150 kph (Li, 2018).

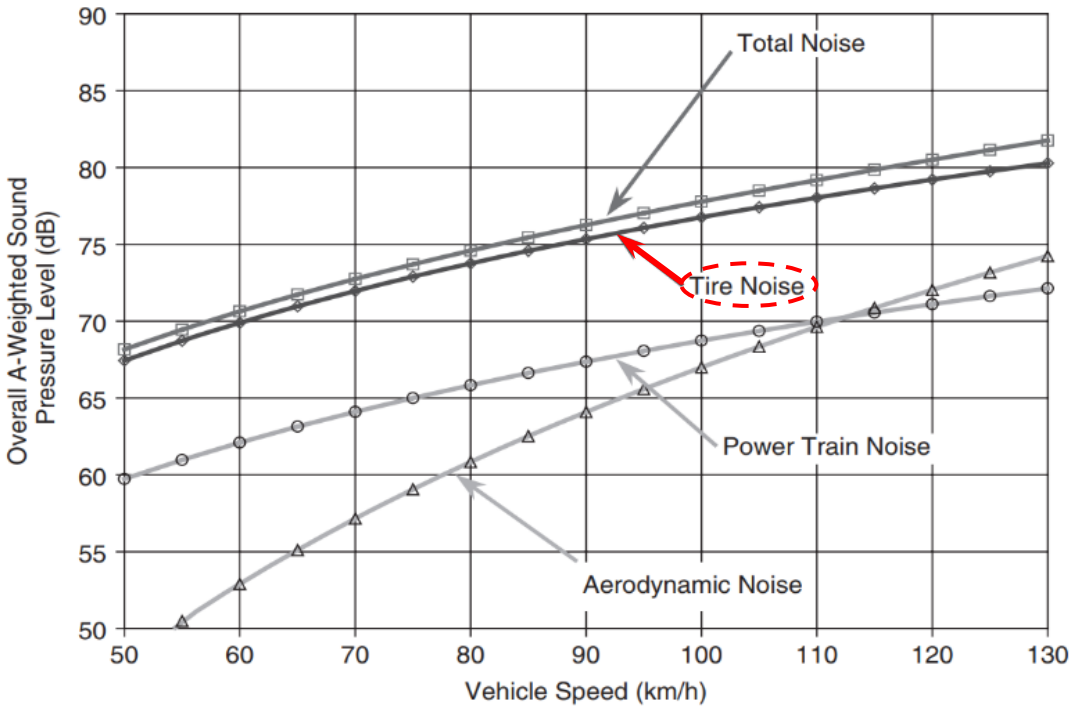

Figure 1.1. Typical contribution of passenger car noise sources as a function of speed measured on pass-by test reported by Donavan et al. (2007).

Multiple strategies to mitigate for TPIN exist. For example, in the United States, the approach is to build barriers around highways or implement traffic management strategies (Spies, 2019). On the other hand, since 2012 the European Union imposed mandatory regulations regarding noise

produced by tires. Tire manufacturers need to provide the label shown in Figure 1.2 for every new tire sold. In this label, fuel efficiency (rolling resistance), wet grip, and noise have to be indicated. The noise levels shown in Figure 1.2 are measured with a pass-by test performed using a two-axle vehicle on a test track. Similar regulations for noise reduction purposes are also being implemented in Asia (Berge et al., 2017).

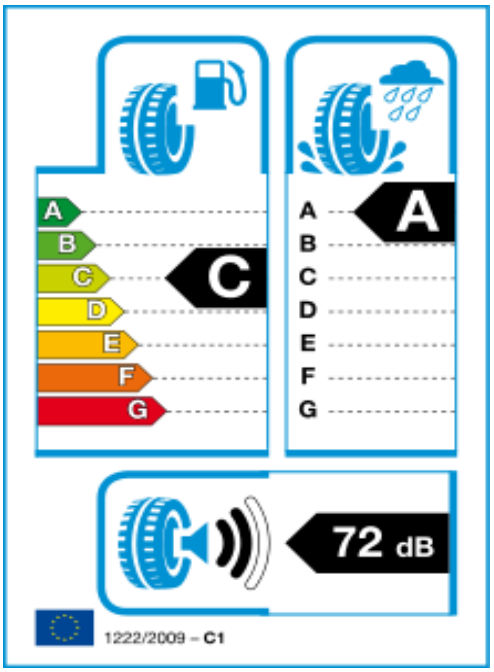

Figure 1.2. EU mandatory tire label (Berge et al., 2017).

TPIN has a characteristic spectral behavior. For example, the noise produced by different tires rolling on the same pavement is shown in Figure 1.3a. Their dominant spectral content is between 500 to 1500 Hz. These results were obtained by performing a large experimental campaign using an Onboard Sound Intensity System (see Figure 1.3b). A total of 47 passenger car commercial tires were tested. Two different sites were used for the measurements: (1) US 460 east and westbound and (2) Virginia Tech Transportation Institute (VTTI) Smart Road. Both are located in Blacksburg, VA, USA. The results in Figure 1.3a were measured at the first test site, where the test pavement is a non-porous, dense-graded hot mix asphalt (see Figure 1c). In addition, these results are consistent with findings from other researchers, as shown by Sanberg (2003).

a) Measured TPIN for various commercial tires.

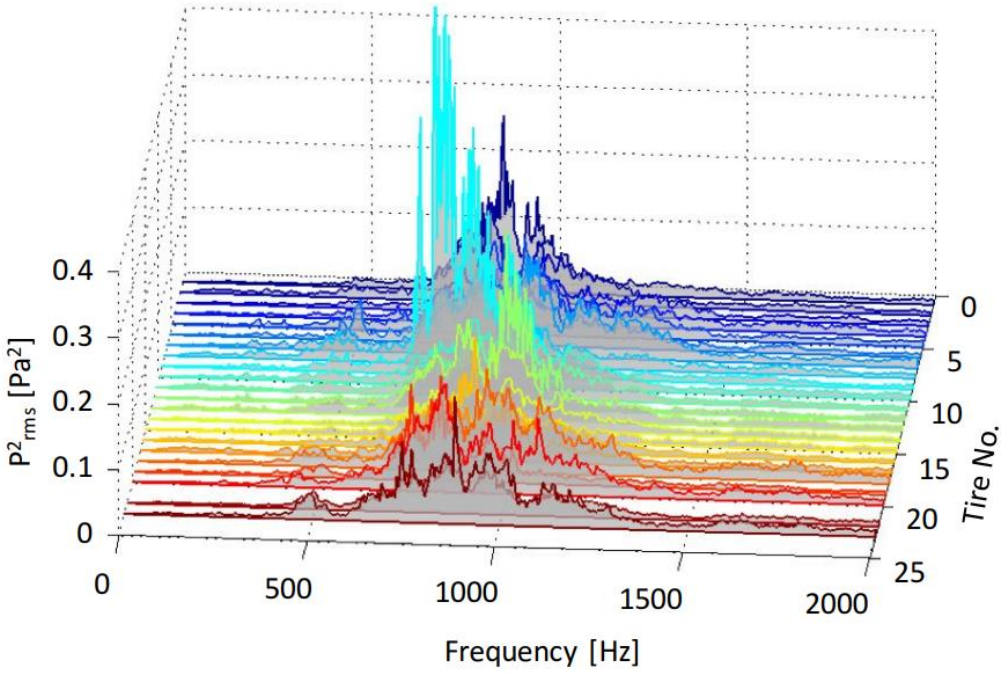

b) Mounted OBSI.

c) Test site for measurements.

Figure 1.3. a) Measured TPIN for different tires on a single pavement (US 460), b) Onboard Sound Intensity System used for testing, c) Test site: US 460, Blacksburg, VA, USA (Li, 2017).

Modeling the mechanisms that produce the TPIN behavior shown in Figure 1.3 is an active research topic. Since the 1970s, the existence of multiple TPIN mechanisms has been speculated without any conclusive proof. A summary of these is presented in Table 1.1 (Sanberg et al., 2002).

The actual contribution from most of them is still a subject of discussion among investigators (Kuijpers et al., 2001). Nevertheless, the noise produced by the vibratory response of the tire and noise generated by air pumping in the contact patch area are the only two well-established mechanisms. In an attempt to model them, current prediction approaches rely on empirical data. For example, the work developed by Losa et al. (2010) and Cesbron et al. (2009) follow a simple set of empirical rules to predict overall noise levels. While more sophisticated semi-empirical models exist, such as the one developed by Che et al. (2012) and Li (2017). The latter is capable of predicting narrowband TPIN very accurately. Still, physical models that do not rely on empirical data are scarce.

Table 1.1. Summary of TPIN generation mechanisms provided in the work by Sanberg et al. (2002).

Type of Mechanism	Specific Phenomenon	Mechanism	Dominant Frequency [Hz]	Potential Noise Variation [dB]
Generation Mechanisms	Impact	Tread Impact	800-1000	7
		Texture Impact	800-1200	5
	Adhesion	Stick/Slip	1000-3000	2
		Stick/Snap	2500-8000	2
	Air Displacement	Air Turbulence	300 & 2000	2
		Air Pumping	1000-4000	10
Amplification Mechanisms	Tire Resonance	Belt Resonance	600-1300	4
		Torus Cavity Resonance	230-280	6
	Air Resonance	Pipe Resonance	1000-3000	6
		Helmholtz Resonance	1000-2500	Unknown
	Horn Effect	Horn Effect	600-2000	10
Reduction Mechanisms	Acoustical Impedance	Pavement Absorption	300-2000	7
	Mechanical Impedance	Vibration Transfer	500-1000	2

This research focuses on developing a physically-based approach to accurately model TPIN due to the vibratory excitation of a rolling tire. Current vibration-induced TPIN prediction tools implement either numerical or analytical methods. Numerical models rely on finite/boundary

elements (FE/BE) that require modeling of the complete tire structure. However, their results are limited only for low frequencies (<500 Hz). Therefore, these cannot be used for the dominant TPIN range. Additionally, these are computationally intensive and have low accuracy on reported overall noise levels. On the other hand, analytical methods typically model the complete tire structure as a uniform shell or plate, to later compute the produced TPIN. These are desirable for computational efficiency and to provide additional physical insight.

In an effort to observe how noise behaves around a tire, Donavan et al. (1981) measured sound intensity levels around a tire mounted on a vehicle while rolling. The results are shown in Figure 1.4. In this case, it can be observed that the highest noise levels are produced near the contact region and decaying along the circumferential direction away from the contact patch. In addition, noise levels are not symmetric. These results suggest that the tire is excited in the contact patch region, where waves that travel along its circumferential direction are excited. These, in turn, generate the noise measured by the sound intensity probes.

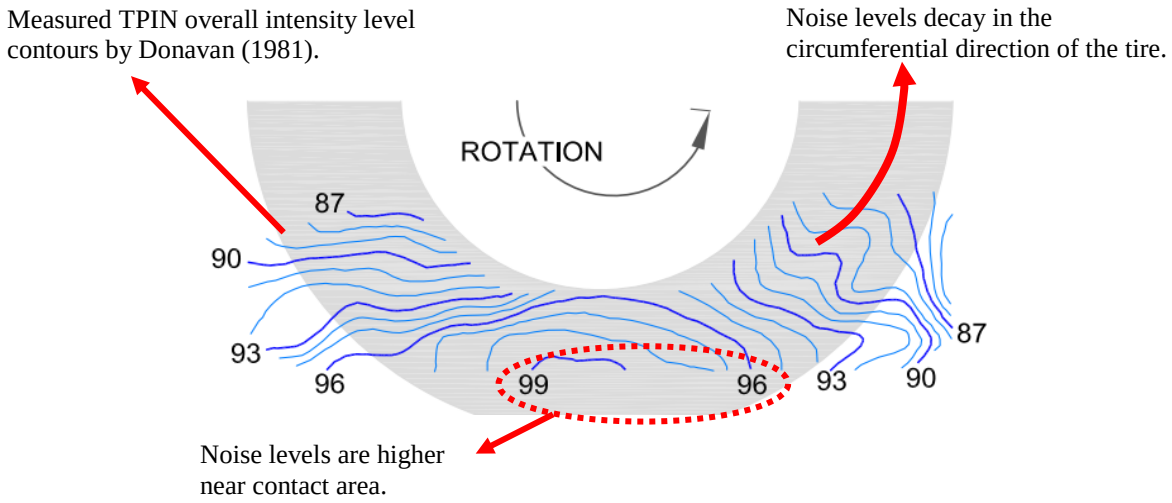

Figure 1.4. Sound intensity levels measured around a rolling tire (Donavan et al., 1981).

On the other hand, Bolton (1998) performed experimental work to study the response of the tire's structure. In this work, a tire of size 215/70R14 was mounted horizontally in a balancer, as shown in Figure 1.5. The tire was excited at the center of the tread with a point force using an

electrodynamic shaker. The normal surface velocities along the tread's centerline were then measured with a laser vibrometer for a range between 100 Hz to 1000 Hz.

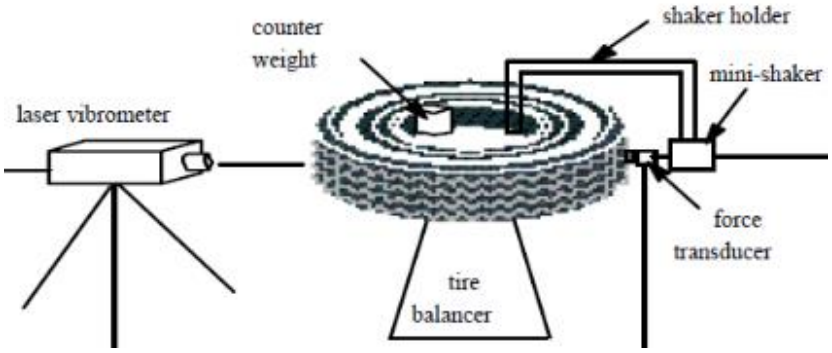

Figure 1.5. Experimental set-up for tire vibrations measurements by Bolton (1998).

Figure 1.6 shows the main results. The process to obtain these plots was to first normalize the normal surface velocities after dividing them by the input force amplitude and the largest value from all frequencies. The outcome of this is shown in Figure 1.6a. In this case, the x-axis shows the angle around the tire's centerline and the y-axis shows the frequencies. A wavenumber transform was then performed along the circumferential direction of the tire, thus obtaining the dispersion plot in Figure 1.6b. These results, therefore, show the measured normal surface velocities along the centerline of the tire, expressed as

$$v_r(\theta) = \sum_{n=-\infty}^{\infty} a_n e^{-in\theta} = \sum_{n=-\infty}^{\infty} a_n e^{-ik_{\theta n} s} \tag{1.1}$$

where $v_r(\theta)$ is the normalized radial velocity as a function of θ, the angle from the drive point to each measurement location on the tire surface, s is the distance between these two points, and the circumferential wavenumber is defined as $k_{\theta n} = 2n/R$, where R is the tread band radius. Therefore, Figure 1.6b shows $|a_n|$ as a function of frequency and the wavenumber $k_{\theta n}$.

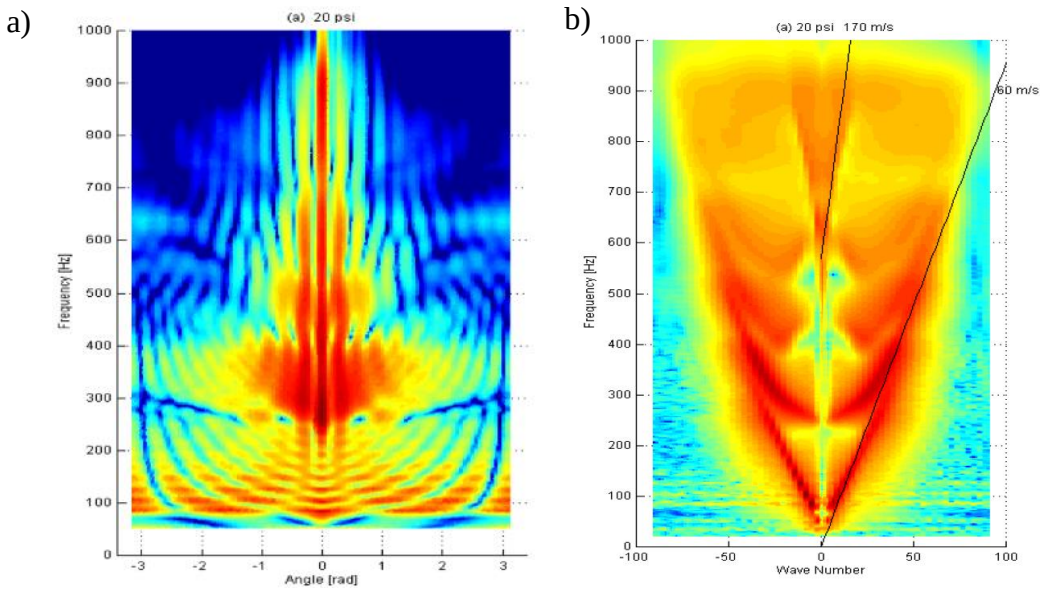

Figure 1.6. Normalized measured surface velocities as a function a) frequency and space, and b) frequency and wavenumber, for a tire of size 215/70R14 inflated at 20 psi, presented in the work by (Bolton, 1998).

Bolton (1998) provided a schematic that explains in more depth the results in Figure 1.6b. This is presented in Figure 1.7, where various curves for positive wavenumbers are illustrated. Each of the curves is associated with the transversal modes $m = 1, 2, 3 ... N_m$ of the tire. The transversal modes are cut-off (decaying or evanescent waves) until they reach a specific cut-on frequency. At this point, they start propagating along the circumferential direction of the tire. The location of the cut-on frequency depends on the structural properties of the tire. The dispersion in Figure 1.6 shows that tires have a waveguide behavior. When a circumferential wavenumber equals to an integer, then a circumferential mode is assumed. Finally, the group velocity of the propagating waves along the circumferential direction is equal to the slope of the curves in Figure 1.7. Therefore, making it possible to track fast and low velocity traveling transversal modes.

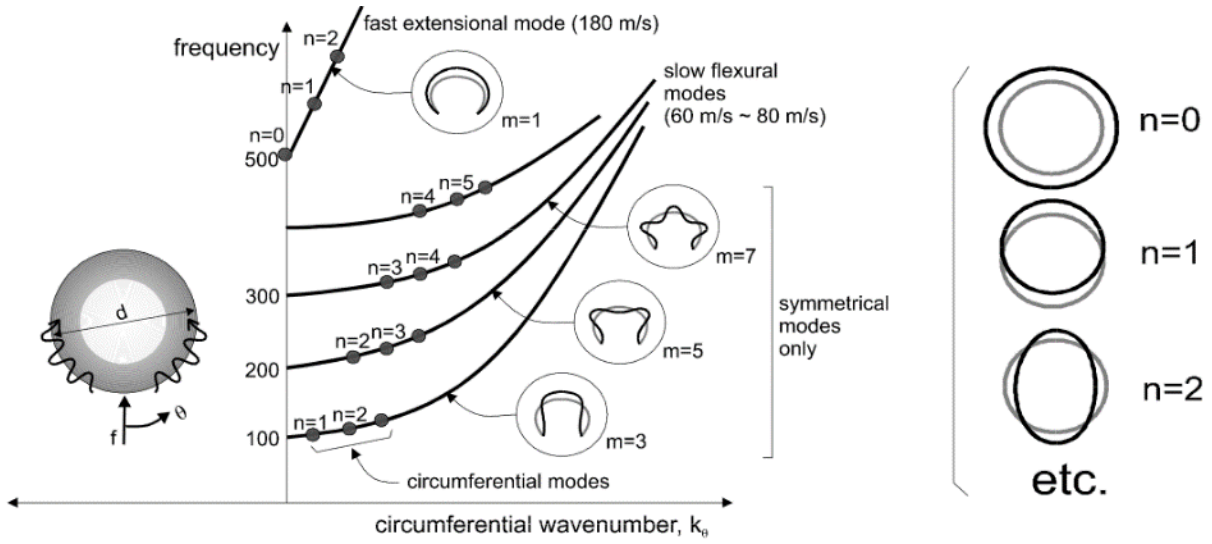

Figure 1.7. Dispersion characteristics of tire carcass vibrations (Bolton, 1998).

The experiments performed by Bolton (1998) were extended to capture the vibration behavior of the tire during rotation. This was presented in the work by Klos et al. (2002), where vibrations of a rolling tire were measured up to a frequency of 1400 Hz using a laser Doppler vibrometer. The experimental set-up is shown in Figure 1.8.

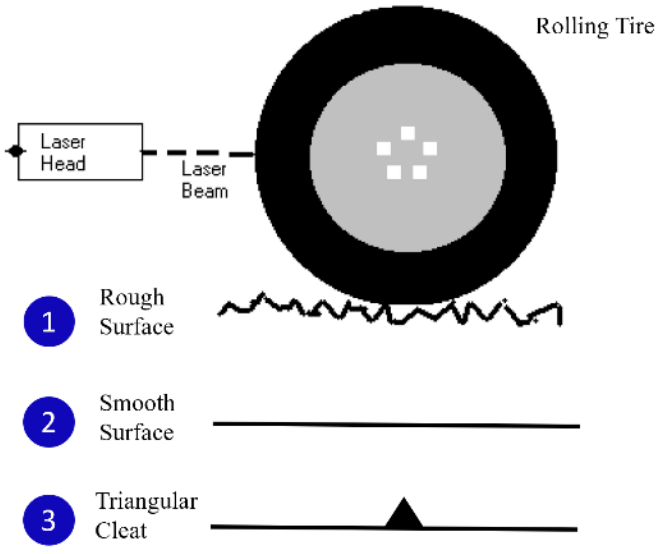

Figure 1.8. Experimental set-up by Klos et al. (2002).

The tire was mounted on a truck frame on top of a roller. Slick and treaded tires were covered with retroreflective tape and their vibrations measured with the vibrometer. Three types of surfaces were used during the experiments. A rough surface made of wood with transversal grooves, a smooth surface corresponding to the metal surface of the roller, and finally a surface with a triangular cleat. The grooved and cleat surfaces are shown in Figure 1.9.

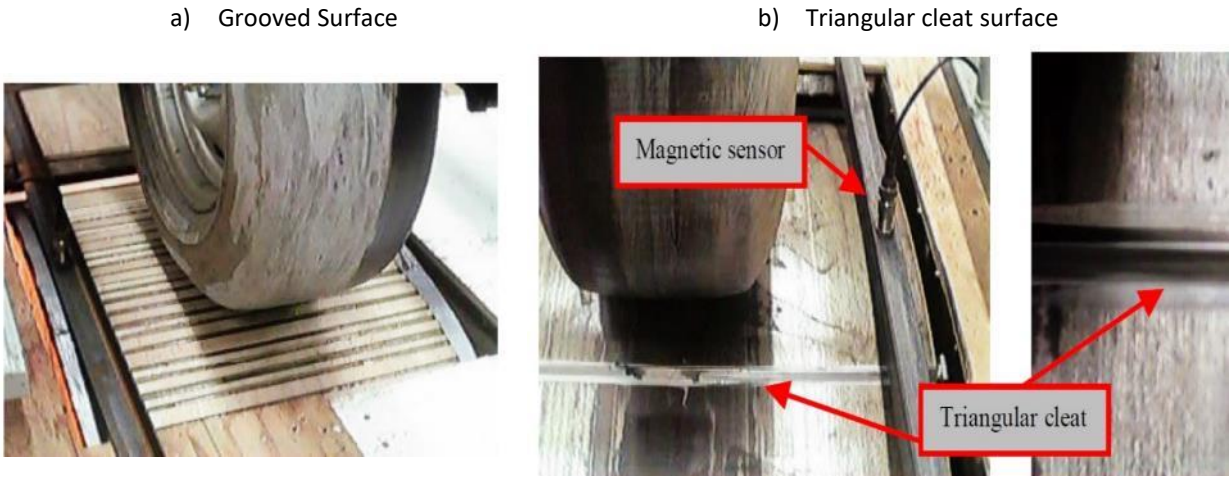

Figure 1.9. Surfaces using during rolling tire test by Klos et al. (2002).

A magnetic sensor was used to detect when the cleat hits the leading edge of the contact patch. The purpose of measuring this signal was to use it as a reference to synchronize the phase of the measured response of the tire. The tire was rolled at three different speeds of 13, 20 and 24 m/s and the applied load on the tire was equal to 1735 N.

The dispersion plots for a rolling velocity of 20 m/s and the static case are compared in Figure 1.10. These results show that the rotation causes a change in the wave speed, i.e. the dispersion curves with positive wavenumbers have a different slope to those with negative wavenumber. The reason is that waves in one direction travel against the rotation of the tire while the other travels in the same direction of rotation. Klos et al. (2002) observed that the change in slope is proportional to the rotational velocity. In addition, stiffening effects due to rotation were negligible. This suggests that accounting for effects of rotation when modeling the structure allows capturing changes of wave speed along the circumferential direction of the tire. However, the findings

presented in this thesis suggest that the amplitudes of the tire's response do not change significant when rotation is included. Therefore, large changes in the produced noise are not expected.

a) Rotating Speed 20 m/s. b) Static Tire

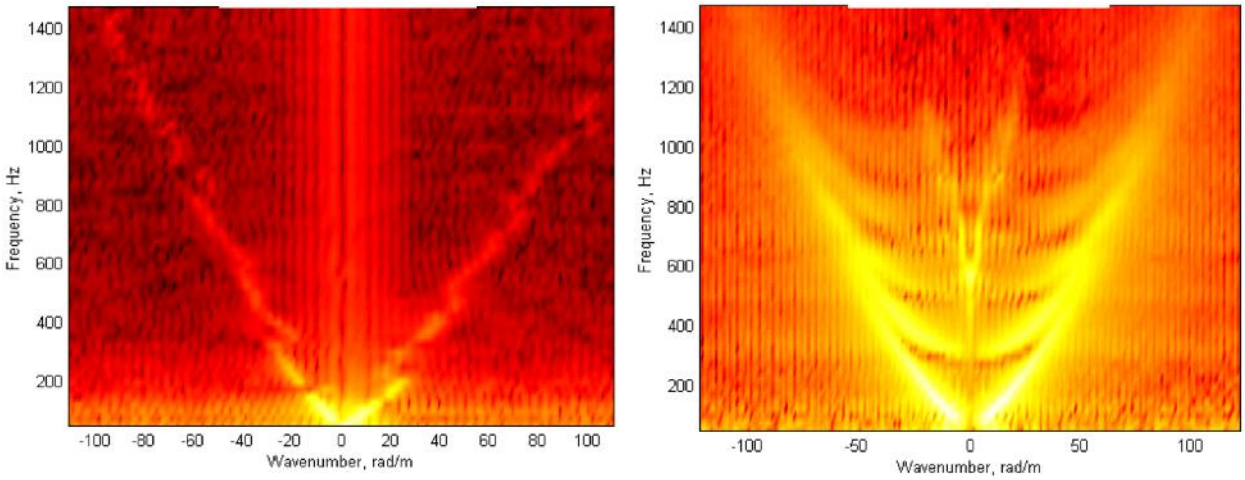

Figure 1.10. Dispersion plots a) for a rotating tire, b) for a static tire, presented in the work by Klos et al. (2002).

Additional insight on a tire's structural response was provided by Bernhard (2000). In this work, the response of the tire was measured with a laser Doppler vibrometer over a 2 cm x 2 cm surface grid on the belt surface of the tire. The tire used for experiments was slick and it was excited using a dynamic shaker at the center of the belt, similar to the set-up shown in Figure 1.5. The main results of this work are presented in Figure 1.11. The real component of the mobility frequency responses on an unwrapped view of the belt is discussed. Figure 1.11a shows result for a frequency of 109 Hz. In this case, modes are observed along both directions of the tire. If the frequency is increased to 653 Hz as shown in Figure 1.11b, modes still exist along the transversal direction. However, along the circumferential direction, resonant behavior is no longer observed. In this case, waves are present, either propagating and decaying. Finally, at a higher frequency of 1231 Hz, Figure 1.11c shows the behavior of a point force acting on an infinite structure, e.g. decaying cylindrical waves. In this case, boundary conditions have an insignificant role in the tire's response.

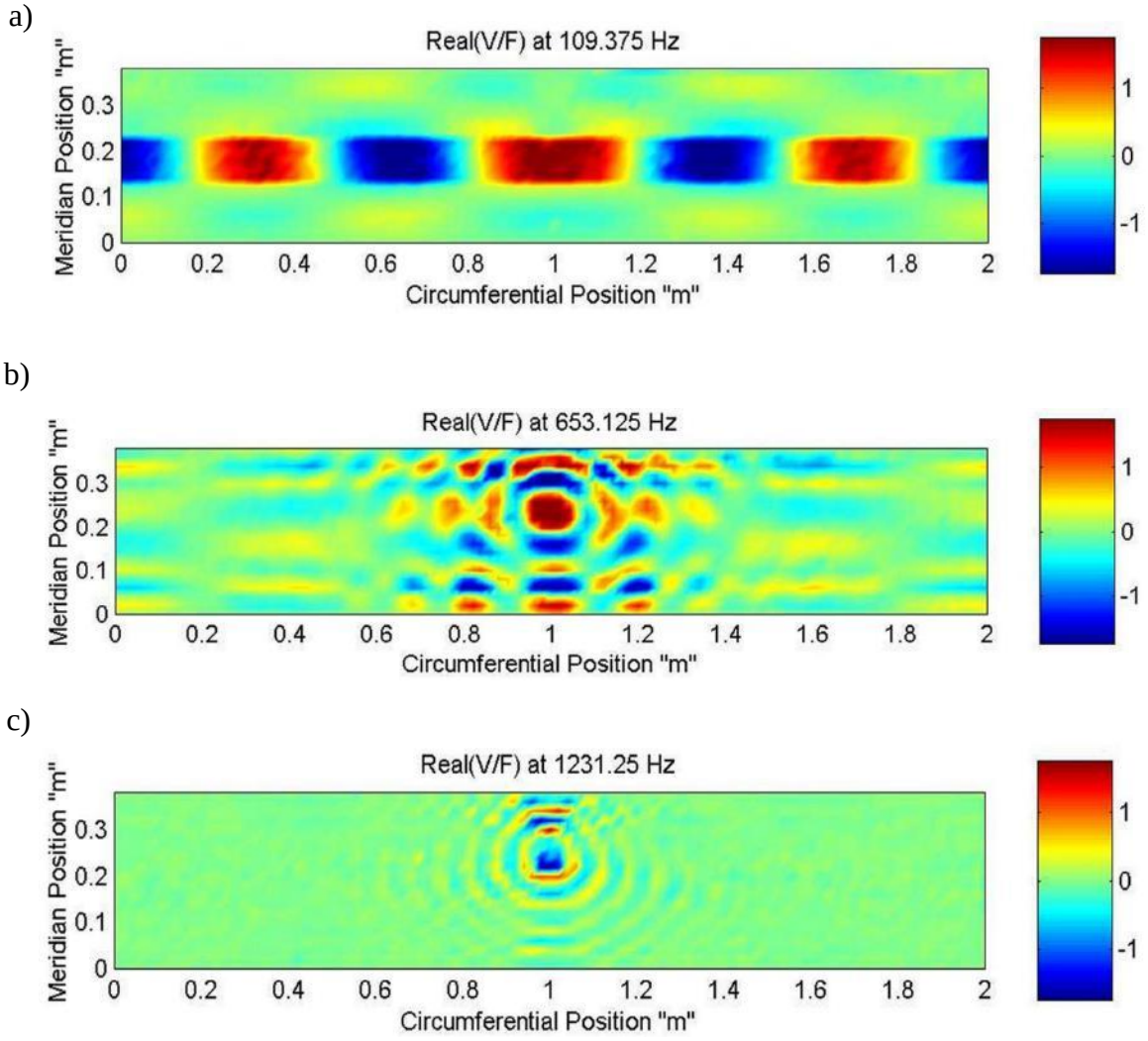

Figure 1.11. 2D display of real frequency response functions at three different frequencies: a) 109 Hz, b) 653 Hz, and c) 1231 Hz, presented in the work by Bernhard (2000).

The experimental evidence shown above demonstrates that in the mid-frequency range, approximately between 500 Hz and 1500 Hz, waves propagate and decay along the circumferential direction of the tire. In order to capture this mid-frequency structural behavior of the tire, an appropriate modeling approach is required. In the next section, a summary of the efforts made by various investigators to model vibration-induced TPIN in the mid-frequency is summarized.

1.1. Review of Mid-Frequency Tire Vibrations and Noise Models

Kropp (1999) provided one of the first approaches intended for predictions of mid-frequency vibration and induced noise produced by a tire. The suggested range of accuracy is within 400-3,000 Hz. The tire's structure was modeled as a simply supported plate. The reason is that above a tire's characteristic ring frequency, typically located between 400 Hz and 500 Hz, the curvature of the tire can be ignored. In such a case, it can be assumed that bending waves dominate the full dynamic response of the tire. However, above 3,000 Hz the model becomes inaccurate because at these high frequencies the plate cannot be assumed to be thin anymore.

The assumed vibratory response for this model consisted of modes along both the tire's circumferential and transversal directions of the tire. In addition, the main structural effects of a tire included in the model are the following: (1) Inflation pressure was accounted in two ways. First, by adding membrane tensions along both circumferential and transversal directions of the tire. Secondly, with a stiffness bed below the belt. (2) The plate was assumed to have orthotropic properties. This accounted for conventional structural characteristics of a tire, where properties along the transversal direction are different from those along its circumferential direction. The reason is that a cross-section of a tire is typically composed of multiple layers including components such as inner-liners, plies, fillers, among others. While, along the circumferential direction, uniformity is expected.

The details of the formulation used in Kropp's structural model will be addressed in Chapter 2. The response of the tire for this model was quantified using mobility frequency response functions i.e. output normal surface velocities divided by the normal input force amplitudes. These were compared to measured data, as shown in Figure 1.12. In this case, the responses were computed for an arbitrary point in the center of the belt i.e. not specified by the author, while excitation was located at the center of the belt.

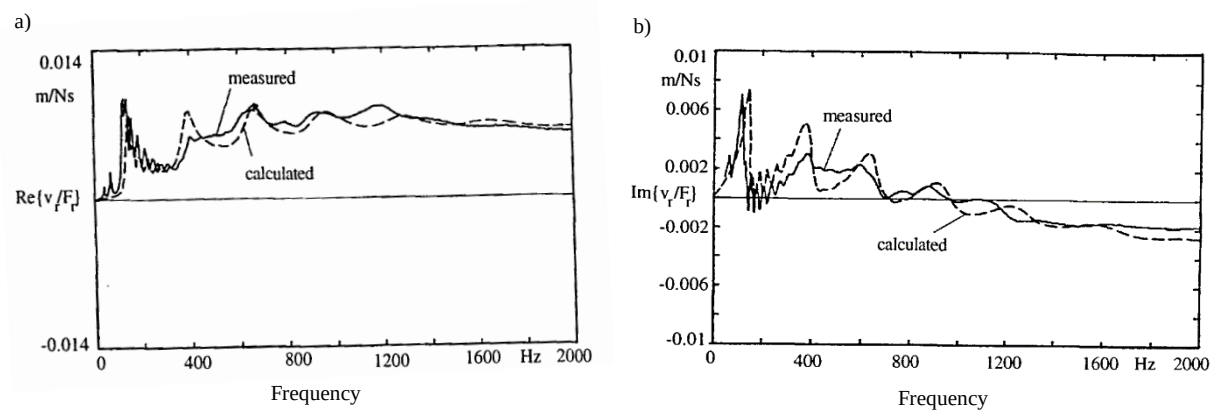

Figure 1.12 a) Real and b) imaginary components mobility FRF of a tire, reported by Kropp (1999).

The measurements and calculation in Figure 1.12 show good agreement at certain peaks above 400 Hz, however, at some frequencies, the model does not perform well. The reason is that at high frequencies modes should not be assumed along the circumferential direction of the tire. Results provided by other researchers (Perisse et al., 2000) show that Kropp's model tends to over-predict the vibratory response of the tire.

Perisse et al. (2000) compared results obtained with Kropp's model to experimental data. The input mobility frequency response function for both cases is shown in Figure 1.13a. In this case, the results obtained with Kropp's model show good agreement at high frequencies. However, below 1500 Hz, this is not the case. In order to address this problem, Perisse et al. (2000) proposed a modified version of Kropp's modeling approach. In this case, the cross-stiffness of the plate was artificially modified to an unrealistically high value. The objective was to improve the model's accuracy below 400 Hz. Figure 1.13b shows Perisse's modified model results. In this case it can be observed that accuracy was improved at low frequencies. However, at high frequencies, overpredictions became very large. The main conclusion from this work is that by controlling the cross-stiffness of Kropp's model, overpredictions at specific frequency ranges can be reduced. This method will be referred to in this work as *Modified Kropp's Model*.

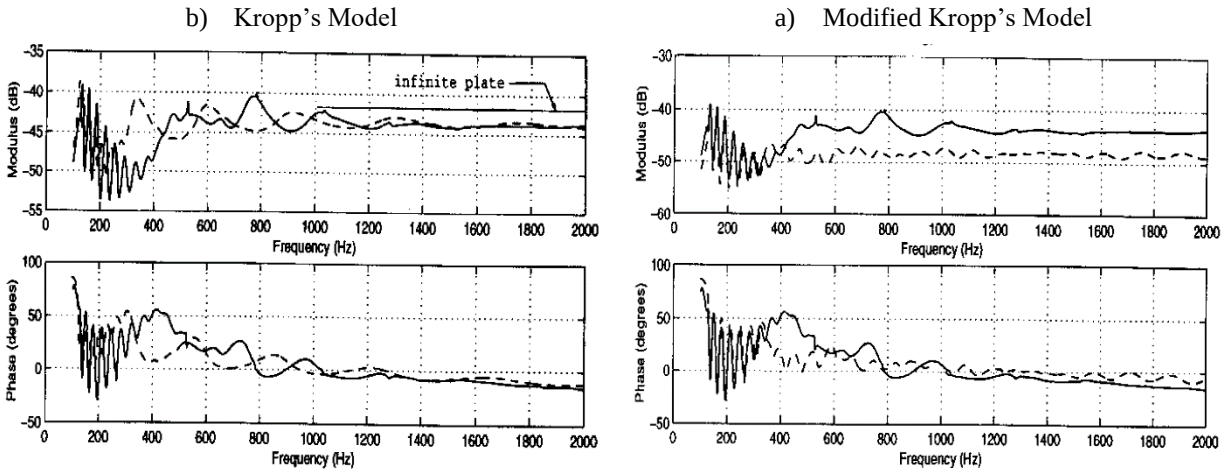

Figure 1.13. Experimental results of Mobility FRF compared to a) Kropp's model amplitude and phase, b) Modified Kropp's model's amplitude and phase (Perisse et al., 2000).

In addition to developing a structural model of the tire, Kropp (1999) also developed a contact model to excite the tire structure during rolling conditions. In order to compute the total response of the system, the pavement induced forces were multiplied by the appropriate impulse response function of the structural model. This is defined as follows

$$w_e = \sum_m F_m(t) \times g_{m,e}(t) \tag{1.2}$$

where $g_{m,e}(t)$ is the impulse response function of a tire excited at a point m, and measured at a point e on the tire surface. On the other hand, the input force amplitudes $F_m(t)$ are calculated by assuming that the local tread deformation follows Hooke's law. For example, if the tire is excited at a point e, as shown in Figure 1.14, then the forces can be computed with the following expression

$$F_e(N\Delta t) = s_e \Delta y_e(N\Delta t) H\left[-\Delta y_e(N\Delta t)\right] \tag{1.3}$$

where,

$$H(x)=\begin{Bmatrix}0 & (x<0)\\ 1 & (x\geq 0)\end{Bmatrix} \tag{1.4}$$

In equation (1.3), time has been discretized into N number of time intervals Δt. Furthermore, s_e corresponds to the local tread's stiffness constant and Δy_e is the corresponding local displacement induced by the pavement profile.

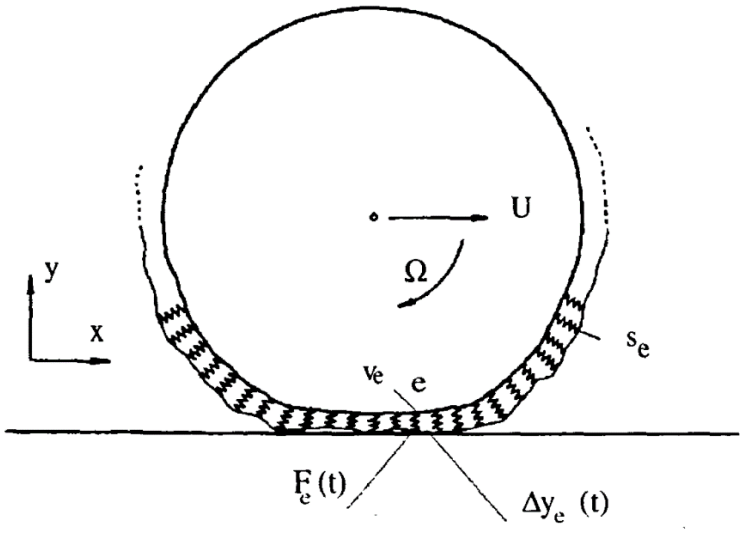

Figure 1.14. Contact model implemented by Kropp (1999).

After Kropp defined the contact and structural model for a tire, an acoustic model was also implemented for noise predictions. The model coupled the vibratory response with its produced noise and consisted of a two-multipole system shown in Figure 1.15. This multipole system approach can only be implemented for high frequencies and fulfills the boundary conditions defined at the vibratory surface of the tire. In order to extend the 2D acoustic model case shown in Figure 1.15, the sources are assumed to be infinite cylinders where only a short part is vibrating i.e. the width of the tire, while the rest is assumed to be rigid.

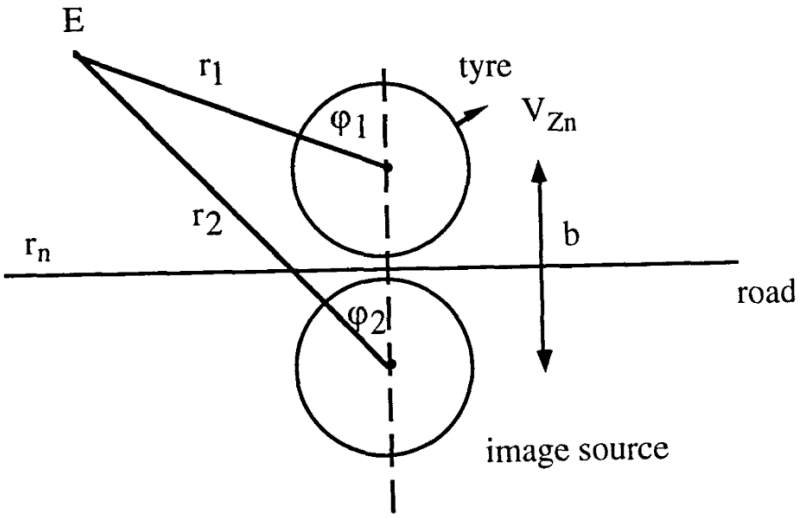

Figure 1.15. Two-multipole acoustic model for tire vibration-induced noise predictions (Kropp, 1999).

The power of the vibrating infinite cylinder is given as

$$P(\omega) = \frac{\rho c a}{8\pi^2} \sum_{\nu=-\infty}^{\infty} \int_{-\infty}^{\infty} \left| v_{r\nu}(\omega, k_z) \right|^2 \sigma_\nu(\omega, k_z)\, dk_z \tag{1.5}$$

where $v_{r\nu}(\omega, k_z) = v_{r\nu}(\omega) \cdot \sin(k_z b)/b$ correspond to the Fourier coefficients of the normal surface velocities of the tire. Therefore, the calculated sound power is related directly to all ν modes in the circumferential direction of the tire, and wavenumbers k_z along its transversal direction. Additional parameters included in equation (1.5) are the radius of the tire a, the speed of sound c and air density ρ. On the other hand, $\sigma_\nu(\omega, k_z)$ corresponds to the sound radiation efficiency defined as

$$\sigma_\nu(\omega, k_z) = \frac{2\omega}{a\pi c} \frac{1}{\sqrt{\frac{\omega^2}{c^2} - k_z^2}} \frac{1}{\left| H_\nu^{(2)\prime}\left(a\sqrt{\frac{\omega^2}{c^2} - k_z^2} \right) \right|^2} \tag{1.6}$$

In this case, the operator $H_{\nu}^{(2)}{}'(\bullet)$ corresponds to the derivative of the Hankel function.

The complete prediction package for vibration-induced noise developed by Kropp (1999), validations were made using a test drum. This test set-up is shown in Figure 1.16. Normal surface accelerations were measured with accelerometers mounted on the tire tread pattern. A laser Doppler vibrometer was also used to measure vibrations in an exterior observer's coordinate system. Finally, the noise was measured using microphones. On the other hand, the drum provided a periodic excitation of the tire structure.

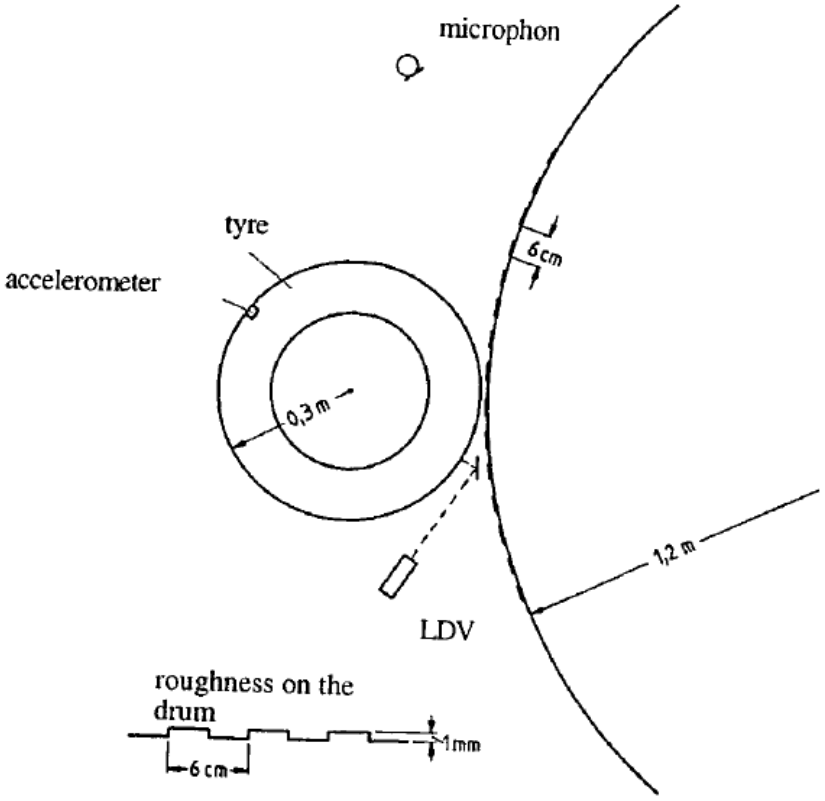

Figure 1.16. Experimental set-up used for validations in the work by Kropp (1999).

The validation results are shown in Figure 1.17 and Figure 1.18. Both, normal surface velocities measured with the laser Doppler vibrometer and the produced noise are shown.

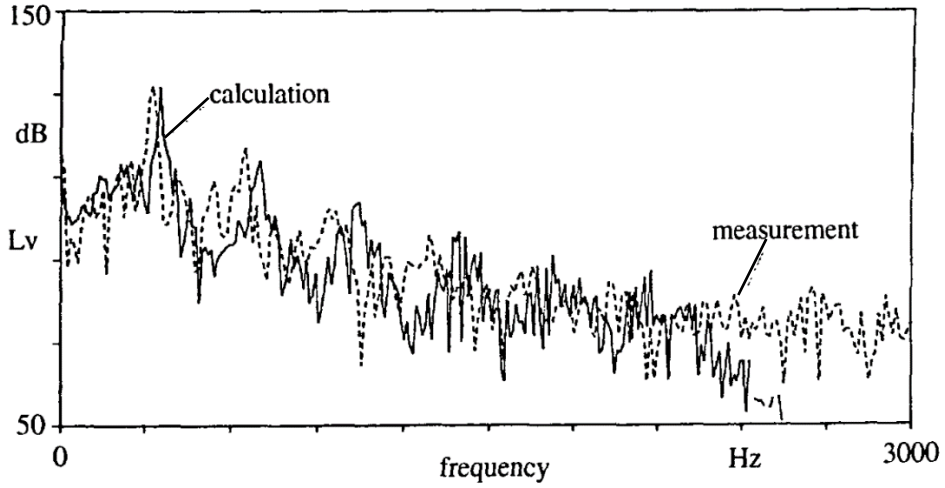

Figure 1.17. Comparison of measured and calculated local velocity, dB ref. 5×10^{-8} [m/s] (Kropp, 1999).

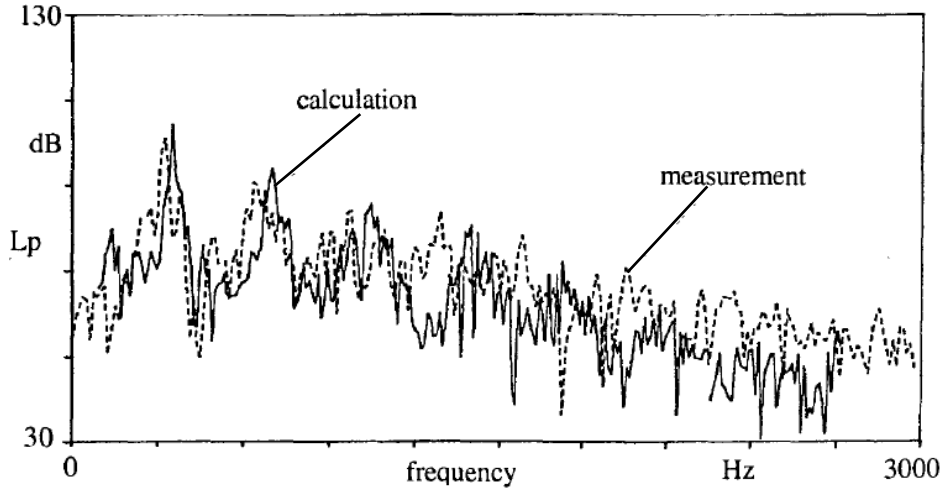

Figure 1.18. Comparison of measured and calculated noise, dB ref. 20×10^{-6} [Pa] (Kropp, 1999).

According to the author, both surface velocities and noise agrees well if predictions are compared to the measurement results. However, large discrepancies can be easily observed in both spectrums. For example, within the mid-frequency range (500-1500 Hz) in Figure 1.18, differences of up to 20 dB can be observed.

Another approach to model the structure of the tire was presented by O'Boy et al. (2009b). In this case, a modification to Kropp's model was presented. This approach assumed that the tire belt

behaves as a Mindlin plate, where shear deformations and rotary inertia play a significant role in the dynamic response. The author suggests that a thin plate is valid only if the flexural wavelength is greater than six times the plate's thickness. In addition, the combined thickness of a tire belt with the added tread rubber cannot be modeled as a thin plate. The intended frequency range of this model is within 200 Hz to 2 kHz.

In order to obtain the response of the tire belt, a modal approach both along the circumferential and transversal directions of the tire was implemented. Wavenumber and Fourier transforms were used to compute the response. However, the main contribution of this study is an alternative approach to define the appropriate tire structural parameters used in the plate model. In order to do this, an optimization was used to reduce the error between the frequency response function of the plate and the cylindrical multilayered model shown in Figure 1.19.

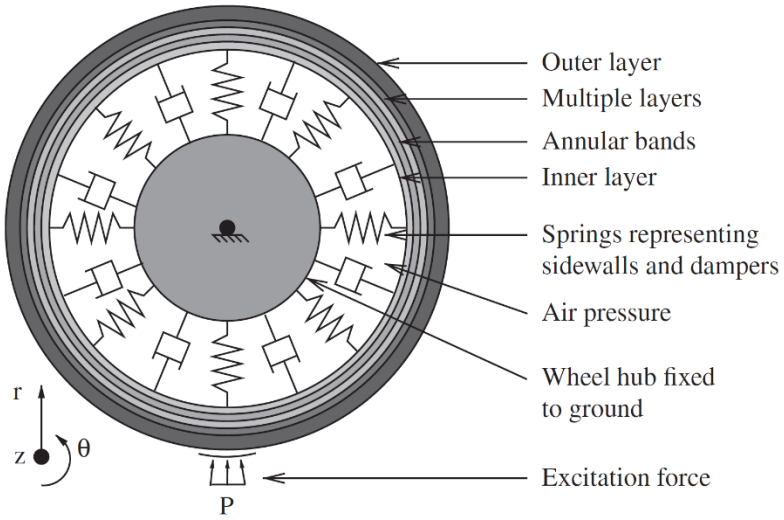

Figure 1.19. Cylindrical multilayered tire model developed by O'Boy et al. (2009a).

The multilayered approach treated each of the layers as a viscoelastic solid defined by its strain-displacement and stress-strain relationships. The latter being defined in terms of each layer material's Lame coefficients. After using Hooke's law and Newton's second law, then the following wave equation was obtained for each layer

$$(\lambda+\mu)\nabla(\nabla\cdot\vec{u})+\mu\nabla^2\vec{u}=\rho\ddot{\vec{u}} \tag{1.7}$$

In this case, λ and μ are the material's Lame constants while the vector $\vec{u}$ corresponds to the 3D displacements along the tire's cylindrical coordinates (r,θ,z). In this case, the displacement vector was defined in terms of a scalar value ∅ and a potential vector $\vec{A}$. Both were defined by the next relationship

$$\vec{u}=\nabla\phi+\nabla\times\vec{A},\qquad \nabla\cdot\vec{A}=0 \tag{1.8}$$

Equation (1.7) was then decoupled in terms of ∅ and $\vec{A}$ as follows

$$\nabla^2\phi=\frac{1}{\alpha^2}\ddot{\phi},\qquad \alpha^2=\left(\frac{\lambda+2\mu}{\rho}\right) \tag{1.9}$$
$$\nabla^2\vec{A}=\frac{1}{\beta^2}\ddot{\vec{A}},\qquad \beta^2=\left(\frac{\mu}{\rho}\right)$$

After a wavenumber and Fourier transforms were applied to both expressions in equation (1.9), analytical solutions were defined as a linear combination of first and second kind Bessel functions. These provided the solution for ∅ and $\vec{A}$, now in the frequency and wavenumber domain. These were then translated back into the displacement $\vec{u}$ and stress $\vec{\sigma}$ by using equation (1.8) and Hooke's law. The resulting system is the following

$$\begin{pmatrix}\vec{\boldsymbol{\sigma}}\\ \vec{\boldsymbol{u}}\end{pmatrix}=\begin{pmatrix}\boldsymbol{G}\\ \boldsymbol{H}\end{pmatrix}\boldsymbol{W}\ \boldsymbol{S}\ \vec{\boldsymbol{C}} \tag{1.10}$$

Where W, S, G, and H are matrices defined by the terms within the implemented Hooke's law and equation (1.8). On the other hand, $\vec{C}$ corresponds to a vector containing six constants and their corresponding Bessel functions. This equation provides the displacements on a single tire layer at any (r,θ,z) location. Furthermore, equation (1.10) can be applied separately for each layer and

then coupled together for the entire multilayered tire response. Finally, a set of six boundary conditions are needed to find the six Bessel function constants in equation (1.10). Three of them defined at the tire's air cavity and three of them on the outer layer in terms of applied forces and atmospheric conditions.

The main limitations of this multilayer viscoelastic model are the following: i) The sidewalls are not modeled but represented by a distributed spring stiffness along the radial direction. This is rather a simplistic approach and may be the source of inaccuracies. ii) The tire's composite materials are approximated by including bands of stiff material between the layers in the circumferential and radial directions. Even though no other model implements such a detailed approach, this may not be representative of a real tire structural construction. ii) Modes are assumed along all directions of the tire instead of waves.

After the optimization procedure was implemented using the multilayered model, the equivalent plate parameters for a treaded tire obtained by O'Boy et al. (2009b) are shown in Figure 1.20. These correspond to the plate bending stiffness, complex loss factor introduced for damping purposes η_D, and additional damping coefficient proportional to the Laplacian of the plate's response velocity η_p (referred as Crighton damping).

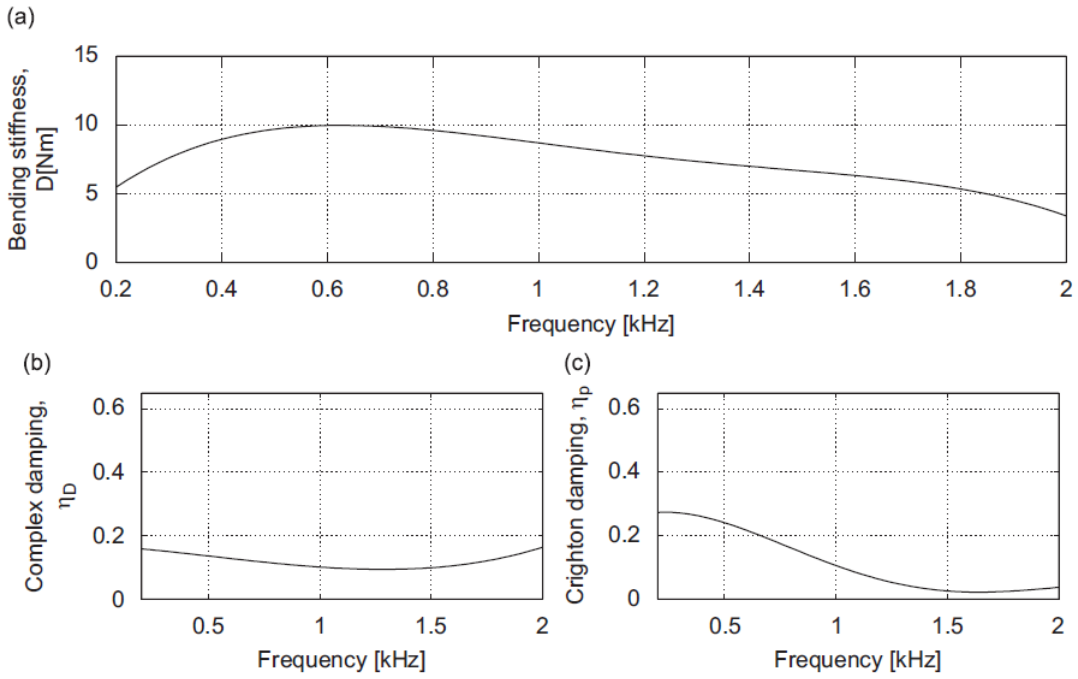

Figure 1.20. Equivalent plate structural parameters for a treaded tire including (a) Bending Stiffness, (b) Complex loss factor, and (c) Crighton damping. All presented in the work by O'Boy et al. (2009b).

Furthermore, this study includes a contact model that defines the total displacement of the tire. The approach is very similar to that implemented by Kropp (1999). The response of the tire, in this case, is defined as

$$u_{\beta}^{belt}(t) = \sum_{\alpha=1}^{N} G_{\beta\alpha}(t-\tau)\, f_{\alpha}(\tau)\, d\tau \tag{1.11}$$

In this case, $u_{\beta}^{belt}(t)$ corresponds to the total normal surface displacement of the tire at a block β due to the excitation on the contact patch. On the other hand, $G_{\beta\alpha}(t)$ is the time domain impulse response function of the plate excited at a block α at time τ, calculated at a block β at time *t*. While, $f_{\alpha}(t)$ is the input force on the tread block α at time τ calculated by a local Hooke's law. The latter defines the input force of the system due to the local block deformation, induced by the pavement profile. The block notation and input force representation for both are shown in Figure 1.21. The

total displacement is defined by convolving $G_{\beta\alpha}(t)$ and $f_{\alpha}(t)$, and finally adding all for the N number of blocks excited in the contact patch.

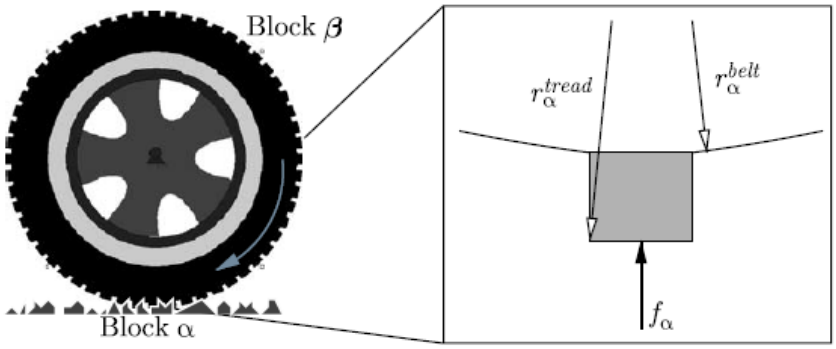

Figure 1.21. Representation of a rolling tire and block α where contact force f_{α} is applied and block β where displacements are predicted by O'Boy et al. (2009b).

Finally, the normal surface vibrations of the tire were coupled with the produced noise by means of a boundary element method. These results were then validated against experimental data collected on a Suzuki Vitara, equipped with a 5-microphone set-up mounted on a metal frame around its rear tire as shown in Figure 1.22.

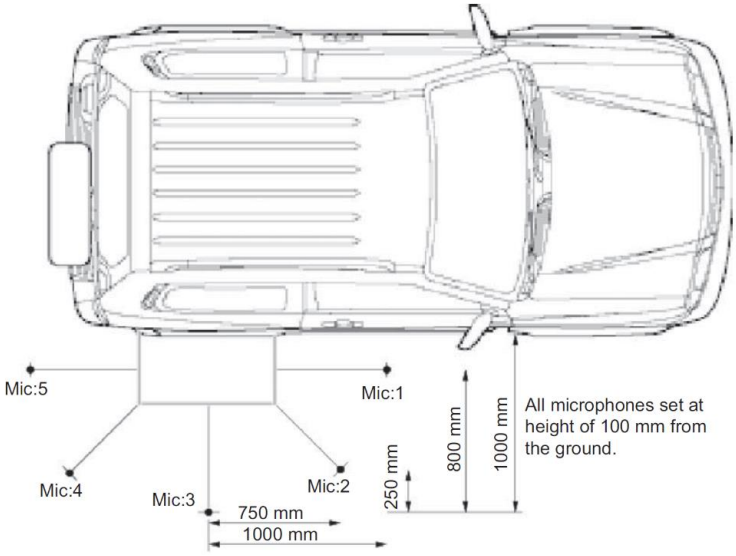

Figure 1.22. Vehicle and microphone set-up used for validation of the model developed by O'Boy et al. (2009b).

The test was run for speeds of 70, 80, and 90 km/h on an ISO-10844 specification road. However, the tire model nor size was specified. The modeled and experimental A-weighted spectrums for all microphone locations are specified shown in Figure 1.23, for a speed of 80 km/h. These results do not show good predictions, as errors of up to 20 dBA can be observed by simple inspection.

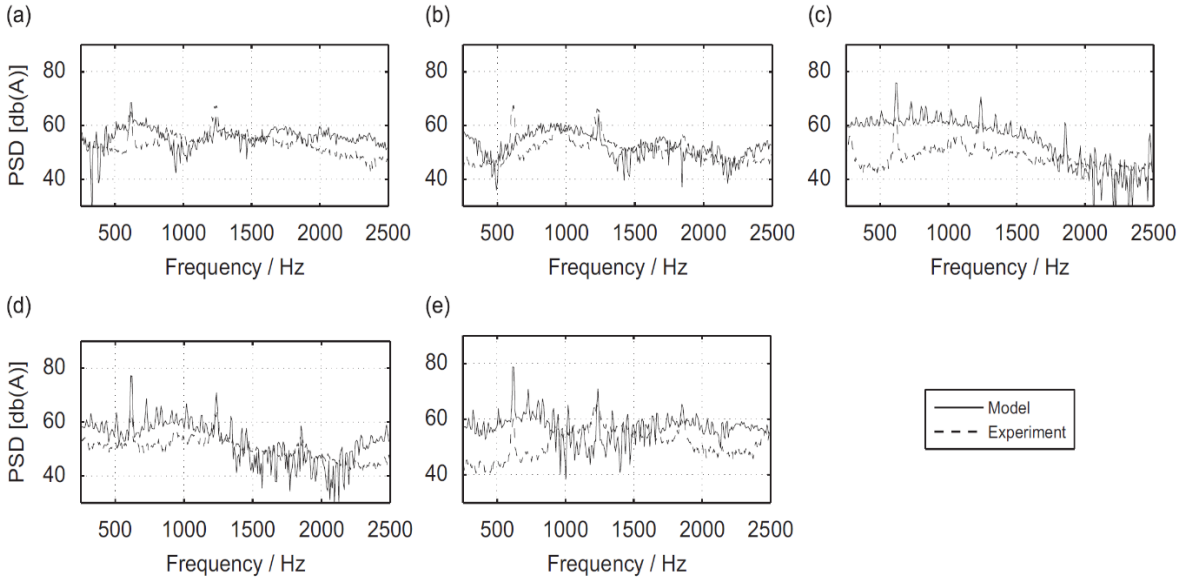

Figure 1.23. A-weighted spectrum for a treaded rolling tire on an ISO-10844 pavement surface at 80 km/h at (a) microphone 1, (b) microphone 2, (c) microphone 3, (d) microphone 4, and (e) microphone 5.

Another modeling approach intended to improve Kropp's structural model by including a wave-propagation formulation was attempted by Larsson et al. (2002). This work proposed a double-layered tire model. Radial and tangential motion were accounted for in this model. Thus, the tire is modeled as a set of two coupled thick plates, as shown in Figure 1.24. The top layer represents the tread rubber, while the bottom layer corresponds to the stiff belt of the tire. In this study, the author mentions that due to the high damping of the rubber materials, it is reasonable to assume that the plate is an infinite waveguide along the circumferential direction.

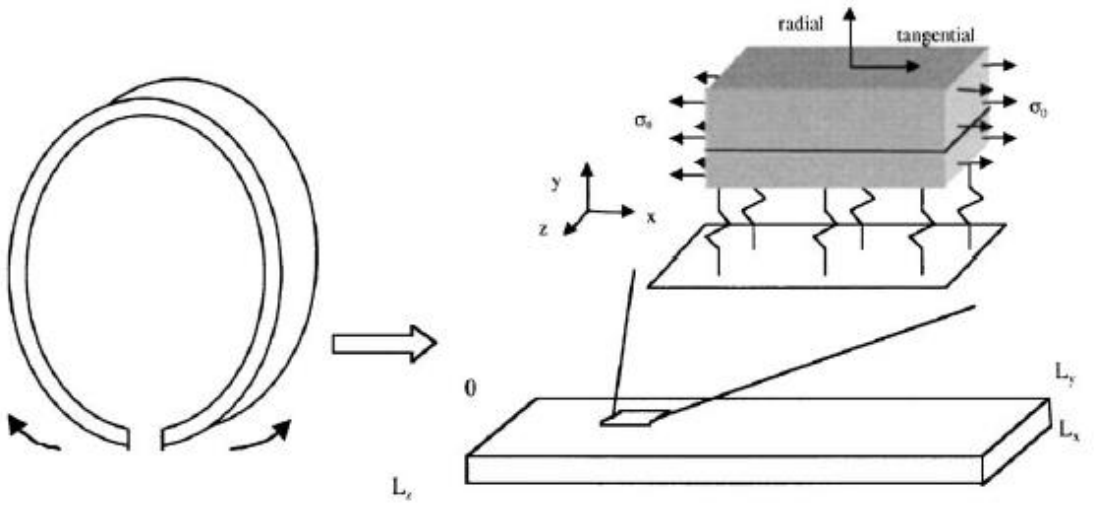

Figure 1.24. Double-layered plate model developed by Larsson et al. (2002).

The homogeneous equations of motion for each layer in the wavenumber domain are the following

$$\begin{pmatrix} m_{11} & m_{12} & m_{13} \\ m_{21} & m_{22} & m_{23} \\ m_{31} & m_{32} & m_{33} \end{pmatrix} \begin{pmatrix} \hat{\xi} \\ \hat{\eta} \\ \hat{\zeta} \end{pmatrix} = k_s^2 \begin{pmatrix} \hat{\xi} \\ \hat{\eta} \\ \hat{\zeta} \end{pmatrix} \tag{1.12}$$

In this case, $\hat{\xi}$, $\hat{\eta}$ and $\hat{\zeta}$ are the mid-surface displacements defined along the x, y and z directions. The system is assumed to be a complex harmonic in time, therefore k_s^2 corresponds to a normalized frequency of the system. On the other hand, all the terms denoted with m are a function of the wavenumber values k_1, k_2 and k_3 along the x, y, and z.

A set of 3 eigenvalue and eigenvectors are obtained after solving equation (1.12). The eigenvalues correspond to the normalized natural frequencies of the system. The eigenvectors provide the relative displacement amplitudes along all three directions of the waves. Therefore, the solution to this eigenvalue problem requires a predefined set of wavenumber values for k_1, k_2 and k_3.

Due to the interaction between the two layers, Larsson et al. (2002) speculated the existence of three types of waves that propagate along the tire's circumferential direction. The first one is dominated by bending effects, the second one is due to longitudinal motion, and the third one is referred to as a rotational wave. These three types of waves are illustrated in Figure 1.25.

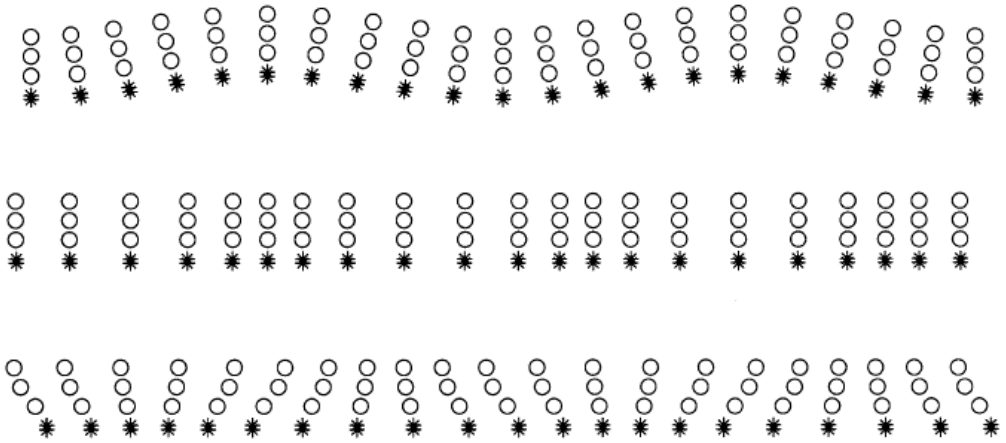

Figure 1.25. Three types of waves propagating along the circumferential direction of the tire. Circles represent points in the tread rubber compound and stars correspond to the stiff belt (Larsson et al., 2002).

Despite clearly acknowledging the existence of waves along the circumferential direction of the tire, the following modal solution was assumed for the radial and tangential displacements of the top surface of the top layer

$$\eta = -4j\sum_{m=1}^{\infty}\sum_{n=1}^{\infty}\eta_{m,n}^{lay2}\left(L_y\right)\cos\left(k_m x\right)\sin\left(k_n z\right) \tag{1.13}$$
$$\xi = -4j\sum_{m=1}^{\infty}\sum_{n=1}^{\infty}\xi_{m,n}^{lay2}\left(L_y\right)\cos\left(k_m x\right)\sin\left(k_n z\right)$$

where $\eta_{m,n}^{lay2}\left(y\right)$ and $\xi_{m,n}^{lay2}\left(y\right)$ are the radial and tangential modal amplitudes, and the wavenumbers k_m and k_n are the circumferential and transversal wavenumbers respectively. These are defined as

$$k_m = \frac{2m\pi}{L_x} \quad \text{for } m = 1, 2, 3... \tag{1.14}$$

$$k_n = \frac{n\pi}{L_z} \quad \text{for n} = 1, 2, 3...$$

The transversal wavenumber is obtained by assuming simply supported boundary conditions on the plate's edges. The circumferential wavenumber is obtained by assuming that a complete wavelength always fits the circumference of the tire. Using a set of discrete wavenumbers, as shown in equation (1.14) results in modes along both the circumferential and transversal directions of the tire.

The input mobility frequency response function for a tire of size 205/60R15 was simulated and the results compared to experimental data. These results are shown in Figure 1.26. The experimental data was obtained by exciting the tire at the belt along its radial direction using a dynamic shaker. Results do not show good agreement, especially for the mid-frequency range.

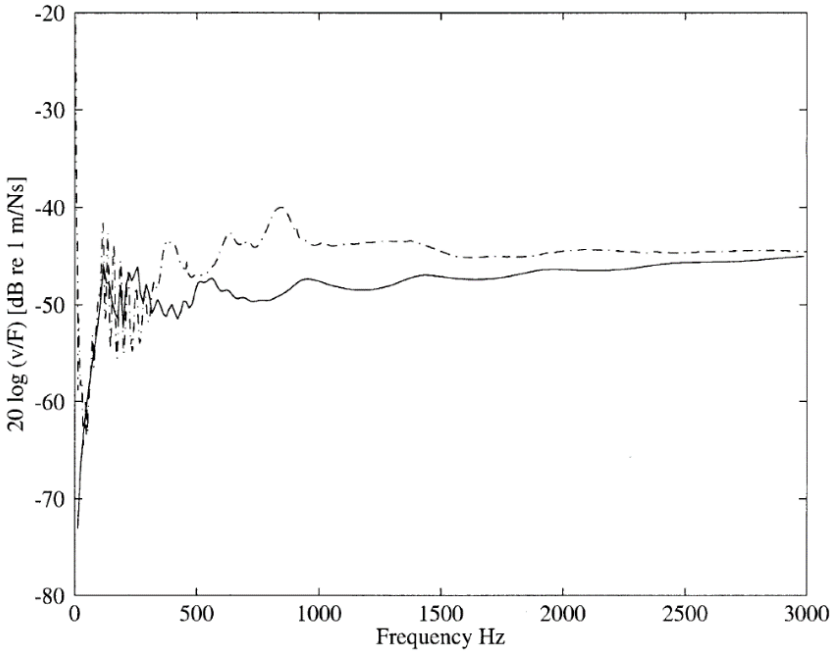

Figure 1.26. Modeled (solid line) and measured (dashed line) input mobility frequency response function reported in the work by Larsson et al. (2002).

Pinnington et al. (2002) approached the mid-frequency tire vibrations modeling approach differently to the models presented above. The approach was to model the tire belt as a Timoshenko beam with its length representing its circumferential direction. Therefore, this model accounted for bending, shear and rotary inertia along the tire's circumferential direction. The sidewalls are accounted for by using a line impedance, as shown in Figure 1.27.

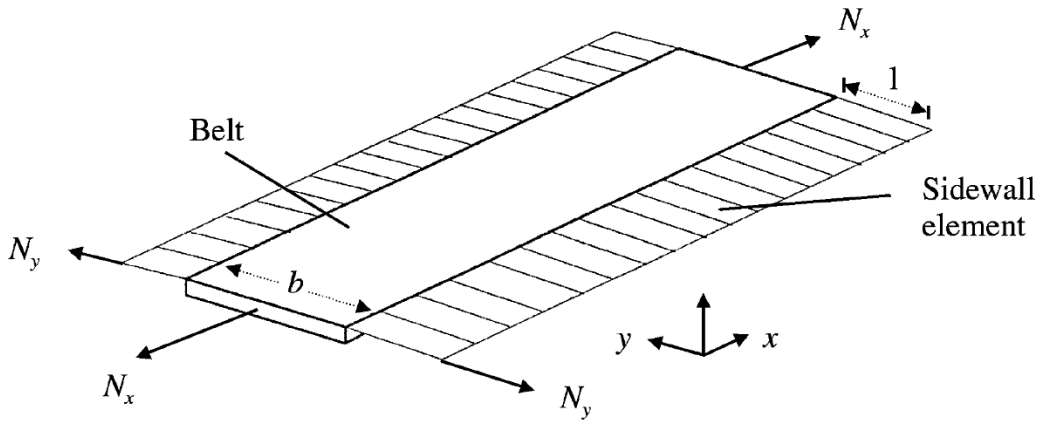

Figure 1.27. Belt and sidewalls model implemented by Pinnington et al. (2002).

Pinnington et al. (2002) derived the following homogeneous equation of motion in the wavenumber domain for the beam model. This resulted in the following expression

$$k^4\left(1+\Phi\right)+k^2\left(\chi-\left(1+\Phi\right)k_{cx}^2-k_{sx}^2\right)+\left(k_{bx}^4-k_{sx}^2k_{cx}^2-\frac{i\omega Z_s}{bB_x}\right)=0 \tag{1.15}$$

In this case, χ and Φ are terms that account for the tension N_x, shown in Figure 1.26. This tension is the result of inflation pressure. On the other hand, k_{cx}, k_{sx}, and k_{bx} are terms that include the frequency ω. Finally, b is the width of the belt, B_x is the bending stiffness of the tire along the x-direction, and Z_s is the sidewall's line impedance. The only unknown in equation (1.15) corresponds to the wavenumber along the circumferential direction of the tire, k. Therefore, two pairs of roots (i.e. wavenumbers) are obtained by setting the frequency ω to the desired value and solving the polynomial.

The forced response was then computed using the following equation

$$\dot{w} = \frac{\omega F}{2(S_x + N_x)(k_1^2 - k_2^2)} \left\{ \frac{1}{k_1} \left[(k_1^2 - k_{cx}^2) + \left(\frac{S_x}{B_x} \right) \right] e^{-ik_1 x} - \frac{1}{k_2} \left[(k_2^2 - k_{cx}^2) + \left(\frac{S_x}{B_x} \right) \right] e^{-ik_2 x} \right\}. \quad (1.16)$$

where $\dot{w}$ is the output surface velocity and F is a harmonic's input force amplitude located at x=0. On the other hand, k_1 and k_2 correspond to the wavenumbers obtained from equation (1.15).

Finally, Pinnington et al. (2002) extended the beam into a plate model. Therefore, the equation of motion was defined as

$$\left\{ B'_x k_{mx}^4 + B'_y \left(\frac{m\pi}{l_y} \right)^4 + T'_x k_{mx}^2 + T'_y \left(\frac{m\pi}{l_y} \right)^2 - \mu' \omega^2 - K_m \right\} w_m = 0 \quad (1.17)$$

In this case, a transversal modal behavior is assumed. The circumferential wavenumbers associated to each mth transversal mode are defined as k_{mx}. These are found using the same approach as was done for the beam equation (1.15). Once these are obtained, the forced response is computed. An example of input mobility FRF simulated with the plate model developed by Pinnington et al. (2002) is shown in Figure 1.28. In this case, different curves are shown corresponding to various transversal modes.

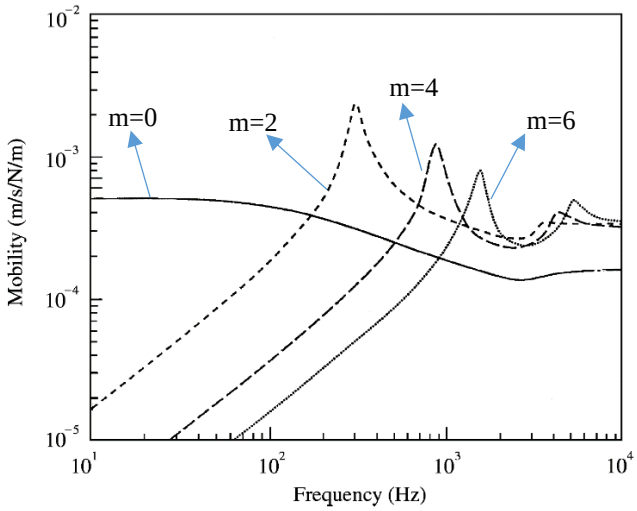

Figure 1.28. Input mobility FRF functions for m=0, m=2, m=4, and m-6 (Pinnington et al., 2002).

This modeling approach was afterward modified again, as shown in the work by Pinnington (2006a) and Pinnington (2006b). In this case, the tire is modeled as a set of three coupled tensioned Mindlin plates, as shown in the tire's cross-section schematic in Figure 1.29.

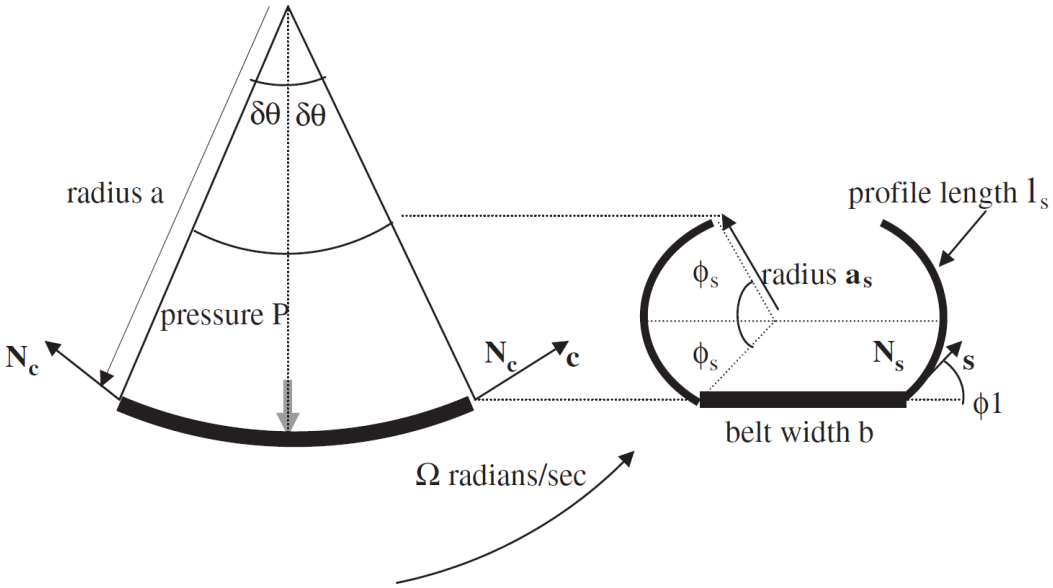

Figure 1.29. Tire's cross-section showing a set of coupled Mindlin plates (Pinnington, 2006a).

This model accounted for the geometric curvature of the tire's circumference and the curvature of the sidewall's cross-section. The equations of motion for each of the plates were defined in the

wavenumber domain. For example, Pinnington (2006b) defined the sidewall's homogeneous equation as follows

$$
\begin{aligned}
0 = {} & z^6(\bar{S}_s + \bar{N}_s) \\
& - z^4[z_{Ls}^2 + \bar{P}a_s - \bar{N}_s\bar{R}_s + (\bar{S}_s + \bar{N}_s)(1 + z_s^2 + z_{Ls}^2)] \\
& + z^2[(-z_{Ls}^2)(1 - \bar{P}a_s - \bar{S}_s - z_{Ls}^2 + \bar{N}_s\bar{R}_s - z_s^2(\bar{S}_s + \bar{N}_s)) + (z_s^2 - \bar{R}_s)(\bar{N}_s + \bar{P}a_s + z_{Ls}^2)] \\
& + (1 - \bar{P}a_s - z_{Ls}^2)(z_s^2 - \bar{R}_s)(z_{Ls}^2).
\end{aligned}
\tag{1.18}
$$

In this case, three pairs of roots (normalized wavenumbers z) can be obtained for any defined frequency. The frequency is embedded within the parameters in equation (1.18). In addition, stiffnesses, tensions due to inflation pressure are also included. It should be noted that the equation of motion for the tire's belt is similar to that defined in equation (1.18).

Once all the roots are known for the sidewalls and the belt, it is possible to obtain the forced response by properly exciting the tire belt and by coupling this excitation through boundaries that connect the sidewalls and the belt. This approach allows modeling both the sidewalls and the belt separately by assuming these have their own properties and geometry.

Finally, vibrations experiments were performed in order to validate the model. The experimental set-up used in this case is shown in Figure 1.30. The stationary tire was excited both with a point and a line harmonic force both in the radial and tangential directions. In order to excite the tire with a line force, the tire was excited with a plywood load spreader along the transversal direction of the belt. Vibrations were measured using a set of piezoelectric transducers attached to the rim. In addition, an accelerometer was used to measure vibrations at 180 degrees from the excitation point. This accelerometer was attached to a wooden bar glued to the belt of the tire.

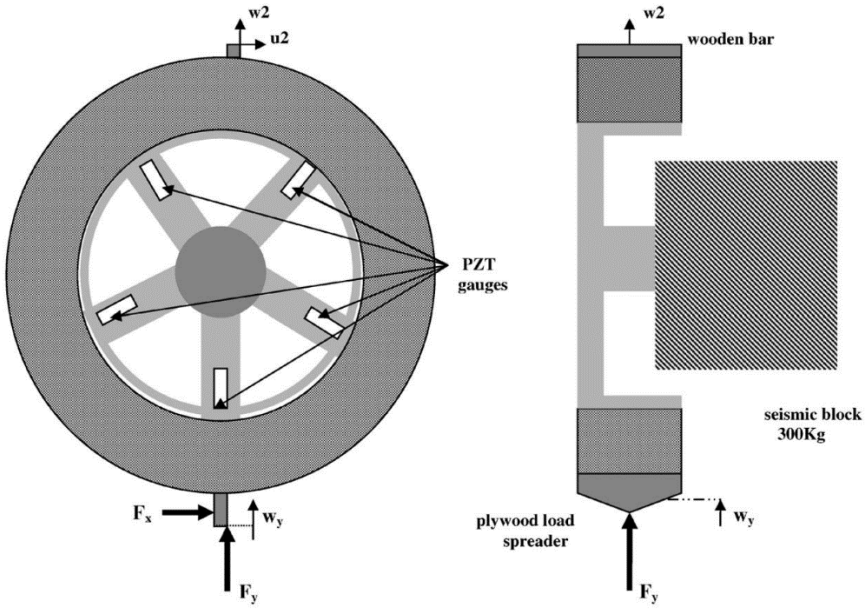

Figure 1.30. Experimental set-up implemented by Pinnington (2006b).

Results from the experiments are shown in Figure 1.31 and Figure 1.32. Figure 1.31 shows the radial input mobility transfer function, while Figure 1.32 shows the mobility transfer function measured at 180 degrees from the excitation point. For both cases, the bold lines correspond to measurements and the regular lines to predictions. Validations were only performed up to 1000 Hz. It can be observed that the model provides good approximations in the low-frequency range. However, above 800 Hz, the model does not perform well as well as for low frequencies.

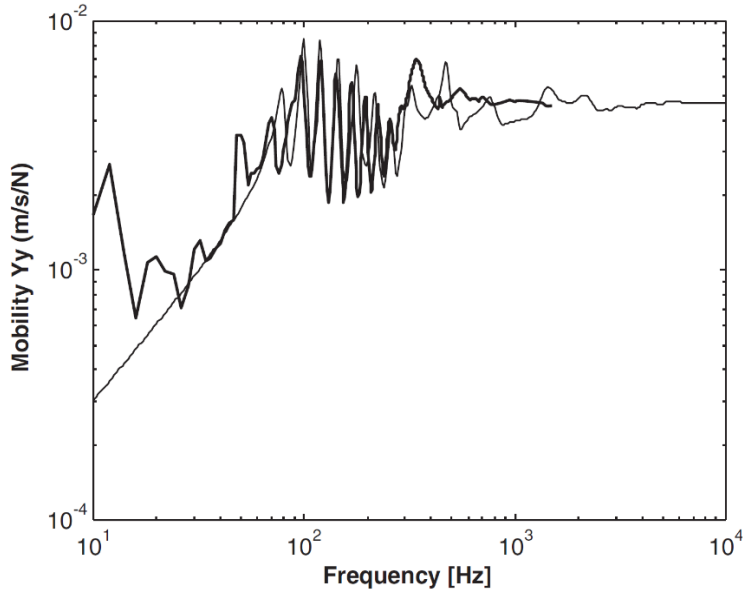

Figure 1.31. Measured and predicted input mobility FRF (Pinnington, 2006b).

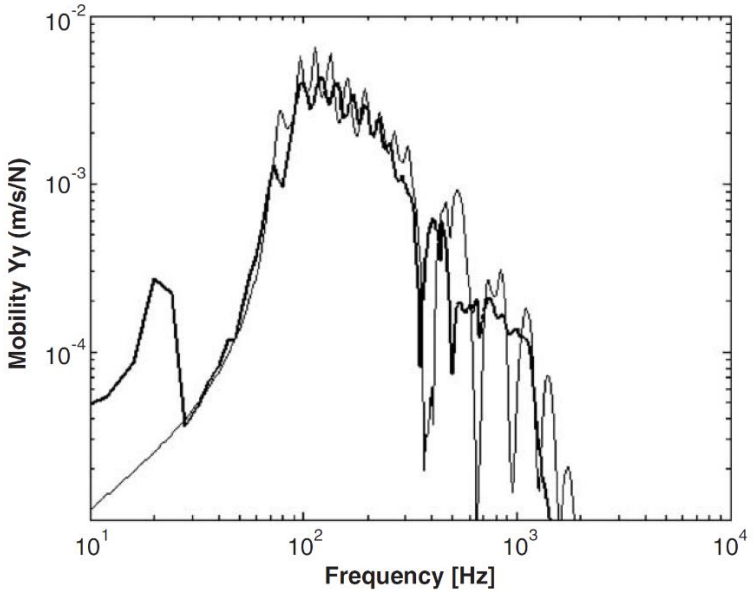

Figure 1.32. Measured and predicted mobility FRF at 180 degrees from excitation point (Pinnington, 2006b).

A different approach to predict vibration-induced TPIN was developed throughout many years in a research effort initiated by Finnveden (1994) who initially developed a method named Wave Finite Element Method or WFEM. This approach was then extended to tire vibrations by Nilsson (2004) and Hoever (2014).

The work by Nilsson (2004) focused on developing the formulation of WFEM by coupling the tire cavity and exterior shell (tire) into a single system, as shown in Figure 1.33. In this work, various types of elements applicable to tires were developed. This includes straight and curved pre-stressed shell elements with isotropic and anisotropic material properties. In addition, fluid elements to account for the tire's cavity were also developed.

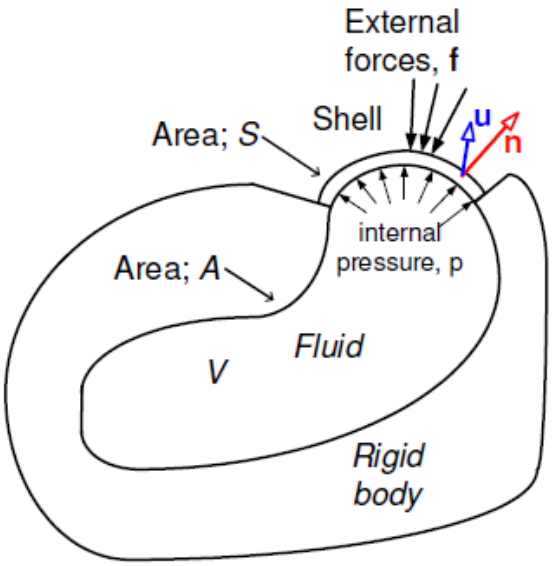

Figure 1.33. Fluid-shell system analyzed by Nilsson (2004).

On the other hand, Hoever (2014) implemented the WFEM approach as part of a unified tool capable of combining rolling resistance, the tire's vibrations response, and radiation of noise during simulations. An overview of the developed tool is shown in Figure 1.34. The input parameters are represented with a dashed line and all computed parameters with a solid line. The inputs are the tire profile, road roughness, axle load, tread pattern, rolling speed, and material properties. The outputs are the tire's input power P_{tyre}, the dissipated power P_{int}, losses due to tread deformations P_{tread}, and the output A-weighted sound pressure levels $L_{p,A}$.

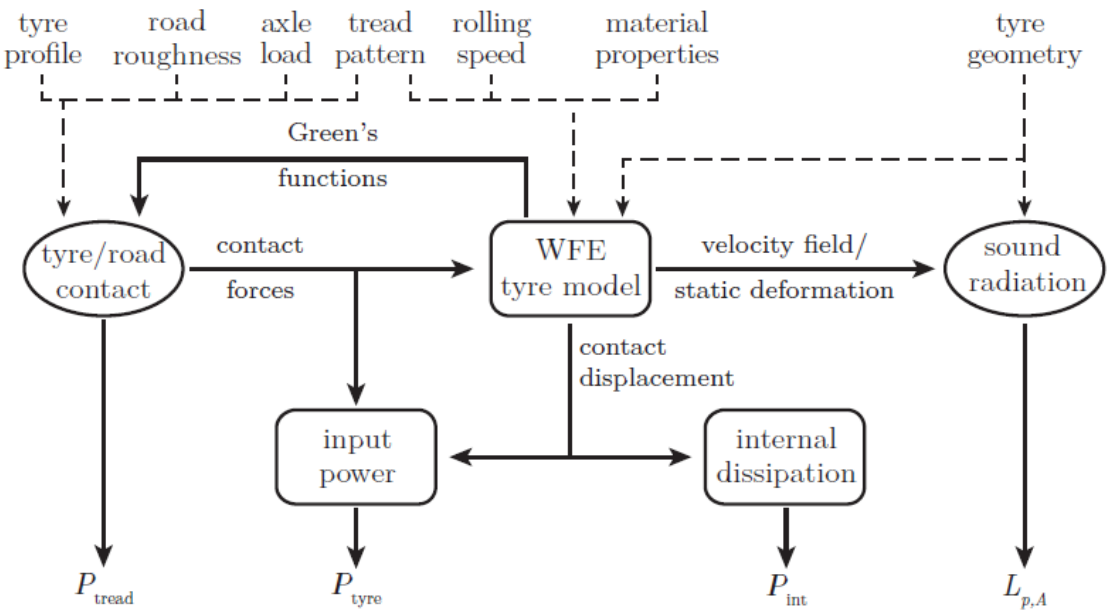

Figure 1.34: Flowchart of the tool developed by (Hoever, 2014).

In this case, the structure of the tire was modeled with an analytical wave formulation along the circumferential direction and finite elements along its transversal direction, as shown in Figure 1.35. This method is based on work by Finnveden et al. (2008). A coordinate system is defined at the center of the tire's structure. Therefore, every point on the tire's structure can be defined in terms of the radius *r*, transversal distance *x*, and angle θ. The displacement of each point is defined as $\vec{u}(r,x,\theta)=\begin{bmatrix}u_r & u_x & u_\theta\end{bmatrix}^T$ where u_r is its radial component, u_x is its transversal component, and u_θ is its angular component.

Each of the displacement components is approximated as follows

$$u_i(r,x,\theta,\omega)=\vec{N}(r,x)\vec{v}_i(\theta,t) \quad i=r,x,\theta \tag{1.21}$$

where, $\vec{N}(r,x)$ is a vector containing interpolation functions along the transversal direction of the tire. These are defined for a two-dimensional mesh over the cross-section of the tire, as shown in

Figure 1.35. On the other hand, $\vec{v}_i(\theta,t)$ is a vector containing the nodal displacements. For example, $\vec{v}_\theta(\theta,t)$ is a vector containing all the nodal displacements along the θ direction.

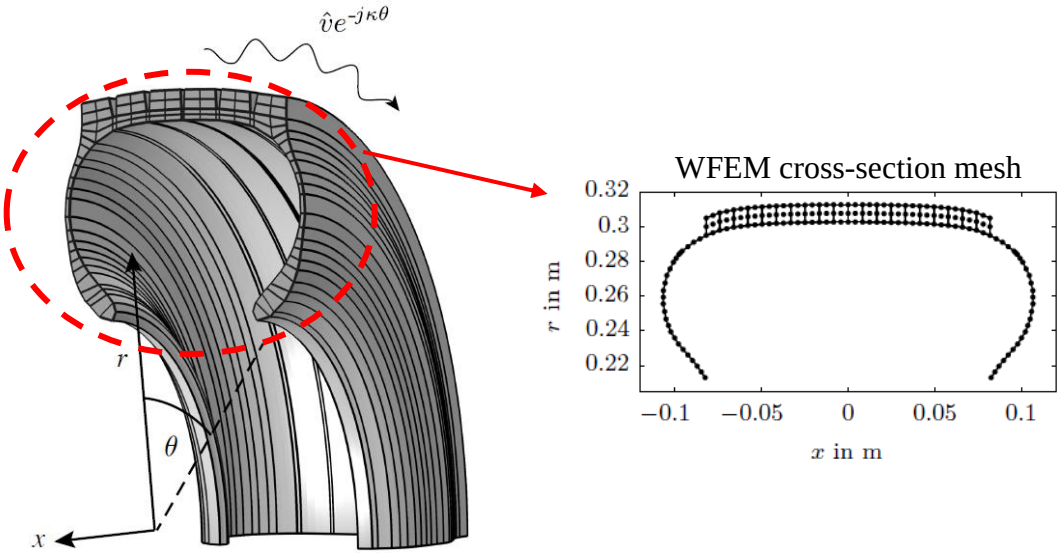

Figure 1.35: Curved waveguide representation of a tire by Hoever (2014).

The tire strains ε are also defined in terms of the nodal displacement, as follows

$$\vec{\varepsilon}(r,x,\theta,\omega) = E_0(r,x)\vec{v}(\theta,t) + E_1(r,x)\frac{\partial\vec{v}(\theta,t)}{\partial\theta} \tag{1.22}$$

where, E_0 and E_1 are matrices that depend on element-specific strain-displacement relations, shape functions, and their derivatives.

Using the expressions in equations (1.21) and (1.22), Finnveden et al. (2008) and Hoever (2014) then implemented Hamilton's principle for a dynamic system. This approach can only be applied if the system is a conservative one, i.e. if it has no energy losses. Hamilton's principle states that the integral of the Lagrangian is stationary. According to this variational principle, the time and

space path of a dynamic system between two states is obtained by minimizing the integral of the Lagrangian, as follows

$$\delta \int_{t_1}^{t_2} (U - K + A)\, dt = 0 \tag{1.23}$$

where, $t_1 < t_2$ are two arbitrary times. *U* and *K* are the system's strain and kinetic energies, while *A* is the potential energy imparted by external loads applied to the system. These are defined in terms of the displacements and strains given in equations (1.21) and (1.22) and result in

$$\begin{aligned} U &= \int_V \vec{\varepsilon}^{aT} D \vec{\varepsilon}\, dV \\ K &= \int_V \rho \omega^2 \vec{u}^{aT} \vec{u} dV \\ A &= -\int_V \left(\vec{f}^{H} \vec{u} + \vec{f}^{T} \vec{u}^{-a} \right) dV \end{aligned} \tag{1.24}$$

In this case, *D* is a complex rigidity matrix, $\vec{f}$ is a vector containing the external forces applied to the system. The superscript *T* defines the transpose operation, while the superscript *H* is the transpose and complex conjugate. Finally, the superscript *a* defines the complex conjugate for an adjoint system. This means that an adjoint or image system with negative damping has been defined. Therefore, the real system (non-conservative with energy losses due to damping) and the adjoint system (non-conservative with negative damping) are ensembled together to form a conservative system. Thus, Hamilton's principle can be applied. A schematic of this approach is shown in Figure 1.36.

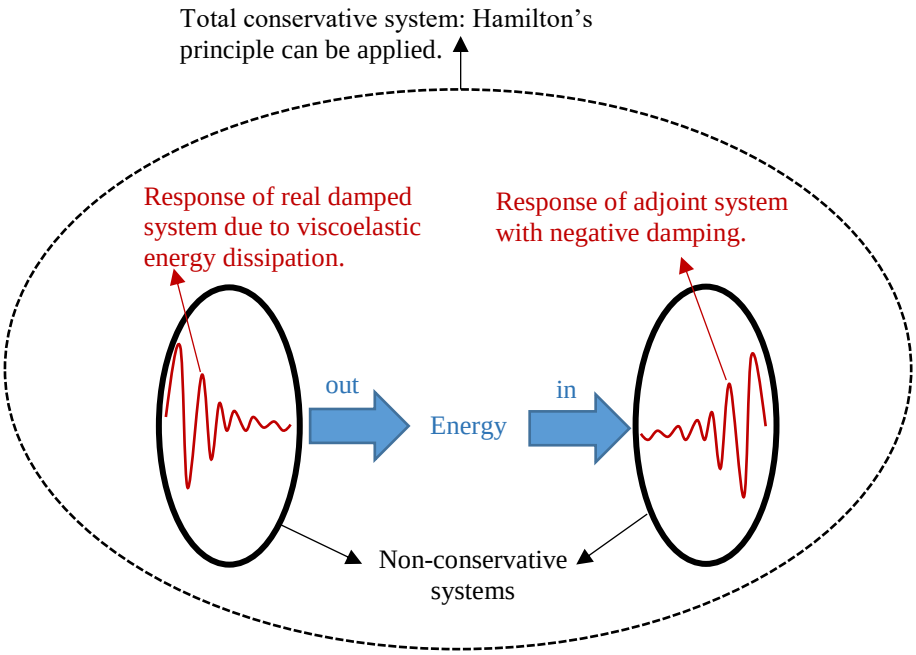

Figure 1.36. Representation of the real system, adjoint system, and total conservative system to which Hamilton's principle can be applied.

Implementing the equations in (1.24) along with the displacement and strain expressions (1.21) and (1.22), the Lagrangian becomes

$$L = (U - K + A) = \int_{-\pi}^{\pi} \left(\sum_{k=0}^{1} \sum_{l=0}^{1} \frac{\partial^k \vec{v}^{aT}}{\partial \theta^k} A_{kl} \frac{\partial^l \vec{v}}{\partial \theta^l} - \omega^2 \vec{v}^{aT} M \vec{v} - \vec{v}^{aT} \vec{f} - \vec{v} \vec{f}^{H} \right) d\theta \tag{1.25}$$

Where, A_{kl} is a generalized stiffness matrix, and M is the system's mass matrix. The Lagrangian in equation (1.25) is then implemented with Hamilton's principle in equation (1.23) to obtain the following system's equation of motion

$$\left(\mathrm{K}_2 \frac{\partial^2}{\partial \theta^2} + \mathrm{K}_1 \frac{\partial}{\partial \theta} + \mathrm{K}_0 - \omega^2 M \right) \vec{v}(\theta, \omega) = 0 \tag{1.26}$$

In this case, the system is not forced and K_0, K_1, and K_2 are stiffness matrices of the system. In addition, if the assumed solution to the nodal displacements are defined by the combination of nodal amplitudes and exponential functions as follows

$$\vec{v}(\theta,\omega) = \vec{\Psi}(\omega)e^{-jk\theta} \tag{1.27}$$

Where, $\vec{\Psi}(\omega)$ are the nodal amplitudes and k are the circumferential wavenumbers. Therefore, equation (1.26) becomes

$$\left(-\mathrm{K}_2k^2 - \mathrm{K}_1k + \mathrm{K}_0 - \omega^2 M\right)\vec{\Psi}(\omega) = 0 \tag{1.28}$$

Once the equation of motion in equation (1.28) is obtained, two approaches to finding the nodal displacements are possible:

i. Specify a single frequency and solve for two eigenvalues (wavenumbers k) per eigenvector $\vec{\Psi}(\omega)$ that defines the transversal mode shapes. This is similar to that implemented by Pinnington (2006a).

ii. Specify a single wavenumber k and solve for one eigenvalue $\omega_{k,s}^2$ per eigenvector $\vec{\Psi}_{k,s}(\omega)$ that defines the transversal mode shapes. That is one eigenvector and eigenvalue for each wavenumber k and transversal mode s. This approach was implemented by Hoever (2014) by solving the eigenvalue problem assuming circumferential wavenumbers that equal to integers i.e. modes along the circumferential direction of the tire. This approach defeats the whole purpose of setting up the problem for wave propagation since modes are assumed in the circumferential direction.

Both approaches have their own set of limitations. According to Orrenius et al. (1996), a physical system that behaves as a waveguide should be composed of an infinite number of propagating wavenumbers for each frequency. However, if the first approach is implemented, then only a finite number of wavenumbers can be obtained according to the equation of motion of the system. On the other hand, if the second approach is implemented then only wavenumbers that result in circumferential modes are selected. For this reason, a new approach is needed and is intended to be explored in this work.

Figure 1.37 shows results obtained by Hoever (2014). It is clearly observed that modes are obtained in the circumferential direction instead of freely propagating waves.

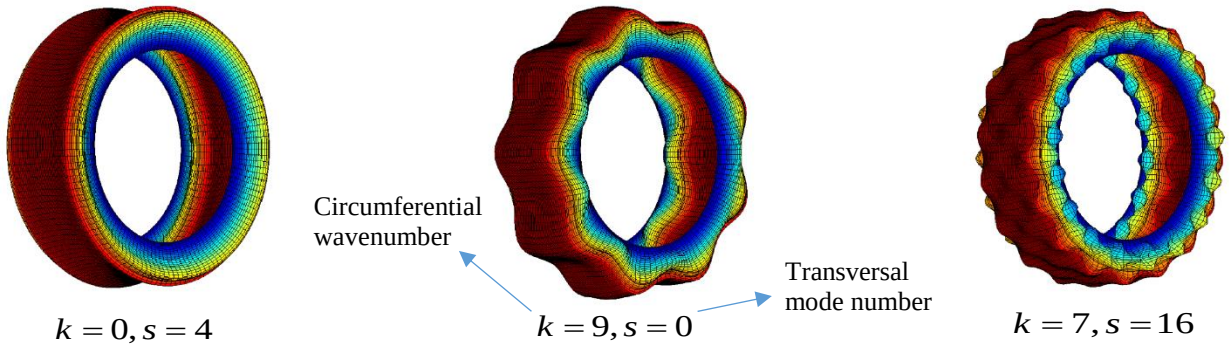

Figure 1.37. Free response results (tire modes) presented in the work by Hoever (2014).

The final step of the WFEM is to compute the forced response. This is done by collecting all eigenvectors into a single matrix $[\Xi]_k$ and assign a set of modal amplitudes $\vec{C}_k$ to each, all per wavenumber k. The result is the following system of equations

$$\left(-\bar{\mathrm{K}}_2 k^2 - \bar{\mathrm{K}}_1 k + \bar{\mathrm{K}}_0 - \omega^2 M\right)[\Xi]_k \vec{C}_k = \vec{F}_k(\omega) \tag{1.29}$$

In this case, the excitation forces are accounted in $\vec{F}_k(\omega)$. On the other hand, damping has been added to the stiffness matrices with a modal loss factor, as follows

$$\bar{\mathrm{K}}_i = (1 + j\eta(\omega))\mathrm{K}_i \tag{1.30}$$

where, $\bar{\mathrm{K}}_i$ corresponds to the damped matrices, $j = \sqrt{-1}$ and $\eta(\omega)$ is the loss factor.

The next step is to multiply by the complex conjugate transpose of $[\Xi]_k$ and integrate, then use orthogonality to obtain the modal amplitudes. This decoupling approach is only possible because modes have been assumed in both the circumferential and transversal directions of the tire, i.e. orthogonality condition is met in both directions. Therefore, the modal amplitudes become

$$C_{k,s} = \frac{\vec{\Psi}^H_{k,s}(\omega)\vec{F}_k(\omega)}{\left[(1 + j\eta)\omega^2_{k,s} - \omega^2\right]\sqrt{m_{k,s}}} \tag{1.31}$$

Finally, the response of the tire is defined as follows

$$\vec{v}(\theta,\omega) = \sum_{k=-K}^{K}\sum_{s=1}^{S} C_{k,s}\frac{\vec{\Psi}_{k,s}}{\sqrt{m_{k,s}}}e^{-jk\theta} \tag{1.32}$$

In this case, the time-harmonic solution is included in both the positive and negative traveling wave amplitudes. In addition, all S transversal modes are added to compute the response. Using these responses, a Boundary Element Method (BEM) was implemented to compute the noise produced by the tire based on its vibrational response.

Hoever (2014) presented results comparing the mobility response functions between WFEM, a classic FE approach, and measurements for a 175/65R14. These are shown in Figure 1.38 for the mobility measured at the same location as the input (i.e. at 0 degrees from the input location), and at 180 degrees from the input location. These are for both the center of the belt (tread band) and

the sidewalls. In this case, all mobilities are shown in dB with a reference of $1\ [N/ms]$. It can be observed that the model is validated only up to 1000 Hz, with better accuracy in the low-frequency range. This is consistent with the work by Nilsson (2004), who mentions that this approach is accurate only up to 800 Hz. This could be attributed to the fact that this modeling approach applied to a tire still assumes modes along the circumferential direction of the tire.

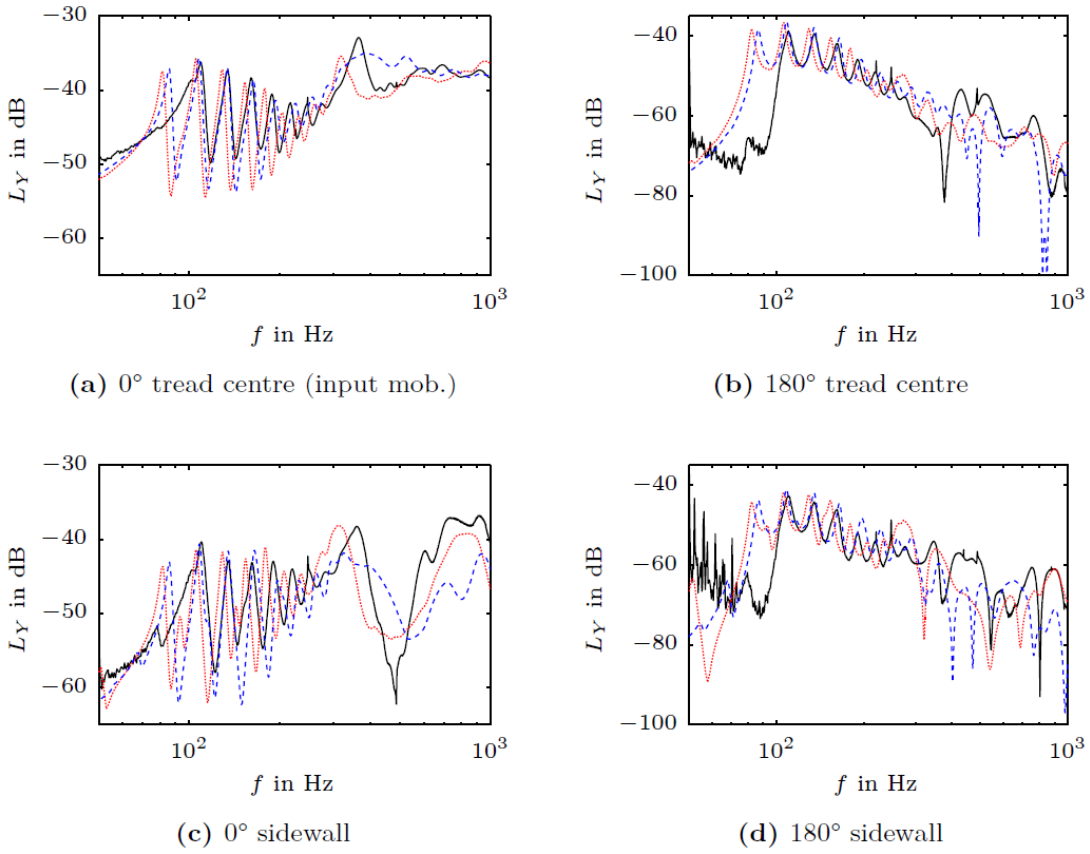

Figure 1.38. Compared mobility FRF for a tire of size 175/65R14 using WFE (blue dashed line), FE (red dotted line), and measured (black full line), at a) center of the tread at 0 deg., b) sidewall at 0 deg., c) center of tread at 180 deg., and c) sidewall at 180 deg (Hoever, 2014).

It should be noted that in this work, one of the most advanced methods found in the open literature to model the excitation of the tread blocks was also presented. This approach was initially developed in the work by Klein et al. (2008) and then improved by Hoever (2014). This approach discretized the belt into multiple squares with equal area, as shown in Figure 1.39. For example,

Figure 1.39a shows a belt with an arbitrary tread pattern, while Figure 1.39b shows the same belt with white-edged squares defining the implemented area discretization. The next step was to calculate the fraction of area covered by a block within each square element. This fraction was defined as $\Phi_{e,r}$. For example, Figure 1.39b highlights two squares denoted by (i) and (ii). The value of $\Phi_{e,r}$ is higher for a square (i) than for square (ii) because the latter has less block-covered area.

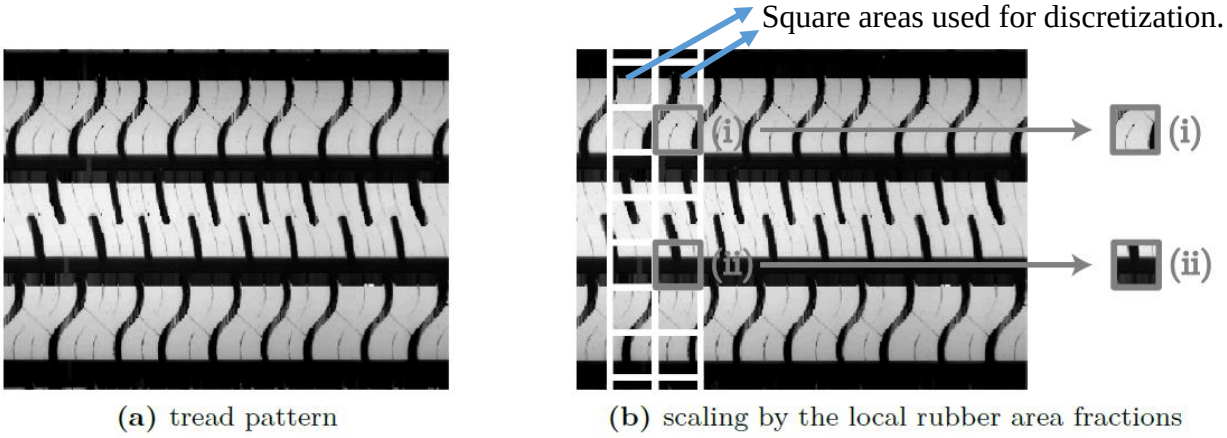

Figure 1.39. a) tread pattern of a tire and b) discretization approach used by Hoever (2014).

A spring was then assigned to each square element. The stiffness of each the spring was defined by multiplying the fraction $\Phi_{e,r}$ with the characteristic rubber stiffness of the tread k_{rubber}. The result is a different stiffness for each area-element on the belt, given by $k_e = k_{rubber}\Phi_{e,r}$.

Based on the tire's rotation, the forces on each element $F_e(t)$ were calculated using the corresponding stiffness k_e. However, the work by Hoever (2014) does not provide details on the behavior of $F_e(t)$ during the tire's rotation. This force was finally coupled to the structure of the tire by convolving it with the structural model's impulse response function, as follows

$$w_m(t) = \sum_e^E F_e(t) * g_{m|e}(t) \tag{1.31}$$

where $w_m(t)$ is the displacement of the tire surface at an arbitrary point *m* due to all E springs in the contact patch. The symbol * corresponds to the convolution operator, while $g_{m|e}(t)$ is the impulse response function for an input at a point e and output at a point *m* on the tire surface. In addition, the forces are not assumed to move as the tire rotates.

The method presented above computes the tire response in the time domain. Furthermore, the behavior of the input force related to the blocks is not fully described. For this reason, a different approach is presented in this section to account for the tread-block excitation. The objective is to model the excitation consistently with the complex harmonic inputs of the structural model which is a better approach since the tread block excitation is periodic.

Additional relevant approaches to model tire vibrations and noise are summarized as follows. Waki et al. (2009) developed an alternative Wave Finite Element (WFE) approach. Instead of developing a structural model for the tire, both mass and stiffness matrices were obtained directly from an FE model of a short segment of the tire. A commercial FE package was used. These matrices were adapted to the wave-propagation formulation, where an eigenvalue similar to that in equation (1.28) was solved, followed by the forced response computation. Comparison between experimental and predicted input mobility frequency response functions presented by Waki et al. (2009) are shown in Figure 1.40.

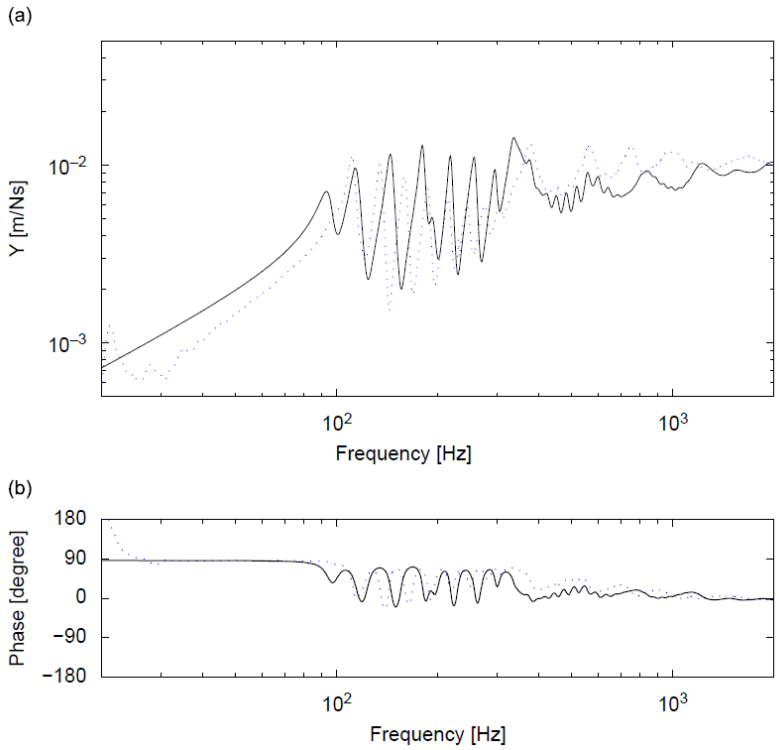

Figure 1.40. Input mobility FRF measurements (dotted line) and predictions (full line) showing: a) magnitude and b) phase (Waki et al., 2009).

Finally, there are other modeling approaches that are briefly discussed here. Lopez et al. (2007) developed a ring model of a tire, mostly for applications in the low-frequency domain. Thus, a modal approached was assumed. On the other hand, Cao (2017) developed the formulation to couple the tire's cavity and structural responses. The tire's structure was modeled using a ring model and a cylindrical shell model similar to that developed by Y. J. Kim et al. (2004). In both cases, a modal solution of the tire is assumed. In addition, a transversal model of a tire consisting of a curved beam was used to analyze how longitudinal modes couple to flexural modes in the belt of the tire.

It can be observed that most of the approaches presented above to model vibration-induced TPIN are based on the modal expansion of the tire's response. Still, many researchers acknowledge the existence of waves along the circumferential direction of the tire and many efforts have been directed towards such formulation. Most of the methods presented above fail to accurately predict

the tire's response above 1000 Hz. Therefore, it is clear that more efforts are necessary in order to predict tire vibrations and noise for higher frequencies using wave propagation methods.

1.2. Research Goals and Main Accomplishments

The main goal of this research is to develop a physically-based computational tool to predict TPIN in the dominant mid-frequency range (500-1500 Hz) due to structural vibrations. The aim is to provide further physical insight into tire vibrations and radiated noise behavior by providing a validated model.

The main contributions and accomplishments of the present study are the following:

1) A set of novel structural models of a tire developed for vibration-induced noise predictions are presented. These include a non-uniform infinite plate and a cylindrical shell model. The proposed models thoroughly account for: i) orthotropic material properties, ii) Structural non-uniformities along the tire's transversal direction, iii) Inflation pressure, and iv) Effects of rotation in the tire's dynamic behavior. A sensitivity analysis is presented to show the significance of each of these effects when modeling the tire's response.

2) A true wave propagation method has been developed to find the response of a tire within the frequency mid-frequency range. This is the first of its kind. Circumferential traveling waves for all possible wavenumbers between $-\infty$ and ∞ are accounted in the model. Other approaches simply select a discrete set of wavenumbers. These are chosen such that an integer set of wavelengths can fit over the tire's circumference. This results in modes along the circumferential direction of the tire and ignores the observed wave propagation behavior for the mid-frequency range.

3) A new contact model formulation is proposed in this study. This approach is unique because it is directly formulated in the frequency domain. Common methods presented in open literature are formulated in the time domain. Therefore, they are less efficient when periodic inputs are used such as a full tread pattern. The reason is that the response needs to be solved for multiple revolutions before the steady-state condition is reached.

4) A prediction tool that predicts TPIN in the mid-frequency range has been developed. The tool incorporates three main components. First, the contact model that accounts for proper tire excitation in the contact area due to the tread pattern. Second, a comprehensive structural tire model to capture the tire's response. Finally, an acoustic model to predict tread pattern noise.

1.3. Thesis Organization

The structure of this thesis is the following. Chapter 1 provides background information and introduces the Tire-Pavement Interaction Noise (TPIN) problem. It provides a brief literature summary on current approaches to model vibration-induced tire noise produced. In addition, it offers experimental evidence of the vibratory and associated tire noise behavior, uncovered by other researchers. Finally, the goals of this research are also presented. Chapter 2 addresses a set of structural tire models that have been developed. The formulation used to define the equations of motion is addressed. In addition, a new wave-propagation approach to find the response of a tire is presented. Chapter 3 describes the contact model developed for the excitation of the tire structure. The formulation for excitation due to the impact of tread-pattern blocks as they enter and leave the contact patch is presented. Chapter 4 provides a set of validation cases for the structural models of the tire and noise. Chapter 5 provides a description of the complete wave propagation TPIN prediction tool named *WavePro Tire*. In this section, an explanation of the tire geometry and meshing strategies used for predictions is presented. In addition, a description is provided on how the resulting response of the tire is used to compute noise. Finally, simulated results and a sensitivity analysis are also presented in this section. Chapter 6 presents concluding remarks, the main contributions from this work, and suggestions for future work.

2. Structural Tire Model

The approach to model the tire structure consists of a set of stages. This will be referred to as *Sequential Modeling Approach.* The aim of this approach is to create a set of models defined by increasing structural improvements. Each stage adds new capabilities that seek to improve physical accuracy. By comparing the modeled responses with experimental data, more insight will be provided regarding the importance of each newly added capability. Figure 2.1 shows the 4 stages sequential modeling process. The start point corresponds to the model developed by Kropp (1999), previously introduced in Chapter 1. This model has been selected as a start point because it provides a simple methodology for mid-frequency tire vibration and predictions. It also offers an initial insight on results for the tire's produced noise.

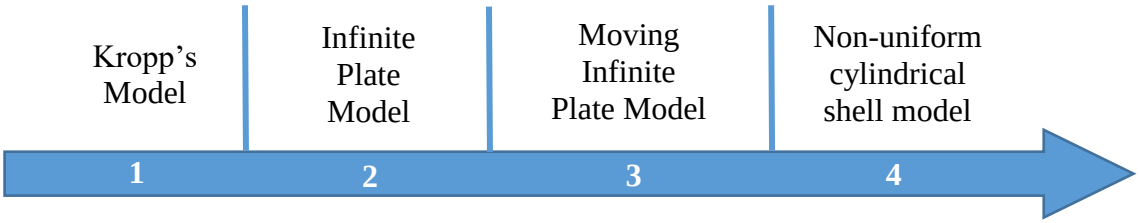

Figure 2.1. Stages in sequential approach to modeling the tire's structure.

A new approach to model the tire's structural dynamics is introduced in the second stage. By assuming that the plate is infinite along the circumferential direction, a true wave propagation approach is implemented. In this case, modes are no longer assumed along the tire's circumferential direction, but waves that can both propagate and/or decay depending on the axial wavenumbers. Furthermore, orthotropic and non-uniform transversal properties are accounted for in this approach. In the third stage, the plate model is extended to include rotation by assuming it to move with a constant velocity along the circumferential direction. In the fourth stage, a cylindrical shell is used to model the tire's structure. This approach accounts for the curvature effects in the model.

It should be noted that all the models presented in the sequential modeling approach are developed so that linear material properties are used as inputs. This follows the experimental results and suggestions presented in the work by Fleischman (1998). In this work, Fleischman (1998) provided the diagram shown in Figure 2.2. In this case, the measured shear moduli are presented as a function of strain amplitude for a typical tire rubber material. The main tire performance attributes were classified according to the strain amplitude. It can be observed that both the storage modulus G' and loss modulus $G"$ have a linear behavior for low strains. Noise, vibrations, harshness, and ride applications are assigned to low such low strains. Therefore, it is reasonable to use linear structural approaches to model TPIN induced by tire vibrations.

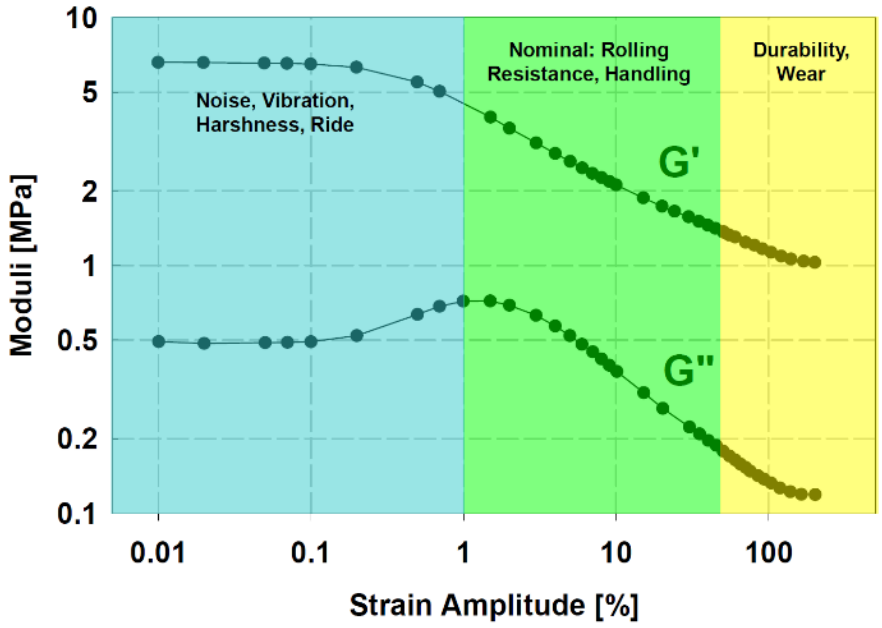

Figure 2.2. Measured shear moduli and classification according to various tire performance attributes (Fleischman, 1998).

2.1. Sequential Modeling Approach

In this section, the development of the models at each of the stages defined in Figure 2.1 is presented. The formulation and assumptions made for each will be addressed, in addition to identifying their limitations and model capabilities.

Kropp's Model

Even though this model is not part of the new developments presented in this thesis, it provides a useful start point for the sequential modeling approach. Therefore, in this sub-section, results from the model developed by Kropp (1999) will be reproduced. In this case, the tire is modeled as a simply supported plate. It is unwrapped along its circumference and cross-section, as shown in Figure 2.3a. This approach ignores the tire's curvature since the author speculates that it does not influence its response above the characteristic ring frequency, typically corresponding to 500 Hz. Therefore, this approach can be implemented for mid-frequency range modeling, i.e. between 500 Hz and 1500 Hz. In this case, bending effects are dominant over membrane effects in the tire structure.

The main limitations of this approach are the following:

i. Below the tire's ring frequency, the model's response is not expected to be accurate because the curvature is ignored.
ii. At high frequencies (>2000 Hz) shear effects cannot be neglected. Thus, assuming a thin plate model is no longer accurate.
iii. The tire's structural properties are assumed to be uniform (belt and sidewall properties should be different).
iv. No effects of rotation in the tire's response have been included in the model.

As shown in Figure 2.3b, the coordinate system is located at the center of the unwrapped tire. Its circumferential direction is defined along the x-axis and its transversal direction along its y-axis. The plate's dimension l_x corresponds to the circumference of the tire defined as $2\pi r_T$, where r_T is the radius of the tire, calculated as follows

$$r_T = r_{rim} + AR \times W_T \tag{2.1}$$

In this case, r_{rim} is the rim's radius, AR is the tire's aspect ratio and W_T is the tire's belt width. On the other hand, the dimension l_y corresponds to the tire's transversal length defined as $l_y = W_T + 2AR \times W_T$. The plate is simply supported on the tire's circumferential outer edges. These edges correspond to those directly in contact with the rim during operation. In addition, the sidewalls and belt limits are marked in Figure 2.3, even if no difference between them is accounted in Kropp's original model.

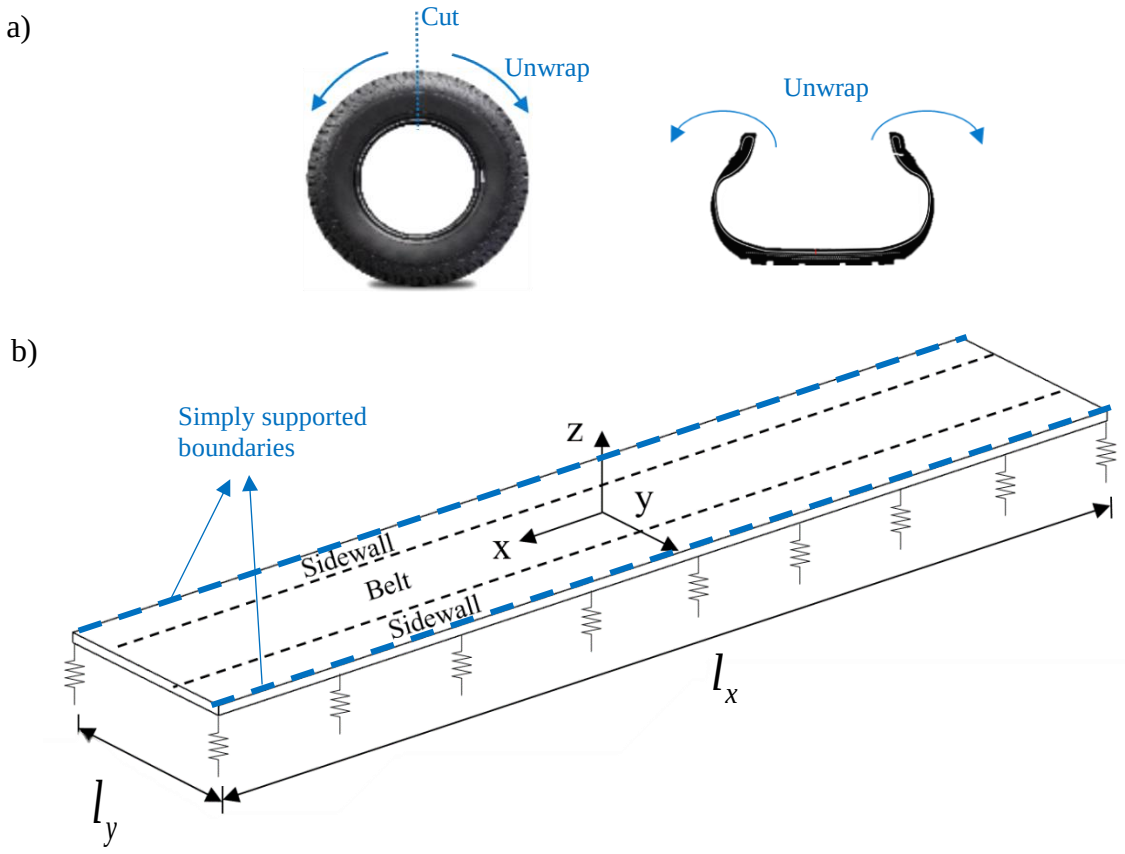

Figure 2.3: Simply supported orthotropic plate tire model introduced by Kropp (1999).

The equation of motion for the plate is given by

$$-T_{0x}\frac{\partial^2 w}{\partial x^2}-T_{0y}\frac{\partial^2 w}{\partial y^2}+B_x\frac{\partial^4 w}{\partial x^4}+2B_{xy}\frac{\partial^4 w}{\partial x^2\partial y^2}+B_y\frac{\partial^4 w}{\partial y^4}+sw+M_p\frac{\partial^2 w}{\partial t^2}=F\left(x,y,t\right) \tag{2.2}$$

Equation (2.2) corresponds to a modified version of the classic equation of motion for an orthotropic thin shell, as specified by Reismann (1988). Here, $w(x,y,t)$ correspond to the mid-surface displacements of the plate. additional terms to account for the inflation pressure of the tire have been included in the formulation. These included membrane tensions along the x and y directions. The tension along the circumferential direction is defined as T_{0x}, while T_{0y} the tension along the transversal direction. The first one is defined as follows

$$T_{0x}=rP \tag{2.3}$$

where P is the inflation pressure and r is the radius of the tire belt. This assumption is defined by Ugural (2009) for thin-walled pressure vessels. For example, if a tire is inflated at 30 psi or 20,6842 Pa, and has a radius of r = 0.32 m, then the circumferential tension is $T_{0x}=6.62\times10^4$ N/m. If the same pressure vessel assumption is followed, the transversal tension T_{0y} is

$$T_{0y}=rP/2 \tag{2.4}$$

For the same tire as above, this would result in $T_{0y}=3.3095\times10^4$ N/m.

On the other hand, B_x B_x, B_y, and B_{xy} correspond to the tire stiffnesses along the circumferential, transversal and cross directions. The latter one is given by $B_{xy}=\sqrt{B_xB_y}$. Additionally, s

corresponds to the stiffness of an elastic bed assumed on the tire's surface, and M_p is the mass of the plate per unit area. Finally, $F(x,y,t)$ is the excitation force per unit area.

If the excitation force corresponds to a point force, then equation (2.2) becomes

$$-T_{0x}\frac{\partial^2 w}{\partial x^2}-T_{0y}\frac{\partial^2 w}{\partial y^2}+B_x\frac{\partial^4 w}{\partial x^4}+2B_{xy}\frac{\partial^4 w}{\partial x^2\partial y^2}+\ldots \qquad (2.5)$$
$$B_y\frac{\partial^4 w}{\partial y^4}+sw+M_p\frac{\partial^2 w}{\partial t^2}=f(t)\delta(x-x_f)\delta(y-y_f)$$

Here, $f(t)$ is the force's harmonic amplitude and the delta functions denote that this is an input point force at the location (x_f, y_f) on the tire's surface.

The solution of equation (2.5) is obtained by the classical modal expansion method. Thus, the assumed solution for the plate is the following

$$w(x,y,t)=\sum_{n=1}^{N}\sum_{m=0}^{M}u_{m,n}(t)\psi_m(x)\Theta_n(y) \qquad (2.6)$$

where $u_{m,n}(t)$ correspond to the time-dependent modal amplitudes. On the other hand, $\psi_m(x)$ are modes along the circumferential direction of the tire and $\Theta_n(y)$ are modes along the transversal direction of the tire. These are defined as follows

$$\psi_m(x) = \cos\left(\frac{2\pi m x}{l_x} + m\pi\right) \tag{2.7}$$

$$\Theta_n(y) = \sin\left(\frac{n\pi y}{l_y} + \frac{n\pi}{2}\right)$$

These functions are obtained by replacing the assumed solution into the homogeneous version of equation (2.2) and using the plate's boundary conditions. In addition, the two transversal and circumferential modes are orthogonal functions. This means that if the transversal mode is pre-multiplied by itself and integrated along the y-direction between $-l_y/2$ and $l_y/2$, the result is the following

$$\int_{-\frac{l_y}{2}}^{\frac{l_y}{2}} \Theta_n(y)\Theta_s(y)\,dy = \int_{-\frac{l_y}{2}}^{\frac{l_y}{2}} \sin\left(\frac{n\pi y}{l_y} + \frac{n\pi}{2}\right)\sin\left(\frac{s\pi y}{l_y} + \frac{s\pi}{2}\right)dy = \begin{cases} 0 \;, & n \neq s \\ l_y/2 \;, & n = s \end{cases} \tag{2.8}$$

Similarly, if the circumferential-mode is pre-multiplied by itself and integrated along the x-directions between $-l_x/2$ and $l_x/2$, the result is the following

$$\int_{-\frac{l_x}{2}}^{\frac{l_x}{2}} \psi_m(y)\psi_r(y)\,dx = \int_{-\frac{l_x}{2}}^{\frac{l_x}{2}} \cos\left(\frac{2\pi m x}{l_x} + m\pi\right)\cos\left(\frac{2\pi r x}{l_x} + r\pi\right)dx = \begin{cases} 0 \;, & m \neq r \\ l_x/2 \;, & m = r \end{cases} \tag{2.9}$$

In order to find the forced response of the tire, the assumed solution presented in equation (2.6) is substituted in the equation of motion (2.5). This is then pre-multiplied by the modes and integrated along the x-direction and y-direction using the orthogonality expressions defined by equations (2.8) and (2.9).

The resulting modal equation is the following

$$M_p \frac{d^2 u_{m,n}(t)}{dt^2} + \left\{ \left[T_0 \left(\frac{2m\pi}{L_x} \right)^2 + T_0 \left(\frac{n\pi}{L_y} \right)^2 + B_x \left(\frac{2m\pi}{L_x} \right)^4 + 2B_{xy} \left(\frac{2m\pi}{L_x} \right)^2 \left(\frac{n\pi}{L_y} \right)^2 + B_y \left(\frac{n\pi}{L_y} \right)^4 + s \right] \right\} u_{m,n}(t) = \frac{4\psi_m(x_f)\Theta_n(y_f)}{l_x l_y} f(t) \tag{2.10}$$

The forcing function is also assumed a harmonic with an amplitude F_0, as $f(t) = F_0 e^{i\omega t}$. Therefore, the response is also assumed a harmonic $u_{m,n}(t) = U_{m,n} e^{i\omega t}$, where $U_{m,n}$ corresponds to the modal response amplitude.

If the right-hand forcing term of equation (2.10) is equal to zero. Then, the natural frequencies of the tire are the following

$$\omega_{m,n} = \sqrt{\frac{T_0 \left(\frac{2m\pi}{L_x} \right)^2 + T_0 \left(\frac{n\pi}{L_y} \right)^2 + B_x \left(\frac{2m\pi}{L_x} \right)^4 + 2B_{xy} \left(\frac{2m\pi}{L_x} \right)^2 \left(\frac{n\pi}{L_y} \right)^2 + B_y \left(\frac{n\pi}{L_y} \right)^4 + s}{M_p}} \tag{2.11}$$

It should be noted that the numerator in equation (2.11) is defined as the equivalent modal stiffness of the tire. With the natural frequencies defined in equation (2.11), the modal equation of motion of the plate is then expressed as

$$\frac{d^2 u_{m,n}(t)}{dt^2} + \omega_{m,n}^2 u_{m,n}(t) = \frac{4\psi_m(x_f)\Theta_n(y_f)}{M_p l_x l_y} f(t) \tag{2.12}$$

Assuming a harmonic response, the solution to equation (2.12) is the following

$$u_{m,n}(t) = \frac{4\psi_m(x_f)\Theta_n(y_f) f(t)}{M_p l_x l_y \left[\omega_{m,n}^2 (1 + i\eta_{m,n}) - \omega^2 \right]} \tag{2.13}$$

In this case, in equation (2.12) it can be observed that a modal loss factor $\eta_{m,n}$ to account for damping has been included in the equation. If equation (2.13) is then substituted into equation (2.6), the complex harmonic response of the tire at any point of its surface becomes the following

$$w(x,y,t) = \sum_{n=1}^{N}\sum_{m=0}^{M} u_{m,n}(t)\psi_m(x)\Theta_n(y) = \sum_{n=1}^{N}\sum_{m=0}^{M} \frac{4\psi_m(x_f)\Theta_n(y_f)F_0 e^{i\omega t}}{M_p l_x l_y \left[\omega_{m,n}^2\left(1+i\eta_{m,n}\right)-\omega^2\right]}\psi_m(x)\Theta_n(y) \tag{2.14}$$

The normal surface velocities of the plate can also be obtained using equation (2.14) by multiplying it by $i\omega$, i.e. taking the time derivative of the normal displacements.

The mobility frequency response function of the tire's structure is calculated from equation (2.14). This is the transfer function between the normal surface velocity of the tire at any arbitrary location of the plate (x_t, y_t) due to a harmonic input point force at a position (x_f, y_f) and is expressed as follows

$$M_K\left((x_t,y_t)\middle|(x_f,y_f),\omega\right) = \sum_{n=1}^{N}\sum_{m=0}^{M}\psi_m(x_t)\Theta_n(y_t)\frac{i\omega 4\psi_m(x_f)\Theta_n(y_f)}{m l_x l_y\left[\omega_{m,n}^2\left(1+i\eta_{m,n}\right)-\omega^2\right]} \tag{2.15}$$

The formulation presented by Kropp (1999) assumes standing wave components along the tire's transversal and circumferential direction as defined in equation (2.6). Thus, the mode shapes for the complete tire can be calculated, as well as their corresponding natural frequencies. However, these modes are not expected to be accurate at low frequencies, since the model ignores tire curvature. Furthermore, high order modes are not accurate either, which include the frequency range of interest (500-1500Hz).

An example of the expected modal solution for a tire of size 155/70R13 is shown in Figure 2.4. The parameters used for this example were extracted from the work by Perisse et al. (2000) and

are listed in Table 2.1. These results show that the initial modes are completely dominated by the circumferential modal components. It is not until the 7th mode when the transversal modal components first appear as shown in Figure 2.4, for the wrapped and unwrapped tire representation (the sidewalls are ignored for improved visualization purposes in the wrapped representation).

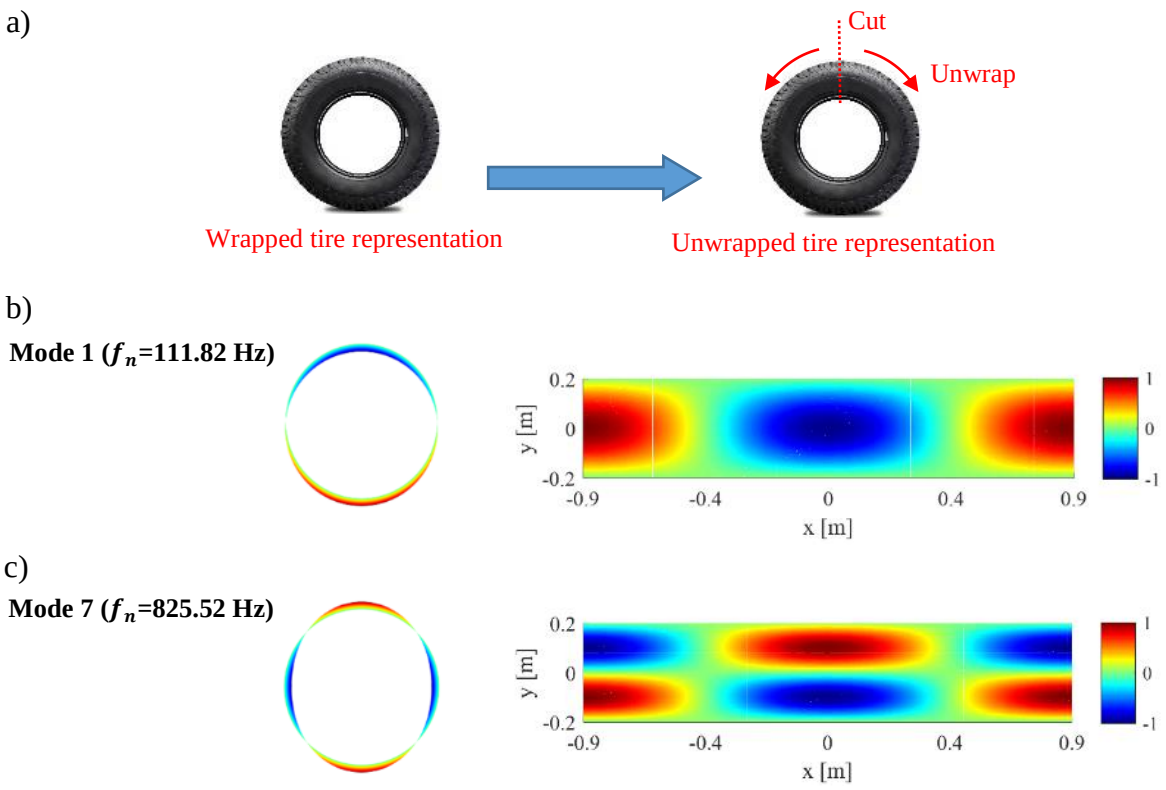

Figure 2.4. a) unwrapped and wrapped tire representation for b) the 1st mode shape, and c) the 7th mode shape of a tire of size 155/70R13 using the modal approach proposed by Kropp (1999).

The experimental results presented by Bernhard (2000) show that above 500 Hz a wave propagation behavior along the circumferential direction of the tire. Waves propagate and decay along the circumferential direction of the tire. Along the transversal direction, modes exist. This behavior is shown in Figure 1.11. Therefore, the development of a model that accounts for this is necessary. In the next sub-sections, new developments on a wave propagation approach for the structural tire model are presented.

Table 2.1. Uniform tire parameters for a 155/70R13, defined in the work by Perisse et al. (2000).

Parameter	Notation	Tire Part, Direction	Value [Units]
Mass per Unit Area	m	Belt and Sidewalls	16.5 $[kg/m^2]$
Bending Stiffness	B_x	Belt and Sidewalls, x-direction	20 $[Nm]$
Bending Stiffness	B_y	Belt and Sidewalls, y-direction	8 $[Nm]$
Bending Stiffness	B_{xy}	Belt and Sidewalls, cross-direction	12.7 $[Nm]$
Elastic Bed Stiffness	s	Belt and Sidewalls	1.3×10^6 $[N/m]$
Membrane Tension (29 PSI)	T_{0x}	Belt and Sidewalls, x-direction (29 psi)	3.08×10^4 $[N/m]$
Membrane Tension (29 PSI)	T_{0y}	Belt and Sidewalls, y-direction (29 psi)	7.73×10^4 $[N/m]$

Infinite Plate Model

In an effort to improve the model's physical accuracy, Kropp's approach is extended by assuming that the simply supported plate is infinite along its circumferential direction as shown in Figure 2.5. Waves initially excited at the contact patch region propagate circumferentially along the tire but rapidly decay. Assuming that the plate is excited close to the coordinate's system origin, waves traveling in the positive and negative x-direction do not interact with each other. Therefore, standing waves i.e. modes, are not formed. This is the expected response of a tire in the mid-frequency range.

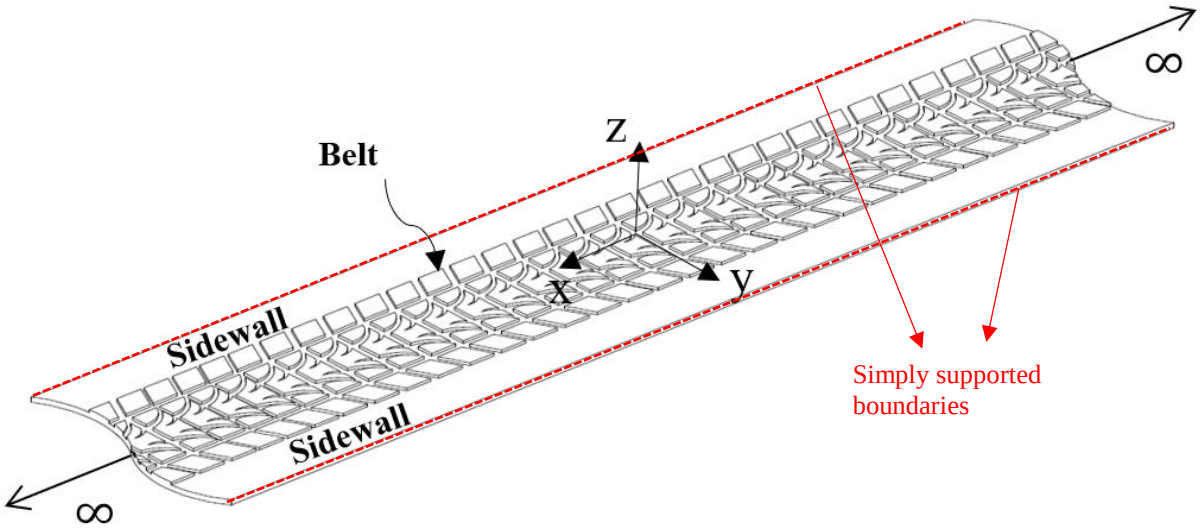

Figure 2.5. Non-uniform infinite plate model of a tire (x-axis denotes the circumferential direction of the tire and y-axis its transversal direction).

If a point force excitation is assumed, then the equation of motion for the plate is similar to the one used in Kropp's model and is defined as follows

$$-T_{0x}\frac{\partial^2 w}{\partial x^2}-T_{0y}\frac{\partial^2 w}{\partial y^2}+B_x\frac{\partial^4 w}{\partial x^4}+2B_{xy}\frac{\partial^4 w}{\partial x^2\partial y^2}+\frac{\partial^2}{\partial y^2}\left(B_y(y)\frac{\partial^2 w}{\partial y^2}\right)-m(y)\frac{\partial^2 w}{\partial t^2}=f(t)\delta\left(x-x_f\right)\delta\left(y-y_f\right) \tag{2.16}$$

In this case, additional capabilities have been added. Non-uniformities along the tire transversal direction are now considered. The transversal stiffness B_y and the mass per unit area of the tire m now depend on y. Table 2.2 shows typical transversal stiffness and mass values for the belt and sidewalls for a tire of size 155/70R13. These values were adapted from the structural properties reported by Pinnington (2006a) and Pinnington (2006b).

Table 2.2. Non-uniform tire parameters for a 155/70R13 adapted from the results presented in the work by Pinnington (2006a) and Pinnington (2006b).

Parameter	Notation	Tire Part, Direction	Value [Units]
Mass per Unit Area	m_b	Belt, cross-direction	20 $[kg/m^2]$
Mass per Unit Area	m_s	Sidewalls, cross-direction	9.35 $[kg/m^2]$
Bending Stiffness	B_{yb}	Belt, y-direction	2.64 $[Nm]$
Bending Stiffness	B_{ys}	Sidewalls, y-direction	0.59 $[Nm]$

The non-uniform mass per unit area and transversal stiffness along the tire's transversal direction are shown in Figure 2.6. This shows that along the transversal direction of the tire, the belt is stiffer than the sidewalls. In addition, the belt contains more mass due to the rubber material added by the tread. On the other hand, many researchers have reported different values of average damping for all frequencies. For example, Perisse et al. (2000) reported an average of 7% damping loss factor for the first 7 tire modes, while Pinnington (2006a) suggests a constant 16% loss factor for all tire modes. Both cases will be used to present results in the next sections. Further investigation on how to find these tire properties is required since they are not consistent in the open literature.

a) Non-uniform mass per unit area.

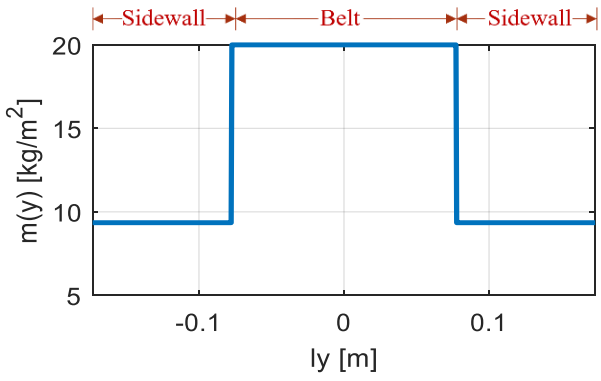

b) Non-uniform transversal stiffness.

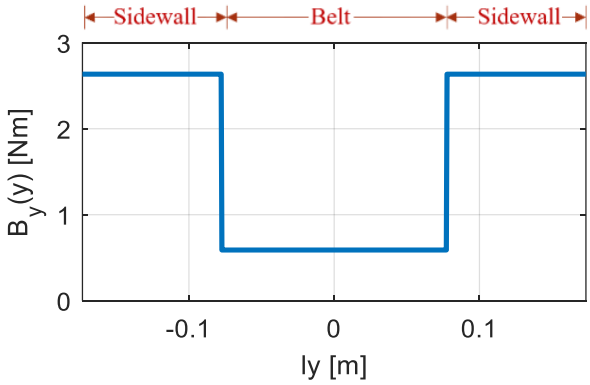

Figure 2.6. a) Transversal mass per unit area of the tire for its belt and sidewalls, b) Transversal tire stiffness for tire belt and sidewalls (Tire size 155/70R13).

The solution to this model is different from Kropp's approach presented in the previous section. The plate shown in Figure 2.5 is finite in the transverse direction. Therefore, modes are still assumed in this direction. On the other hand, the plate is infinite in the circumferential direction.

Therefore, waves are assumed instead of modes. In this case, waves propagating along the positive and negative x-axis will not interact with each other. Thus, the proposed solution to the equation of motion (2.16) is the following

$$w(x,y,t)=\sum_{n}^{N} q_n \phi_n(y) X_n(x) T(t) \tag{2.17}$$

where q_n is the nth modal amplitude, $\phi_n(y)$ is the associated transversal mode of the tire, $X_n(x)=e^{-ik_x x}$ defines the waves propagating along the circumferential direction, and finally $T(t)$ is a time-harmonic of the form $e^{i\omega t}$.

The transversal modes of the tire $\phi_n(y)$ are computed in terms of admissible functions. These are defined as sine functions that satisfy the essential boundary conditions of the tire (see simply supported boundaries in Figure 2.5). Therefore, the transversal mode shapes are defined as

$$\phi_n(y)=\sum_{m}^{M} A_{mn}\ \psi_m(y)=\sum_{m}^{M} A_{mn}\ \sin\left(\frac{m\pi y}{l_y}+\frac{m\pi}{2}\right) \tag{2.18}$$

where, A_{mn} are the corresponding admissible function amplitudes associated with the mth function and nth transversal mode. In general, this definition of the transversal modes will consistently be used for all wave propagation models presented in this chapter.

In order to obtain the mode shapes, e.g. admissible function amplitudes A_{mn}, a homogeneous equation that is only a function of y is constructed. For this specific model, only the 5th and 6th terms of equation (2.16) are selected and equated to zero. The transversal modes are substituted into this equation. The resulting expression is then pre-multiplied by a vector of admissible functions and integrated over the transversal direction y. The following eigenvalue problem is then obtained

$$[K]\{A_n\} - \lambda_n [M]\{A_n\} = 0 \tag{2.19}$$

In this case, $\{A_n\}$ is a vector that collects all admissible function amplitudes per mode; $[M]$ is the equivalent mass matrix; $[K]$ is the equivalent stiffness matrix; finally, λ_n corresponds to the eigenvalues or ω_n^2. It should be noted that the eigenvalue problem in equation (2.19) is an approximation. The only way to find an exact solution is to implement an eigenvalue problem using all terms in equation (2.16), for all possible values of k_x. However, this approach would be computationally intensive.

Figure 2.7 shows examples of the first four admissible functions along a 155/70R13 tire's transversal direction.

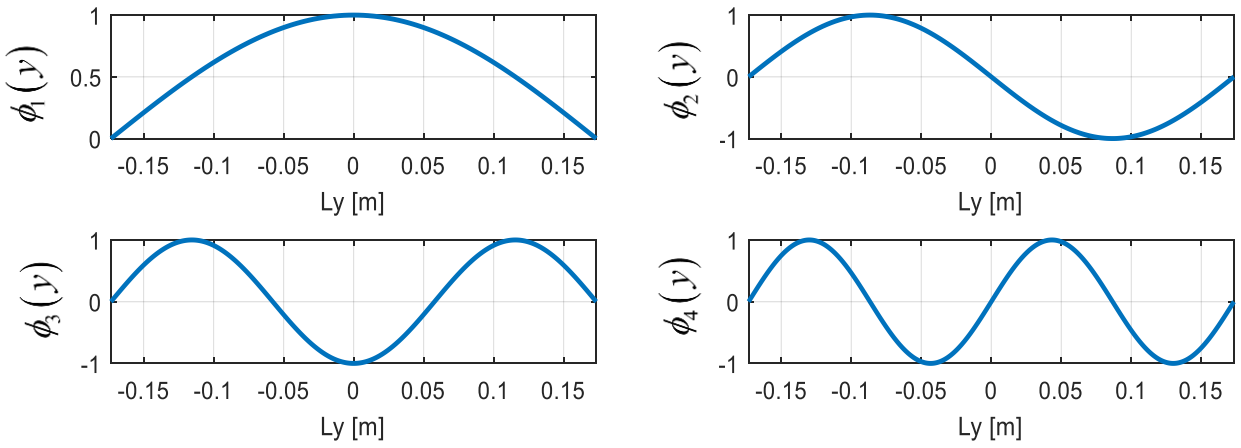

Figure 2.7. Example of first four admissible functions implemented to represent tire transversal modes over the non-uniform infinite plate representing an unwrapped tire.

On the other hand, Figure 2.8 shows an example of the 9th transversal mode of a tire of size 155/70R13. Two cases are shown, Figure 2.8a was obtained using the uniform stiffness and mass given in Table 2.1. Figure 2.8b was obtained using the non-uniform transversal properties given

in Table 2.2. The reason this mode was selected as an example is that its natural frequency is typically located at the center the frequency range of interest, around 1000 Hz.

The mode shape for the uniform case shows equal amplitudes for the belt and sidewalls. However, for the non-uniform case, larger amplitudes are observed for the sidewalls if compared to the belt. In addition, a shift in the natural frequency of approximately 160 Hz was observed between the uniform and non-uniform case. This characteristic behavior was observed for all the transversal modes within the frequency range of interest.

a) Uniform transversal mode 9, f_n=1196 Hz.

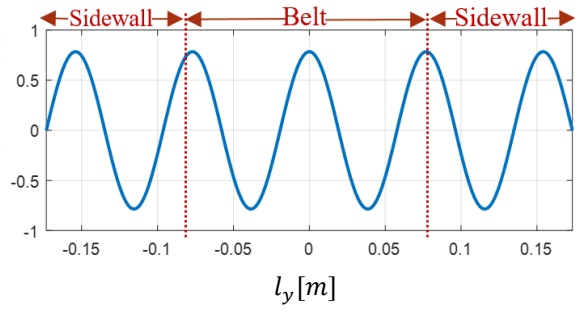

b) Non-Uniform transversal mode 9, f_n=1030 Hz.

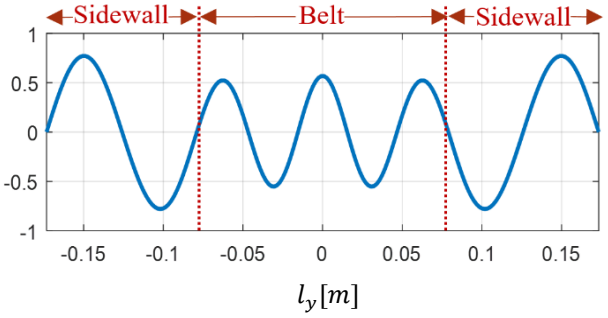

Figure 2.8. a) Uniform transversal mode 9, and b) non-uniform transversal mode 9 for a tire of size 155/70R13.

In order to find the response of the system, the non-homogeneous equation of motion is used, i.e. including the forcing terms in equation (2.16). The procedure is the following. First, the assumed solution in equation (2.17) is substituted in equation (2.16), then the result is pre-multiplied by the transversal modes and integrated along the transversal direction y. This results in the following

$$\left[A\right]^T\left[\left[K_{xx}\right]\frac{\partial^4}{\partial x^4}+\left[K_{xy}\right]\frac{\partial^2}{\partial x^2}+\left[K\right]-\omega^2\left[M\right]\right]\left[A\right]\left\{q_n X_n\left(x\right)\right\}=\left\{F_n\left(x\right)\right\} \tag{2.20}$$

For this particular case, matrices $\left[K_{xx}\right]$ and $\left[K_{xy}\right]$ are diagonal. On the other hand, matrix $\left[A\right]$ collects all eigenvectors $\left\{A_n\right\}$. Finally, $\left\{q_n X_n\left(x\right)\right\}$ is a vector containing the modal amplitudes

multiplied by the assumed circumferential solution. It should also be noted that time-dependent term $T(t)=e^{i\omega t}$ is not included in equation nor in all subsequent equations since it simplifies.

The next step is to perform a wavenumber transform to equation (2.20). The following system in the wavenumber domain is obtained

$$\left[\left[C_{xx}\right]k_x^4+\left[C_{xy}\right]k_x^2+\left[\lambda_n\right]-\omega^2\left[I\right]\right]\left\{q_nX_n\left(k_x\right)\right\}=\left\{F_n\left(k_x\right)\right\} \tag{2.21}$$

Matrices $\left[C_{xx}\right]$ and $\left[C_{xy}\right]$ in equation (2.21) are fully populated. However, the diagonal terms are dominant. Thus, the off-diagonal terms can be ignored and the entire system can be completely decoupled in the wavenumber domain. Matrix $\left[\lambda_n\right]$ is a diagonal matrix containing all eigenvalues ω_n^2, while $\left[I\right]$ is an identity matrix. Finally, the vector $\left\{F_n\left(k_x\right)\right\}$ contains the modal forces applied to the system in the wavenumber domain, as follows

$$F_n\left(k_x\right)=F_0e^{ik_xx_f}\left[\sum_m^M A_{mn}\sin\left(\frac{m\pi y_f}{L_y}+\frac{m\pi}{2}\right)\right] \tag{2.22}$$

After decoupling the system in equation (2.21), the unknown values of the product $q_nX_n\left(k_x\right)$ for each transversal mode can be found in the spatial domain by taking the inverse wavenumber transform as follows

$$q_nX_n\left(x\right)=\frac{1}{2\pi}\int_{-\infty}^{\infty}\frac{F_n\left(k_x\right)e^{-ik_xx}}{C_{xx,n}k_x^4+C_{xy,n}k_x^2+\lambda_n-\omega^2},\ \text{for } n=1,2,3...N \tag{2.23}$$

$$\textit{all } k_x \textit{ from} -\infty \textit{ to } +\infty$$

where $C_{xx,n}$ and $C_{xy,n}$ are the $^{\text{nth}}$ diagonal values of matrices $\left[C_{xx}\right]$ and $\left[C_{xy}\right]$. Finally, after substituting equation (2.23) into equation (2.17), the total response of the tire then becomes

$$w(x,y,t)=\sum_{n}^{N}\phi_n(y)\frac{1}{2\pi}\int_{-\infty}^{\infty}\frac{F_n(k_x)e^{-ik_x x}}{C_{xx,n}k_x^4+C_{xy,n}k_x^2+\lambda_n-\omega^2}dk_x e^{i\omega t} \tag{2.24}$$

It should be noted that an analytical solution to the integral exists, as defined in the work by Bateman (1954). This is a significant advantage of this approach because it significantly reduces computational time while computing the total response for many points on the tire's belt and sidewalls.

The mobility frequency response function for the non-uniform infinite plate model is the following

$$M_{IP}\left((x_t,y_t)\middle|(x_f,y_f),\omega\right)=\frac{i\omega}{F_0}\sum_{n}^{N}\phi_n(y)\frac{1}{2\pi_0}\int_{-\infty}^{\infty}\frac{F_n(k_x)e^{-ik_x x}}{C_{xx,n}k_x^4+C_{xy,n}k_x^2+\lambda_n-\omega^2}dk_x \tag{2.25}$$

If a modal damping loss factor η_n is incorporated, then the mobility in equation (2.25) becomes

$$M_{IP}\left((x_t,y_t)\middle|(x_f,y_f),\omega\right)=\frac{i\omega}{F_0}\sum_{n}^{N}\phi_n(y)\frac{1}{2\pi}\int_{-\infty}^{\infty}\frac{F_n(k_x)e^{-ik_x x}}{C_{xx,n}k_x^4+C_{xy,n}k_x^2+\lambda_n(1+i\eta_n)-\omega^2}dk_x \tag{2.26}$$

The formulation provided above shows that the wave propagation approach is intrinsically different from the model proposed by Kropp (1999). It can potentially capture the tire's response with improved accuracy since propagating and decaying waves along the circumferential direction are assumed instead of standing waves. In addition, structural tire non-uniformities are accounted for. However, inaccuracies at very low and high frequencies are still a limitation for this model because the curvature of the tire is not accounted for. Furthermore, the effects of rotation in the propagating waves also need to be included in the model. This is addressed in the next section.

Finally, it should be noted that the wave-propagation assumption will be used for all the following modeling stages. Therefore, the same novel process proposed in this stage to find the response of the tire will be used.

Moving Infinite Plate

In an effort to include the effects of the tire's rotation, the tire is modeled as a simply supported infinite plate. However, the plate is assumed to be moving along the circumferential direction with velocity V_p, as shown in Figure 2.9. This translational velocity is equivalent to the rotation of the tire during rolling condition.

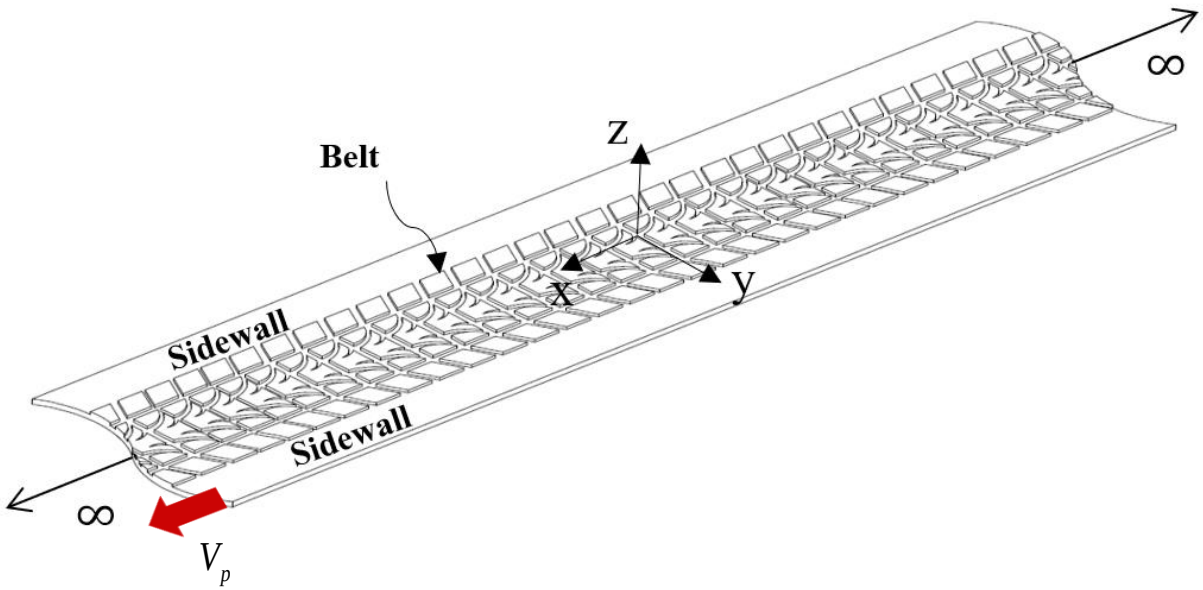

Figure 2.9. Tire modeled as an infinite simply supported plate traveling with a velocity V_p.

In order to compute the response of a moving plate, orthotropic structural properties are assumed. Thus, different bending stresses along the circumferential and circumferential directions are used. Secondly, terms that account for inflation pressure are also included. In addition, non-uniformities along the transversal direction of the tire are also assumed to account for differences between the sidewalls and the belt. Finally, the translational velocity of the tire V_p also needs to be accounted for. The resulting equation of motion of the moving plate for an input point force then becomes the following

$$-T_{0x}\frac{\partial^2 w}{\partial x^2}-T_{0y}\frac{\partial^2 w}{\partial y^2}+\left(\frac{\partial^2}{\partial y^2}\left(B_y(y)\frac{\partial^2 w}{\partial y^2}\right)+2B_{xy}\frac{\partial^4 w}{\partial y^2\partial x^2}+B_x\frac{\partial^4 w}{\partial x^4}\right)- \tag{2.27}$$
$$m(y)\frac{\partial^2 w}{\partial t^2}+m(y)\left(V_p^2\frac{\partial^2 w}{\partial x^2}+2V_p\frac{\partial^2 w}{\partial x\partial t}\right)=f(t)\delta\left(x-x_f\right)\delta\left(y-y_f\right)$$

In this case, the additional terms that account for the velocity V_p are defined by Lee (2009).

The transversal modes are obtained by following the same process as specified in the previous section (see equation (2.19), Figure 2.7 and Figure 2.8). That is, the transversal modes are exactly the same as those computed for the stationary plate presented in the previous section.

The forced response is obtained by substituting the assumed solution into the equation of motion (2.27), then pre-multiplied by the transversal modes and integrated over the transversal direction. The following system of equations is obtained after being wavenumber transformed

Results coming from $V_p^2\frac{\partial^2 w}{\partial x^2}$ are accounted in the diagonal terms of this matrix.

$$\left[[C_{xx}]k_x^4+[C_{xy}]k_x^2+[C_V]\omega k_x+[\lambda_n]-\omega^2[I]\right]\{q_n X_n(k_x)\}=\{F_n(k_x)\} \tag{2.28}$$

Fully populated matrices.

Diagonal matrix with its terms coming from $2V_p\frac{\partial^2 w}{\partial x\partial t}$.

In this case, matrices $[C_{xx}]$ and $[C_{xy}]$ are fully populated. Thus, this system can be decoupled by ignoring their non-diagonal terms. In addition, matrices $[C_V]$ and $[C_{xy}]$ contain the terms that account for the velocity V_p. Finally, the forcing vector in equation (2.28) is the same one defined in equation (2.22).

After decoupling the system, the following modal equations are obtained

$$q_n X_n(k_x) = \frac{F_n(k_x)}{\left(C_{xx,n}k_x^4 + C_{xy,n}k_x^2 + C_{V,n}\omega k_x + \lambda_n - \omega^2\right)}, \text{ for } n = 1,2,3...N \quad \text{all } k_x \text{ from} -\infty \text{ to } +\infty \tag{2.29}$$

The response in the spatial domain is obtained by taking the inverse wavenumber transform of equation (2.29). The results are the following

$$q_n X_n(x) = \frac{1}{2\pi}\int_{-\infty}^{\infty} \frac{F_n(k_x)}{\left(C_{xx,n}k_x^4 + C_{xy,n}k_x^2 + C_{V,n}\omega k_x + \lambda_n - \omega^2\right)} dk_x \tag{2.30}$$

The integral in equation (2.30) can only be solved numerically. Therefore, the computational time needed to find the response of the tire is higher.

The mobility frequency response function for the non-uniform infinite plate model is the following

$$M_{MIP}\left((x_t, y_t)\middle|(x_f, y_f), \omega\right) = \frac{i\omega}{F_0}\sum_n^N \phi_n(y)\frac{1}{2\pi}\int_{-\infty}^{\infty} \frac{F_n(k_x)e^{-ik_x x}}{\left(C_{xx,n}k_x^4 + C_{xy,n}k_x^2 + C_{V,n}\omega k_x + \lambda_n - \omega^2\right)} dk_x \tag{2.31}$$

If a modal damping loss factor is accounted, then the mobility in equation (2.31) becomes

$$M_{MIP}\left((x_t, y_t)\middle|(x_f, y_f), \omega\right) = \frac{i\omega}{F_0}\sum_n^N \phi_n(y)\frac{1}{2\pi}\int_{-\infty}^{\infty} \frac{F_n(k_x)e^{-ik_x x}}{\left(C_{xx,n}k_x^4 + C_{xy,n}k_x^2 + C_{V,n}\omega k_x + \lambda_n(1+i\eta_n) - \omega^2\right)} dk_x \tag{2.32}$$

Non-Uniform Cylindrical Shell Model

In an effort to include the effects of curvature in the structural model, the tire is modeled with the cylindrical shell shown in Figure 2.10. It is assumed that it is simply supported at its two transversal boundaries. The dynamic response of the shell is defined in terms of three mid-surface

displacement components, in accordance with Kirchhoff's hypothesis (Leissa, 1973). Thus, u corresponds to the transversal displacements along the y-axis, v corresponds to the displacements tangential to the shell's curvature defined by the angle θ, and w corresponds to the radial displacements along the z-axis. In addition, the shell's radius is defined by a, its thickness by h, and its transversal length with L_T. Finally, rotation of the tire can be accounted for by the for spinning velocity Ω [rad/s]. This is the typical behavior of thin cylindrical shells as presented by Fahy (2007).

The structural behavior of the cylindrical shell is governed by the following four kinematic assumptions:

i) The ratio of its thickness to mid-surface curvature must be very small.
ii) Displacements are small if they are compared to the shell's thickness.
iii) Plane sections across the shell thickness remain normal to the mid-surface. This implies that both shear strains parallel to the mid-surface, and those along the radial direction can be assumed to be negligible.
iv) Stresses normal to the mid-surface are assumed to be small compared to other stress components.

This set of assumptions is commonly referred to as the first approximation of shell theory defined by Love. Finally, additional simplifications that follow Donnell-Mushtari-Vlaslov (DMV) theory are implemented in this model. In such case, the mid-surface displacements on the shell's tangent plane, and their derivatives have negligible effects in its curvature and twist.

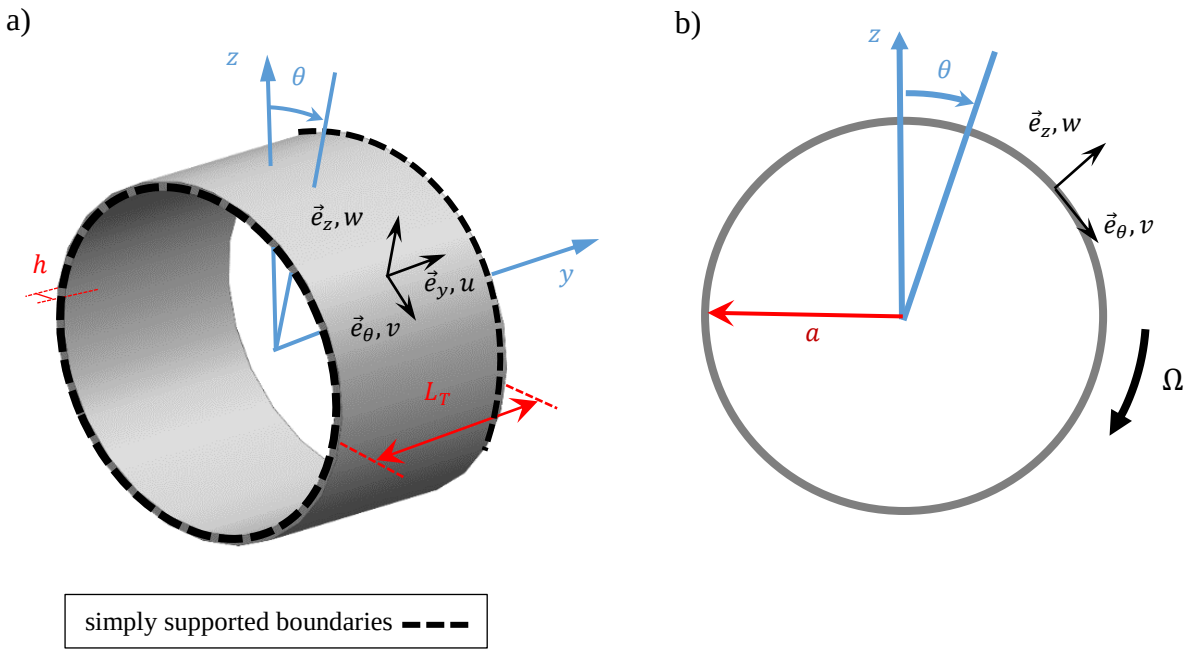

Figure 2.10. Cylindrical shell model showing coordinate system (blue), geometric parameters (red), and mid-surface displacements (black) in a) three-dimensional view and b) side view.

In accordance with the set of assumptions provided above, a set of fully coupled equations of motion can be obtained for a cylindrical shell with a uniform mass per unit area defined as m (W. Soedel, 2005). If the effects of rotation are not yet accounted, the force equilibrium equations for an element of the shell are defined by

$$-\frac{\partial N_y}{\partial y}-\frac{1}{a}\frac{\partial N_{y\theta}}{\partial \theta}+m\frac{\partial^2 u}{\partial t^2}=0 \tag{2.33}$$

$$-\frac{\partial N_{y\theta}}{\partial y}-\frac{1}{a}\frac{\partial N_{\theta}}{\partial \theta}-\frac{Q_{\theta z}}{a}+m\frac{\partial^2 v}{\partial t^2}=0 \tag{2.34}$$

$$-\frac{\partial Q_{yz}}{\partial y}-\frac{1}{a}\frac{\partial Q_{\theta z}}{\partial \theta}+\frac{N_{\theta}}{a}+m\frac{\partial^2 w}{\partial t^2}=0 \tag{2.35}$$

Here, all subscripts correspond to the direction of the resultant forces and moments. N are the normal resultant forces and Q are the shear forces related to the resultant moments M. These are defined as

$$Q_{yz} = \frac{\partial M_y}{\partial y} + \frac{1}{a}\frac{\partial M_{y\theta}}{\partial \theta} \qquad Q_{\theta z} = \frac{\partial M_{y\theta}}{\partial y} + \frac{1}{a}\frac{\partial M_{\theta}}{\partial \theta} \tag{2.36}$$

A similar approach was implemented by Y. J. Kim et al. (2004) to predict the complete structural response of a rotating tire. However, this approach is not suitable for predictions of vibration-induced noise of a tire. The reason is that the generation of sound by a vibrating surface is dominated by its normal acceleration. This is the only one responsible for the fluid's compression and thus, the radiation of sound (Fahy, 2007). Therefore, a simplified cylindrical shell model is presented in this work, such that curvature of the tire is still accounted but only the radial displacement is kept.

A simplified cylindrical shell model is thus required for prediction of vibration-induced noise. The motion of the tire must be assumed to be dominated by radial vibrations. Thus, inertia effects on its tangent plane are negligible. Furthermore, it is assumed that the shell's radius is much larger than its thickness. Consequently, shear forces $Q_{\theta z}$ can be neglected as well. In such case, equation (2.33) and equation (2.34) become the following

$$\frac{\partial N_y}{\partial y} + \frac{1}{a}\frac{\partial N_{y\theta}}{\partial \theta} = 0 \qquad \frac{\partial N_{y\theta}}{\partial y} + \frac{1}{a}\frac{\partial N_{\theta}}{\partial \theta} = 0 \tag{2.37}$$

A shell that follows these simplifications is typically referred to as a shallow shell. However, this denomination is needless. W. Soedel (1983) demonstrated that the simplified approach provides excellent modal agreement if compared to classic Love theory for isotropic shells (Leissa, 1973). The same can be concluded if the shell's transversal stiffness is larger than the circumferential one. The only case where inaccuracies could be observed when stiffness along the circumferential direction is larger than its transversal one. This is the case for regular passenger car tires, as shown by the structural properties provided by Pinnington et al. (2002)

Figure 2.11 shows the results presented by W. Soedel (1983). Here, natural frequencies for different modes are compared between finite element modeling results and those obtained with the simplified approach. In this case, *n* correspond the circumferential modes and *m* to the transversal modes (see Figure 2.12). Figure 2.11a corresponds to a shell that has a larger transversal stiffness,

while Figure 2.11b shows results for a larger circumferential stiffness i.e. the typical case for a passenger-car tire. Significant discrepancies are only observed for the first two circumferential modes in Figure 2.11b.

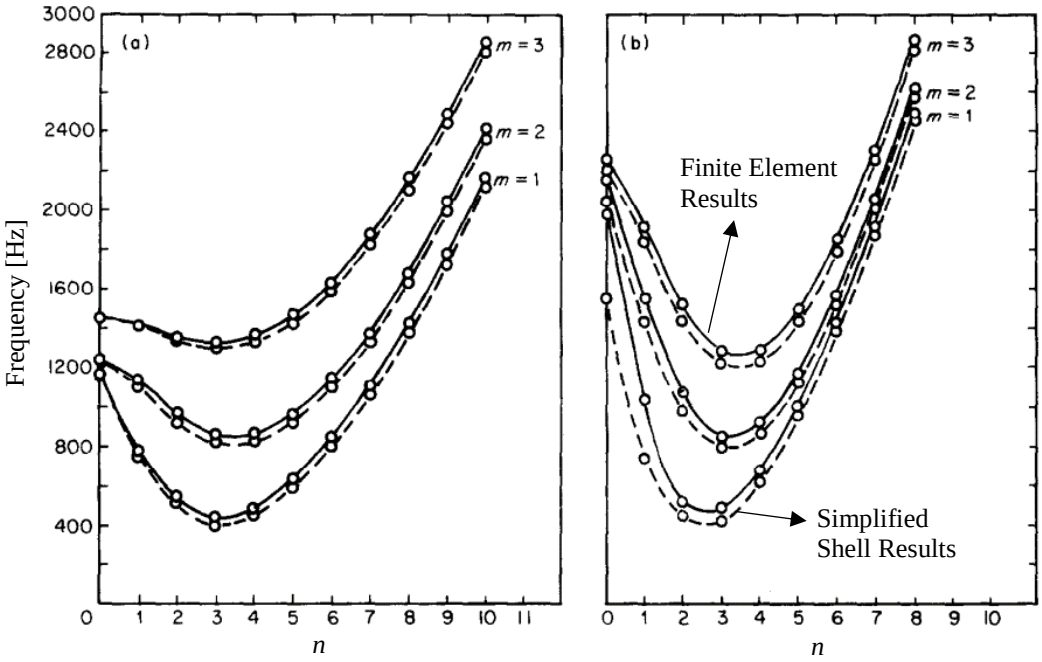

Figure 2.11. Natural frequencies for orthotropic shell a) stiffer along its transversal direction and b) stiffer along its circumferential direction (W. Soedel, 1983).

a) Circumferential Modes

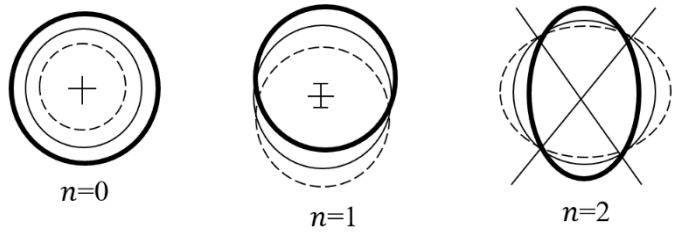

b) Transversal Modes

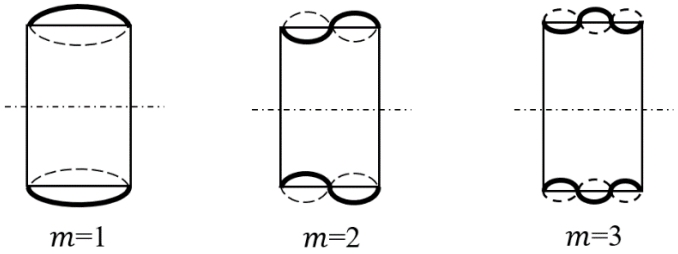

Figure 2.12. Example of the first three a) circumferential modes and b) transversal modes.

The next step in the formulation of the simplified cylindrical shell is to define a set of expressions for the resultant forces in equation (2.35) and equation (2.37). To obtain them, the following kinematic relationships must be defined as

$$\begin{Bmatrix} e_y \\ e_\theta \\ \gamma_{y\theta} \end{Bmatrix} = \begin{Bmatrix} \varepsilon_y \\ \varepsilon_\theta \\ \varepsilon_{y\theta} \end{Bmatrix} + z \begin{Bmatrix} k_y \\ k_\theta \\ \tau \end{Bmatrix} \tag{2.38}$$

Here, e_y, e_θ and $\gamma_{y\theta}$ are the strains at any arbitrary location in the shell. , ε_y, ε_θ and $\varepsilon_{y\theta}$ are the normal and shear strains of the mid-surface. , k_y, k_θ and τ are the mid-surface change in curvature and twist. According to DMV theory, these are given by

$$\varepsilon_y = \frac{\partial u}{\partial y} \qquad k_y = -\frac{\partial^2 w}{\partial y^2}$$
$$\varepsilon_\theta = \frac{1}{a}\left(\frac{\partial v}{\partial \theta} + w\right) \qquad k_\theta = -\frac{1}{a^2}\frac{\partial^2 w}{\partial \theta^2} \tag{2.39}$$
$$\varepsilon_{y\theta} = \left(\frac{\partial v}{\partial y} + \frac{1}{a}\frac{\partial u}{\partial \theta}\right) \qquad \tau = -\frac{2}{a}\frac{\partial^2 w}{\partial \theta \partial y}$$

The stress resultants across the shell can, therefore, be obtained by simply applying Hooke's law written in a tri-dimensional form as

$$\sigma_y = \frac{E}{1-\nu_i^2}\left(e_y + \nu_i e_\theta\right) \qquad \sigma_\theta = \frac{E}{1-\nu_i^2}\left(e_\theta + \nu_i e_y\right) \qquad \sigma_{y\theta} = G\gamma_{y\theta} \tag{2.40}$$

where G corresponds to the shear modulus, ν_i is the isotropic material's Poison ratio, and E is the isotropic material's modulus of elasticity.

Finally, the force and moment resultants across the shell can be obtained by integrating the stresses equation (2.40) over its thickness, as follows

$$\begin{Bmatrix} N_y \\ N_\theta \\ N_{y\theta} \end{Bmatrix} = \int_{-h/2}^{h/2} \begin{Bmatrix} \sigma_y \\ \sigma_\theta \\ \sigma_{y\theta} \end{Bmatrix} dz \qquad \begin{Bmatrix} M_y \\ M_\theta \\ M_{y\theta} \end{Bmatrix} = \int_{-h/2}^{h/2} \begin{Bmatrix} \sigma_y \\ \sigma_\theta \\ \sigma_{y\theta} \end{Bmatrix} z dz \tag{2.41}$$

It is convenient to write the solution to these integrals in matrix form as follows

$$\begin{Bmatrix} N_y \\ N_\theta \\ N_{y\theta} \end{Bmatrix} = \begin{bmatrix} K_{11} & K_{12} & 0 \\ K_{12} & K_{22} & 0 \\ 0 & 0 & K_{33} \end{bmatrix} \begin{Bmatrix} \varepsilon_y \\ \varepsilon_\theta \\ \varepsilon_{y\theta} \end{Bmatrix} \qquad \begin{Bmatrix} M_y \\ M_\theta \\ M_{y\theta} \end{Bmatrix} = \begin{bmatrix} D_{11} & D_{12} & 0 \\ D_{12} & D_{22} & 0 \\ 0 & 0 & D_{33} \end{bmatrix} \begin{Bmatrix} k_y \\ k_\theta \\ \tau \end{Bmatrix} \tag{2.42}$$

Here, the resulting forces and moments are now expressed in terms of its strains and stiffnesses. K_{ij} denotes membrane stiffnesses and D_{ij} bending stiffnesses. For the case of an isotropic shell, these stiffnesses are given as

$$K_{11} = K_{22} = K \qquad K_{12} = \nu_i K \qquad K_{33} = (1-\nu_i)K/2$$
$$D_{11} = D_{22} = D \qquad \mathrm{D}_{12} = \nu_i D \qquad \mathrm{D}_{33} = (1-\nu_i)D/2 \tag{2.43}$$

where, D and K are the characteristic isotropic stiffnesses of the cylindrical shell, given as follows

$$K = \frac{Eh^3}{12(1-\nu_i^2)} \qquad \mathrm{D} = \frac{Eh}{(1-\nu_i^2)} \tag{2.44}$$

An alternate approach to define the normal resultant forces is given in the work by W. Soedel (1983). In this case, these are defined by

$$N_y = \frac{1}{a^2}\frac{\partial^2\phi}{\partial\theta^2} \qquad N_\theta = \frac{\partial^2\phi}{\partial y^2} \qquad N_{y\theta} = -\frac{1}{a}\frac{\partial^2\phi}{\partial\theta\partial y} \tag{2.45}$$

where $\phi(y,z,\theta)$ correspond to Airy's stress function. In addition, all expressions given in equation (2.45) satisfy equation (2.37). Therefore, they follow the dominant radial vibration assumption for cylindrical shells.

Substituting into equation (2.35), both expressions in equation (2.36), the second expression in equation (2.45), and the resultant moments and strains from both equations (2.42) and (2.39), results in

$$D\nabla^4 w + \frac{1}{a}\frac{\partial^2\phi}{\partial y^2} + m\frac{\partial^2 w}{\partial t^2} = 0 \tag{2.46}$$

Where $\nabla^4(\bullet) = \frac{1}{a^2}\frac{\partial^4(\bullet)}{\partial\theta^4} + \frac{\partial^4(\bullet)}{\partial y^4} + \frac{2}{a^2}\frac{\partial^4(\bullet)}{\partial y^2\partial\theta^2}$.

On the other hand, from the six strain-displacement in equation (2.39), the following compatibility equation is found

$$-\frac{1}{a}\frac{\partial^2 w}{\partial y^2}+\frac{\partial^2 \varepsilon_\theta}{\partial y^2}-\frac{1}{a}\frac{\partial^2 \varepsilon_{y\theta}}{\partial y \partial \theta}+\frac{1}{a^2}\frac{\partial^2 \varepsilon_y}{\partial y^2}=0 \tag{2.47}$$

This equation is obtained by performing a set of substitutions, additions, and subtractions using all expressions in equation (2.39) (W. Soedel, 2005). Furthermore, if the strains in equation (2.47) are expressed in terms of the normal forces defined by equation (2.42), and equations (2.45), then the compatibility equation becomes

$$\frac{Eh}{a}\frac{\partial^2 w}{\partial y^2}-\nabla^4 \phi=0 \tag{2.48}$$

Equations (2.46) and (2.48) are the equations of motion for the simplified shell model of a tire.

Up to this point, the shell's coupled equations of motion have been reduced from three to two. The two unknowns, in this case, are the shell's normal displacement $w(y,z,\theta)$, and the stress function $\phi(y,z,\theta)$. However, further simplification can be achieved by operating equation (2.46) with the double Laplacian $\nabla^4(\bullet)$, and equation (2.48) with $\partial^2(\bullet)/\partial y^2$. After combining the two, the following equation of motion is obtained

$$\nabla^8 w+\frac{Eh}{a^2}\frac{\partial^4 w}{\partial y^2 \partial \theta^2}-m\omega^2\nabla^4 w=0 \tag{2.49}$$

Here, it has been assumed that all displacements are harmonic of the form $e^{i\omega t}$. Thus, the last term in the left-hand side of equation (2.49) is multiplied by the square of the frequency ω.

The assumptions made in this section simplified the fully coupled equations (2.33) to (2.36) into a single equation of motion, given by equation (2.49). This simplified approach defines the structural motion of a tire solely in terms of the dominant radial displacement. The objective of this process is to avoid unnecessary complications during Vibro-acoustic response computations. However, additional improvements are still needed in order to more accurately capture the

characteristic structural behavior of a tire. The following set of novel extensions to the model have been implemented:

i) Orthotropic material properties and radial forcing terms in the formulation.
ii) Non-uniform properties along the transversal direction of the tire that account for structural differences between the tire's belt and sidewalls.
iii) Additional membrane tension terms that account for inflation pressure.
iv) Effects of rotation in the tire's structural dynamic behavior.

The first extension is first addressed. The combination of composite materials typically used in tire results in different structural properties along its circumferential and transversal directions (Pinnington, 2006a). Thus, a physically accurate model of a tire's structure must account for its orthotropic properties. Accordingly, it is appropriate to change the tri-dimensional Hooke's law given in equation (2.40) to the following

$$\sigma_y = E_y e_y + E_{y\theta} e_\theta \qquad \sigma_\theta = E_\theta e_\theta + E_{y\theta} e_y \qquad \sigma_{y\theta} = G\gamma_{y\theta} \tag{2.50}$$

where G corresponds to the shear modulus and the orthotropic elasticity moduli are

$$\begin{aligned} E_y &= E_y^{'} \big/ \left(1 - \nu_y \nu_\theta\right) \\ E_\theta &= E_\theta^{'} \big/ \left(1 - \nu_y \nu_\theta\right) \\ E_{y\theta} &= \nu_\theta E_y^{'} \big/ \left(1 - \nu_y \nu_\theta\right) = \nu_y E_\theta^{'} \big/ \left(1 - \nu_y \nu_\theta\right) \end{aligned} \tag{2.51}$$

where the right-hand side terms containing the prime superscript correspond to the effective moduli of the material, while v_y and v_θ are the effective Poisson's ratios (Ugural, 2018). The resultant forces and moments in the shell then become the following

$$\begin{Bmatrix} N_y \\ N_\theta \\ N_{y\theta} \end{Bmatrix} = \begin{bmatrix} E_y h & E_{y\theta} h & 0 \\ E_{y\theta} h & E_\theta h & 0 \\ 0 & 0 & Gt \end{bmatrix} \begin{Bmatrix} \varepsilon_y \\ \varepsilon_\theta \\ \varepsilon_{y\theta} \end{Bmatrix} \tag{2.52}$$

$$\begin{Bmatrix} M_y \\ M_\theta \\ M_{y\theta} \end{Bmatrix} = \begin{bmatrix} E_y h^3/12 & E_{y\theta} h^3/12 & 0 \\ E_{y\theta} h^3/12 & E_\theta h^3/12 & 0 \\ 0 & 0 & Gh^3/12 \end{bmatrix} \begin{Bmatrix} k_y \\ k_\theta \\ \tau \end{Bmatrix}$$

If the same process to obtain equation (2.46) is followed, this time using the bending stiffnesses in equation (2.52), then the next equation is obtained

$$D_{11}\frac{\partial^4 w}{\partial y^4} + \frac{2\left(D_{12}+2D_{33}\right)}{a^2}\frac{\partial^4 w}{\partial y^2 \partial \theta^2} + \frac{D_{22}}{a^4}\frac{\partial^4 w}{\partial \theta^4} + \frac{1}{a}\frac{\partial^2 \phi}{\partial y^2} + m\frac{\partial^2 w}{\partial t^2} = F_r \tag{2.53}$$

This is analogous to equation (2.46), but with the orthotropic effects included. In addition, it should be noted that the radial forcing term F_r has also been included. This is assumed equal to a point force defined by $F_r = f(t)\delta\left(x - x_f\right)\delta\left(y - y_f\right)$, as was also done for the previous modeling stages.

On the other hand, if the same process to obtain equation (2.48) is followed, but the membrane stiffnesses in equation (2.52) are used, then the following orthotropic compatibility equation is obtained

$$-\frac{1}{a}\frac{\partial^2 w}{\partial y^2} + \alpha_1\frac{\partial^4 \phi}{\partial \theta^4} + \alpha_2\frac{\partial^4 \phi}{\partial y^4} + \alpha_3\frac{\partial^4 \phi}{\partial y^2 \partial \theta^2} = 0 \tag{2.54}$$

where,

$$\alpha_2 = \frac{K_{11}}{K_{11}K_{22} - K_{12}^2} \qquad \alpha_1 = \frac{K_{22}}{a^4\left(K_{11}K_{22} - K_{12}^2\right)} \qquad \alpha_3 = \frac{1}{a^2}\left(\frac{1}{K_{33}} - \frac{2K_{12}}{K_{11}K_{22} - K_{12}^2}\right) \tag{2.55}$$

In order to simplify equation (2.53) and equation (2.54) into a single equation of motion for an orthotropic shell, equation (2.53) must now be operated as follows

$$\nabla_D^4(\bullet) = \alpha_1 \frac{\partial^4(\bullet)}{\partial\theta^4} + \alpha_2 \frac{\partial^4(\bullet)}{\partial y^4} + \alpha_3 \frac{\partial^4(\bullet)}{\partial y^2 \partial\theta^2} \tag{2.56}$$

On the other hand, equation (2.54) is operated as it was done for equation (2.48). After combining both equations, the resulting single equation of motion for the forced, orthotropic cylindrical shell becomes

$$\begin{aligned} &\chi_1 \frac{\partial^8 w}{\partial y^8} + \chi_2 \frac{\partial^8 w}{\partial y^6 \partial\theta^2} + \chi_3 \frac{\partial^8 w}{\partial y^4 \partial\theta^4} + \chi_4 \frac{\partial^8 w}{\partial y^2 \partial\theta^6} + \chi_5 \frac{\partial^8 w}{\partial\theta^8} + \chi_6 \frac{\partial^4 w}{\partial y^4} \\ &\quad -m\omega^2 \left(\alpha_1 \frac{\partial^4 w}{\partial\theta^4} + \alpha_2 \frac{\partial^4 w}{\partial y^4} + \alpha_3 \frac{\partial^4 w}{\partial y^2 \partial\theta^2} \right) = \alpha_1 \frac{\partial^4 F_r}{\partial\theta^4} + \alpha_2 \frac{\partial^4 F_r}{\partial y^4} + \alpha_3 \frac{\partial^4 F_r}{\partial y^2 \partial\theta^2} \end{aligned} \tag{2.57}$$

The multiplying constants in equation (2.57) are given by

$$\begin{aligned} \chi_1 &= (D_{11}\alpha_2) & \chi_2 &= \left[\alpha_3 D_{11} + \frac{2\alpha_2 (D_{12} + 2D_{33})}{a^2} \right] \\ \chi_3 &= \left[\alpha_1 D_{11} + \frac{\alpha_2 D_{22}}{a^4} + \frac{2\alpha_3 (D_{12} + 2D_{33})}{a^2} \right] & \chi_4 &= \left[\frac{2\alpha_1 (D_{12} + 2D_{33})}{a^2} + \frac{\alpha_3 D_{22}}{a^4} \right] \\ \chi_5 &= \left(\frac{\alpha_1 D_{22}}{a^4} \right) & \chi_6 &= \frac{1}{a^2} \end{aligned} \tag{2.58}$$

The next step is to include transversal non-uniformities. Though the cylindrical shell tire model does not accurately represent a tire's actual transversal geometry, structural differences between the belt and sidewalls need to be accounted for. This corresponds to the second extension of the model by including non-uniform properties. A smear representation of the tread is used to include its added mass in the tire's belt, as shown in Figure 2.13. This results in different structural properties between the belt and the sidewalls.

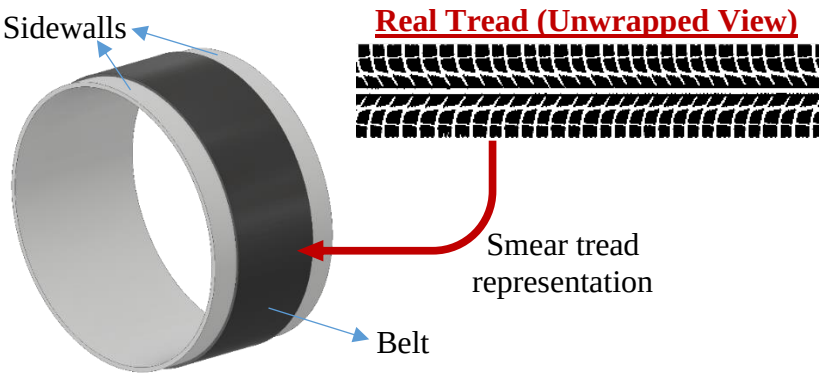

Figure 2.13. Non-uniform cylindrical shell model with a smear tread representation.

Varying bending stiffness and mass distribution along the tire's transversal direction account for the shell's non-uniformities. These two were selected following the assumption that the radial vibratory motion is dominant. In this case, equation (2.53) becomes the following

$$\frac{\partial^2}{\partial y^2}\left(D_{11}(y)\frac{\partial^2 w}{\partial y^2}\right)+\frac{2\left(D_{12}+2D_{33}\right)}{a^2}\frac{\partial^4 w}{\partial y^2\partial\theta^2}+\frac{D_{22}}{a^4}\frac{\partial^4 w}{\partial\theta^4}+\frac{1}{a}\frac{\partial^2\phi}{\partial y^2}+m(y)\frac{\partial^2 w}{\partial t^2}=F_r \tag{2.59}$$

As shown in equation (2.59), the bending stiffness D_{11} and the mass m now depend on the transversal direction along the tire i.e., y. Following the same operating process described in the previous sections, equation (2.59) and the compatibility equation (2.54) is used to derive a single equation of motion for an orthotropic non-uniform cylindrical shell, as follows

$$\begin{aligned}&\alpha_1\frac{\partial^6}{\partial\theta^4\partial y^2}\left(D_{11}(y)\frac{\partial^2 w}{\partial y^2}\right)+\alpha_2\frac{\partial^6}{\partial y^6}\left(D_{11}(y)\frac{\partial^2 w}{\partial y^2}\right)+\alpha_3\frac{\partial^6}{\partial y^4\partial\theta^2}\left(D_{11}(y)\frac{\partial^2 w}{\partial y^2}\right)+\\&\left(\chi_2-D_{11}(y)\alpha_3\right)\frac{\partial^8 w}{\partial y^6\partial\theta^2}+\left(\chi_3-D_{11}(y)\alpha_1\right)\frac{\partial^8 w}{\partial y^4\partial\theta^4}+\chi_4\frac{\partial^8 w}{\partial y^2\partial\theta^6}+\chi_5\frac{\partial^8 w}{\partial\theta^8}+\\&\chi_6\frac{\partial^4 w}{\partial y^4}-\omega^2\left(\alpha_1 m(y)\frac{\partial^4 w}{\partial\theta^4}+\alpha_2\frac{\partial^4 m(y)w}{\partial y^4}+\alpha_3\frac{\partial^4 m(y)w}{\partial y^2\partial\theta^2}\right)=\alpha_1\frac{\partial^4 F_r}{\partial\theta^4}+\alpha_2\frac{\partial^4 F_r}{\partial y^4}+\alpha_3\frac{\partial^4 F_r}{\partial y^2\partial\theta^2}\end{aligned} \tag{2.60}$$

Additional effects of inflation pressure are also accounted for in this model. This is done by the addition of residual membrane tensions along with the circumferential and transversal directions of the shell, as shown in the work by Y. J. Kim et al. (2004). Their approach was modified to account for these effects in the simplified cylindrical shell. In this case, equation (2.59) is modified to

$$\frac{\partial^2}{\partial y^2}\left(D_{11}(y)\frac{\partial^2 w}{\partial y^2}\right)+\frac{2\left(D_{12}+2D_{33}\right)}{a^2}\frac{\partial^4 w}{\partial y^2\partial\theta^2}+\ldots \\ \frac{D_{22}}{a^4}\frac{\partial^4 w}{\partial\theta^4}+\frac{1}{a}\frac{\partial^2\phi}{\partial y^2}-\frac{N_\theta^r}{a^2}\frac{\partial^2 w}{\partial\theta^2}-N_y^r\frac{\partial^2 w}{\partial y^2}+m(y)\frac{\partial^2 w}{\partial t^2}=F_r \tag{2.61}$$

where the membrane tension along the transversal direction of the tire have been approximated by $N_\theta^r = pa$, while the circumferential tension has been approximated by $N_y^r = pa/2$. In both cases, p is to the tire inflation pressure. The shell's equation of motion for this case becomes

$$\alpha_1\frac{\partial^6}{\partial\theta^4\partial y^2}\left(D_{11}(y)\frac{\partial^2 w}{\partial y^2}\right)+\alpha_2\frac{\partial^6}{\partial y^6}\left(D_{11}(y)\frac{\partial^2 w}{\partial y^2}\right)+\alpha_3\frac{\partial^6}{\partial y^4\partial\theta^2}\left(D_{11}(y)\frac{\partial^2 w}{\partial y^2}\right)+ \\ \left(\chi_2-D_{11}(y)\alpha_3\right)\frac{\partial^8 w}{\partial y^6\partial\theta^2}+\left(\chi_3-D_{11}(y)\alpha_1\right)\frac{\partial^8 w}{\partial y^4\partial\theta^4}+\chi_4\frac{\partial^8 w}{\partial y^2\partial\theta^6}+\chi_5\frac{\partial^8 w}{\partial\theta^8}+ \\ \chi_6\frac{\partial^4 w}{\partial y^4}-\frac{N_\theta^r}{a^2}\left(\alpha_1\frac{\partial^6 w}{\partial\theta^6}+\alpha_2\frac{\partial^6 w}{\partial y^4\partial\theta^2}+\alpha_3\frac{\partial^6 w}{\partial y^2\partial\theta^4}\right)-N_y^r\left(\alpha_1\frac{\partial^6 w}{\partial y^2\partial\theta^4}+\alpha_2\frac{\partial^6 w}{\partial y^6}+\alpha_3\frac{\partial^6 w}{\partial y^4\partial\theta^2}\right)- \\ \omega^2\left(\alpha_1 m(y)\frac{\partial^4 w}{\partial\theta^4}+\alpha_2\frac{\partial^4 m(y)w}{\partial y^4}+\alpha_3\frac{\partial^4 m(y)w}{\partial y^2\partial\theta^2}\right)=\alpha_1\frac{\partial^4 F_r}{\partial\theta^4}+\alpha_2\frac{\partial^4 F_r}{\partial y^4}+\alpha_3\frac{\partial^4 F_r}{\partial y^2\partial\theta^2} \tag{2.62}$$

Finally, the fourth extension of the model corresponds to the addition of rotation effects to the formulation of the cylindrical shell. These effects are briefly shown in Figure 2.14.

Figure 2.14. Wave interaction with the rotation of the tire.

A wave propagation behavior for the mid-frequency range is assumed. In this case, if the tire is excited at the contact region, waves that travel along the circumferential direction of the tire are produced. Those traveling against the rotation of the tire will be slowed down. On the other hand, the velocity of the waves traveling in the same direction as the rotation will be higher. Thus, a difference in wavelength between waves traveling in opposite directions is expected. In this case, the equilibrium equations become

$$
\begin{aligned}
&-\frac{\partial N_y}{\partial y}-\frac{1}{a}\frac{\partial N_{\theta y}}{\partial \theta}=0 \\
&-\frac{\partial N_{y\theta}}{\partial y}-\frac{1}{a}\frac{\partial N_{\theta}}{\partial \theta}+2m(y)\Omega\frac{\partial w}{\partial t}=0 \\
&-\frac{\partial Q_{yz}}{\partial y}-\frac{1}{a}\frac{\partial Q_{\theta z}}{\partial \theta}+\frac{N_{\theta}}{a}+m(y)\frac{\partial^2 w}{\partial t^2}-m(y)\Omega^2 w=F_r
\end{aligned}
\tag{2.63}
$$

Note that these equations include the tire's rotational velocity Ω. Furthermore, since the first two expressions in equation (2.63) need to be satisfied, N_θ previously defined in equation (2.45) changes to the following

$$
N_\theta=\frac{\partial^2\phi}{\partial y^2}+2m(y)a\Omega\int\frac{\partial w}{\partial t}d\theta \tag{2.64}
$$

This type of formulation is similar to that proposed by Flügge (1960).

If the same process as in the previous sections is followed, but now using equation (2.63) and equation (2.64), the following single equation of motion is obtained

$$\begin{aligned}
&\alpha_1\frac{\partial^6}{\partial y^2\partial\theta^4}\left(D_{11}(y)\frac{\partial^2 w}{\partial y^2}\right)+\alpha_2\frac{\partial^6}{\partial y^6}\left(D_{11}(y)\frac{\partial^2 w}{\partial y^2}\right)+\alpha_3\frac{\partial^6}{\partial y^4\partial\theta^2}\left(D_{11}(y)\frac{\partial^2 w}{\partial y^2}\right)+\left(\chi_2-D_{11}(y)\alpha_3\right)\frac{\partial^8 w}{\partial y^6\partial\theta^2}\\
&+\left(\chi_3-D_{11}(y)\alpha_1\right)\frac{\partial^8 w}{\partial y^4\partial\theta^4}+\chi_4\frac{\partial^8 w}{\partial y^2\partial\theta^6}+\chi_5\frac{\partial^8 w}{\partial\theta^8}+\chi_6\frac{\partial^4 w}{\partial y^4}-\omega^2\left(\alpha_1 m(y)\frac{\partial^4 w}{\partial\theta^4}+\alpha_2\frac{\partial^4 m(y)w}{\partial y^4}+\alpha_3\frac{\partial^4 m(y)w}{\partial y^2\partial\theta^2}\right)\\
&-\frac{1}{a^2}\left(\alpha_1 N_\theta^r(y)\frac{\partial^6 w}{\partial\theta^6}+\alpha_2\frac{\partial^6 N_\theta^r(y)w}{\partial y^4\partial\theta^2}+\alpha_3\frac{\partial^6 N_\theta^r(y)w}{\partial y^2\partial\theta^4}\right)-N_y^r\left(\alpha_1\frac{\partial^6 w}{\partial y^2\partial\theta^4}+\alpha_2\frac{\partial^6 w}{\partial y^6}+\alpha_3\frac{\partial^6 w}{\partial y^4\partial\theta^2}\right)\\
&+2i\omega\Omega\left(\alpha_1 m(y)\frac{\partial^3 w}{\partial\theta^3}+\alpha_3\frac{\partial^3 m(y)w}{\partial y^2\partial\theta}+\alpha_4\frac{\partial^3 m(y)w}{\partial y^2\partial\theta}\right)-\Omega^2\left(\alpha_1 m(y)\frac{\partial^4 w}{\partial\theta^4}+\alpha_2\frac{\partial^4 m(y)w}{\partial y^4}+\alpha_3\frac{\partial^4 m(y)w}{\partial y^2\partial\theta^2}\right)\\
&=\left(\alpha_1\frac{\partial^4 F_r}{\partial\theta^4}+\alpha_2\frac{\partial^4 F_r}{\partial y^4}+\alpha_3\frac{\partial^4 F_r}{\partial y^2\partial\theta^2}\right)
\end{aligned} \tag{2.65}$$

This is the equation of motion for an orthotropic, non-uniform, inflated, and rotating shell. Note that, in this case, the left-hand side term that is multiplied by Ω now includes a new constant $\alpha_4 = K_{12}/a^2\left(K_{11}K_{22}-K_{12}^2\right)$. Furthermore, additional residual stress appears due to a rotation-induced static deflection of the tire (Y. J. Kim et al., 2004). This is added to the circumferential membrane stress coming from the inflation pressure. Therefore, the previously defined $N_\theta^r = pa$ now becomes $N_\theta^r(y) = pa + m(y)a\Omega^2$.

Previous work in tire modeling has assumed a full modal solution to compute the response of the tire, as shown in Chapter 1. However, for the frequency range of interest, this approach is no longer physically accurate, as shown in the experimental findings by Bernhard (2000).

As presented for the plate models, a wave propagation approach is implemented to find the tire's response. The following solution is proposed

$$w(\theta,y,t) = \sum_n^N q_n\beta_n(y)X_n(\theta)e^{i\omega t} \tag{2.66}$$

Similar to the previous cases, modes are again assumed in the transversal direction of the tire. These are defined as $\beta_n(y)$ in equation (2.66). Waves are assumed along the circumferential direction. In this case, these are defined in terms of the angle θ, shown in Figure 2.10.

In order to compute the transversal modes of the cylindrical shell, a homogeneous equation that is only a function of y is constructed. For this specific case, the 2nd, 8th, 10th, 16th, and 22nd terms of equation (2.65) are selected and equated to zero. Similar to the previous models, the transversal modes are substituted into this equation. The resulting expression is then pre-multiplied by a vector of admissible functions and integrated over the transversal direction y. The outcome is an eigenvalue problem and its solution define the transversal modes of the tire.

On the other hand, the forced response is obtained by substituting equation (2.66) into equation (2.65), then this is pre-multiplied by a vector of the transversal modes, integrated over the transversal direction, and finally, wavenumber transformed. The following system of equations is obtained

$$\begin{bmatrix} [C_1]k_\theta^8 + [C_2]k_\theta^6 + [C_3]k_\theta^4 + [C_4]k_\theta^2 + [\lambda_n] + \\ \omega[C_5]k_\theta^3 + \omega[C_6]k_\theta - \omega^2[N_1]k_\theta^4 - \omega^2[N_2]k_\theta^2 - \omega^2[I] \end{bmatrix} \{q_n X_n(k_\theta)\} = \{F_n(k_\theta)\} \tag{2.67}$$

Here, the matrix $\left[\omega_n^2\right]$ is a diagonal matrix containing all the natural frequencies of the system. On the other hand, $[I]$ is a diagonal identity matrix. Finally, matrices $[C_{1\ldots6}]$ and $[N_{1\ldots2}]$ are fully populated matrices. It should also be noted that equation (2.67) is expressed in terms of the wavenumber k_θ.

The next step is to decouple the system of equations. To do so, the off-diagonal terms of all fully populated matrices are ignored. This decoupling assumption is adequate if the matrices' off-diagonal terms are negligible compared to its diagonal ones. This is typically the case for an orthotropic tire. The result is the following modal equation

$$q_n X_n(k_\theta) = \frac{F_n(k_\theta)}{C_{1,nn}k_\theta^8 + C_{2,nn}k_\theta^6 + C_{3,nn}k_\theta^4 + C_{4,nn}k_\theta^2 + \lambda_n + \omega C_{5,nn}k_\theta^3 + \omega C_{6,nn}k_\theta - \omega^2 N_{1,nn}k_\theta^4 - \omega^2 N_{2,nn}k_\theta^2 - \omega^2} \tag{2.68}$$

for $n = 1, 2, 3...N$ modes and all k_θ from $-\infty$ to $+\infty$

Finally, the inverse wavenumber transform must be computed to define the modal solution in the spatial domain. This results in the following

$$q_n X_n(\theta) = \frac{1}{2\pi}\int_{-\infty}^{\infty} \frac{F_n(k_\theta)e^{-ik_\theta\theta}}{C_{1,nn}k_\theta^8 + C_{2,nn}k_\theta^6 + C_{3,nn}k_\theta^4 + C_{4,nn}k_\theta^2 + \lambda_n + \omega C_{5,nn}k_\theta^3 + \omega C_{6,nn}k_\theta - \omega^2 N_{1,nn}k_\theta^4 - \omega^2 N_{2,nn}k_\theta^2 - \omega^2} dk_\theta \tag{2.69}$$

In this case, the modal input force in equation (2.69) is given by

$$F_n(k_\theta) = F_0 e^{ik_\theta\theta_f}\left[\alpha_1\beta_n(y_f)k_\theta^4 + \alpha_2\frac{\partial^4\beta_n(y_f)}{\partial y^4} - \alpha_3\frac{\partial^2\beta_n(y_f)}{\partial y^2}k_\theta^2\right] \tag{2.70}$$

This expression is found by assuming that the input radial force F_r in equation (2.65) is the following harmonic point force

$$F_r(y,\theta,t) = F_0\delta(y - y_f)\delta(\theta - \theta_f)e^{i\omega t} \tag{2.71}$$

where, F_0 is the input force amplitude, and the coordinates (y_f, θ_f) is the location of excitation on the shell's surface.

The mobility frequency response function for the cylindrical shell model is the following

$$M_{CS}\left((x_t,y_t)\middle|(x_f,y_f),\omega\right) = \frac{i\omega}{F_0}\times \sum_n^N \beta_n(y)\frac{1}{2\pi}\int_{-\infty}^{\infty}\frac{F_n(k_\theta)e^{-ik_\theta\theta}}{C_{1,nn}k_\theta^8 + C_{2,nn}k_\theta^6 + C_{3,nn}k_\theta^4 + C_{4,nn}k_\theta^2 + \lambda_n + \omega C_{5,nn}k_\theta^3 + \omega C_{6,nn}k_\theta - \omega^2 N_{1,nn}k_\theta^4 - \omega^2 N_{2,nn}k_\theta^2 - \omega^2} dk_\theta \tag{2.72}$$

If a modal damping loss factor is accounted, then the mobility in equation (2.72) becomes

$$M_{CS}\left((x_t,y_t)\middle|(x_f,y_f),\omega\right)=\frac{i\omega}{F_0}\times \tag{2.73}$$
$$\sum_n^N \beta_n(y)\frac{1}{2\pi}\int_{-\infty}^{\infty}\frac{F_n(k_\theta)e^{-ik_\theta\theta}}{C_{1,nn}k_\theta^8+C_{2,nn}k_\theta^6+C_{3,nn}k_\theta^4+C_{4,nn}k_\theta^2+\lambda_n(1+i\eta_n)+\omega C_{5,nn}k_\theta^3+\omega C_{6,nn}k_\theta-\omega^2N_{1,nn}k_\theta^4-\omega^2N_{2,nn}k_\theta^2-\omega^2}dk_\theta$$

The generalized approach for the non-uniform cylindrical shell development is intended to capture the characteristic structural properties of a tire, defined by a wave propagation behavior along its circumferential direction. Properly modeling this behavior by accounting for curvature, non-uniform transversal properties, inflation pressure, and rotation is a challenging task. The theoretical work presented in this paper shows a simplified approach to do this while maintaining physical accuracy. In addition, this model is intended to be implemented for TPIN vibration-induced noise. Therefore, the tire's radial displacements have been assumed dominant. This is the first time that such a formulation is proposed.

2.2. Dispersion Analysis

A dispersion analysis for the plate models is presented in this section. Their straightforward formulation allows to examine in detail the behavior of the waves present in the tire's response and check if results agree with those presented in the open literature. Various conditions are explored, including the effects of rotational velocity and inflation pressure. Still, it should be noted that the analysis presented in this section is not needed to compute the response of the tire. Its only purpose is to provide further physical insight.

First, the effects of the rotating velocity of the tire are analyzed. This is accounted with a translational velocity V_p, if the moving plate model is used. In this case, the following homogeneous equation of motion for an isotropic and uniform moving plate is used

$$D\left(\frac{\partial^4 w}{\partial y^4}+2\frac{\partial^4 w}{\partial y^2\partial x^2}+\frac{\partial^4 w}{\partial x^4}\right)+m\left(\ddot{w}+V_p^2\frac{\partial^2 w}{\partial x^2}+2V_p\frac{\partial^2 w}{\partial x\partial t}\right)=0 \tag{2.74}$$

In this case, $D = Eh^3/12\left(1-v^2\right)$ corresponds to the isotropic bending stiffness of the plate and $m = \rho h$, i.e. the density of the plate multiplied by its thickness. If the wave propagation solution previously defined in equation (2.17) is substituted, then the following expression is obtained

$$D\left(a_n^4 + 2a_n^2 k_x^2 + k_x^4\right) + M_p\left(-\omega^2 - k_x^2 V_p^2 + 2V_p k_x \omega\right) = 0 \tag{2.75}$$

where $a_n = n\pi/L_y$ for all transversal modes $n = 1...N$. Equation (2.75) is then re-arranged into a fourth-order polynomial in terms of the wavenumber k_x as follows

$$Dk_x^4 + \left(2Da_n^2 - \rho h V_p^2\right)k_x^2 + \left(2V_p \rho h \omega\right)k_x + \left(Da_n^4 - \rho h \omega^2\right) = 0 \tag{2.76}$$

Since this is a fourth-order polynomial, a set of 4 wavenumbers or roots can be found for each transversal mode, as a function of frequency ω. Each of the roots has specific characteristics, and are summarized as follows:

- Root 1: Purely imaginary until cut-on frequency, where it becomes positive real.
- Root 2: Purely imaginary until cut-on frequency, where it becomes negative real.
- Root 3: Complex root for all frequencies with the positive imaginary component.
- Root 4: Complex root for all frequencies with the negative imaginary component.

The real roots can have either a positive or negative sign. A positive sign corresponds to waves traveling in the positive x-direction. A negative sign corresponds to those traveling in the opposite direction. On the other hand, the imaginary component of the complex roots defines a decaying behavior. These contribute only near the location of the input force or the boundaries.

Figure 2.15 provides an example of the behavior of the four roots for a plate moving with a velocity of 32 m/s (this is equivalent to a tire of radius 0.32m traveling at 100 rad/s or on a vehicle traveling at ~70 mph). The four complex roots (both imaginary and real components) for the 3rd transversal mode of the tire are shown. A frequency range of up to 4,000 Hz has been selected. The first two

roots show a decaying imaginary component up to the cut on frequency located around 850 Hz. Above this frequency, waves start propagating. On the other hand, root 3 and root 4 show complex wavenumbers for all frequencies. They show a decaying component that is frequency-dependent, while their propagating component is independent of frequency. Finally, it should be noted that the results in Figure 2.15 correspond to a tire with structural properties defined in the work by Y. J. Kim et al. (2004).

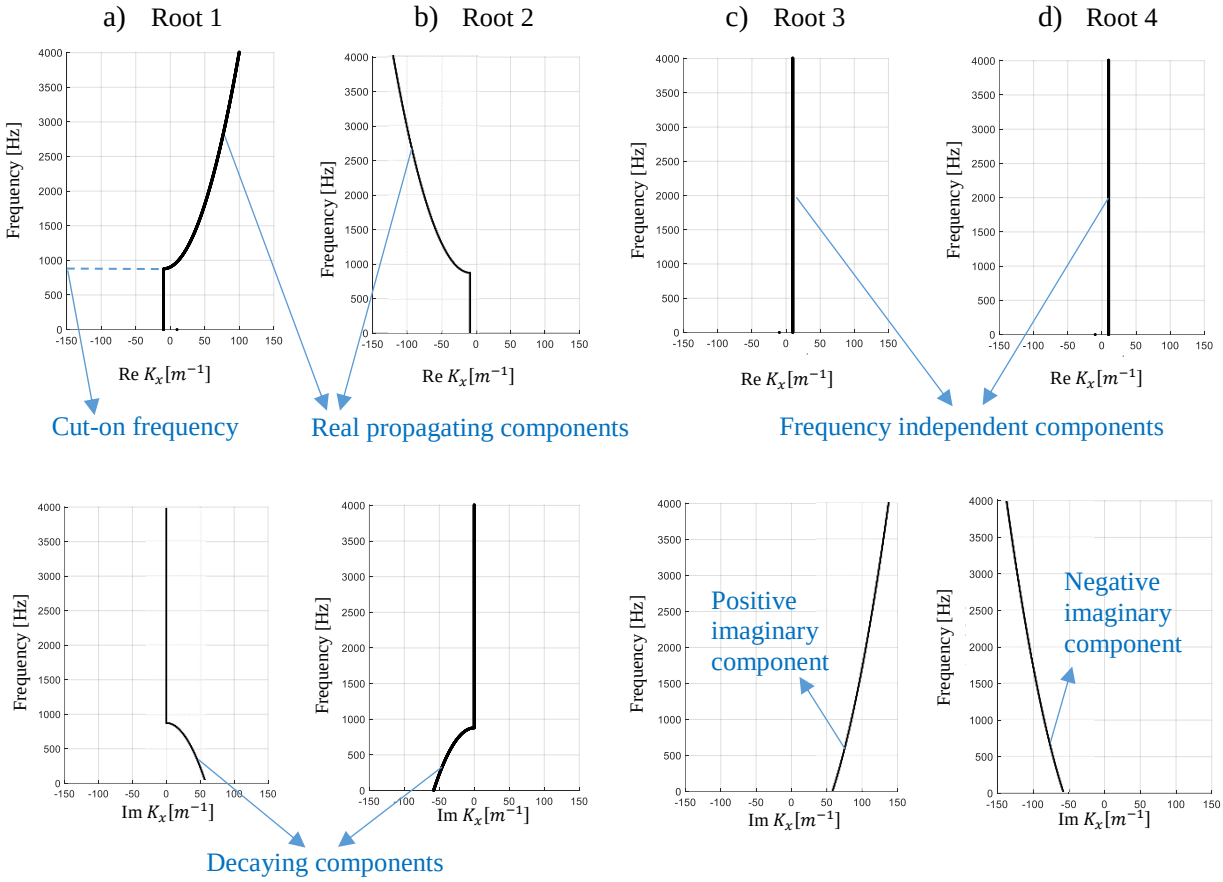

Figure 2.15. Real and imaginary dispersion curves for the 3rd transversal mode shape of a moving plate showing a) 1st root, b) 2nd root, c) 3rd root and d) 4th root.

Figure 2.16 shows the real component of all cut-on modes collected in a single plot. Figure 2.16a shows the curves for a plate traveling at 32 m/s. The purely real roots are shown in black, while the real components of the complex roots are shown in blue. On the other hand, Figure 2.16b shows

the curves for a stationary plate. In this case, the purely real roots are shown in black, while the line in red corresponds to the purely imaginary roots, thus equal to zero for all frequencies.

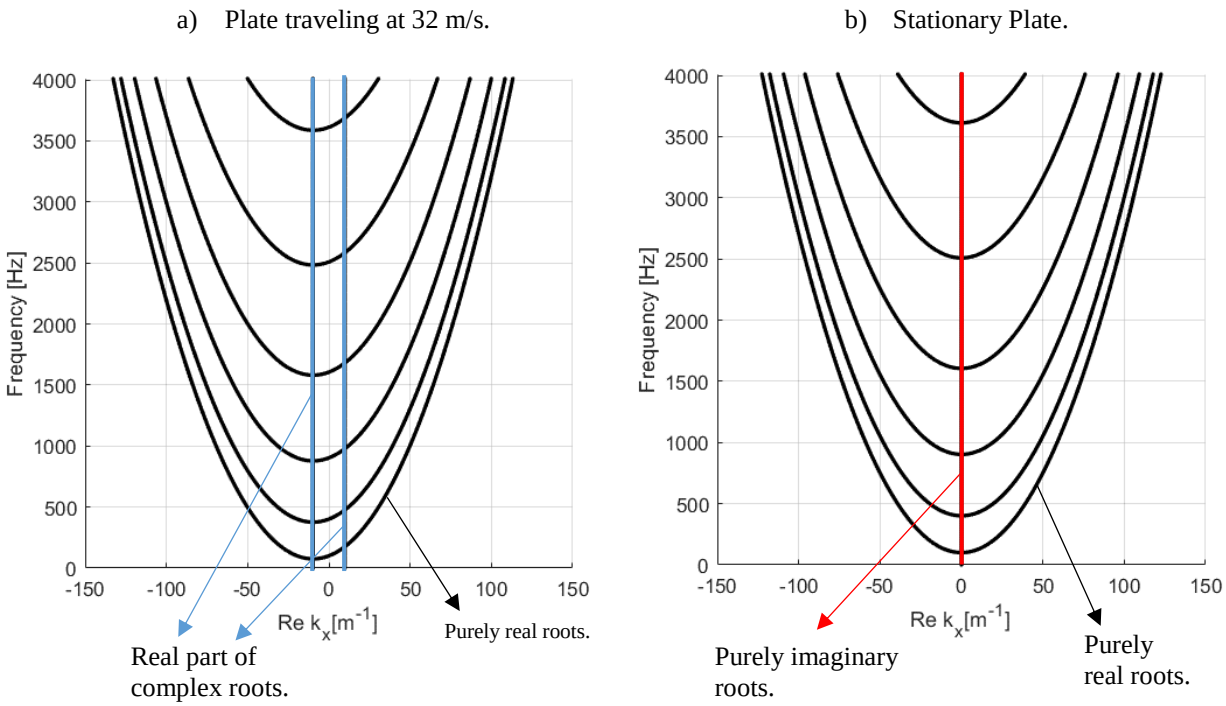

Figure 2.16. Dispersion plots for a tire modeled as a) a plate traveling at 32 m/s and b) a stationary plate.

A closer examination of only the positive purely real roots for both the moving and stationary plate models is presented in Figure 2.17. The slope of all these curves corresponds to the phase velocity of the propagating cut-on modes along the positive x-direction of the plate. In this case, it can be observed that the slopes of the moving plate curves are larger than those of the stationary plate, for all cut-on modes. Thus, the wavelength along the positive plate's x-direction is increased due to the plate's positive translational velocity of $V_p = 32$ m/s, e.g. plate motion stretches the waves in the x-direction. Finally, it can be observed that for the frequency range shown in Figure 2.17, only the first six transversal modes of the tire are excited. However, this depends on the structural properties of the tire.

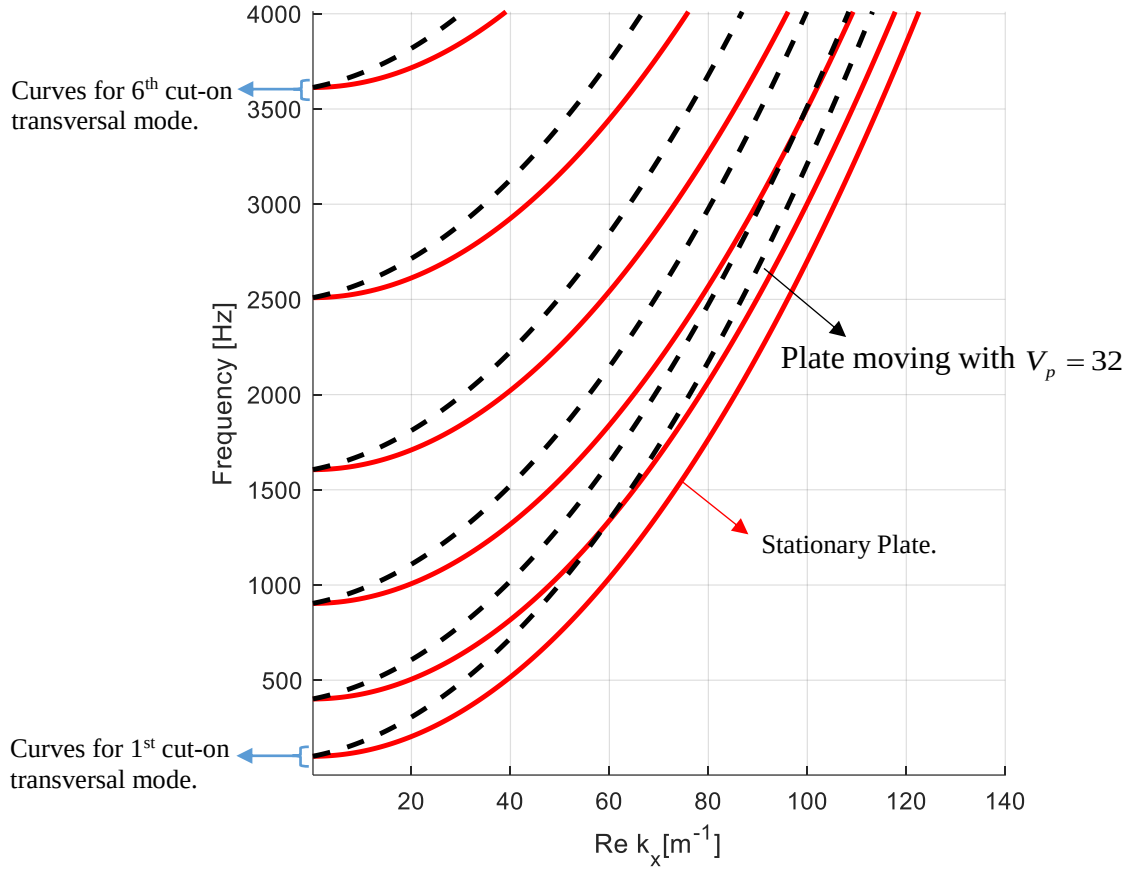

Figure 2.17. Propagating dispersion curves in the positive direction of a stationary and moving plate.

The imaginary dispersion curves for a plate moving with the plate velocity of 32 m/s are shown in Figure 2.18. Figure 2.18a shows two roots per transversal mode (one positive and one negative). It can be observed that the first 6 transversal modes become cut-on within frequencies of up to 4,000 Hz. An example of this behavior is shown for the 3rd transversal mode. This mode is cut-off up to a frequency of ~850 Hz, where the imaginary component of the wavenumber becomes zero. Figure 2.18b shows how the imaginary component of those roots that are complex. For these roots, the real component does not change with frequency, but the imaginary component does.

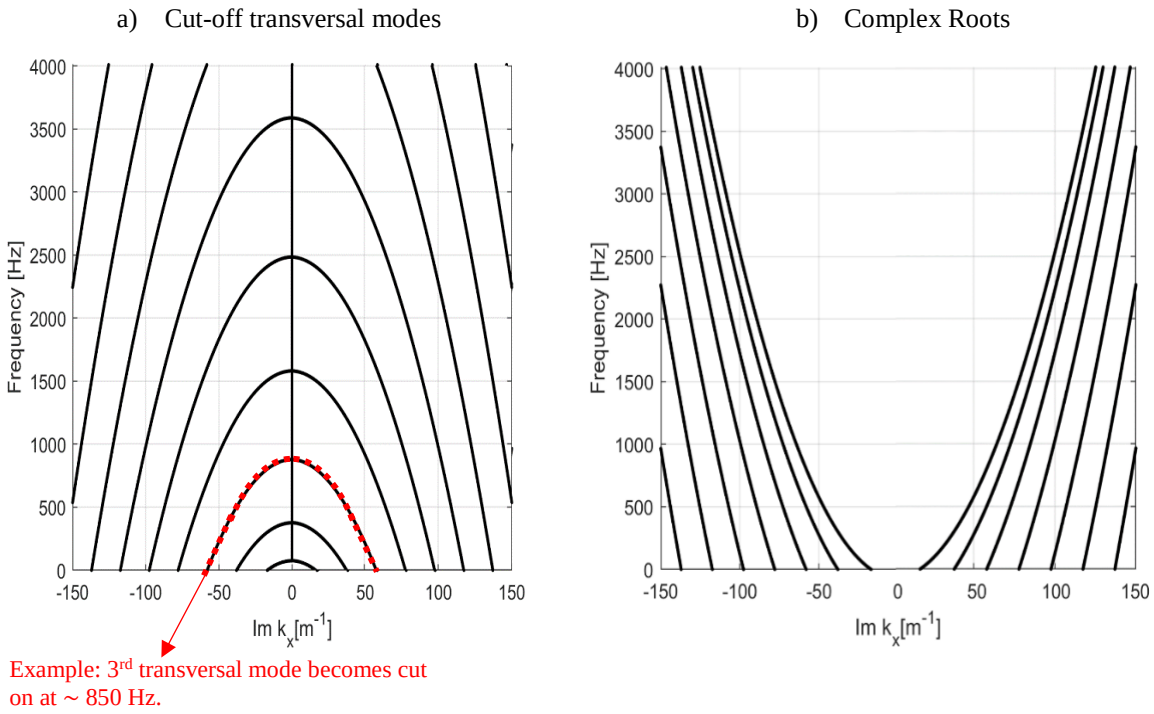

Figure 2.18. Imaginary components of dispersion curves for a plate moving with 32 m/s, where a) correspond to cut-off transversal modes and b) correspond to the complex roots of the system.

Finally, all results shown above can be compared to those reported by Y. J. Kim et al. (2004), since the same structural properties have been used. In their work, a tire was modeled by using a rotating cylindrical shell. The calculated dispersion curves for a tire rotating with an angular speed of 100 rad/s is shown in Figure 2.19. In this case, three types of waves are present in the response corresponding to bending waves denoted with $\bullet$, shear waves denoted with $\times$, and longitudinal waves denoted with $+$. Only the response corresponding to bending waves can be compared.

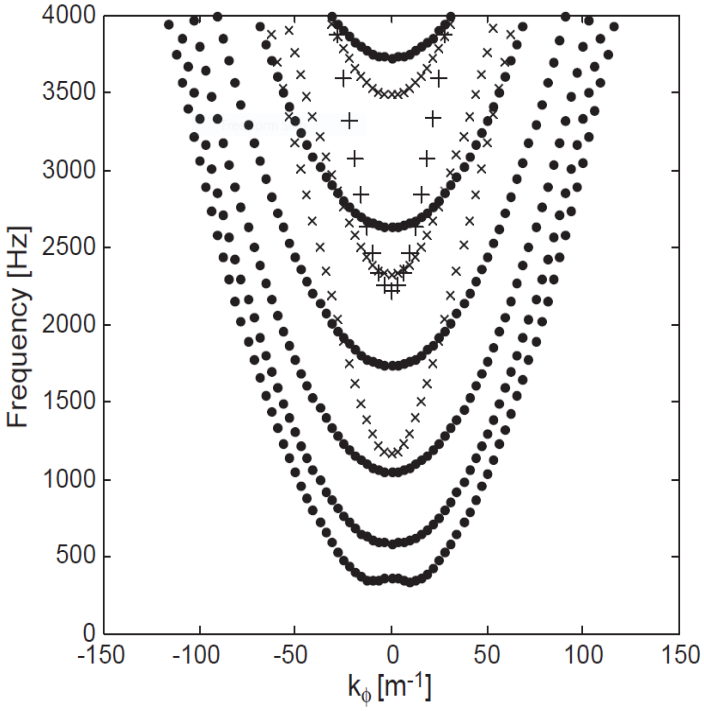

Figure 2.19. resulting dispersion curves obtained from the work by Kim et al. (2004).

First, the results in Figure 2.16a are compared to the bending waves in Figure 2.19. It can be observed that both wavenumber and frequency content are very similar. That is, wavenumbers are within ~ -120 to 120 m^{-1} for a frequency range from 0 to 4000 Hz. In addition, both results show that only the first six transversal modes are cut-on within this frequency range. In the work by Y. J. Kim et al. (2004), the authors mention that rotation cause the dispersion curves to be slightly asymmetrical with respect to the zero-wavenumber axis. This behavior is referred to as a "bifurcation" effect and is also observed in the moving plate (see Figure 2.16a). Finally, the main discrepancy between Figure 2.16a and Figure 2.19 is that cut-on frequencies of all modes differ by about 250 Hz. This could be because pressure effects have not yet been accounted in the plate model, while the work by Y. J. Kim et al. (2004) does. The coupling of the bending waves with the other types of waves in the cylindrical shell may also affect the response.

Therefore, the effects the inflation pressure in the structural response of the tire are also analyzed. Several approaches to do this are found in literature. For example, Y. J. Kim et al. (2004) included

membrane tensions in a cylindrical shell model. This approach was used for all the developed models in the sequential modeling approach and will also be used for this analysis. Other approaches found in the literature include the one proposed by Kung et al. (1986), where an elastic foundation in a ring model that accounts for stiffness changes due to inflation pressure and sidewall properties.

If the membrane tensions due to inflation pressure are accounted, then the equation (2.74) becomes the following

$$-T_{0x}\frac{\partial^2 w}{\partial x^2}-T_{0y}\frac{\partial^2 w}{\partial y^2}+D\left(\frac{\partial^4 w}{\partial y^4}+2\frac{\partial^4 w}{\partial y^2\partial x^2}+\frac{\partial^4 w}{\partial x^4}\right)+M_p\left(\ddot{w}+V_p^2\frac{\partial^2 w}{\partial x^2}+2V_p\frac{\partial^2 w}{\partial x\partial t}\right)=0 \tag{2.77}$$

The tensions can be calculated with equations (2.3) and (2.4). If the wave propagation assumed solution in equation (2.17) is replaced in the homogeneous equation of motion, then the following expression is obtained

$$T_{0x}k_x^2+T_{0y}a_n^2+D\left(a_n^4+2a_n^2k_x^2+k_x^4\right)+\rho h\left(-\omega^2-k_x^2V_p^2+2V_pk_x\omega\right)=0 \tag{2.78}$$

After re-arranging the terms in a fourth-order k_x polynomial form, equation (2.78) becomes

$$Dk_x^4+\left(2Da_n^2-\rho hV_p^2+T_{0x}\right)k_x^2+\left(2V_p\rho h\omega\right)k_x+\left(Da_n^4-\rho h\omega^2+T_{0y}a_n^2\right)=0 \tag{2.79}$$

Equation (2.79) is identical to equation (2.74), except for the pressure-induced membrane tension terms. Thus, four wavenumbers k_x can be obtained per frequency

Figure 2.20a shows the real component of the dispersion curves for a stationary plate inflated with 0 psi (shown in black) and 30 psi (shown in red). It can be observed that the effect of inflation

pressure corresponds to a shift of the cut-on frequencies for all transversal modes. If the plate model is assumed to be inflated and moving the dispersion curves change, as shown in Figure 2.20b. In this case, the curves show that all roots have a real component that is frequency-dependent, unlike the uninflated tire (if compared to the results in Figure 2.16a).

Figure 2.21 shows the imaginary roots for the case in Figure 2.20b. These have been divided into two. In Figure 2.21a, the dispersion curves corresponding to the cut-off transversal modes are shown. On the other hand, Figure 2.21 b shows the imaginary components of those curve that are complex along the whole spectrum.

a) Static simply supported plate model.

b) Plate model moving at 32 m/s and inflation pressure of 30 psi.

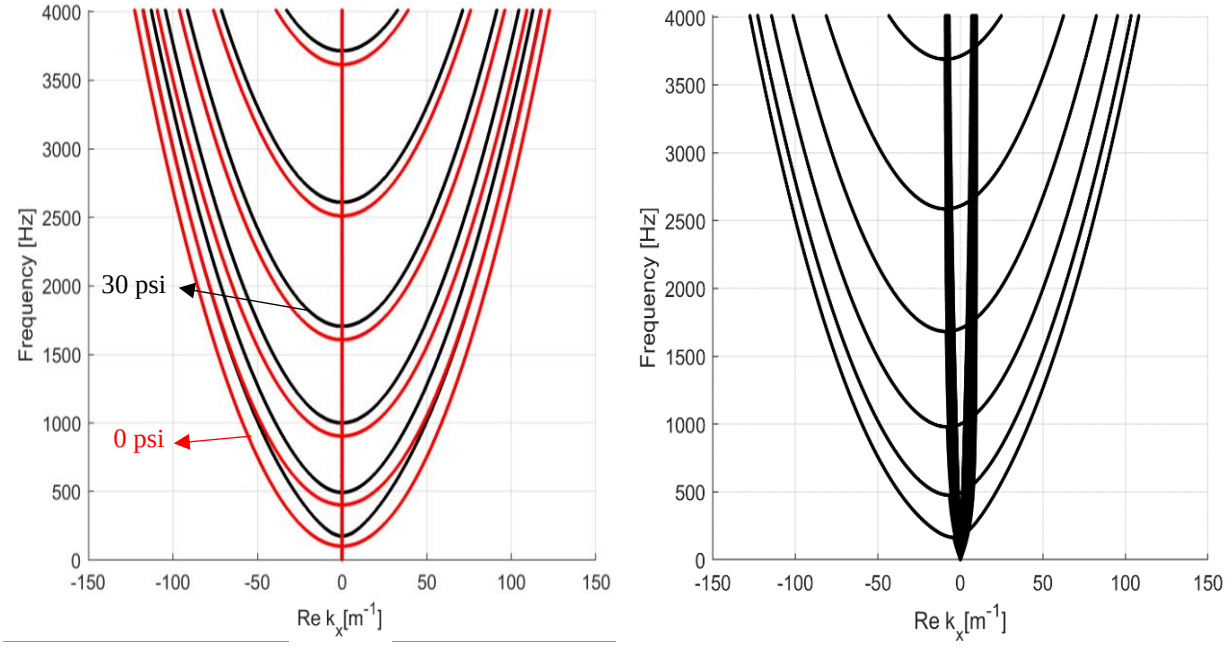

Figure 2.20. Real-component dispersion curves for a) static plate model with an inflation pressure of 0 psi and 30 psi and b) moving plate model inflated with 30 psi.

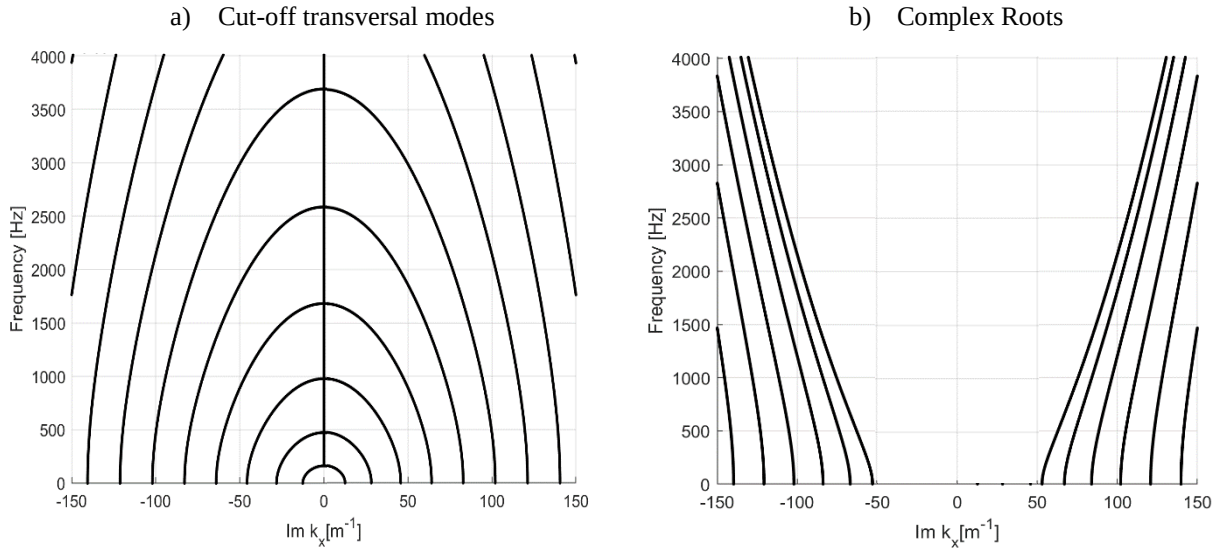

Figure 2.21. Imaginary-component dispersion curves for a moving plate model inflated with 30 psi, divided into a) cut-off transversal mode components and b) components from the complex roots.

In order to make the behavior of the dispersion curves, Figure 2.22 shows the four roots of the plate moving with 32 m/s and inflation pressure of 30 psi. These roots correspond exclusively to the 3rd transversal mode. The results are very similar to the case were the tire did not have any inflation pressure (compare to Figure 2.15). There are two main differences between them: i) the cut-on frequencies are higher; ii) the real part of the complex roots (root 3 and root 4) is no longer frequency-independent.

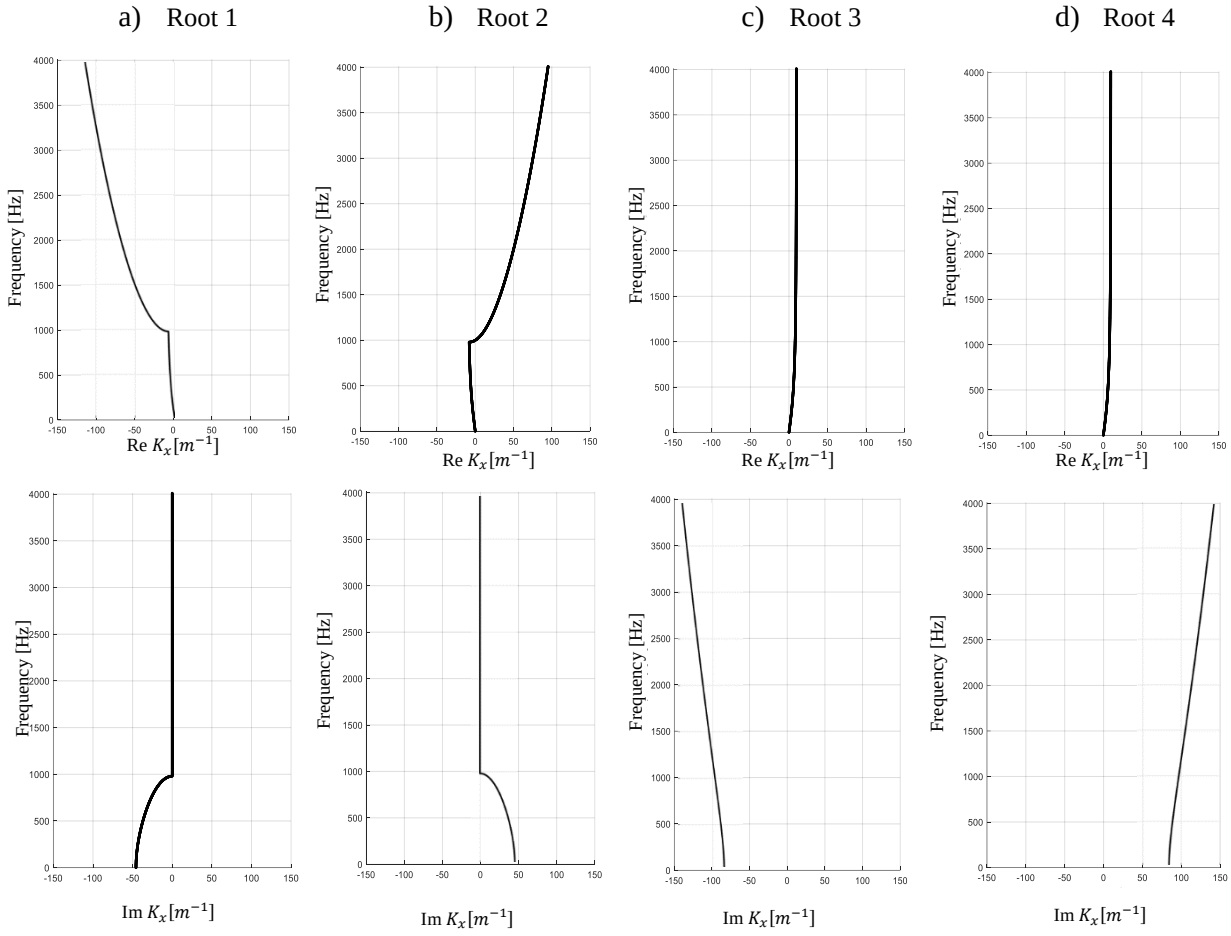

Figure 2.22. Real and imaginary dispersion curves for the 3rd transversal mode shape of a moving plate and inflation pressure of 30 psi, showing a) 1st root, b) 2nd root, c) 3rd root and d) 4th root.

2.3. Summary of Sequential Structural Models

In this section, a summary of the newly developed models for mid-frequency tire vibrations is summarized. The equations of motion solved for each of them are presented. In addition, a summary of the full wave-propagation solution method implemented in this study is also discussed.

The equations of motion (EOM) that must be solved for each of the new models presented in this chapter is summarized here. In addition, their corresponding homogeneous equation used to compute the transversal modes are also presented. These are defined as follows:

Stationary Infinite Plate Model

EOM:

$$-T_{0x}\frac{\partial^2 w}{\partial x^2}-T_{0y}\frac{\partial^2 w}{\partial y^2}+B_x\frac{\partial^4 w}{\partial x^4}+2B_{xy}\frac{\partial^4 w}{\partial x^2\partial y^2}+\frac{\partial^2}{\partial y^2}\left(B_y(y)\frac{\partial^2 w}{\partial y^2}\right)-m(y)\frac{\partial^2 w}{\partial t^2}=f(t)\delta\left(x-x_f\right)\delta\left(y-y_f\right) \tag{2.80}$$

Homogeneous Equation:

$$\frac{\partial^2}{\partial y^2}\left(B_y(y)\frac{\partial^2 w}{\partial y^2}\right)-m(y)\frac{\partial^2 w}{\partial t^2}=0 \tag{2.81}$$

Moving Infinite Plate Model

EOM:

$$\begin{aligned}&-T_{0x}\frac{\partial^2 w}{\partial x^2}-T_{0y}\frac{\partial^2 w}{\partial y^2}+\left(\frac{\partial^2}{\partial y^2}\left(B_y(y)\frac{\partial^2 w}{\partial y^2}\right)+2B_{xy}\frac{\partial^4 w}{\partial y^2\partial x^2}+B_x\frac{\partial^4 w}{\partial x^4}\right)-\\&m(y)\frac{\partial^2 w}{\partial t^2}+m(y)\left(V_p^2\frac{\partial^2 w}{\partial x^2}+2V_p\frac{\partial^2 w}{\partial x\partial t}\right)=f(t)\delta\left(x-x_f\right)\delta\left(y-y_f\right)\end{aligned} \tag{2.82}$$

Homogeneous Equation:

$$\frac{\partial^2}{\partial y^2}\left(B_y(y)\frac{\partial^2 w}{\partial y^2}\right)-m(y)\frac{\partial^2 w}{\partial t^2}=0 \tag{2.83}$$

Moving Cylindrical Shell Model

EOM:

$$\alpha_1 \frac{\partial^6}{\partial y^2 \partial \theta^4}\left(D_{11}(y)\frac{\partial^2 w}{\partial y^2}\right)+\alpha_2 \frac{\partial^6}{\partial y^6}\left(D_{11}(y)\frac{\partial^2 w}{\partial y^2}\right)+\alpha_3 \frac{\partial^6}{\partial y^4 \partial \theta^2}\left(D_{11}(y)\frac{\partial^2 w}{\partial y^2}\right)+ \tag{2.84}$$

$$\left(\chi_2 - D_{11}(y)\alpha_3\right)\frac{\partial^8 w}{\partial y^6 \partial \theta^2}+\left(\chi_3 - D_{11}(y)\alpha_1\right)\frac{\partial^8 w}{\partial y^4 \partial \theta^4}+\chi_4 \frac{\partial^8 w}{\partial y^2 \partial \theta^6}+\chi_5 \frac{\partial^8 w}{\partial \theta^8}+\chi_6 \frac{\partial^4 w}{\partial y^4}-$$

$$\omega^2\left(\alpha_1 m(y)\frac{\partial^4 w}{\partial \theta^4}+\alpha_2 \frac{\partial^4 m(y) w}{\partial y^4}+\alpha_3 \frac{\partial^4 m(y) w}{\partial y^2 \partial \theta^2}\right)-\frac{1}{a^2}\left(\alpha_1 N_\theta^r(y)\frac{\partial^6 w}{\partial \theta^6}+\alpha_2 \frac{\partial^6 N_\theta^r(y) w}{\partial y^4 \partial \theta^2}+\alpha_3 \frac{\partial^6 N_\theta^r(y) w}{\partial y^2 \partial \theta^4}\right)-$$

$$N_y^r\left(\alpha_1 \frac{\partial^6 w}{\partial y^2 \partial \theta^4}+\alpha_2 \frac{\partial^6 w}{\partial y^6}+\alpha_3 \frac{\partial^6 w}{\partial y^4 \partial \theta^2}\right)+2i\omega\Omega\left(\alpha_1 m(y)\frac{\partial^3 w}{\partial \theta^3}+\alpha_3 \frac{\partial^3 m(y) w}{\partial y^2 \partial \theta}+\alpha_4 \frac{\partial^3 m(y) w}{\partial y^2 \partial \theta}\right)-$$

$$\Omega^2\left(\alpha_1 m(y)\frac{\partial^4 w}{\partial \theta^4}+\alpha_2 \frac{\partial^4 m(y) w}{\partial y^4}+\alpha_3 \frac{\partial^4 m(y) w}{\partial y^2 \partial \theta^2}\right)=\left(\alpha_1 \frac{\partial^4 F_r}{\partial \theta^4}+\alpha_2 \frac{\partial^4 F_r}{\partial y^4}+\alpha_3 \frac{\partial^4 F_r}{\partial y^2 \partial \theta^2}\right)$$

where, $F_r = f(t)\delta(\theta-\theta_f)\delta(y-y_f)$

Homogeneous Equation:

$$\alpha_2 \frac{\partial^6}{\partial y^6}\left(D_{11}(y)\frac{\partial^2 w}{\partial y^2}\right)+\chi_6 \frac{\partial^4 w}{\partial y^4}-N_y^r \alpha_2 \frac{\partial^6 w}{\partial y^6}-\Omega^2 \alpha_2 \frac{\partial^4 m(y) w}{\partial y^4}-\omega^2 \alpha_2 \frac{\partial^4 m(y) w}{\partial y^4}=0 \tag{2.85}$$

The solution to the equations of motion (2.80), (2.82), and (2.84) can be defined in a generic form as follows:

The response consists of modes in the transverse direction and waves in the circumferential direction as

$$w(\xi,y,t)=\sum_n^N q_n \phi_n(y) X_n(\xi) e^{i\omega t} \tag{2.86}$$

.... ξ corresponds to x for plate models

ξ corresponds to θ for shell model

where the generic coordinate ξ corresponds to x for the plate models and θ for the cylindrical shell model. Along this direction, a full wave-propagation is assumed with $X_n(\xi) = e^{-ik_\xi \xi}$. On the other hand, y is the coordinate along the transversal direction. Along this direction, a total of N transversal modes are defined with modal amplitude q_n and a function $\phi_n(y)$. It should be noted that in the formulation presented above, the modal function $\phi_n(y)$ was found by solving an eigenvalue problem using the homogeneous equations defined in (2.81), (2.83) and (2.85), for each of the developed models. This is an approximation; however, an exact solution is possible if all the terms on the equations of motion are used to construct the homogeneous equations, and the eigenvalues solved for all wavenumbers k_ξ. This would be a computationally intensive approach.

The developed method to find the full wave-propagation solution to equations (2.80) through (2.84) is the following:

1. Substitute the assumed solution (2.86) into the desired structural equation of motion, i.e., equation (2.80), (2.82), or (2.84).

2. Pre-multiply by $\phi_n(y)$, integrate over y, and perform wavenumber transform. After this process, the following generic system is obtained

$$\left[\sum [C_m] k_\xi^m + [\lambda_n] - \omega^2 [I]\right]\left\{q_n X_n\left(k_\xi\right)\right\} = \left\{F_n\left(k_\xi\right)\right\} \tag{2.87}$$

where, k_ξ^m corresponds to the wavenumber along the circumferential direction elevated to the mth power. In this case, m is associated with the mth derivative with respect to ξ in the equation of motion. Each of the mth expression is associated with a stiffness matrix defined as $[C_m]$ and added to each other. On the other hand, $[\lambda_n]$ is a diagonal matrix containing the transversal natural frequencies of the tire, $[I]$ is the identity, and finally $\left\{F_n\left(k_\xi\right)\right\}$ is a vector containing

all modal forces. This equation corresponds to equation (2.21) for the infinite plate, equation (2.28) for the moving infinite plate, and equation (2.67) for the cylindrical shell.

3. Decouple the system in equation (2.87) by only accounting the diagonal terms of matrices $[C_m]$ and perform an inverse wavenumber transform as follows

$$q_n X_n(\xi) = \frac{1}{2\pi} \int_{-\infty}^{\infty} \frac{F_n(k_\xi) e^{-ik_\xi \xi}}{\sum C_{m,n} k_\xi^m + \lambda_n - \omega^2} dk_\xi \tag{2.88}$$

where, $C_{m,n}$ correspond to the nth diagonal value of the matrix $[C_m]$ associated with the nth transversal mode. This equation corresponds to equation (2.23) for the infinite plate, equation (2.30) for the moving infinite plate, and equation (2.69) for the cylindrical shell. Finally, now that $q_n X_n(\xi)$ is known, it can be substituted into the assumed solution (2.86) to find the full wave-propagation response of tire.

3. Contact Model

3.1. Introduction to Excitation Mechanisms

The contact model is used to define the excitation process of a tire during rotation. The input forces excite the tire, which in turn generate noise. Two excitation mechanisms drive the structural model. Both mechanisms of excitation are illustrated in Figure 3.1. The first one accounts for structural excitation induced by the impact of the tire tread-blocks against the pavement. This is referred to as *tread-block excitation*. The second one corresponds to excitation by input forces induced by the indentation of pavement profile into the tire tread. This is referred to as *pavement profile excitation*.

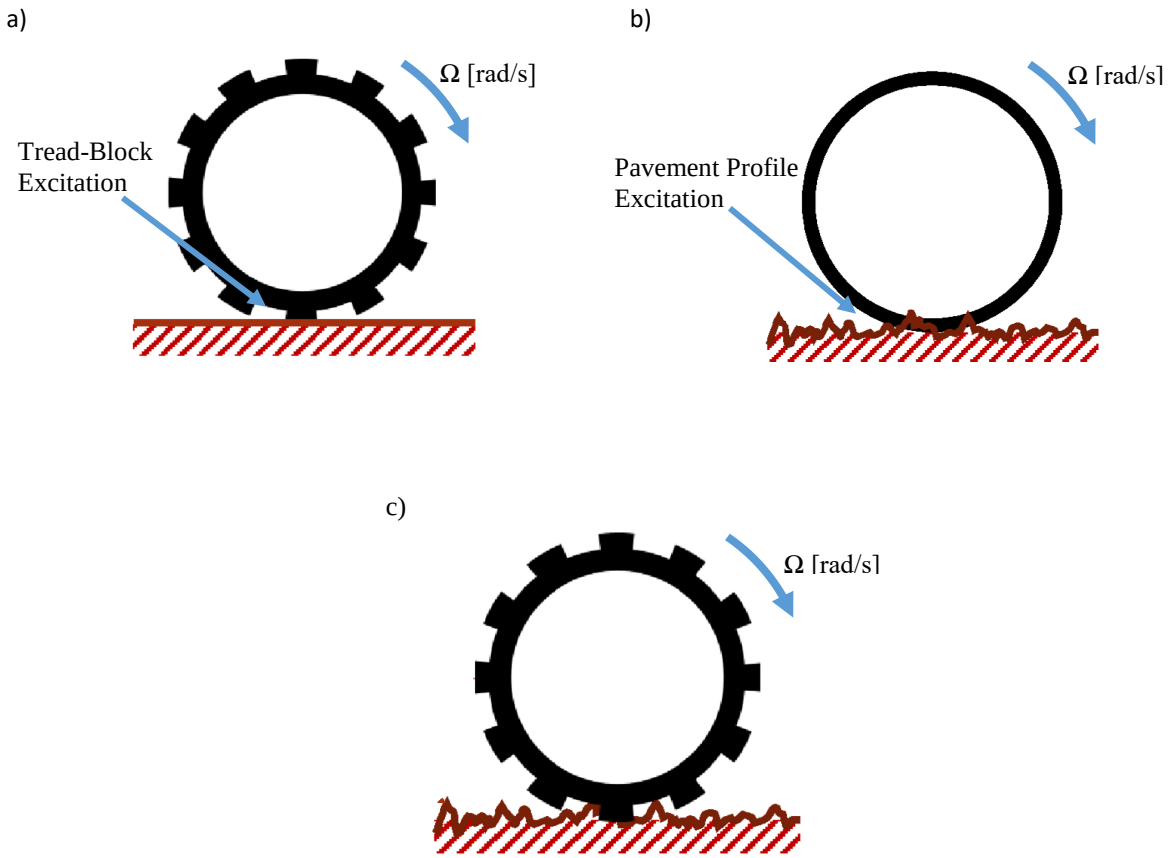

Figure 3.1. a) Tread-block excitation b) pavement excitation of the tire structure, and c) real rolling conditions where tread-block and pavement excitations are accounted.

In order to properly model real rolling conditions, both excitation mechanisms need to be accounted and combined as shown in Figure 3.1c. These two mechanisms are independent of each other, i.e. tread-block excitation does not affect the pavement excitation. This assumption is made based on the experimental data presented by Spies (2019), where tire noise was measured using an On-Board Sound Intensity System (OBSI). In this work, the total noise was successfully separated into Tread-Pattern Noise (TPN) and Non-Tread Pattern Noise (NTPN) components. Figure 3.2 shows the TPN spectrum produced by a winter tire of size 215/60R16 measured for 28 different types of pavements, including asphalt and concrete. No significant noise level changes were observed between different types of pavements. In addition, their spectral shape was very similar to all of them.

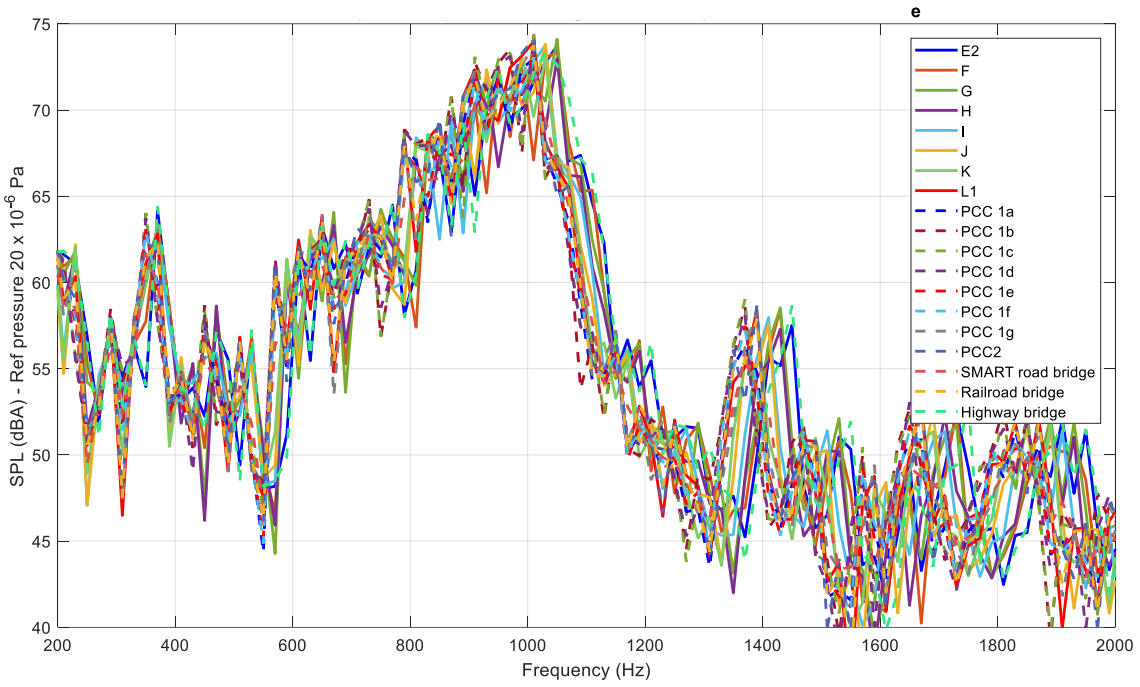

Figure 3.2. Measured TPN spectrum for 28 different pavements at Virginia Tech Transportation Institute Smart Road (winter tire of size 215/60R16 inflated at 32 psi, for a vehicle speed of 60 mph) (Spies, 2019).

On the other hand, Figure 3.3 shows that the measured NTPN component is different for each type of pavement. Different noise levels and spectral shapes are observed depending on the pavement type. Therefore, it can be concluded that the excitation mechanisms related to the tread-pattern i.e. the tread-block excitation is independent of the pavement-excitation and can be treated separately.

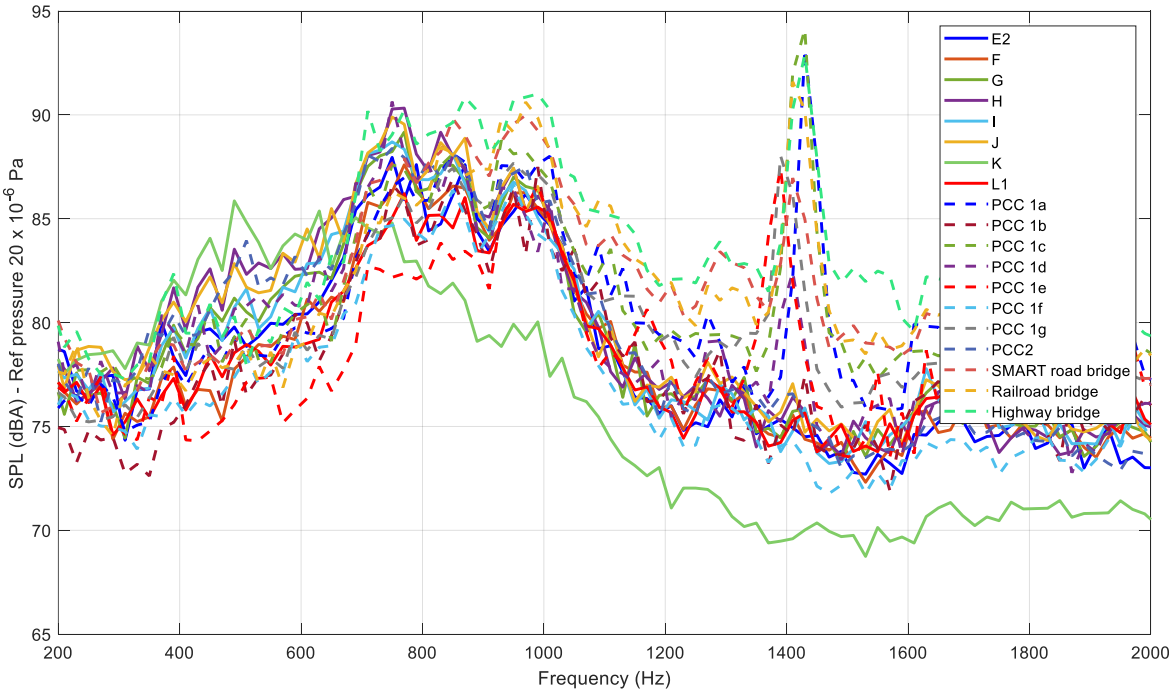

Figure 3.3. Measured NTPN spectrum for 28 different pavements at Virginia Tech Transportation Institute Smart Road (winter tire of size 215/60R16 inflated at 32 psi, for a vehicle speed of 60 mph) (Spies, 2019).

In this thesis, only the block excitation will be modeled. The pavement profile excitation will not be addressed. The proposed formulation for the block excitation is unique for two reasons. First, it is defined in the frequency domain. In contrast, current approaches are defined in the time domain. In such case, the approach is to convolve the impulse response of the tire with a set of discretely approximated input forces at different locations in the contact patch. This method was first proposed by Kropp (1999) and then adapted it by many authors including O'Boy et al. (2009b) and Hoever (2014). However, it is an inefficient approach for a periodic input such as a tire's tread pattern. The response would need to be solved for multiple revolutions in order to reach a steady-state condition.

The second contribution of the proposed formulation is that for the first time a detailed characterization of individual moving block forces in the contact patch is included in the contact formulation. In addition, a unique analysis of the input power provided by different tread pattern designs is performed. The block forces are modeled with a thorough model initially developed by

Liu et al. (2010), where coupled normal and tangential forces are modeled using static and dynamic friction effects between the pavement surface and the tire's tread blocks. In contrast, approaches proposed by other researchers are less sophisticated. For example, O'Boy et al. (2009b) simply assigning a spring to each block. In this case, only a uniform tread pattern with equal size blocks is used as an approximation. On the other hand, Hoever (2014) defined a non-uniform distribution of springs along the tire tread band in an effort to capture the forces induced by a specific tread pattern as the springs enter and leave the contact area. Still, these authors do not explain in depth how these contact models are implemented.

In the following sections of this chapter, the proposed contact model theory in this study is addressed. This includes its formulation, calculation of individual block forces, and verification of the total loads applied to the tire. Finally, a section for the analysis of tread-pattern excitation characteristics has been included.

3.2. Contact Model Theory

Formulation

The first step to model the tread-pattern excitation is to define the geometry of the tire's tread and its properties. For example, Figure 3.5a shows the tread geometry of a typical all-season tire. This corresponds to an unwrapped view both circumferentially and transversally, showing the belt with the tread pattern and the sidewalls. As shown in Figure 3.5a, tread pattern design can be complicated. The tire's blocks can be positioned using multiple configurations of voids, ribs, slots, and grooves. This results in a set of blocks arranged with variable or regular spacing and intricate changing or repeating shapes. The objective of these complex designs is to comply with traction characteristics, optimized contact area, and reduce noise (Erman et al., 2013).

In this work, the tread design will be simplified with a geometric approximation. This is carried out because the most advanced block contact-force model found in the literature developed by Liu et al. (2010) is limited to rectangular non-skewed blocks. This model will be implemented in this thesis. The details of this model are discussed in the next section. Thus, the tread-pattern blocks

are approximated with a rectangular shape, as shown in Figure 3.4b. This results in the equivalent block distribution shown in Figure 3.4c. It is not believed that this simplification is a significant limitation, however, future work should address this in further details i.e. predicting forces for arbitrarily shaped blocks. In addition, more advanced contact models could include additional improvements, such as accounting for thermal or wear effects when computing the block-impact forces.

a) Rectangular block assumption.

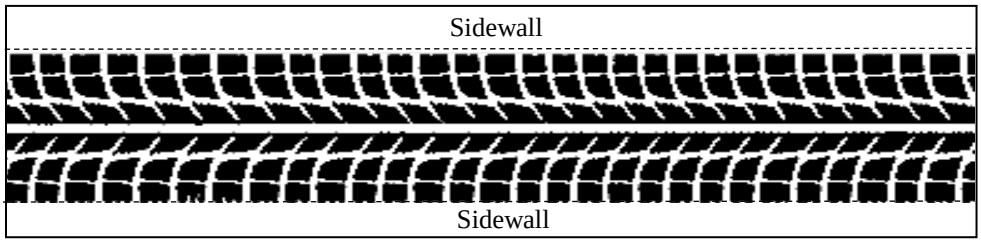

b) Rectangular block assumption.

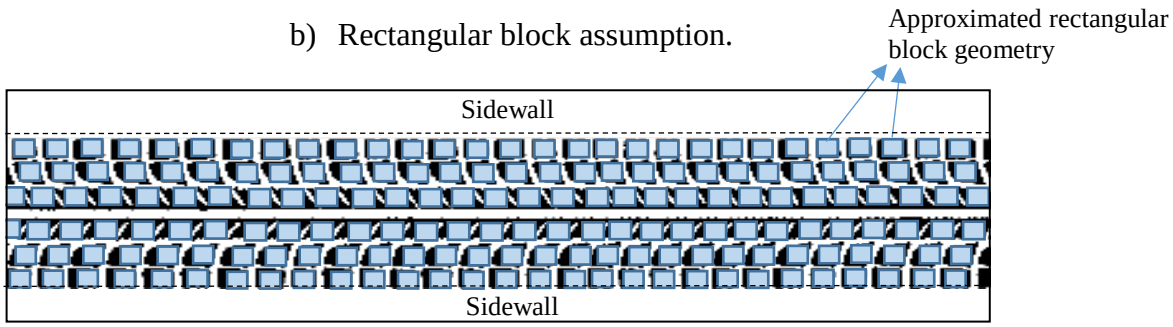

c) Approximated block distribution used for contact model.

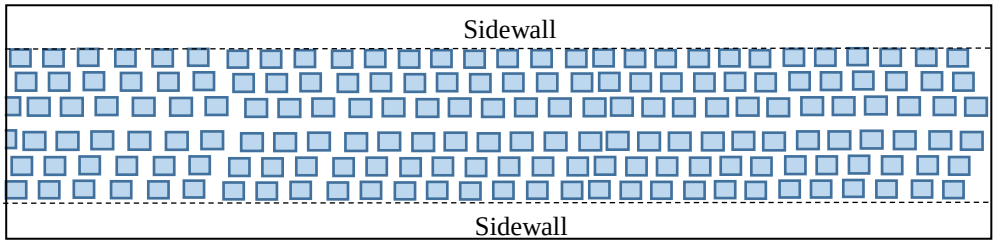

Figure 3.4. Unwrapped view of a typical all-season tire: a) real tread geometry, b) rectangular block assumption and c) resulting block distribution used for the contact model.

As shown in Figure 3.5, a simple rectangular contact patch with dimensions $\left(d_{px}, d_{py}\right)$ is located at the center of the belt. The contact patch dimensions are dictated by the structural properties of the tire, the load, and tire pressure. Simple approaches to estimate the contact patch include using an ellipse that depends on the tire size and load, as defined by Taghavifar et al. (2017). In this thesis, the contact patch is assumed to be rectangular. The distance between leading and trailing edge is defined by the formulation proposed by Holtschulze et al. (2005). In this case, the tire radius and the total load applied to the tire is used for this calculation. The width of the contact patch is assumed to be the same as the tire belt's width. The structural model coordinate system on the tread belt is also defined at its center, i.e. center of the contact patch. It is important to note that the structural coordinate system is fixed, i.e. not moving with the tire rotation. Since the tire is rolling, the belt is moving with a velocity V_T.

The block enters at the contact patch leading edge (LE) and exits later at the trailing edge (TE). It will develop a force normal to the tire surface that will be equal to zero as it enters the LE, then increases and stabilizes for a brief period of time. Finally, it decreases to zero when leaving the contact patch at the TE. During the block-pavement contact, other forces will also be present, i.e. tangential forces due to friction. These are not accounted for in this model. The reason is that during steady-state rolling conditions, tangential forces will produce small out of plane motion. Thus, the tangential forces are small if compared to the normal ones, as shown in the work by Liu et al. (2010). Furthermore, it is thought that since the structural vibrations of the tire are dominated by its bending components, the effects of tangential input forces may be neglected.

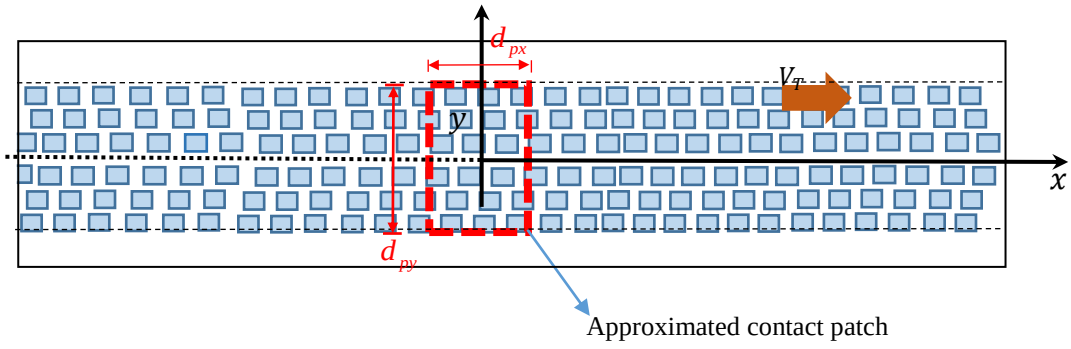

Figure 3.5. Contact patch approximation for a moving tire belt.

The analysis of the tread excitation will be performed by first modeling a single arbitrary block and then use superposition to coherently add the contributions of all the other blocks. As shown in Figure 3.5, the center of a block is located at (x_b, y_b), at an arbitrary time (it could be zero). The block is assumed to have dimensions (d_{bx}, d_{by}). As shown in Figure 3.6a, as the tire rotates the center of the block reaches and leaves the contact patch leading and trailing edges at a time t_i and t_e, respectively. It is important to track these times to properly add the contributions of all the blocks later. They are given by

$$t_i = -\frac{(x_b - x_{LE})}{V_T} \quad \text{and} \quad t_e = -\frac{(x_b + x_{TE})}{V_T} \tag{3.1}$$

where $x_{LE} = -d_{px}/2$ and $x_{LE} = d_{px}/2$ are the x-coordinates of the LE and TE of the contact patch. This process repeats with each tire revolution with a period of $T_T = \ell_T / V_T$, where ℓ_T is the circumference of the tire (see Figure 3.6b).

For the sake of clarity, Figure 3.6c shows the side-view representation of the single block moving on top of the pavement. When the block enters the contact patch region, an excitation force begins acting on the tire. Figure 3.6d shows the force will increase and decrease back to zero when the block exits the contact patch region. The force is moving relative to the structural coordinate system and changing its amplitude as it travels through the contact patch. An observer moving with the block will see a time-dependent moving force. The force is also a function of space because the block's displacement is related to time through the tire's velocity as $x = V_T t$. This time-dependent moving force is referred to as $f_b(x_b(t), y_b, t)$ and requires careful consideration during its modeling.

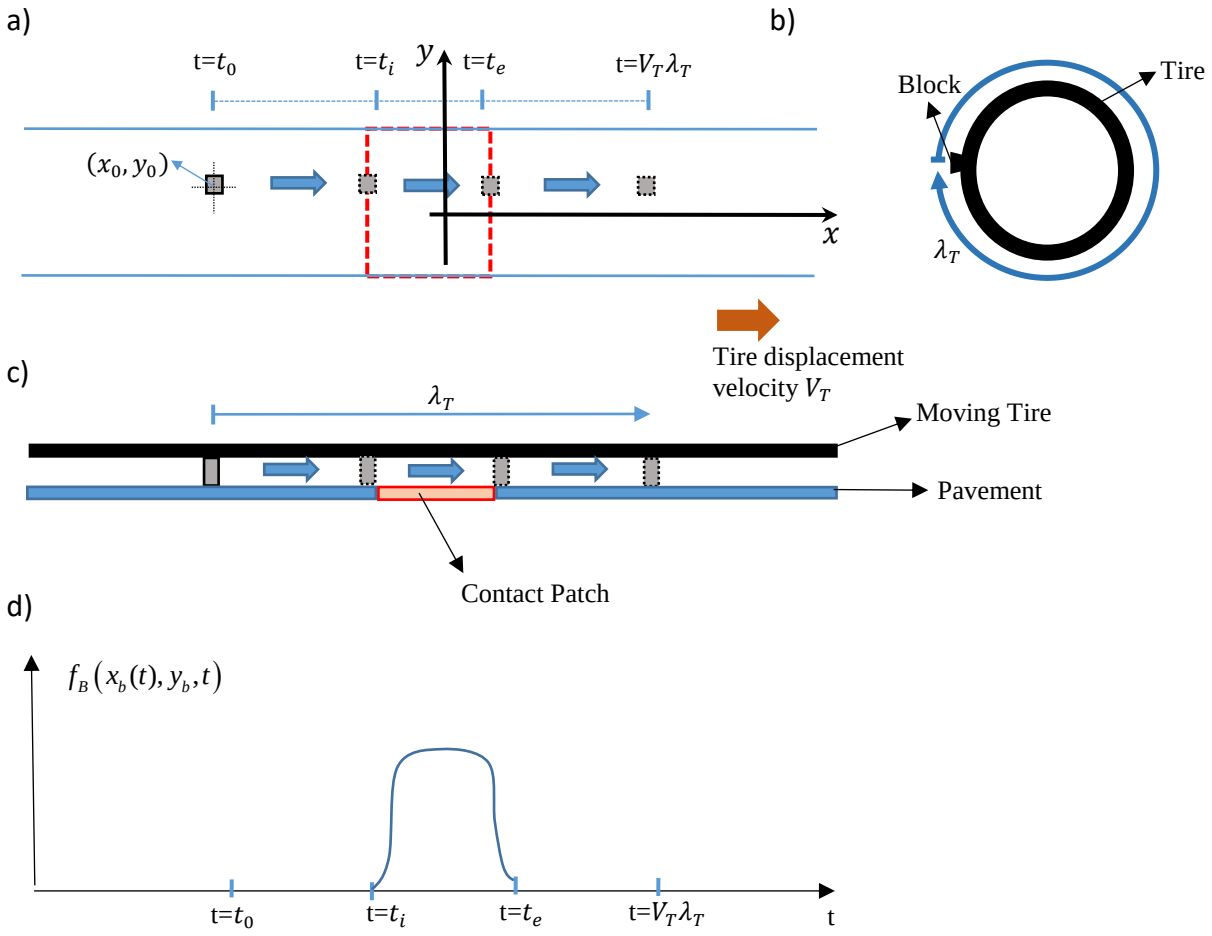

Figure 3.6. a) Single block on tire belt moving through contact patch region. b) Block displacement through one revolution of the tire. c) Side view of the unwrapped tire moving on the pavement. d) The Behavior of moving force as block passes through the contact area.

The moving time-varying force $f_b(x_b(t), y_b, t)$ is then approximated as a series of pulses at fixed locations within the contact patch. To this end, the time it takes the block to travel through the contact patch length d_{px} is divided into evenly spaced N_k time intervals $\Delta t = (t_e - t_i)/N_k = d_{px}/(V_T N_k)$. The time at the center of the intervals is computed as

$$t_k = t_i + (k - 1/2)\Delta t \quad k = 1, 2, \cdots, N_k \tag{3.2}$$

Considering equation (3.1)

$$t_k = \frac{\left(x_{LE} - x_b\right)}{V_T} + \left(k - 1/2\right)\Delta t \qquad k = 1, 2, \cdots, N_k \tag{3.3}$$

The corresponding axial position of the force at these times is computed as

$$x_k = x_{LE} + V_T\left(t_k - t_i\right) = x_{LE} + V_T\left(k - 1/2\right)\Delta t \qquad k = 1, 2, \cdots, N_k \tag{3.4}$$

As shown in Figure 3.7b, the force $f_b\left(x_b(t), y_b, t\right)$ is then approximated as an impulse-train with time-changing amplitudes. That is

$$f_b\left(x_b(t), y_b, t\right) \approx \sum_{k=1}^{N_k} f_B\left(x_k, y_b, t_k\right)\Delta t\,\delta\left(t - t_k\right)\delta\left(x - x_k\right)\delta\left(y - y_b\right) \tag{3.5}$$

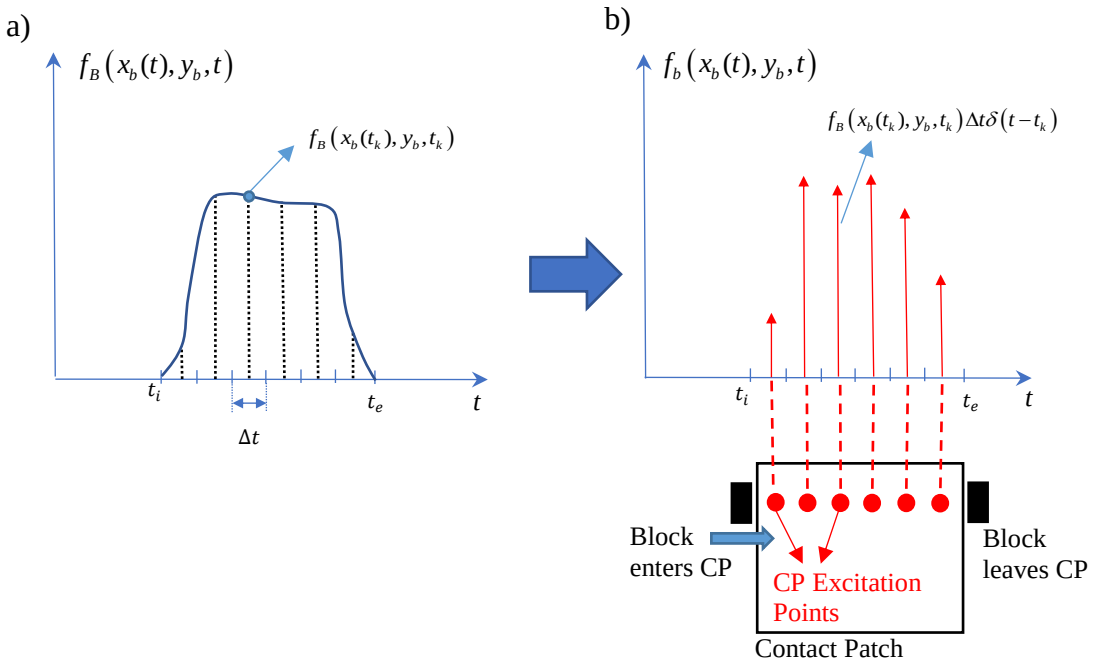

Figure 3.7. a) The Behavior of time moving force applied to a single block, b) approximation of force behavior using an impulse train and associated contact patch excitation points.

The impulses $f_B(x_k, y_b, t_k)\Delta t\delta(t-t_k)$ are now at fixed forces located at (x_k, y_b) within the contact patch. These locations are referred to as the contact patch excitation points, defined as the block enters, passes through, and finally leaves the contact patch.

Since the normal force for the block will be periodic with period T_T, the force can be expressed in the frequency domain by applying the Discrete Fourier Transform (DFT) to equation (3.5). The frequency of this periodic behavior is defined as $\omega_T = \frac{2\pi V_T}{\ell_T} = \frac{2\pi}{T_T}$.

Using the DFT pair for the special case of an impulsive time function leads to

$$\begin{cases} f(t) \approx \sum_{n=-N}^{n=N} F_n(n\omega_T) e^{in\omega_T t} \\ F_n(n\omega_T) = \frac{\omega_T}{2\pi} \int_0^{\frac{2\pi}{\omega_T}} \delta(t-t_o) e^{-in\omega_T t} dt = \frac{\omega_T}{2\pi} e^{-in\omega_T t_o} \end{cases} \tag{3.6}$$

The block force in the time domain given by equation (3.5) then becomes

$$f_b(x_b(t), y_b, t) \approx \sum_{k=1}^{N_k} \left\{ \sum_{n=-N}^{n=N} \frac{\omega_T}{2\pi} f_B(x_k, y_b, t_k) \Delta t e^{-in\omega_T t_k} e^{in\omega_T t} \right\} \delta(x-x_k)\delta(y-y_b) \tag{3.7}$$

where the complex amplitudes (DFT coefficient) for each impulse in the block force approximation is

$$F_b^{kn}(x_b(t), y_b, n\omega_T) = \frac{\omega_T}{2\pi} f_B(x_k, y_b, t_k) \Delta t e^{-in\omega_T t_k} \qquad n = \pm 1, \pm 2, , \cdots, \pm N \tag{3.8}$$

The complex amplitude response at an arbitrary location (x_r, y_r) on the tire is computed using the mobility function computed in the structural model developed in Chapter 2. That is

$$v(x_r, y_r, n\omega_T) \approx \sum_{k=1}^{N_k} f_B(x_k, y_b, t_k)\Delta t e^{-in\omega_T t_k} M_s\left((x_r, y_r)\middle|((x_k, y_b)), n\omega_T\right) \qquad n = \pm 1, \pm 2, , \cdots, \pm N \tag{3.9}$$

where $M_s\left((x_r, y_r)\middle|((x_k, y_b)), n\omega_T\right)$ is the mobility function between a harmonic force at (x_k, y_b) and the response at (x_r, y_r).

The next step is to extend the formulation shown above from a single block to the full tread pattern, i.e. multiple blocks. The most important consideration in modeling a tread pattern is to properly account for the relative time delay of the block forces. Using Figure 3.8, in this model the tread pattern will be defined as:

- It will consist of N_r circumferential arrays of blocks (ribs) at different y transversal positions, e.g. y_r for $r = 1, 2, \cdots, N_r$.
- The block dimensions in each array will be the same, e.g. d_{rx} and d_{ry} for $r = 1, 2, \cdots, N_r$.
- Each array has N_{br} number of blocks which can be evenly or irregularly distributed. The x-position of the blocks in the array will be defined by setting the coordinate of one block x_1^r and then defining the position of the other blocks relative to x_1^r, i.e. Δx_m^r for $m = 1, 2, \cdots, N_{br}$ and $r = 1, 2, \cdots, N_r$. Thus, the coordinate of the m^{th} block in the r^{th} array will be

$$x_m^r = x_1^r + \Delta x_m^r \tag{3.10}$$

  where obviously $\Delta x_1^r = 0$. The reason for using the relative position of the blocks rather than absolute coordinates is that Δx_m^r is related to the time delay that needs to be accounted for in the formulation as it will be discussed later.
- To account for the time delay between arrays, the coordinate of the 1st block in each array is defined relative to the first block of the first array. That is

$$x_1^r = x_1^1 + \Delta r_r \tag{3.11}$$

where once again it is obvious that $\Delta r_1 = 0$.

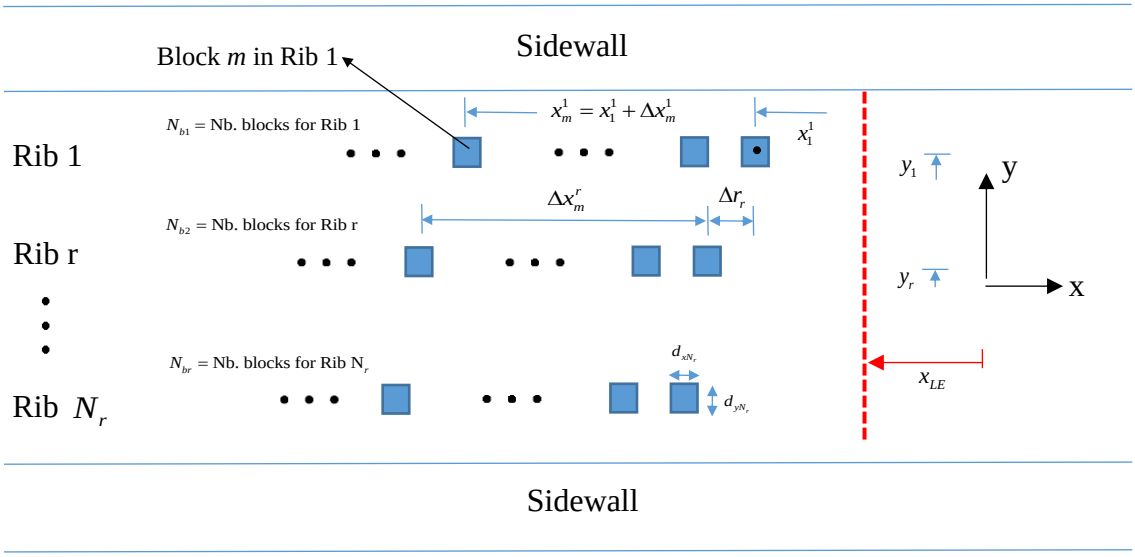

Figure 3.8. The notation used for tread pattern modeling.

The tread pattern as defined above is a good approximation of most of the actual tread patterns in commercial tires. However, some of its constrains can be relaxed in a future version of the model. These will be discussed in Chapter 6.

The forces developed at the contact patch due to the tread pattern will now be developed as a function of the tread pattern parameters N_r, y_r, d_{rx}, d_{ry} N_{br}, Δr_r, and Δx_m^r consistent with the single block formulation, N_k points are defined along the x-direction of the contact patch where the time-dependent moving block forces will be defined. For the sake of simplicity, the same number of N_k points will be used for all ribs. Thus, the excitation of the tire due to the tread pattern will be defined by impulse trains at $N_k \times N_r$ points in the contact patch area.

As mentioned, the most important consideration in modeling the tread pattern excitation is to account for the proper timing of the block forces, i.e. time delay between block forces. Based on the definition of the tread pattern before, the relative time delay between block forces is determined by the relative x-position between the blocks and the velocity V_T. Thus, the time delay for two arbitrary blocks in the tread pattern can easily be computed. In general, the time delay between the m^{th} block in the r^{th} rib, b_m^r, and the n^{th} block in the s^{th} rib, b_n^s, is

$$\Delta t\left(b_m^r \middle| b_n^s\right) = \Delta t_{mr|ns} = \frac{\left(x_m^r - x_n^s\right)}{V_T} \tag{3.12}$$

Considering equations (3.10) and (3.11), it can be also written as

$$\begin{aligned} \Delta t_{mr|ns} &= \frac{\left(x_m^r - x_n^s\right)}{V_T} = \frac{\left(x_1^r + \Delta x_m^r\right) - \left(x_1^s + \Delta x_m^s\right)}{V_T} \\ &= \frac{\left(x_1^1 + \Delta r_r + \Delta x_m^r\right) - \left(x_1^1 + \Delta r_s + \Delta x_m^s\right)}{V_T} = \frac{\left(\Delta r_r + \Delta x_m^r\right) - \left(\Delta r_s + \Delta x_m^s\right)}{V_T} \end{aligned} \tag{3.13}$$

Using equation (3.5), the force due to m^{th} block in the r^{th} rib, b_m^r, modeled as an impulse-train is given as

$$f_m^r\left(x_m^r(t), y_r, t\right) \approx \sum_{k=1}^{N_k} f^r\left(x_k, y_r, \left(t_m^r\right)_k\right) \Delta t \delta\left(t - \left(t_m^r\right)_k\right) \delta\left(x - x_k\right) \delta\left(y - y_r\right) \tag{3.14}$$

where $f^r\left(x_k, y_r, \left(t_m^r\right)_k\right)$ is the block force at discrete times $\left(t_m^r\right)_k$ for the r^{th} rib. The discrete times $\left(t_m^r\right)_k$ are given as

$$\left(t_m^r\right)_k = \frac{\left(x_{LE} - x_m^r\right)}{V_T} + \left(k - 1/2\right)\Delta t \qquad k = 1, 2, \cdots, N_k \tag{3.15}$$

Where the x-position of the block b_m^r is

$$x_m^r = \left(x_1^1 + \Delta r_r + \Delta x_m^r\right) \tag{3.16}$$

The force in equation (3.14) in the time domain can be approximated according to equation (3.5) as follows

$$f_m^r\left(x_m^r(t), y_r, t\right) \approx \sum_{k=1}^{N_k}\left\{\sum_{n=-N}^{n=N}\frac{\omega_T}{2\pi} f^r\left(x_k, y_r, \left(t_m^r\right)_k\right)\Delta t e^{-in\omega_T\left(t_m^r\right)_k} e^{in\omega_T t}\right\}\delta\left(x - x_k\right)\delta\left(y - y_r\right) \tag{3.17}$$

where the complex amplitude (DFT coefficient) acting on the k^{th} point of the r^{th} rib due to the m^{th} block is approximated as

$$F_{rm}^{kn}\left(x_m^r(t), y_r, n\omega_T\right) = \frac{\omega_T}{2\pi} f^r\left(x_k, y_r, \left(t_m^r\right)_k\right)\Delta t e^{-in\omega_T\left(t_m^r\right)_k} \qquad n = \pm 1, \pm 2, , \cdots, \pm N \tag{3.18}$$

The complex amplitude response at an arbitrary location $\left(x_a, y_a\right)$ on the tire is computed using the mobility function of the tire structure and the forcing function in equation (3.19). That is,

$$v_{Total}\left(x_a, y_a, n\omega_T\right) \approx \sum_{r=1}^{N_r}\sum_{m=1}^{N_{br}}\sum_{k=1}^{N_k}\frac{\omega_T}{2\pi} f^r\left(x_k, y_r, \left(t_m^r\right)_k\right)\Delta t e^{-in\omega_T\left(t_m^r\right)_k} M_s\left(\left(x_a, y_a\right)\middle|\left(\left(x_k, y_r\right)\right), n\omega_T\right) \qquad n = \pm 1, \pm 2, , \cdots, \pm N \tag{3.19}$$

Block Forces

The moving radial force $f_B\left(x_b(t), y_b, t\right)$ defined above for a single tread block of the tire is computed using the model developed by Liu et al. (2010). This approach is valid only for blocks with a

rectangular non-skewed cross-section. The block is modeled as a discrete number of viscoelastic springs, shown in Figure 3.9. Its geometry is defined by its cross-section dimensions d_{bx}, d_{by}, as well as the height h_t. The number of springs used for a single block is defined by n.

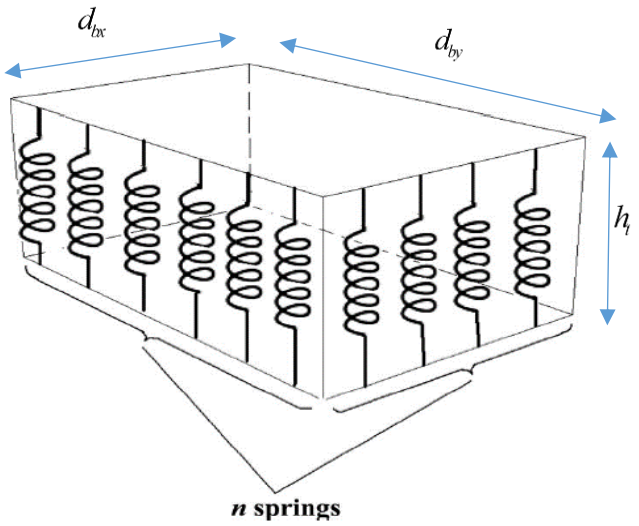

Figure 3.9. a) Multiple viscoelastic radial springs of a block presented by Liu et al. (2008).

Figure 3.9 shows springs that define forces along the radial direction of the block. However, during rolling, tangential forces also act on the block. Both are related to each other by static and dynamic friction coefficients. In order to account for these tangential forces in the model, longitudinal springs are attached to the bottom node of the radial springs. The set of both the tangential and normal springs are referred to as *spring elements*.

In order to compute the radial forces generated as the block enters the contact patch, an initial maximum radial compression of the springs Δ is assumed. This is shown in Figure 3.10. The model assumes that at the contact patch of the tire the belt profile is flat. The contact patch length is defined as ℓ and R_d is the radius of two arcs on both sides of the contact patch. When a block enters the contact patch, the block compresses to the assumed maximum compression Δ.

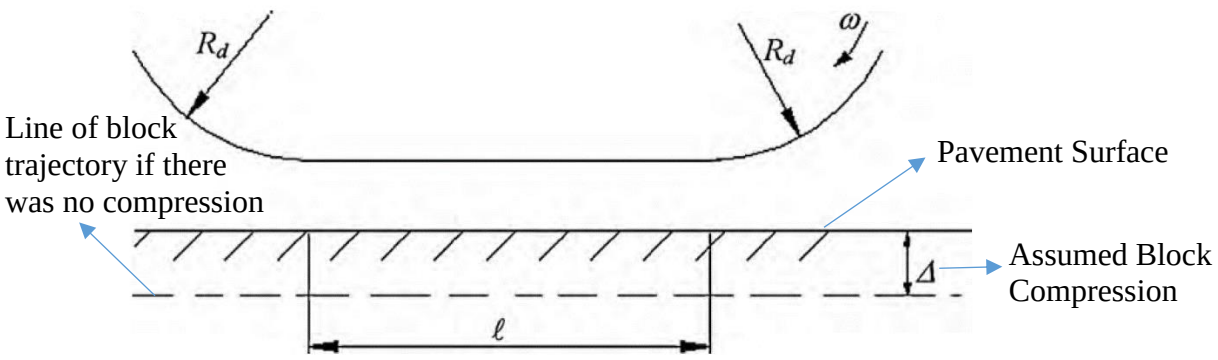

Figure 3.10. Tire geometry in contact patch region (Liu et al., 2010).

Once the maximum compression has been assumed, the radial forces can be calculated by implementing the following process. First, the total radial stiffness $S_r(t)$ and longitudinal stiffness $S_l(t)$ of each block are defined as follows

$$S_r(t) = \frac{E(t) d_{bx} d_{by}}{h_t} \tag{3.20}$$

$$S_l(t) = \frac{E(t) d_{bx} d_{by}}{2(1+\nu) h_t}$$

where, $E(t)$ is the elastic modulus of the tire's tread block. On the other hand, ν corresponds to the material's Poisson ration. Since a viscoelastic material is assumed, the time-dependent elastic modulus is approximated as follows

$$E(t) = E_0 + \left(1 - \sum_{i=1}^{N} p_i \left(1 - e^{-(t/\tau_i)}\right)\right), \qquad N = 1, 2, 3.... \tag{3.21}$$

The stiffness of each spring is then calculated by dividing equations (3.20) by the number of springs per block *n*, as follows

$$k_r(t) = \frac{S_r(t)}{n} \tag{3.22}$$

$$k_l(t) = \frac{S_l(t)}{n}$$

The radial forces $f_B(x_b(t), y_b, t)$ and the tangential forces $f_T(x_b(t), y_b, t)$ applied on the block are finally calculated as follows

$$f_B(x_b(t), y_b, t) = \int_{-\infty}^{t} k_r(t-\tau)\frac{d\delta}{d\tau}d\tau \tag{3.23}$$

$$f_T(x_b(t), y_b, t) = \int_{-\infty}^{t} k_l(t-\tau)\frac{d\chi}{d\tau}d\tau$$

where, $\delta(t)$ and $\chi(t)$ correspond to the compressed lengths of the radial and longitudinal springs and depend on the assumed compression Δ.

If a single spring element is analyzed, then the process to compute $\delta(t)$ and $\chi(t)$ as a block enters and leaves the contact patch is the following. First, it is assumed that the belt is traveling at a velocity V_0, as shown in Figure 3.11. The surface of the tread block that is in contact with the road travels with a speed $V_0 + \xi V_0$, where ξ is defined as the creep ratio of the block.

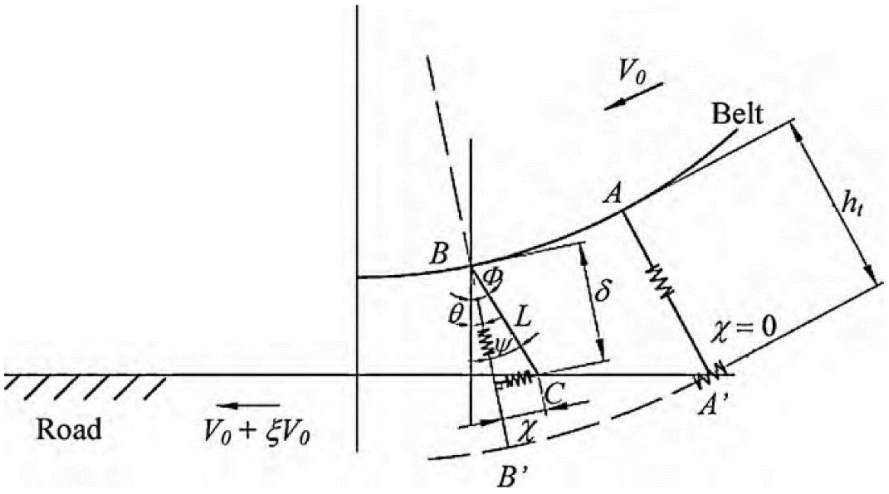

Figure 3.11. Behavior of a spring element as it enters the contact patch (Liu et al., 2010).

Right before the spring element enters the contact patch, the radial and longitudinal springs are not deformed. Thus, the top and bottom nodes of the element are defined by A and A' in Figure 3.11. At this moment, $\delta = h_t$ and $\chi = 0$. A moment later, the element has entered the contact region and the springs compress. The top and bottom nodes of the tire now are defined by B and C, and the distance between them is L. In this case, the angle θ is defined between the vertical line and the line defined between the nodes B and B'. On the other hand, the angle Φ is defined between the vertical line and the line defined between the nodes B and C. Therefore, the angle $\psi(t) = \Phi(t) - \theta(t)$. The deflection of the springs can now be calculated as follows

$$\delta(t) = L(t)\cos\psi(t) \tag{3.24}$$

$$\chi(t) = L(t)\sin\psi(t)$$

After defining the spring deformation functions in equation (3.24), the forces on the block can be calculated using equations (3.23). However, an additional step is required to account for slip of the block. Slip of the block happens only if $|F_l(t)| > \mu_s F_r$, where μ_s is a static friction coefficient.

Therefore, the time derivative of $\chi(t)$ is defined for both slip and non-slip conditions with the following differential equations

$$\frac{d\chi}{dt} = \xi V_0 \qquad \left| f_T\left(x_b(t), y_b, t\right)\right| \le \mu_s f_B\left(x_b(t), y_b, t\right)_r \text{ (no slip condition)} \tag{3.25}$$

$$\bar{m}\frac{d^2\chi}{dt^2} + f_T\left(x_b(t), y_b, t\right) = sign\left(\xi V_0 - \frac{d\chi}{dt}\right)\mu_k f_B\left(x_b(t), y_b, t\right) \qquad \left| f_T\left(x_b(t), y_b, t\right)\right| > \mu_s f_B\left(x_b(t), y_b, t\right) \text{ (slip condition)}$$

In this case, $\bar{m} = M/n$ where M is the total mass of the block. On the other hand, μ_k is the kinetic friction coefficient between the road and the rubber block, defined as

$$\mu_k\left(p, \xi V_0\right) = \frac{\alpha\left|p\right|^{\eta-1} + \beta}{a + b\left|\xi V_0\right|^{-1/\kappa} + c\left|\xi V_0\right|^{-2/\kappa}} \tag{3.26}$$

where, p is the normal pressure applied on the pavement surface by the block. The rest of the symbols correspond to empirical constants defined for the specific contact problem being analyzed, i.e. rubber on pavement.

Liu et al. (2010) presented an example of the produced forces on a block of size 25 mm x 20 mm x 8 mm. These are shown in Figure 3.12. A traveling velocity of the belt of 16.7 m/s (vehicle speed of 37 mph) is used for simulation. The contact patch has a total length of 0.17 m. In addition, a contact pressure of 0.4MPa has been applied to the block, resulting in a maximum normal force of approximately 200 N (see Figure 3.12). This is approximately equivalent to a 2,000 kg vehicle with its load distributed along 24 blocks in each of the tire's contact patch. The results in Figure 3.12 are for an assumed maximum block compression $\Delta = 0.2$ mm. A creep ratio of 0.3 % was used and a radius $R_d = 0.5$ m.

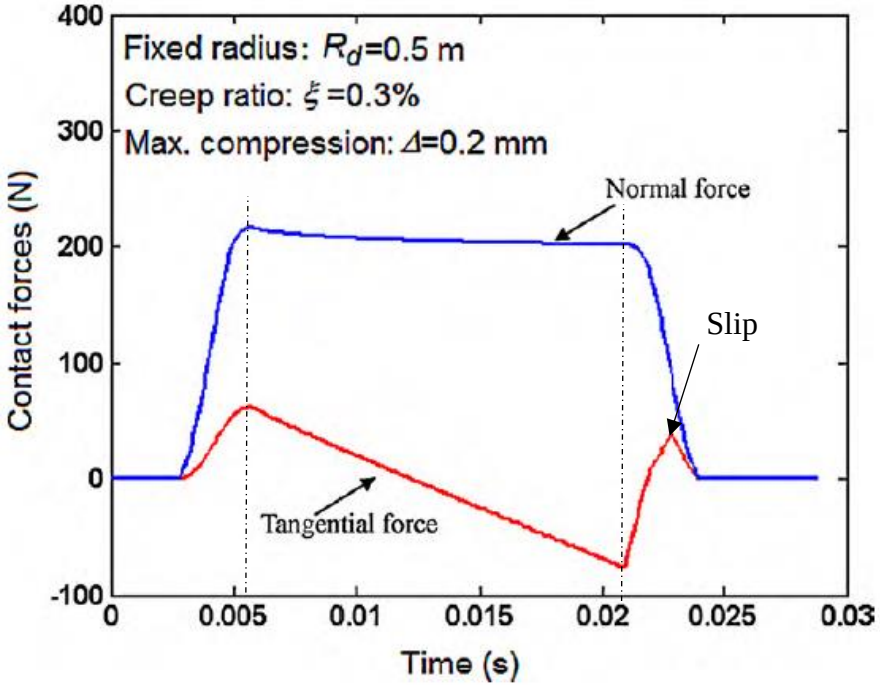

Figure 3.12. Comparison of block tangential and normal forces developed on a tread-block during steady-state rolling, presented in the work by Liu et al. (2010).

The process to compute the normal and tangential forces for a sing block using the model described above is summarized as follows:

1. Assume maximum block compression Δ (see Figure 3.10) and define all additional inputs required by the model. Example values of these inputs are listed in Table 3-1.
2. Compute $\delta(t)$ and $\chi(t)$ using equation (3.24).
3. Compute the normal and tangential forces on the block using equation (3.23).
4. Verify slip condition based on the criteria specified in equation (3.25):
    - If the block is entering the contact patch or it is fully compressed in the contact patch and slip happens, then start the process again assuming a smaller creep.
    - If the block is leaving the contact patch and is slipping, solve the differential equation for the slip condition. Slip is only allowed when the block is leaving the contact patch since it cannot be avoided. This will allow updating $\chi(t)$, $d\chi(t)/dt$ and $\delta(t)$ for the next time step and thus compute the corresponding forces.

5. Repeat steps 2 through 4 for each time step.

Finally, it should be noted that the number of selected time steps (or equivalently contact patch excitation points) selected was determined by iteratively increasing it until the initial slope of the normal block force (see Figure 3.12) converges to an error less than 10%. This guarantees that the forces are accurately captured in the model.

Table 3.1. Input parameters for the block contact model. Prony series coefficients obtained from the work by Lopez Arteaga (2014). Friction law parameters obtained from the work by Hofstetter et al. (2006).

Parameter	***Sign***	***Value [units]***
Maximum Block Compression	Δ	0.2 [mm]
Belt velocity	V_0	26.8×10^{3} [mm/s]
Creep ratio	ξ	0.3%
Block density	ρ_b	1000 [kg/m^3]
Block material poison's ratio	ν	0.47
Block surface area	$A_b = d_{bx} \times d_{by}$	5 [cm^2]
Block height	h_t	0.8[cm]
Kinetic friction law parameters (rubber on concrete surface)	α β η $(1/\kappa)$ a b c	0.1399 0.4091 0.8680 0.1672 0.9203 -1.1188 0.9677
Elastic modulus Prony series coefficients	E_0 p_1 p_2 τ_1 τ_2	3.3×10^{6} [Pa] 0.487 0.137 9.96×10^{-5} [s] 1.20×10^{-3} [s]
Tire radius at contact patch edges	R_d	0.5 [m]
Contact patch length	ℓ	0.17 [m]
Block contact pressure	p	0.4 [N/mm^2]
Number of springs per block	n	100

Total Tire Load

The 5-step process in the previous section is implemented to compute the radial forces for each individual block in the tread pattern. These forces depend on the specified parameters in Table 3.1, including the initially assumed spring compression Δ. Once all the forces for all the blocks in the tread pattern are obtained, the appropriate force applied at the contact patch excitation points can be computed by means of equation (3.18) and thus the response of the tire using equation (3.19). Still, an additional step is taken in order to verify that the total load being applied to the tire is correct. To this end, the calculation of the total tire load is presented.

The first step is to define the force acting on the k^{th} point of the r^{th} rib due to the m^{th} block, defined as follows

$$f_{krm}(t) = f^{r}\left(x_k, y_r, \left(t_m^r\right)_k\right)\Delta t\delta\left(t - \left(t_m^r\right)_k\right) \tag{3.27}$$

Linearly adding the contribution from all the blocks in the r^{th} rib yields

$$f_{kr}(t) = \sum_{m=1}^{N_{br}} f_{krm}(t) = \sum_{m=1}^{N_{br}} f^{r}\left(x_k, y_r, \left(t_m^r\right)_k\right)\Delta t\delta\left(t - \left(t_m^r\right)_k\right) \quad k = 1, 2, \cdots, N_k \quad r = 1, 2, \cdots, N_r \tag{3.28}$$

The total force time history over the contact patch is then the contribution of all the ribs. Thus,

$$f_{cp}(t) = \sum_{k=1}^{N_k}\sum_{r=1}^{N_r} f_{kr}(t) = \sum_{k=1}^{N_k}\sum_{r=1}^{N_r}\sum_{m=1}^{N_{br}} f_{krm}(t) = \sum_{k=1}^{N_k}\sum_{r=1}^{N_r}\sum_{m=1}^{N_{br}} f^{r}\left(x_k, y_r, \left(t_m^r\right)_k\right)\Delta t\delta\left(t - \left(t_m^r\right)_k\right) \tag{3.29}$$

that must be the same as the load over the tire at all times, e.g. $f_{cp}(t) = L_T$. In this case, L_T is the total time-independent load over the tire. This can also be approximated as follows for a vehicle whose total load is evenly distributed on its four wheels

$$L_T = \frac{M_V \times g}{4} \tag{3.30}$$

where M_V is the total mass of the vehicle and g is gravity's acceleration. If the value of L_T obtained with equation (3.29) does not match with that obtained with equation (3.30), then the assumed initial compression Δ for the blocks needs to be modified. This task is performed multiple times in an iterative process until the value of L_T converges to the desired one.

It should be noted the total load calculated with equation (3.29) approximates the true distribution in the contact patch. For example, Figure 3.13 shows the total load after implementing equation (3.29). In this case, the results were computed for a full revolution of a tire mounted on a vehicle traveling at 70 mph. This case is for a vehicle with a total mass $M_V = 1500$ Kg and an expected total load of $L_T = 3675$ N. The assumed maximum compression for all blocks has been assumed to be $\Delta = 0.8$ mm. However, it can be observed that the approximated total load is not constant and has small fluctuations with a mean value of 3365 N. Therefore, in this case, the value of the initial compression Δ should be increased such that the mean value of the total load converges to the expected load of 3675 N.

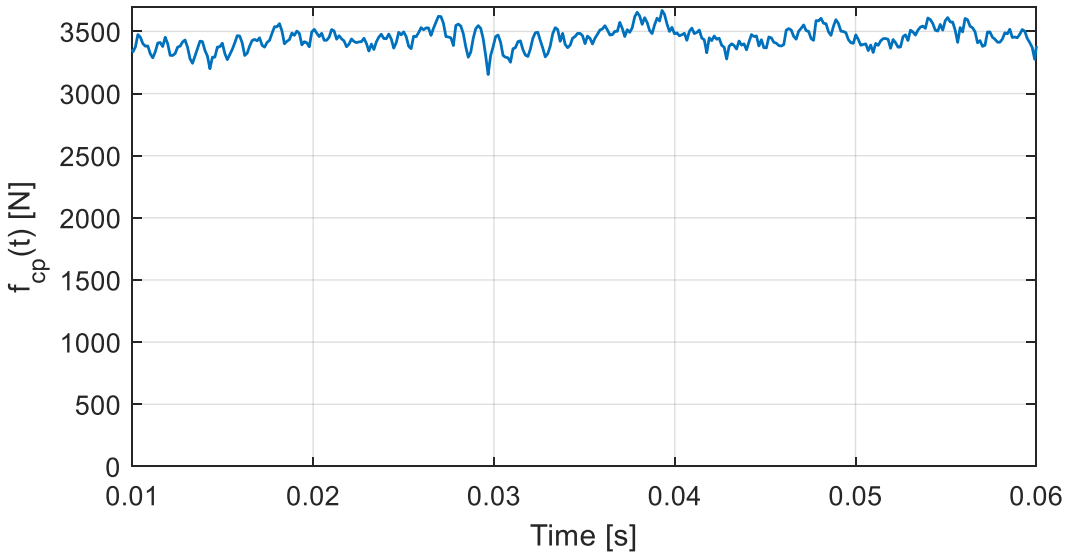

Figure 3.13. $f_{cp}(t)$ computed for a full revolution of a tire of size 225/45R17 on a vehicle traveling at 70 mph.

3.3. Tread-pattern Excitation Characteristics

Input Forces

In this section, a study on the characteristics of the tread pattern excitation is presented. Three different tread patterns are studied in order to provide more insight into how they excite the tire. All the blocks presented for these study cases were modeled with the properties presented in Table 3.1, except for the surface area. The total load on the tire is of 3675 [N] which is typically the tire load of a midsize vehicle. The selected tire shown in the following results is 225/45R17.

For the first case, all the blocks in the tread have the same size, all ribs have the same amount of uniformly spaced blocks, and the ribs themselves are also evenly spaced. An example of this tread is shown in Figure 3.14. In this case, a total of 60 blocks for 6 ribs have been selected. These numbers have been chosen because this is typically the case for all-season tires mounted on small and midsize vehicles. This is based on experience after testing over 47 tires with an OBSI (see Chapter 1). The surface area of all blocks is 2 cm by 2.5 cm.

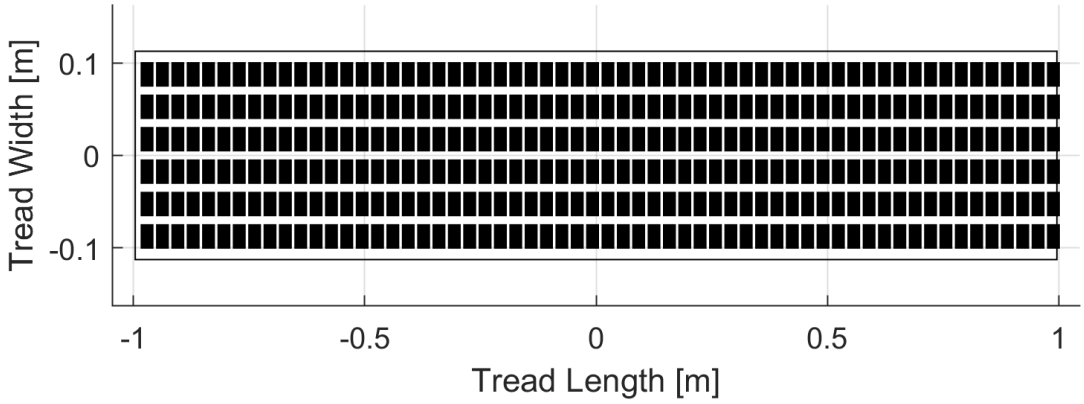

Figure 3.14. Uniform tread pattern with 60 uniformly separated equal blocks for 6 ribs (tire size 225/45R17).

The frequencies excited due to the impact of the tread-blocks on the pavement can be calculated for a set of discrete locations in the contact patch. For example, a contact patch excitation point can be selected for the first rib of the tread-pattern in Figure 3.14. This example point is shown in Figure 3.15a. In this case, the 60^{th} harmonic of the tire's fundamental frequency and the

corresponding harmonic multiples are excited, as shown in Figure 3.15b. These are the only frequencies excited because 60 evenly separated blocks have been used in the selected rib. Since all ribs are equal, then this excitation will be the same for all ribs. In this case, the excited block forces are approximately equal to 33 N.

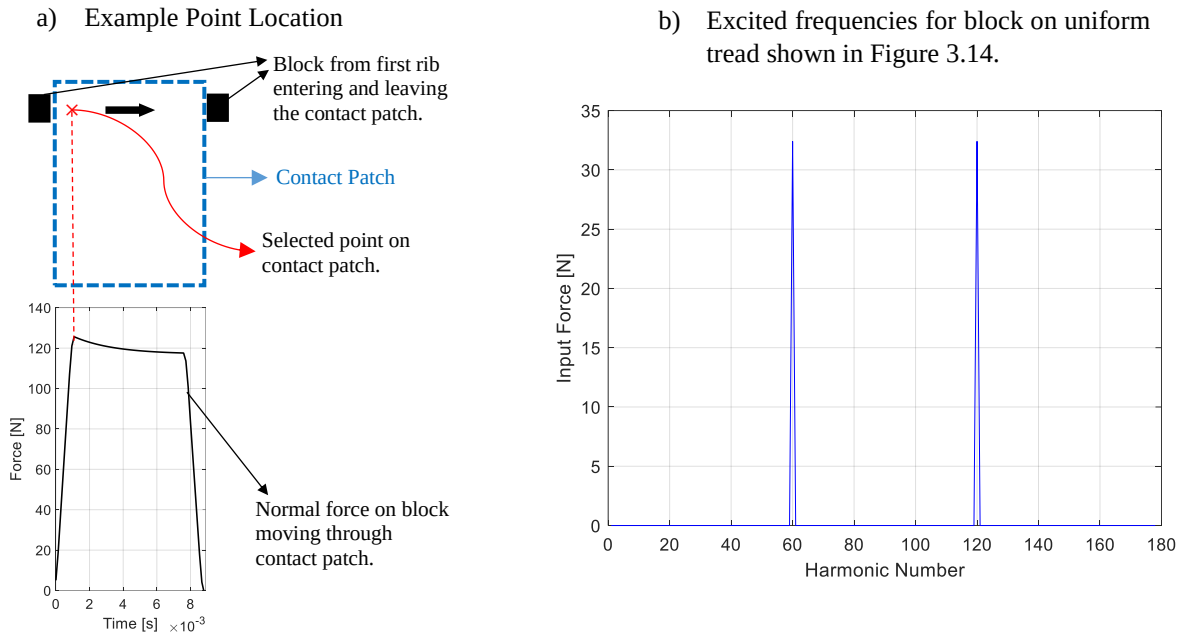

Figure 3.15. a) Point of maximum normal force b) Excited frequencies for the maximum normal point force.

A second case is studied where 60 blocks have been used for two ribs with a block surface area of 2 cm by 2.5 cm. The other 4 ribs have 65 blocks with a surface area of 1.5 cm by 2 cm. In both cases, all blocks are uniformly separated. The resulting tread-pattern is shown in Figure 3.16. The excited frequencies for the same point as in Figure 3.15a, for the two types of ribs, are shown in Figure 3.17. Figure 3.17a corresponds to the first rib and Figure 3.17b to the second rib from the top of the tread pattern. It should be noted that the excited amplitudes for the two cases are different. For rib 1, the force is approximately 26 N and for rib 2, the force is 42 N. These results indicate that the surface area of the blocks is related to the amplitude of the excited forces. In this case, it is observed that the smaller the block, the lower the amplitude. Furthermore, it can be observed that for the 60-block rib, the 60^{th} harmonic and its multiples are excited. For the 65-block rib, the 65^{th} block and its multiples are excited.

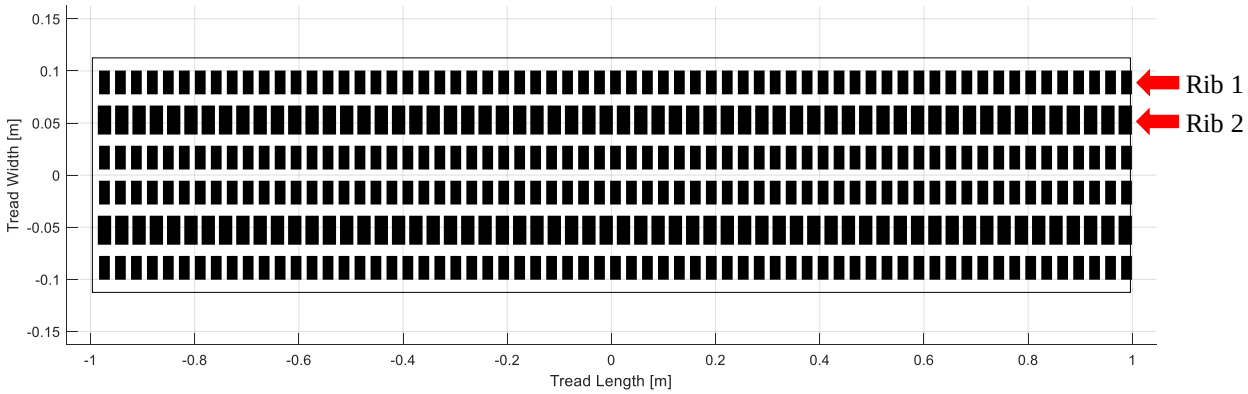

Figure 3.16. Uniform tread pattern with two 60-block ribs and four 65-block ribs (tire size 225/45R17). The two 60-block ribs have blocks of size 2 cm x 2.5 cm and the four 65-block ribs have blocks of size 1.5 cm x 2 cm.

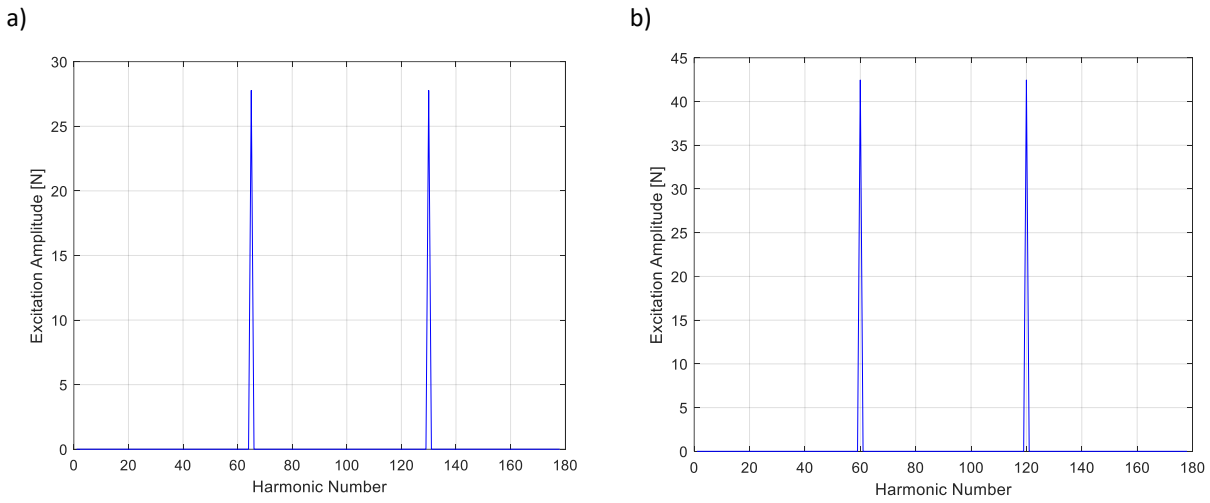

Figure 3.17. Excitation amplitudes for a) Rib 1 and b) Rib 2 for the tread-pattern shown in Figure 3.17.

Finally, a third case is analyzed for a tread pattern that has the same number of blocks and ribs as in the case shown in Figure 3.16. However, the gap between blocks is not uniform anymore and has been randomized. The resulting tread pattern is shown in Figure 3.18.

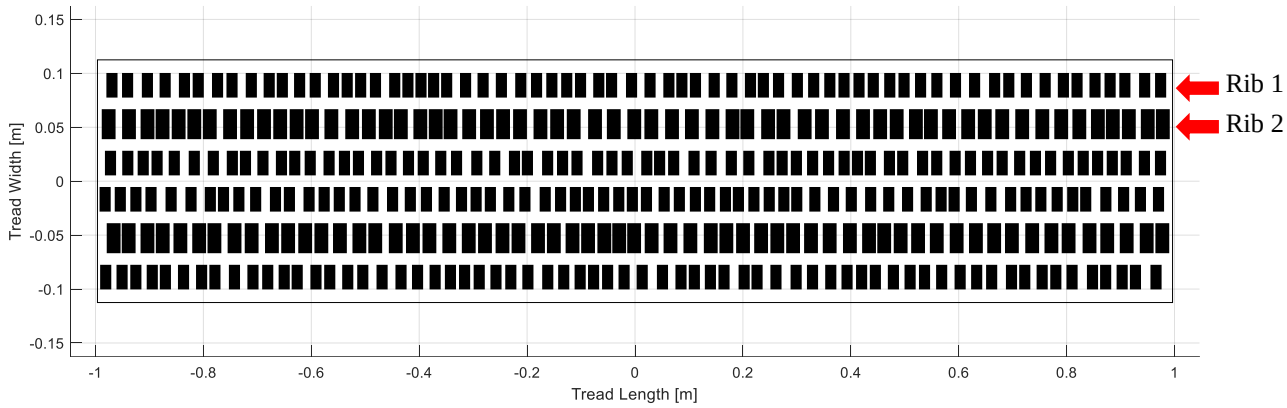

Figure 3.18. Randomized tread pattern with 60 separated blocks for 6 ribs (tire size 225/45R17). Two ribs have blocks of size 2 cm x 2.5 cm and 4 ribs have blocks of size 1.5 cm x 2 cm.

The frequencies excited for the first two top ribs of the tread pattern in Figure 3.18 are shown in Figure 3.19. It can be observed that in this case, all the harmonics are excited. The dominant content is still around the 65^{th} and 60^{th} harmonic for Rib 1 and Rib 2, respectively. However, if the results in Figure 3.19 are compared to those in Figure 3.18, it can be observed that the maximum excitation amplitude has been greatly reduced for all ribs. That is, from 26 N to 11 N for rib1 and from 42N to 15 N for rib 2. This indicates that by randomizing the tread-pattern design, the energy of the input force spectrum is distributed on all harmonics. Thus, reducing the maximum input forces applied to the tire. Finally, it should be noted that for a vehicle traveling at 70 mph and a tire size of 225/45R17, the 60^{th} harmonic corresponds to 942 Hz and the 65^{th} harmonic corresponds to 1020 Hz. This is consistent with the typical range of frequencies where dominant TPIN is observed for passenger car tires (see literature review in Chapter 1).

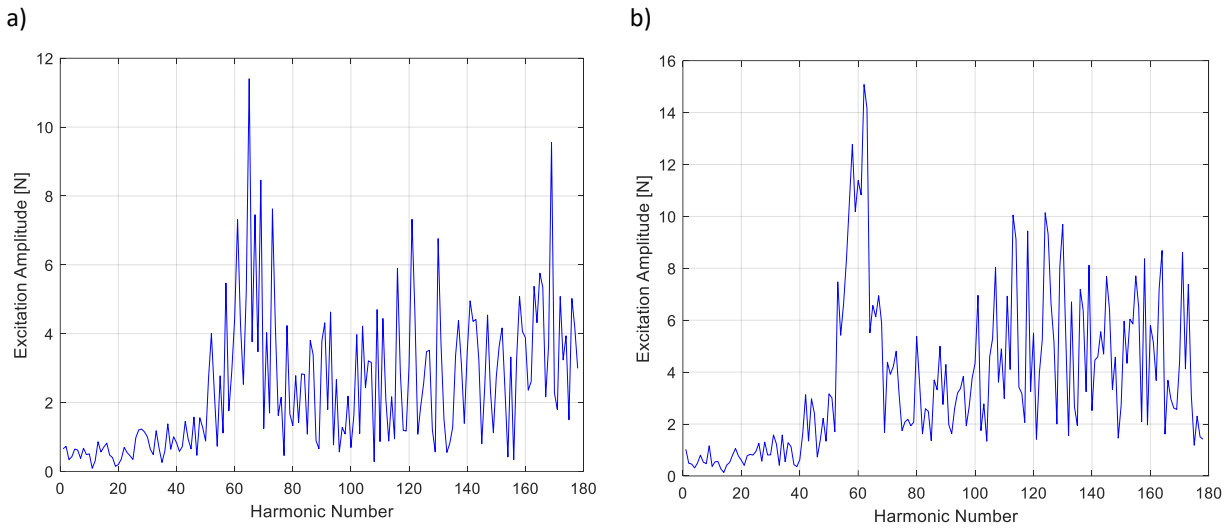

Figure 3.19. Excitation amplitudes for a) Rib 1 and b) Rib 2 for the tread-pattern shown in Figure 3.19.

The overall input power provided by the impact of the contact patch blocks against the pavement can also be quantified. This allows determining which frequencies of the tire's structure are excited. In addition, it could potentially lead to the improvement of tread pattern design. For example, an improved tread pattern design would distribute the overall input power along the spectrum instead of exciting certain frequencies with very high amplitudes.

Input Power

The input power provided in the contact patch of the tire can be approximated as follows

$$W_{CP}(f) = \frac{1}{2}\sum_{p}^{P_{CP}} \text{Real}\left[F_p(f) \times V_p^*(f)\right] \tag{3.31}$$

where, $W_{CP}(f)$ is the input power provided to the tire in the contact patch. In this case, the forces are applied at a set of discrete points $p = 1, 2, 3, ..P_{CP}$ in the contact patch. In addition, $F_p(f)$ is the input force at each one of these points and $V_p(f)$ is the tire's velocity response at the point locations. It should be noted that the superscript * denotes a complex conjugate operation.

Example of the overall power for the uniform tread patterns (see Figure 3.14 and Figure 3.16) and randomized tread patterns (see Figure 3.18) are shown in Figure 3.20 and Figure 3.21. These were

computed for a tire mounted on a vehicle traveling at 70 mph. In this case, the non-uniform infinite plate model from chapter 2 and the properties from Table 2.2 were used for a tire of size 245/45R17.

Figure 3.20 shows that when the tread pattern is uniform, i.e. not randomized, the input power amplitudes are very high and localized at specific frequencies. On the other hand, Figure 3.21 shows that when the tread-pattern is randomized, the maximum input power is reduced. In this case, the energy is distributed within a range of 500 Hz to 1500 Hz with a peak at around 1000 Hz. If the results in Figure 3.21 are compared to those in Figure 3.20b, it can be observed that the maximum input power is reduced from approximately 98 [W] to 17 [W] by simply randomizing the same tread pattern.

a) Uniform Tread Patten from Figure 3.14.

b) Uniform Tread Patten from Figure 3.16.

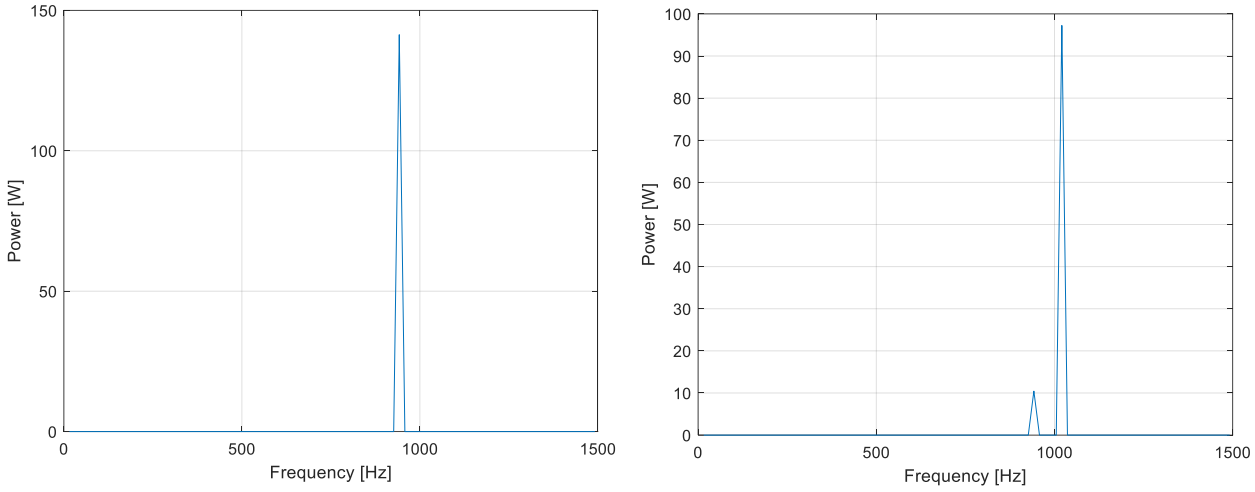

Figure 3.20. Input block excitation power for the tread-patterns shown in a) Figure 3.16 and b) Figure 3.17 coupled to the non-uniform infinite plate model.

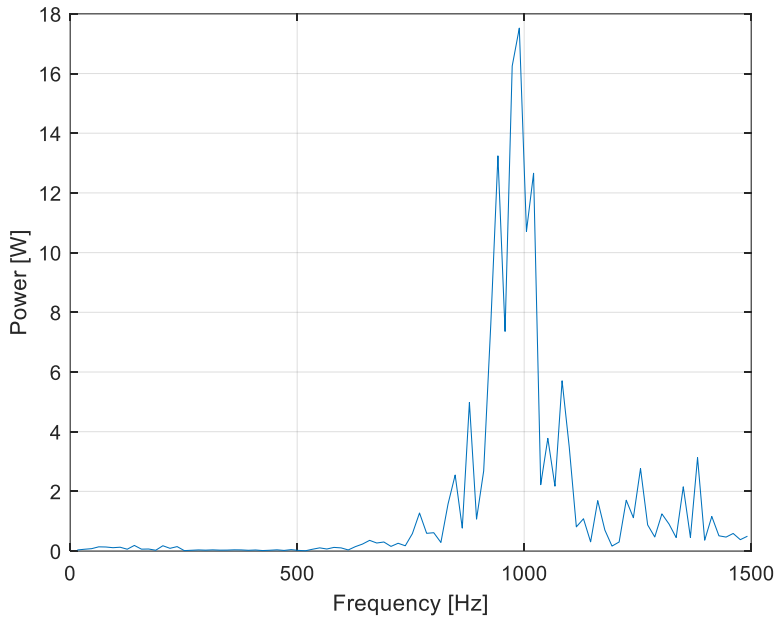

Figure 3.21. Input block excitation power for randomized tread pattern shown in Figure 3.18.

The overall input power provided by each tread pattern can potentially be used as a metric to preliminary assess the performance of the tread pattern design. In general terms, a reasonable hypothesis is that a tread pattern with the lowest overall input power has the potential to be the quietest. However, this approach does not account for other important factors such as the spreading of the energy between many frequencies and the A-weighting effect of human perception with frequency.

Thus, the input power was computed by adding the spectral powers up to 1500 Hz. This is done by adding the power from all the spectral lines within this frequency range. For example, the overall power for the uniform tread pattern in Figure 3.16 is 141.32 [W]. The overall power for the uniform tread pattern with different block sizes in Figure 3.17 is 107.69 [W]. Finally, the overall power for the randomized tread pattern in Figure 3.18 is 148.55 [W]. These preliminary results indicate that the main parameter affecting the overall input power of a tread pattern is the number of blocks in the ribs, size of the blocks, and distribution. It appears that different number of blocks in each rib and block sizes leads to reduction in the input power. On the other hand, simply randomizing the tread pattern without changing the number and size of the blocks not necessarily leads to a reduction in the input power.

4. Experimental Validation

In this chapter, experimental validation cases for the structural response of the tire and the noise that it produces are presented. In order to validate the structural models, a set of experiments were performed on a slick tire of size 225/45 R17. The tire was excited with an electrodynamic shaker at the center of its tread band. Its vibratory response was measured at 199 points on its surface using a laser Doppler vibrometer. On the other hand, in order to validate the produced noise of the tire, predictions were made using a boundary element code. These results were compared to the experimental results presented in the work by Yum et al. (2006). In this case, a tire of size 205/70R14 was excited with an electrodynamic shaker at the center of its tread band. Noise was measured at 40 locations, 5 cm away from the tread band. Finally, it is important to mention that vibrations and noise data for an actual rotating tire is very limited in open literature. In addition, it requires unique facilities and equipment to perform such measurements. Therefore, true validation is not possible at this time for such cases.

4.1. Structural Models Validation

In order to validate the structural models presented in Chapter 2, an experiment was performed. A slick tire of size 225/45R17 was used. The tire was inflated to 32 psi and hanged horizontally with elastic chords as shown in Figure 4.1. A Bruel & Kjaer permanent magnetic vibration exciter type 4808 was used to excite the tire. A stinger was connected between the shaker and a point located at the center of the tire's belt. In addition, an ICP force sensor PCB208C02 was fitted to the tip of the stinger and glued to the tire's surface as shown in Figure 4.1a. This allowed measuring the actual input force that excites the tire at the input location.

A total of 199 points were marked on the tire surface with retroreflective tape. The response of the tire at these points was measured with a Polytec PSV-400 scanning laser vibrometer as shown in Figure 4.1b. 71 of the marked points were located along the mid-belt circumferential line of the tire. Therefore, its dynamic response was measured at every 5 degrees along the belt's circumference. It should be noted that it was not possible to measure the response at the point of

excitation. Another 72 points were marked at the top sidewall of the tire. Finally, the response of the tire was also measured at 14 points along its transversal direction, including the belt and sidewalls. This was done at 0, 90, 180 and 270 degrees from the excitation location.

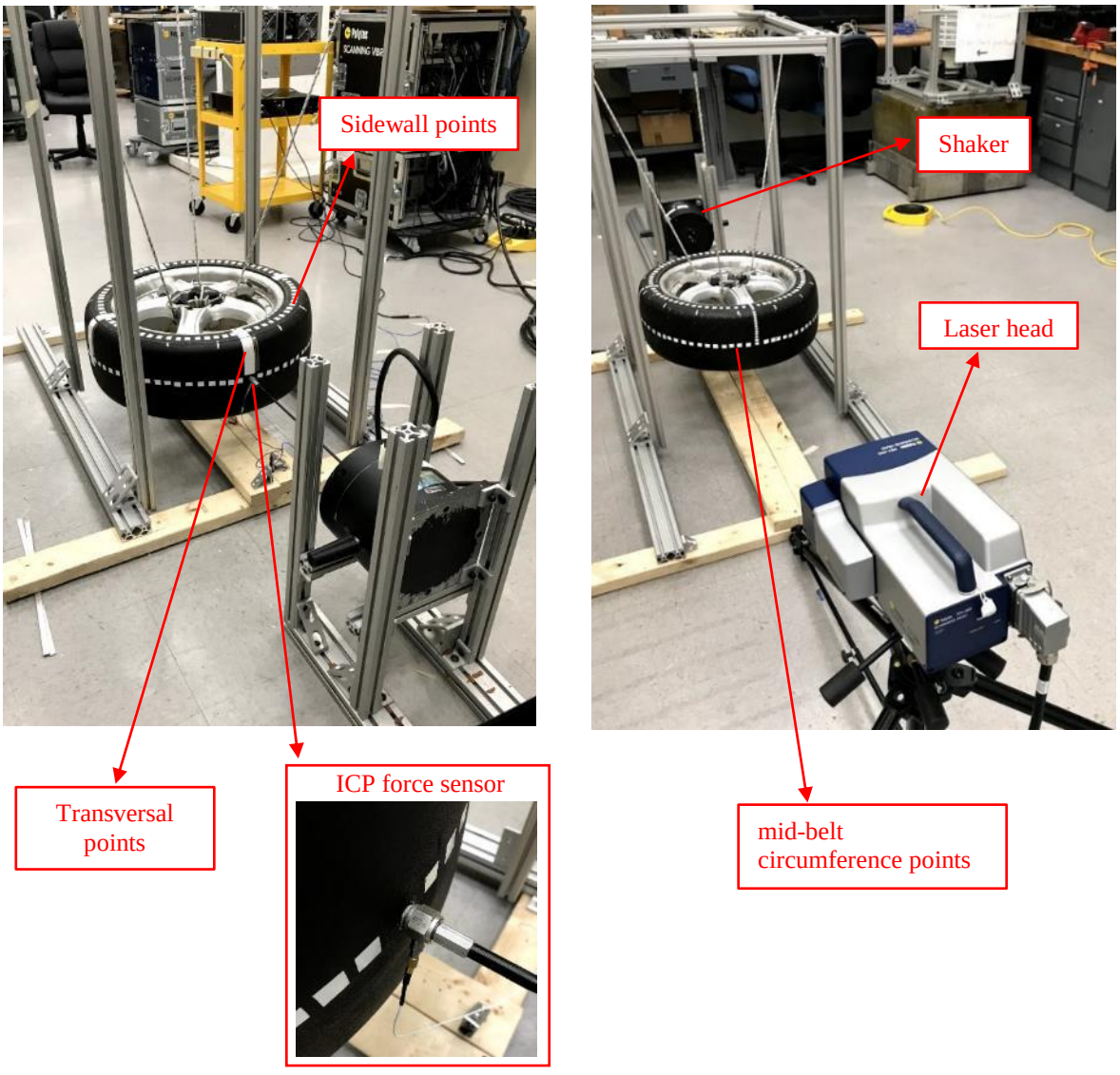

Figure 4.1. a) Tire hanged in experimental rig and shaker. b) Laser vibrometer head pointing towards tire belt.

The measured input mobility FRFs are initially analyzed. However, since the response could not be measured at the exact point of excitation, approximated results for a point at 1 cm above the excitation location will be used for comparisons. Figure 4.2 shows simulated input mobility FRFs using the structural modeling approaches presented in Chapter 2. These are compared to the measured mobility FRF at the same location. In this case, all the modeled results assume a constant 16% damping loss factor, as suggested in the work by Pinnington (2006b). Figure 4.2 shows the frequency response functions in decibels (dB) referenced to 1 m/Ns. This scale was chosen in order to be consistent with how results are usually presented in the literature (see the literature review provided in Chatper1, where most results are presented using this scale). Finally, it should be noted that all the structural properties of the tire for this validation case are shown in Table 4.1. These values were modified from those from the work by B. S. Kim et al. (2007). Specifically, the circumferential stiffness was reduced. The reason is that a different tire was used for experiments and by modifying the properties presented in this work, better predictions were obtained.

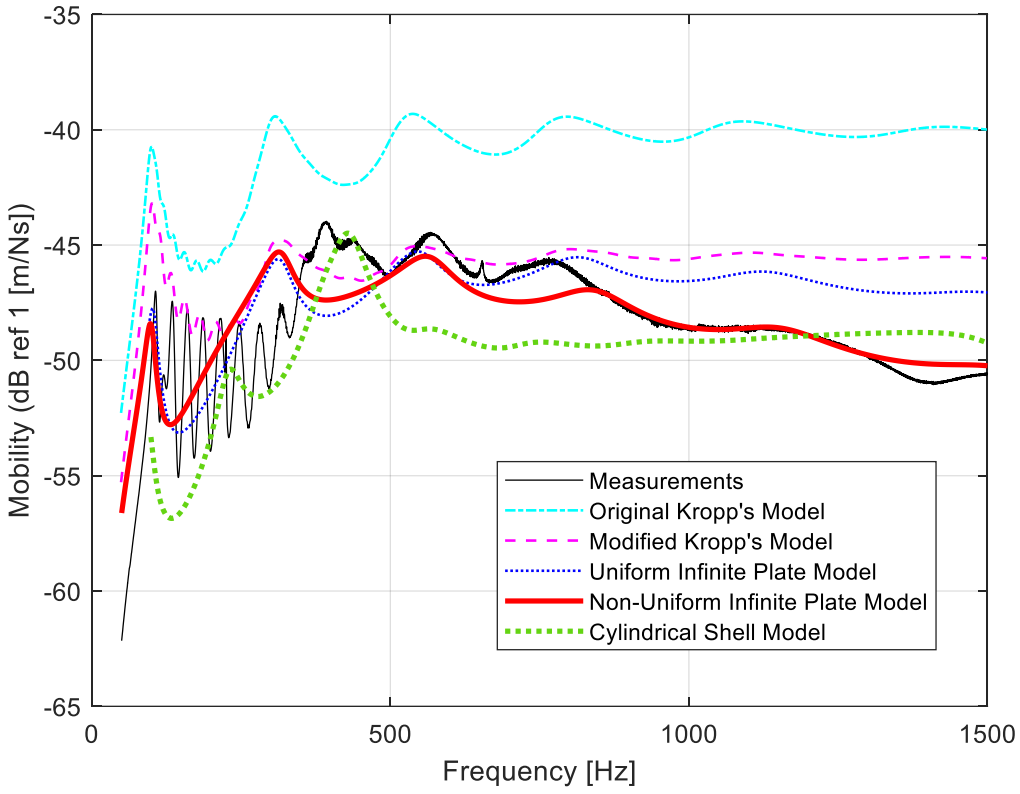

Figure 4.2. Measured and simulated mobility FRFs measured at a point located at 1 cm above excitation location for a tire of size 225/45R17.

Table 4.1. Uniform and Non-uniform Tire Parameters used for FRF simulations.

Parameters	Notation	Tire Part, Direction	Value [Units]
Non-Uniform Case			
Mass per Unit Area	m_b	Belt, cross-direction	17.4 $[kg/m^2]$
Mass per Unit Area	m_s	Sidewalls, cross-direction	12.3 $[kg/m^2]$
Bending Stiffness	B_{yb}	Belt, y-direction	6.9 $[Nm]$
Bending Stiffness	B_{ys}	Sidewalls, y-direction	1.2 $[Nm]$
Uniform Case			
Mass per Unit Area	m	Belt and Sidewalls	16 $[kg/m^2]$
Bending Stiffness	B_x	Belt and Sidewalls, x-direction (modified from 34.3 Nm, reported by B. S. Kim et al. (2007))	6 $[Nm]$
Bending Stiffness	B_y	Belt and Sidewalls, y-direction	4.05 $[Nm]$
Membrane Tension	T_{0x}	Belt and Sidewalls, x-direction (32 psi)	3.49×10^4 $[N/m]$
Membrane Tension	T_{0y}	Belt and Sidewalls, y-direction (32 psi)	6.99×10^4 $[N/m]$

The results in Figure 4.2 are presented for a frequency range of up to 1500 Hz for completeness. However, results are only comparable for 500 Hz to 1500 Hz since the structural models were constructed to be accurate only for this range.

If the response calculated with Kropp's original model is analyzed in Figure 4.2, large over-predictions can be identified. These are then reduced if the modified Kropp's model proposed by Perisse et al. (2000) is implemented. The modification consists of artificially increasing the value of the cross-stiffness of the plate instead of calculating it as suggested by Kropp (1999). The reason to do this is to avoid excessive over-predictions. For example, for Kropp's original model the cross-stiffness was defined as $B_{xy} = \sqrt{B_x B_y} = 4.93$ Nm. On the other hand, a cross-stiffness $B_{xy} = 130$ Nm was implemented for the modified version. Still, both approaches are very inaccurate for frequencies above 750 Hz.

On the other hand, Figure 4.2 also shows that the response computed with the uniform infinite plate model is significantly more accurate over the high-frequency range if compared with Kropp's modified approach. In this case, the wave propagation solution formulated in Chapter 2 is used (see equations (2.83) through (2.85)). Still, the most accurate modeling approach is the non-uniform infinite plate. An average of 2 dB error is observed over the range of interest. This is less than the average 3dB to 10 dB errors observed in literature. In addition, very good agreement with the experimental data is shown between 800 Hz and 1300 Hz, i.e. most of the frequency range of interest. This shows how important it is to account for structural non-uniformities along its transversal direction in the model.

Finally, it can also be observed that the response predicted with the non-uniform infinite plate is better than that obtained with the cylindrical shell model, especially between 500 Hz and 800 Hz. The cylindrical shell model is more accurate between 300 Hz and 500 Hz, even though this is out of the frequency range of interest. This is probably because this model includes curvature effects, which are important below the tire's ring frequency (usually located around 500 Hz). However, it should be noted that the accuracy of the cylindrical shell depends on how well the input structural parameters are selected. This might be a challenging task due to the large amount of them. Future work should address this problem. In addition, a proposed alternative is to combine the cylindrical shell model for frequencies between 300 Hz to 500 Hz and then the non-uniform flat plate model for frequencies above 500 Hz.

In order to further analyze the response of the tire, not only the approximated input mobility FRF is analyzed. The mobility has been also calculated along a transversal and circumferential centerline of the tire. A schematic of these two lines is shown in Figure 4.3.

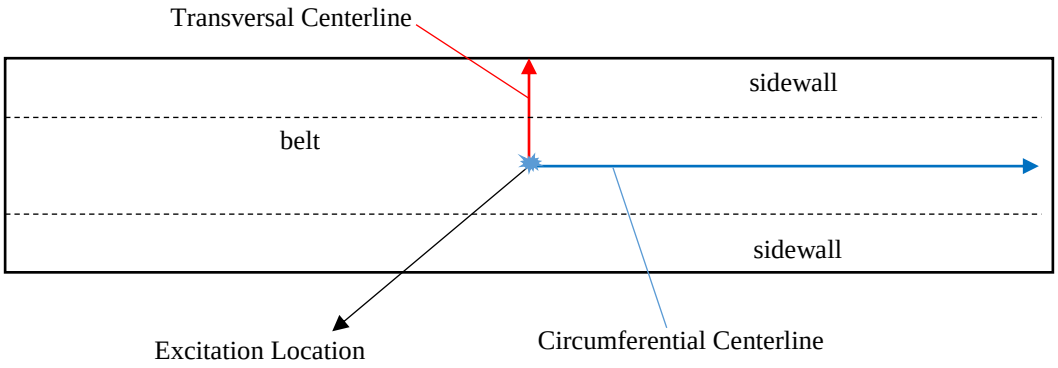

Figure 4.3. Unwrapped view of a tire showing transversal and circumferential centerlines.

Figure 4.4 shows measured mobilities along the transversal centerline of the tire. These show the differences in the response between the sidewall and the belt for the tire used in the experiments. It can be observed that the highest response of the tire is located close to the excitation location and extends up to approximately 0.07 m, mostly within 500 Hz to 1,000 Hz. In addition, it can also be observed that within the same frequency range, the sidewall's response is also high especially close to the shoulder of the tire. This observation is consistent with the results presented by other researchers (see the work by Yum et al. (2007)).

On the other hand, Figure 4.5 shows the experimental mobility FRF along a circumferential center line on the tire's belt. It can be observed that for the frequency range of interest (500 Hz-1,500 Hz), the response prominently decays. For example, in Figure 4.5, there is approximately a 25-dB decay at 90 degrees away from the excitation location along the belt's centerline. This supports the hypothesis of the existence of propagating and decaying waves along the circumferential direction of the tire for the frequency range of interest.

dB ref. 1 [m/Ns]

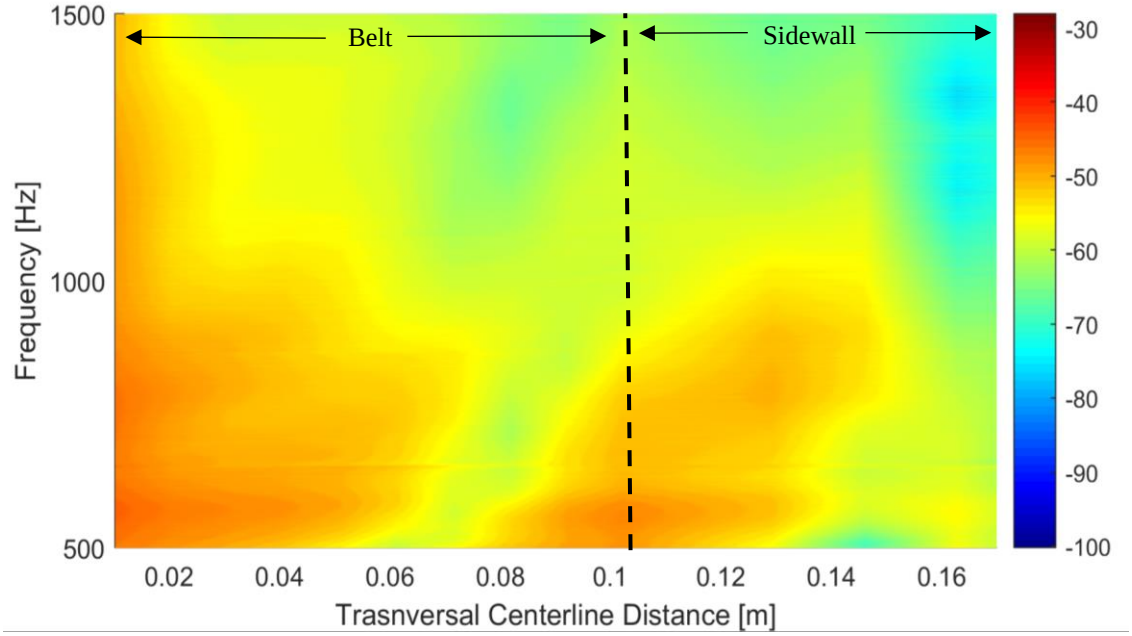

Figure 4.4. Experimental mobility FRF along the center transversal line for a tire of size 225/45R17.

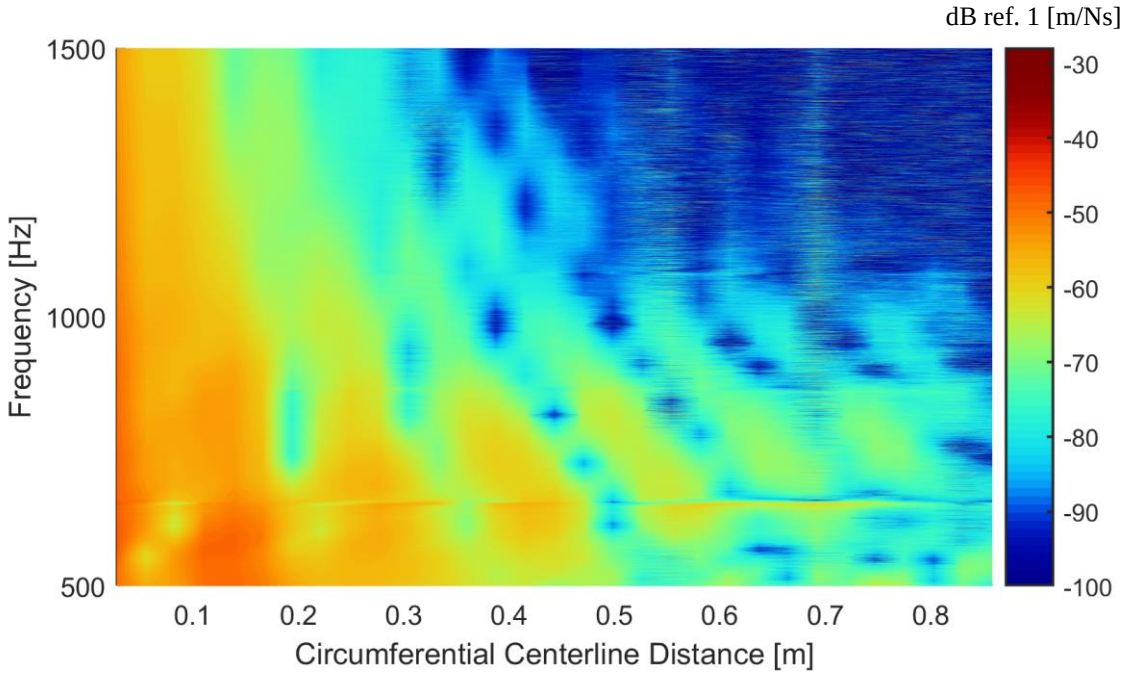

Figure 4.5. Experimental mobility FRF along the center circumferential line for a tire of size 225/45R17.

The experimental vibration responses presented in Figure 4.4 and Figure 4.5 were simulated using the non-uniform infinite pate structural model (most accurate model for input mobility in Figure 4.2). The simulated results for these cases along the transversal centerline are shown in Figure 4.6. It can be observed that the simulated results successfully capture the response of the tire in the belt near the excitation area. In addition, the response spike near the tire's shoulder region of the sidewall is also captured reasonably well. On the other hand, the simulated responses along the circumferential centerline of the tire are shown in Figure 4.7. In this case, decay along the circumferential direction is captured and agrees well with the experiments. Especially, since larger decay is observed for higher frequencies. However, experiments show a larger decay and the model tends to overpredict the response for the furthest locations away from the excitation. This could be attributed to the fact that the model uses constant modal damping for all cut-on modes, however, in reality, this could not be the case.

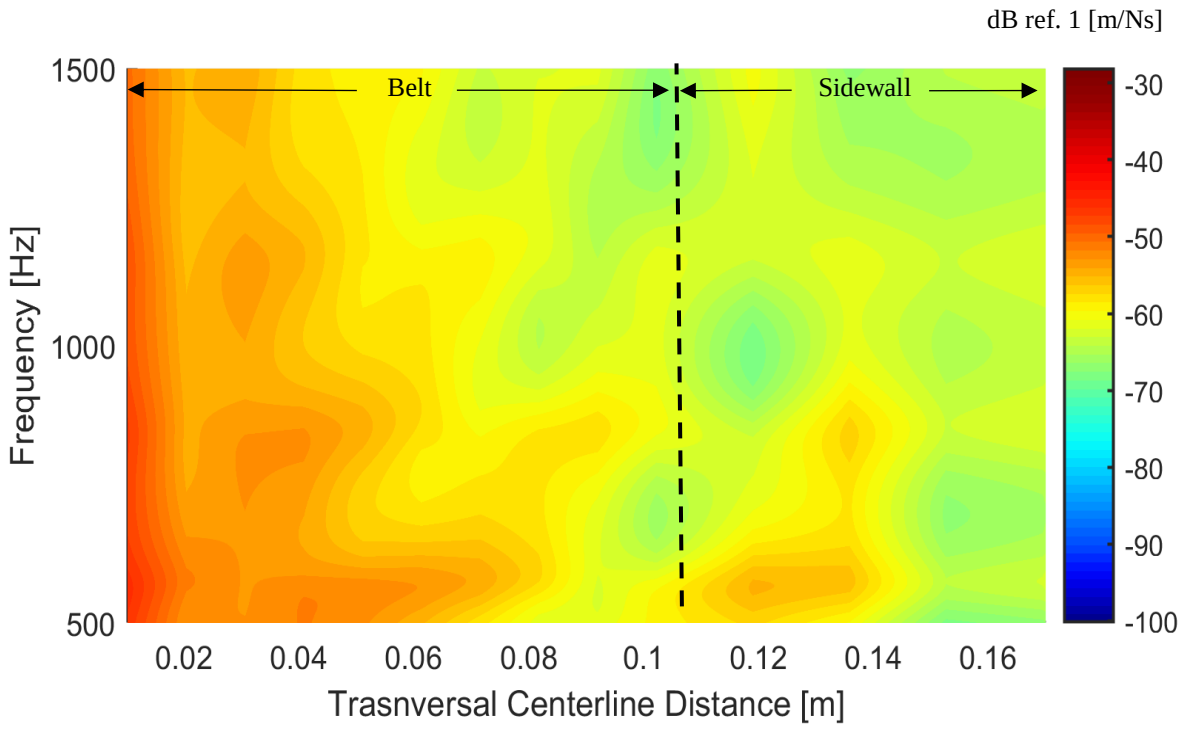

Figure 4.6. Simulated mobility FRF along the center transversal line for a tire of size 225/45R17

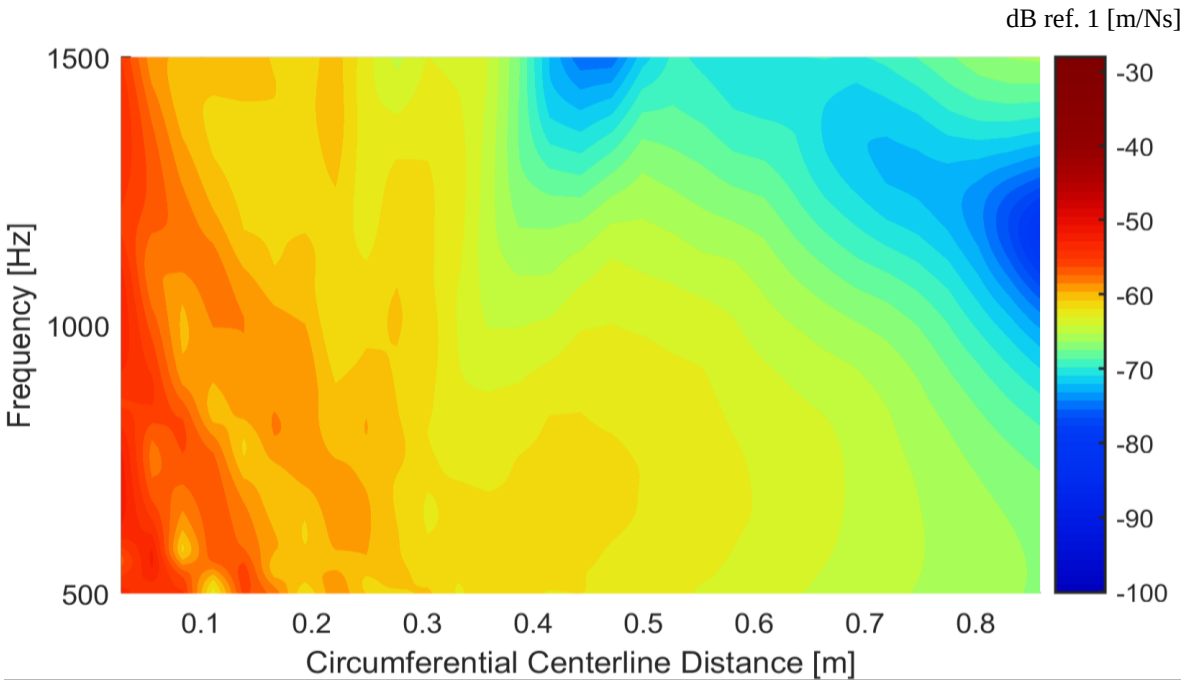

Figure 4.7. Simulated mobility FRF along the center circumferential line for a tire of size 225/45R17.

Further comparison of measurements and simulations are performed by selecting 5 points along the transversal direction of the tire and comparing their individual spectrum. These results are shown in Figure 4.8. In this case, the distance along the transversal centerline is specified above each one of the plots in Figure 4.8.

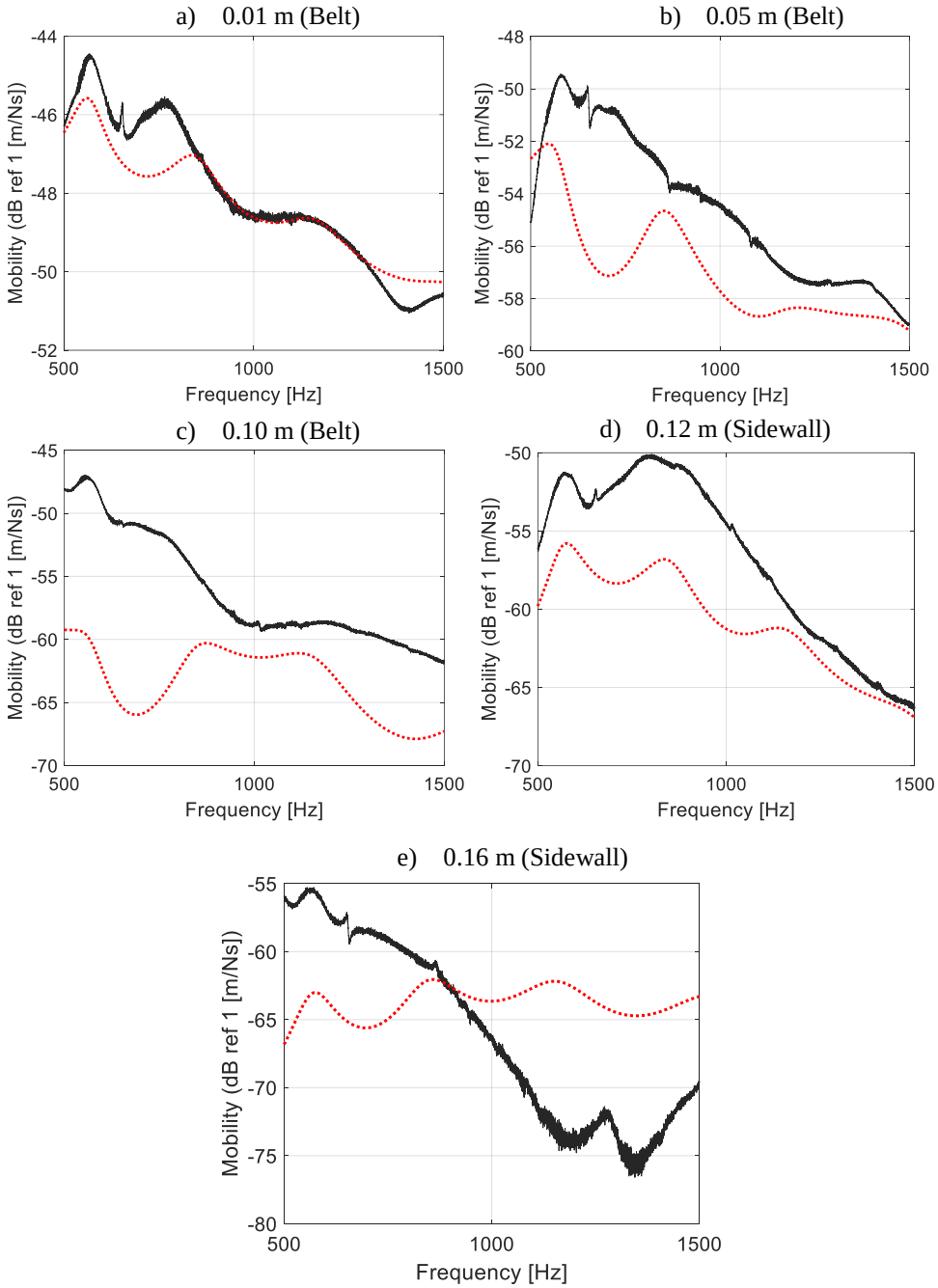

Figure 4.8. Mobility FRF for 5 points along the transversal centerline of the tire. Solid line corresponds to measurements while the dotted line corresponds to predictions.

The results shown in Figure 4.8 suggest that while predictions are the most accurate between 800 Hz and 1300 Hz, for the lowest frequencies the model tends to underpredict the tire's response along the transversal direction. This suggests that damping for the low frequencies is less

prominent. Still, for most of the cases, the predicted response curves have similar decaying trends as the measurements, except at the furthest distance from of 0.16m, which is the closest to the sidewall-rim edge. In this case, the response was overpredicted for the highest frequencies.

On the other hand, the individual spectrum for measurements and simulations were also compared along the circumferential direction of the tire. These results are shown in Figure 4.9. In this case, it can be observed that the model performs well for points closest to the excitation location. However, as points further away from it are selected, it can be clearly observed that the model tends to overpredict the tire's response, especially at high frequencies above 1200 Hz. This phenomenon was also be observed in Figure 4.5 is compared to Figure 4.7. This could be because of two reasons. First, the experimental results suggest that damping grows as frequencies become higher. However, the model accounts for only a constant loss factor for all frequencies. Second, since the sidewall mobilities appear to be more accurate than those of the belt, it could be argued that a more careful selection of modeling belt structural parameters such as stiffnesses should be selected. These two improvements are suggested for future work in order to improve accuracy of the model. Finally, it should be noted that for higher frequencies and points further away from the excitation location, the measurements' signal to noise ratio is very low. This could also introduce some uncertainty in the measurements. Still, the model provides very good estimates of the tire's response.

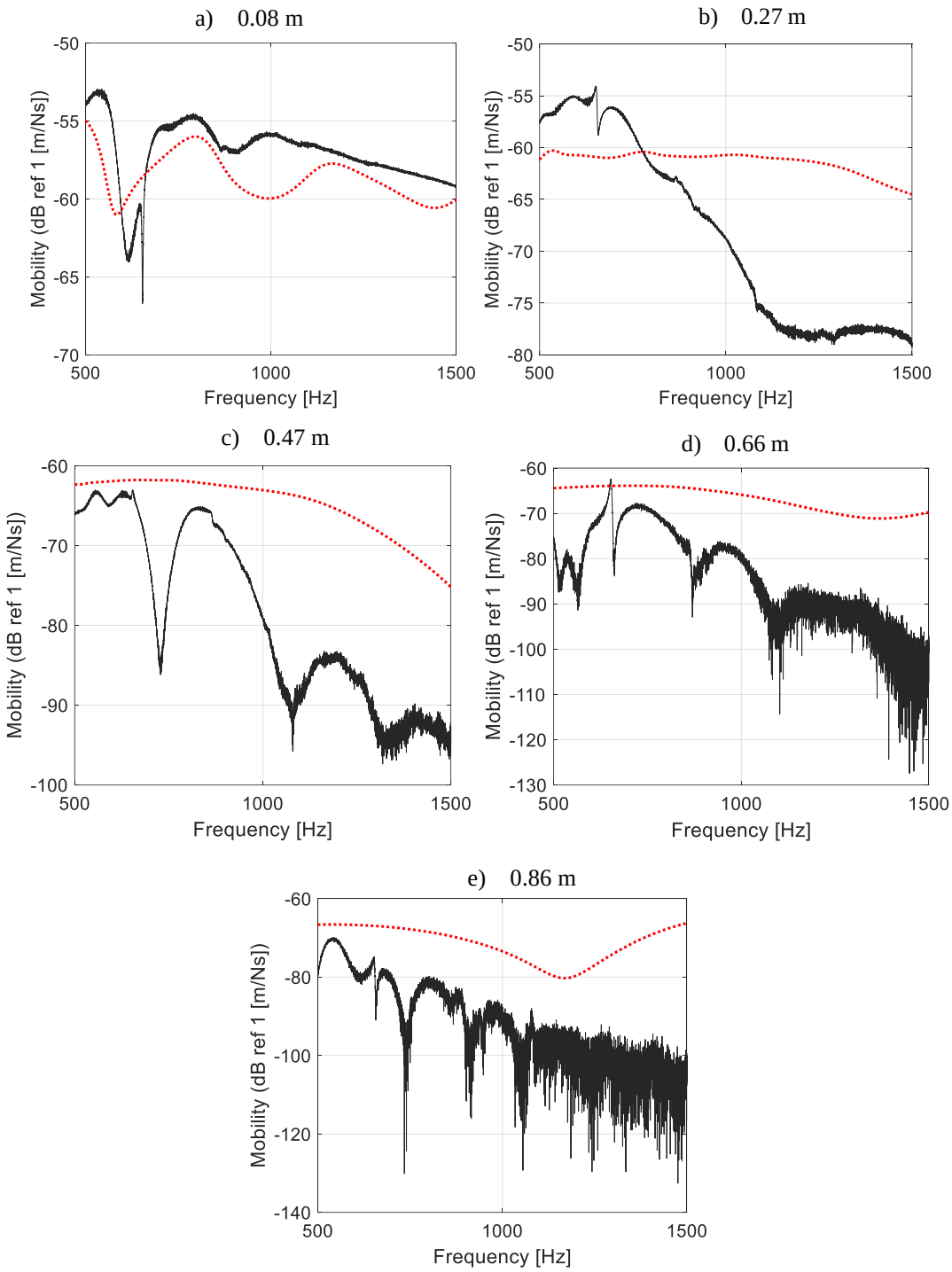

Figure 4.9. Mobility FRF for 5 points along the circumferential centerline of the tire. Solid line corresponds to measurements while dotted line corresponds to predictions.

In order to further analyze the response of the tire, the spatially averaged mean square value mobility FRFs were computed as follows

$$M_{MSV}(f) = \frac{1}{N}\sum_{i}^{N}\frac{|M_i(f)|^2}{2} \tag{4.1}$$

where, $|M_i(f)|$ corresponds to the frequency-dependent absolute value of the mobility FRF at a point i on the tire's surface and N corresponds to the total amount of points selected on the tire's surface. The mean square value mobility FRFs computed with equation (4.1) is a simple metric that provides an overall view of the tire's response. For example, Figure 4.10 shows the predicted M_{MSV} for the tire used in the experiments.

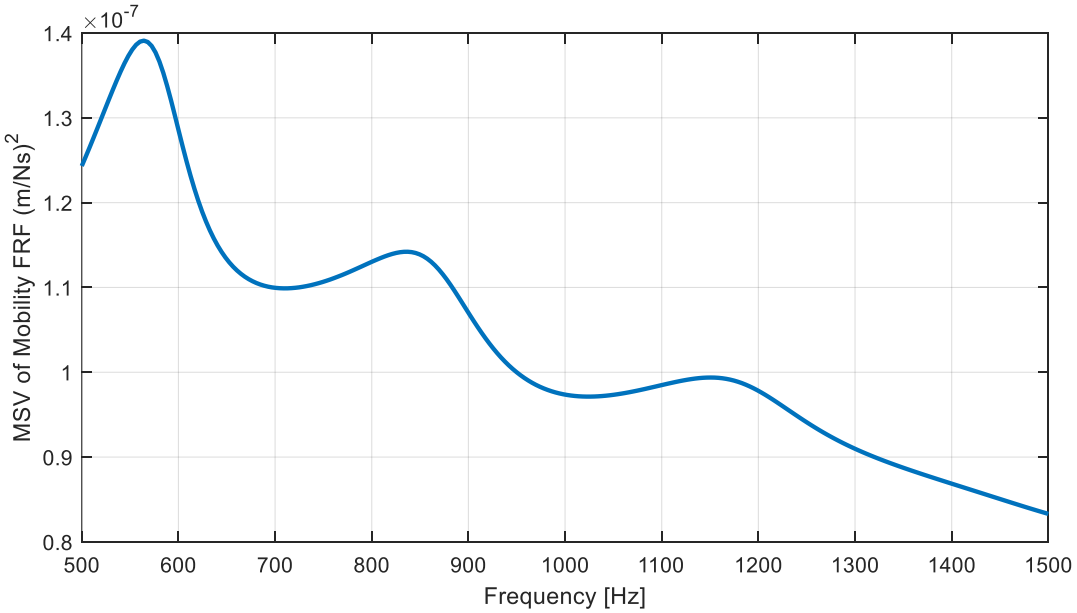

Figure 4.10. Predicted M_{MSV} for a tire of size 225/45R17.

The M_{MSV} can be computed separately for a set of points on the belt and a set of points on the sidewall. The selected points correspond to a set of 72 points on the sidewall of the tire and 71 points on its belt. These are the same points marked for experiments, shown in Figure 4.1.

Therefore, experimental and prediction results can be compared. The resultant predicted and measured M_{MSV} for the belt are compared in Figure 4.11a. On the other hand, the resultant predicted and measured M_{MSV} for sidewall are compared in Figure 4.11b.

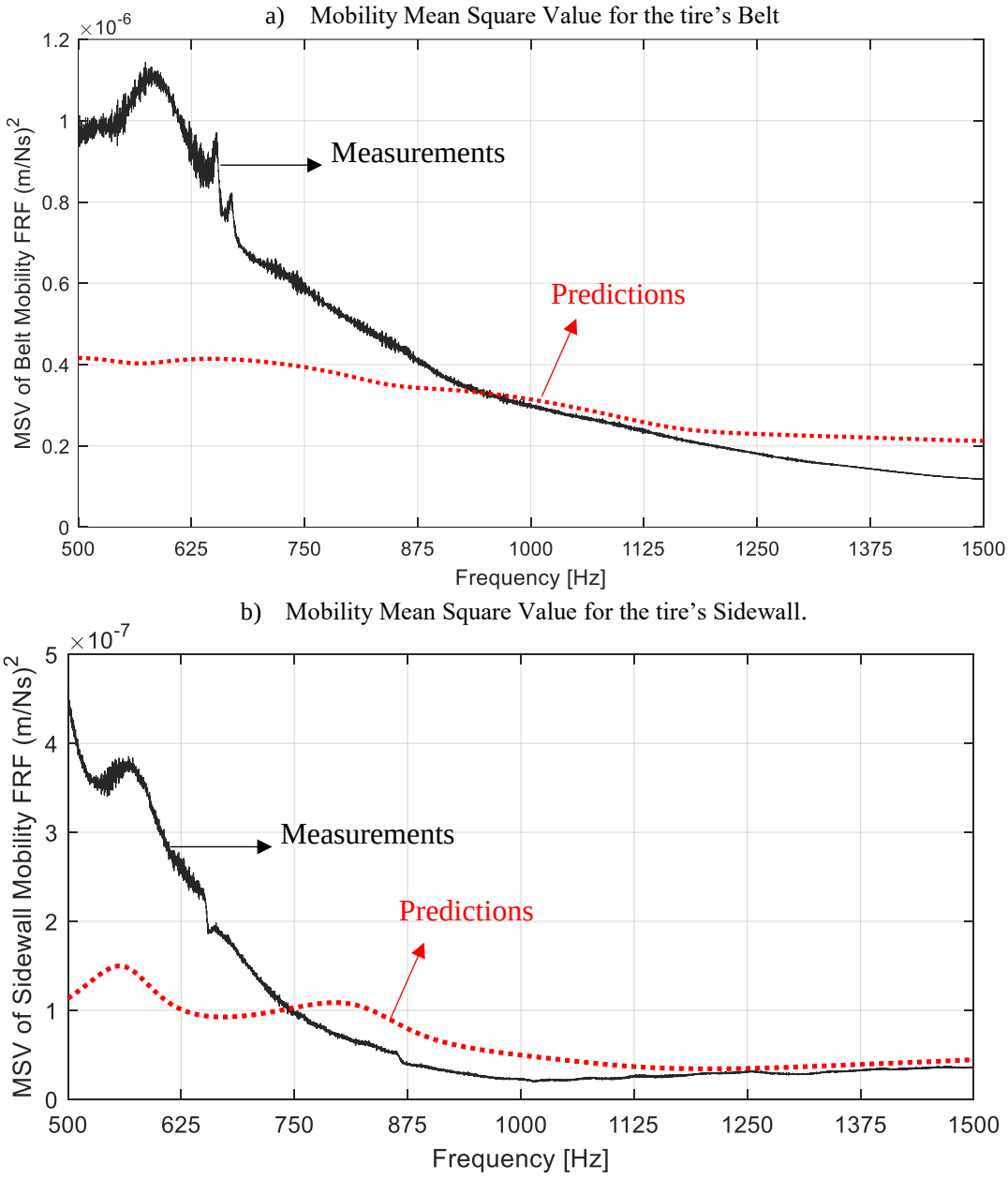

Figure 4.11. M_{MSV} validation for a) the tire's Belt and b) the tire's Sidewall (tire size 224/45R17).

It can be observed that predictions are the most accurate over most of the frequency range of interest, especially above 750 Hz through 1500 Hz for both the sidewall and the belt. In this case, the belt vibrates with higher amplitudes than the sidewall.

4.2. Tire Noise Validation

Experimental results for tire noise are very limited in open literature. Mainly because accurately measuring the noise produced by the tire is a challenging task. In addition, most of the work found in open literature focuses on the low-frequency range, i.e. below 500 Hz. Still, a good source of experimental work was found in the work by Yum et al. (2006).

In this section, the experimental data provided in the work by Yum et al. (2006) is used for validations. In this case, the noise was measured using microphones located at 5 cm away from the tire belt circumferential centerline, as shown in Figure 4.12a. All measurements were performed inside a semi-anechoic room using the set-up shown in Figure 4.12b. The tire was separated by 1 mm from the tire ground to avoid transferring vibrations from the tire to the ground. The tire was excited with a shaker Bruel and Kjaer type 810 electrodynamic shaker located below the ground. An input force amplitude of 1 N was applied for all frequencies. Two stingers with a PCB 208A03 force transducer was used to excite the tire and measure the input forces. All the measurements were performed using a tire of size 205/70R14 inflated at 30 psi.

a) Location of noise measurements

b) Experimental set-up

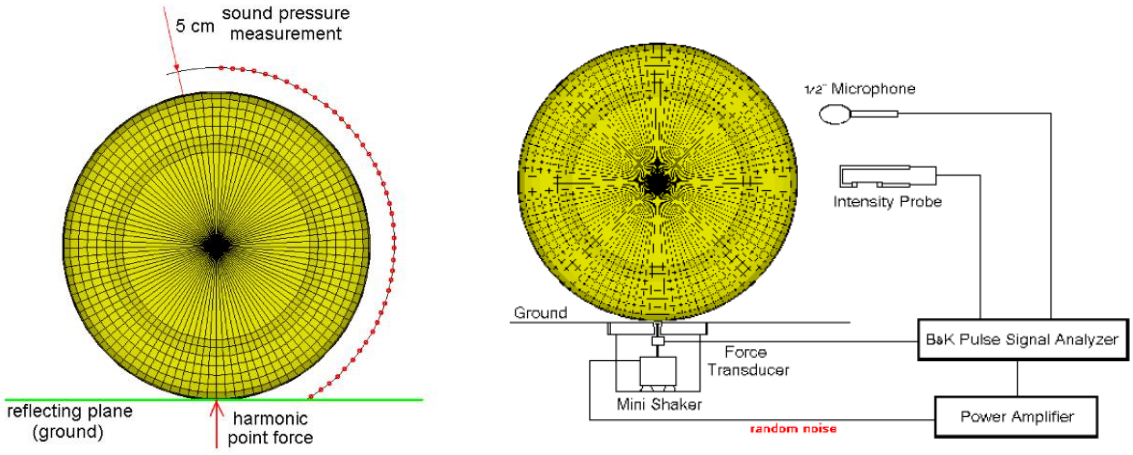

Figure 4.12. a) Location of noise measurements and b) experimental set-up performed by Yum et al. (2006).

On the other hand, noise predictions were computed by using a Boundary Element Method (BEM). The implemented mesh and set of 40 field points located at 5 cm away from the tire's mid-tread-band line are shown in Figure 4.13. In addition, 15 chief points located within the tire's surface. In addition, the ground surface was assumed a rigid boundary; thus, the reflected component was also accounted in the simulations using an image source. Further details on how the mesh is constructed and regarding the implemented BEM code are given in Chapter 5.

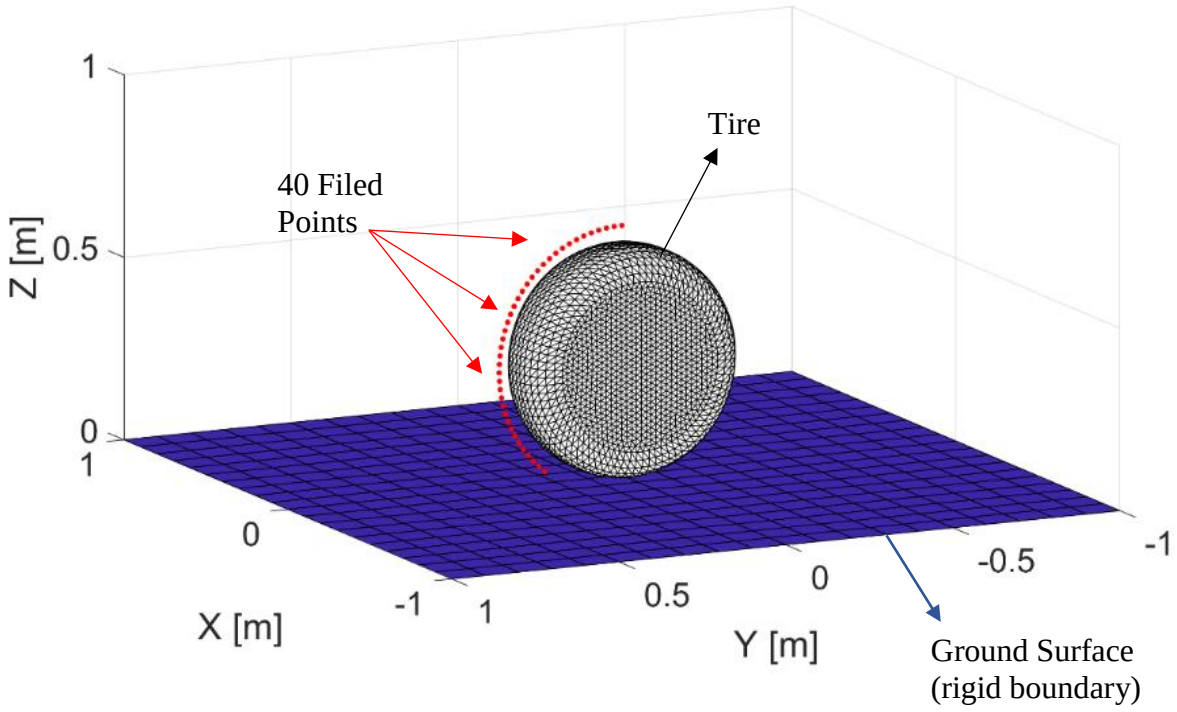

Figure 4.13. Field points for noise measurements of tire on top of a rigid surface.

The measured noise obtained from these experiments is shown in Figure 4.14a. It can be observed that the highest noise levels are located close to the excitation location. That is, approximately around 35 degrees form the input force location. Decay is very prominent above 1,100 Hz. On the other hand, it can be observed that between 500 Hz and 1,000 Hz noise decays at specific combinations of frequency and circumferential location. Still, decay is not as prominent within this range. Finally, in the lower frequency range below 500 Hz, the produced noise is induced by the modal vibratory behavior of the tire.

For comparison purposes, the predicted results are shown in Figure 4.14b. In this case, it can be observed that outside of the intended range of interest (below 500 Hz), predictions are not accurate. The reason is that the wave propagation approach assumes waves instead of modes along the circumferential direction of the tire. The low-frequency response is dominated by the tire's resonances. Within 500 Hz and 1000 Hz, Figure 4.14b shows that that the decay along the

circumferential direction is not as prominent as for higher frequencies. Similar behavior can be observed for the measurements in Figure 4.14a, however predictions show more decay than the experimental results. Finally, for high frequencies (above 1000 Hz), decay is very prominent for both cases. Finally, it should be noted that the noise level range for both simulations and experiments are similar. Thus, indicating that the modeling approach is capable of predicting vibration-induced tire noise with acceptable accuracy.

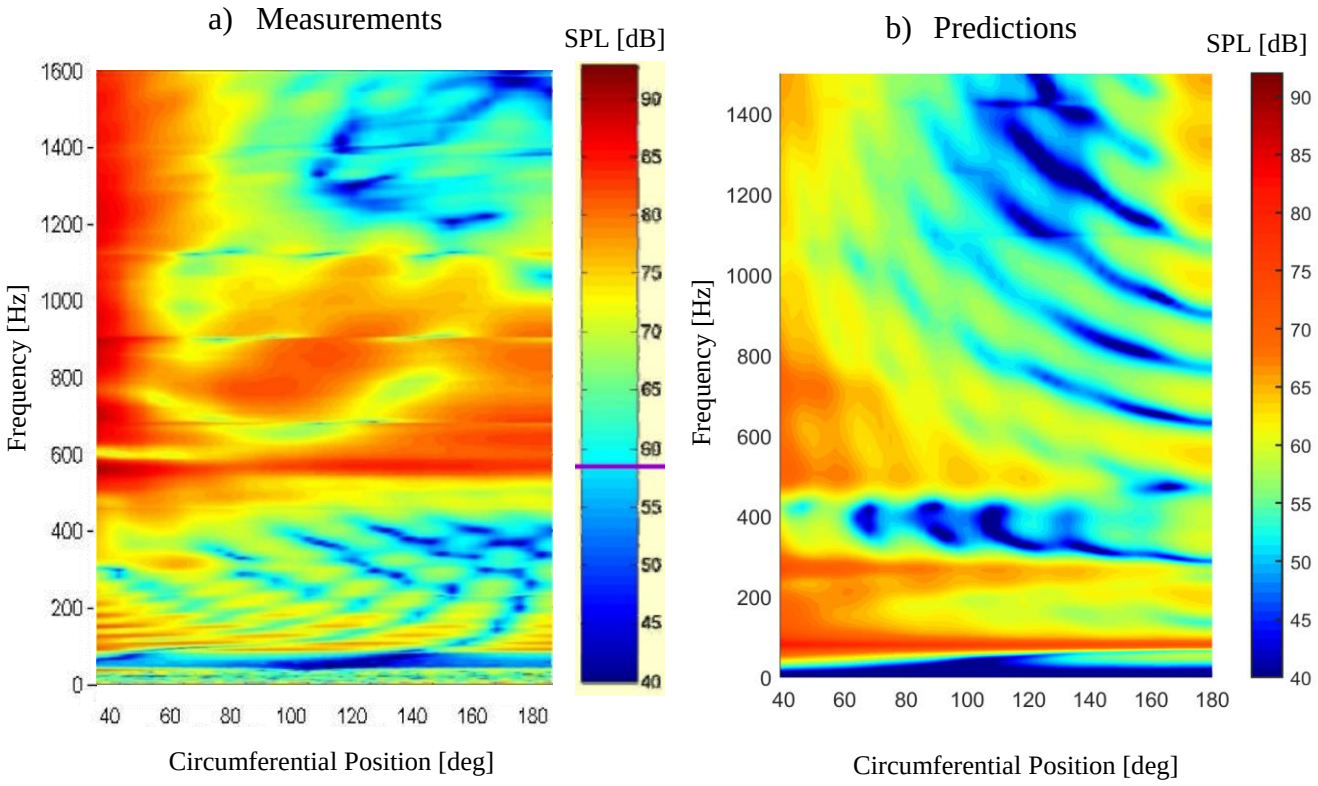

Figure 4.14. Noise around a tire of size 205/70R14: a) measurements provided in the work by Yum et al. (2006) and b) noise predictions.

5. TPIN Prediction Tool (WavePro Tire)

The aim of this chapter is to provide the details on how the structural tire model and the contact models presented in the previous sections are implemented within a single tool that predicts TPIN. This computational tool has been developed in Matlab and is named WavePro Tire. Furthermore, in this chapter main results computed with WavePro Tire are presented.

5.1. Structure of WavePro Tire

A schematic of the main structure of WavePro Tire is shown in Figure 5.1. The tool has four main inputs, shown at the left-hand side. The main inputs are tire size parameters, rotational velocity, main structural parameters, and the tread pattern. On the other hand, the outputs are shown on the right-hand side. That is, the TPIN produced by the vibratory response of the tire at any arbitrary location around the tire and user-defined frequency.

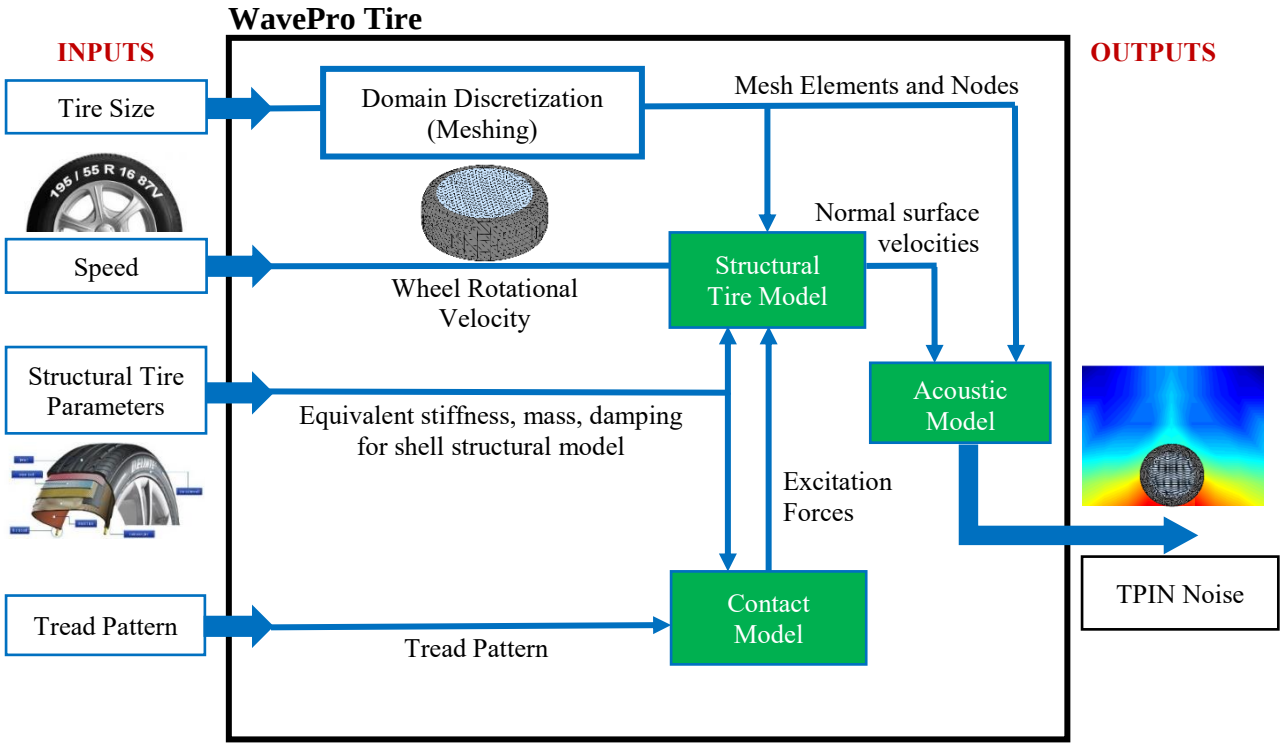

Figure 5.1. Diagram of WavePro Tire.

The main tool is sketched within the center black box of Figure 5.1. It can be observed that it contains three main modules highlighted in green. The first one is the structural tire module which is capable of implementing any of the structural models presented in Chapter 2, specifically equations (2.80), (2.81) and (2.82). The second one is the contact model that computes the excitation forces as presented in Chapter 3. Finally, the third one is the acoustic module that implements a Boundary Element Method (BEM). This code computes the noise produced by the tire's normal surface vibrations. It should be noted that the BEM code implemented in this tool is simply a modified version of the code provided in the work by Wu (2000).

As shown in Figure 5.1, one of the most important tasks that WavePro Tire performs is to appropriately characterize the tire's geometry and discretize it into an appropriate number of elements. In order to achieve this, the transversal geometry of the tire is approximated by its carcass ply shape. The model developed by Kounty (2007) provides a very good approximation of this, as shown in Figure 5.2. In this case, the typical cross-section of a tire is shown. The curve $f(r)$ in red denotes the curve that follows its carcass ply for the top part of the tire's cross-section.

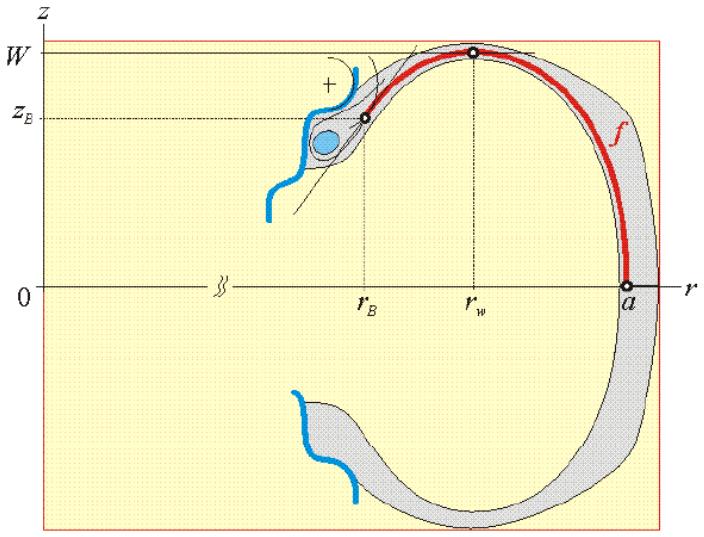

Figure 5.2. Typical transversal geometry of a tire and curve that follows the carcass ply in red (Kounty, 2007).

The carcass ply curve is defined in the r-z plane, where the r-direction denotes the radial direction of the tire and the z-direction is defined along its width. Three points are needed in order to compute $f(r)$. The first point is (r_B, Z_B), where r_B is approximated with the rim diameter and Z_B with the rim's width. The second point is $(a, 0)$, where a is the maximum radius of the tire, estimated as follows

$$a = r_B + 2 \times AR \times TW \tag{5.1}$$

where AR is the tire's aspect ratio and TW is the tire's section width. Finally, the third point required by the model is (r_w, W), where $W = TW/2$ and the radius r_w is approximated with the following equation

$$r_w = \frac{a\left(\frac{r_B}{a} + \sqrt{1-\left(\frac{Z_B}{W}\right)^2}\right)}{1+\sqrt{1-\left(\frac{Z_B}{W}\right)^2}} \tag{5.2}$$

The carcass ply curve $f(r)$ is then calculated as follows

$$f(r) = Z_B + \int_{r_B}^{r} \frac{\sin\theta(u)}{\sqrt{1-\sin^2\theta(u)}} du \tag{5.3}$$

Where the sinusoidal function can be approximated as

$$\sin\theta(u) = \frac{\left(u^2 - r_w^2\right)}{\left(a^2 - r_w^2\right)} \tag{5.4}$$

Equations (5.1) through (5.4), show that by simply defining a set of geometrical parameters the carcass ply curve of the tire can be estimated. The main geometrical parameters required by the code are shown in Figure 5.3. Figure 5.3a shows those parameters defined by the conventional tire size definition, while Figure 5.3b shows an additional parameter required from the rim, that is the rim width.

a) Conventional Tire Size Parameters

b) Additional Rim Parameters

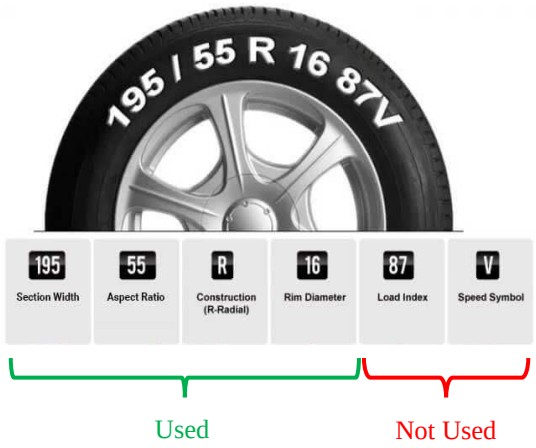

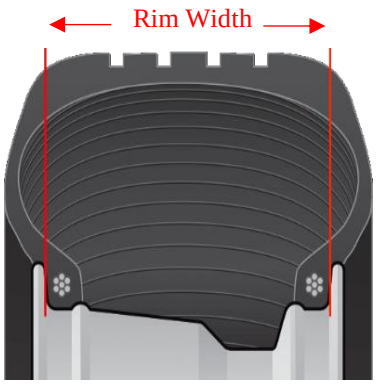

Figure 5.3. a) Conventional tire size parameters used in WavePro Tire (image retrieved from https://tyres.cardekho.com/news/how-to-read-a-tyre/) and b) additional rim parameters (image retrieved from https://www.discounttire.com/learn/tire-dimensions).

An example of the carcass ply curve of a tire is shown in Figure 5.4a. This shows the carcass ply curve for a tire of size 245/55R18, attached to a rim of 8 in width. If the carcass ply curve is revolved around the rotational axis of the tire, then a mesh can be constructed. Figure 5.4b shows an example of the mesh constructed for this tire. In addition, it can be observed that meshes for the rim surfaces have also been created. In this example, the mesh contains a total of 5,000 nodes and 10,000 elements with an average element size of 1.3 cm. The mesh is used in the structural and acoustic models of WavePro Tire. For the structural model, only the nodal locations are used. This is where the response of the tire is computed. On the other hand, for the acoustic model both the nodes and the connectivity the corresponding connectivity matrix are required by the BEM code.

It is important to note that an appropriate element size should be chosen depending on the frequencies of interest intended for simulations. It is recommended that the average size of the elements is ten times smaller than the acoustic wavelength at the maximum simulated frequency. For example, the wave propagation approach in this research is intended for predictions at a maximum of 1,500 Hz. At this frequency, the acoustic wavelength is approximately 23 cm. This means that the average size of the elements in the mesh should be 2.3 cm or lower in order to accurately capture the response at 1,500 Hz. Thus, the example mesh shown in Figure 4.4b is suitable for all simulations.

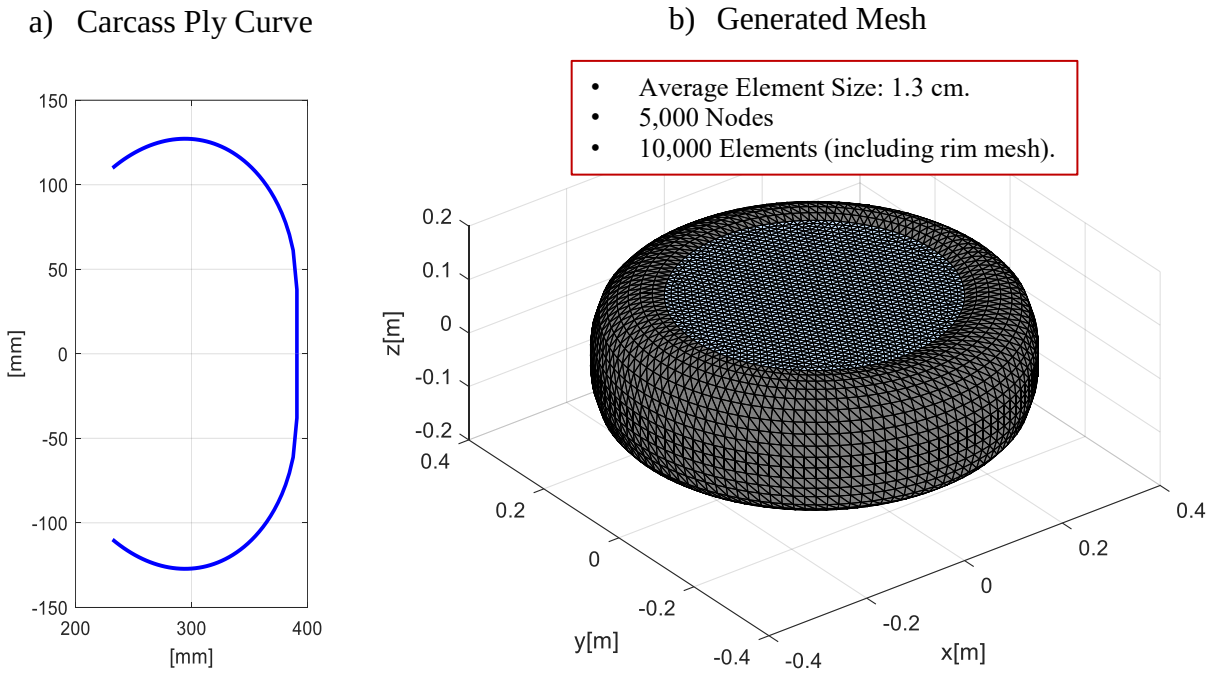

Figure 5.4. Example of a) Carcass ply curve for a tire of size 245/55R18 attached to an 8 in diameter rim and b) Created mesh containing 5,000 nodes and 10,000 elements.

Once the structural response is calculated for a specific tire on all the nodes of its mesh, the induced noise is computed using the BEM code implemented in the acoustic module. The BEM code solves the acoustic Helmholtz integral equation for an unbounded exterior domain V, as shown in Figure 5.5. A vibrating surface S that produces noise is located within the domain and is surrounded by

a far-field boundary surface S_R. The acoustic pressure at a point within the domain is therefore calculated as follows

$$p(P) = -\int_S \left(i\rho\omega v_n G \right) + p_n \left(\frac{\partial G}{\partial \vec{n}} \right) ds \tag{5.5}$$

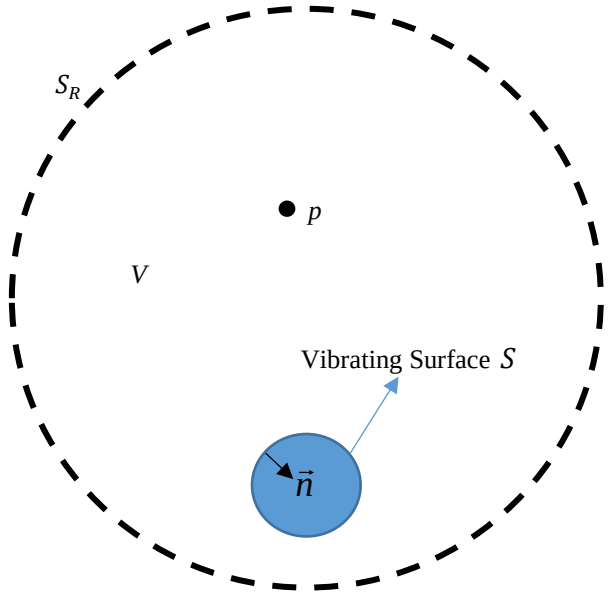

Figure 5.5. Point *P* located in an excluded exterior domain V.

Green's second identity is used to find equation (5.5) (Wu, 2000). In this case, $p(P)$ corresponds to the acoustic pressure at the point p. On the other hand, ρ corresponds to the domain's density, ω is the frequency, v_n is the vibrating surface's normal surface velocity and p_n is the pressure at its boundary. Finally, G is the generalized acoustic Green's function.

The vibrating normal surface velocity v_n is computed using equation (3.19). In this case, the tire is excited by the blocks impacting the pavement in the contact patch area. These forces are then

multiplied by the mobility FRF of the desired structural model. That is, with either equation (2.26), equation (2.32), or equation (2.73).

Since only one boundary condition is specified i.e. the normal surface velocity v_n, the additional boundary condition p_n needs to be found. In order to do this, equation (5.5) is first solved by collocating the point p on the vibrating surface and finding the pressure boundary condition p_n. Once this has been done, the acoustic pressure at any arbitrary point in the domain can be computed. The approach to integrate equation (5.5) is to discretize the boundary of the vibrating surface into elements and numerically find a solution. Therefore, if the response of the tire is computed in a mesh such as that shown in Figure 5.4, the BEM code can be implemented.

Finally, it should be noted that the code provided by Wu (2000) has been modified. This has been recompiled to 64-bits and now the tire meshes of up to 15,000 elements can be used. In addition, up to 15,000 points around the tire can be used for near field and far field predictions.

In the next section, simulations performed with WavePro Tire will be provided. Structural tire responses and their corresponding noise predictions will be presented. The objective is to provide further physical insight and understanding of the tire's response.

5.2. Noise and Vibrations Simulations

In this section, results for the structural response of the tire are presented for several cases. This includes an examination of the simulated harmonic response of the tire, a sensitivity analysis, and finally noise results simulated for a treaded tire.

Tire Harmonic Response

In order to demonstrate the wave propagation behavior for the structural models proposed in Chapter 2, simulated harmonic response results are presented in this section. Figure 5.6 shows a snapshot of an unwrapped tire's harmonic response. Three cases are shown, the first one

corresponds to Kropp's model while the other two correspond to uniform and non-uniform infinite plate models. All simulations show the response for an input point force located at the center of the tire. The selected frequency is 1200 Hz and the input amplitude F_0 =1 N. A tire of size 245/55R18 is used and a loss factor of 7% is implemented, as suggested by Perisse et al. (2000). In addition, an inflation pressure of 30 psi has been selected and the structural properties presented in Table 2.1 are used for predictions.

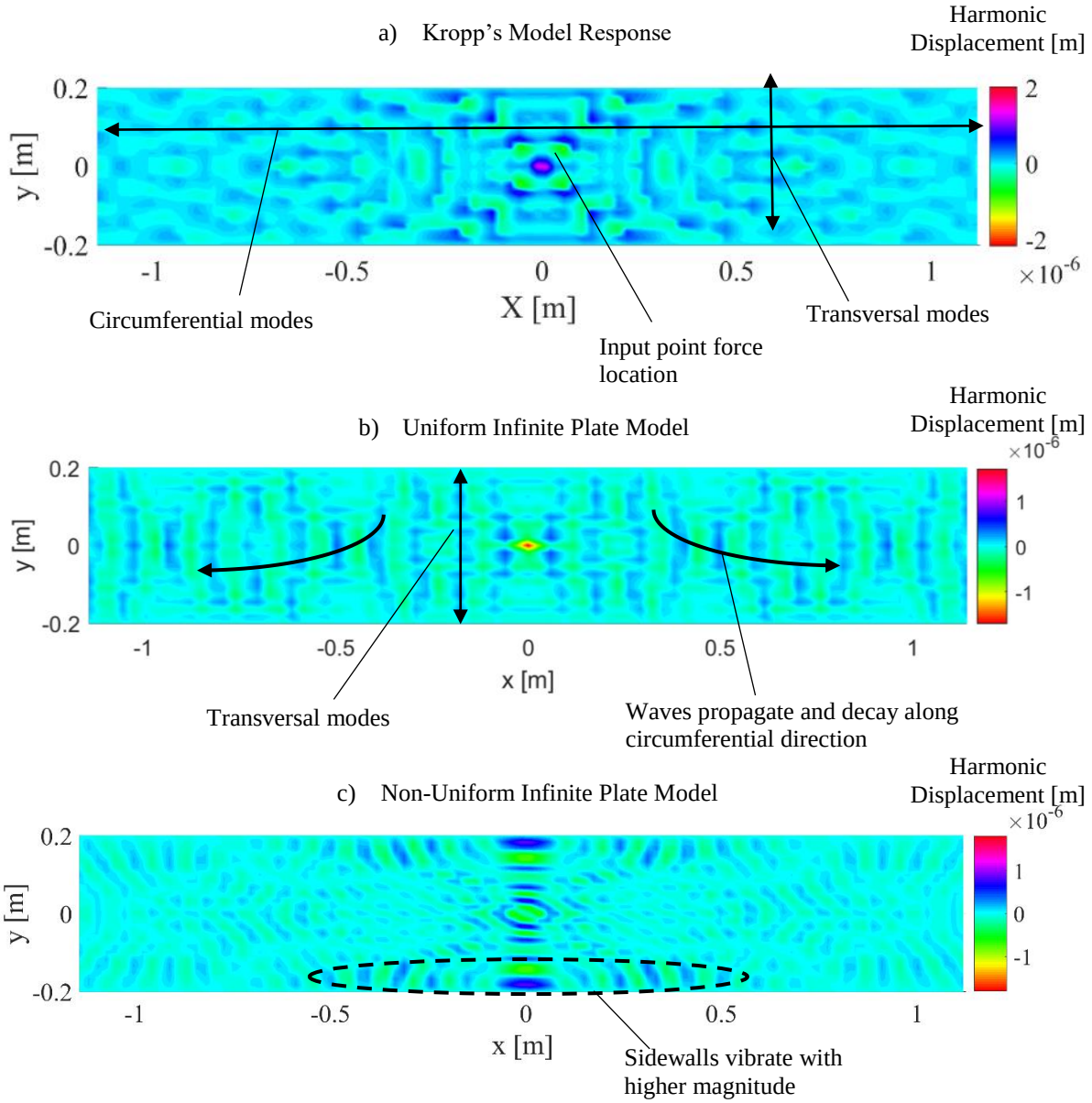

Figure 5.6. Harmonic response snap-shot by exciting the tire at the center of the tire belt, for solution found with a) Kropp's model, b) infinite plate model (uniform properties), and c) infinite plate model (non-uniform properties).

Figure 5.6a shows the harmonic response obtained with Kropp's approach. The modal behavior in both the transversal and circumferential tire directions can be observed. On the other hand, the wave propagation approaches in Figure 5.6b and Figure 5.6c show a different behavior that consists of decaying and propagating waves along the circumferential direction. In this case, there is a set of transversal modes that are cut-off. These decay along the tire's circumferential direction. Another set of transversal modes are cut-on and propagate freely along the circumference of the tire. Additional decay is also present for all waves and is accounted for in the model with the introduced modal damping loss factor.

It should also be noted that the response of the tire is different for the uniform and the non-uniform case. The average mass per unit area of the uniform case is equal to that of the non-uniform one. In the latter, the sidewalls vibrate with higher amplitudes than the belt. Similar results are expected for the entire frequency range within 500-1500 Hz. This behavior is consistent with the experimental results presented in the work by Yum et al. (2007). However, this behavior is subject to change depending on the properties of the tire. It can also be observed that the displacement amplitudes predicted with Kropp's approach are higher to the wave propagation approaches. This indicates that Kropp's model tends to overpredict the response of the tire. This problem can be averted with modifications to Kropp's model, as shown in the work by Perisse et al. (2000).

The same inputs as for the plate models above can be used for the cylindrical shell model. The harmonic response for this case is shown in Figure 5.7. In this case, non-uniformities along the transversal direction of the tire are clear as well. The response is higher for the sidewalls, as expected. However, the decay for both sidewalls and its belt is more prominent if compared to the infinite plate model. The sidewall response amplitudes decay very close to the vicinity of the excitation, unlike the non-uniform plate. In addition, it can be observed that the amplitude levels are higher than for the plate models. This difference could be because the cylindrical shell model requires additional structural parameter inputs and appropriately tuning them in the model is a challenging task. Finding appropriate methods to accurately obtaining all the required input parameters for this model should be addressed in the future.

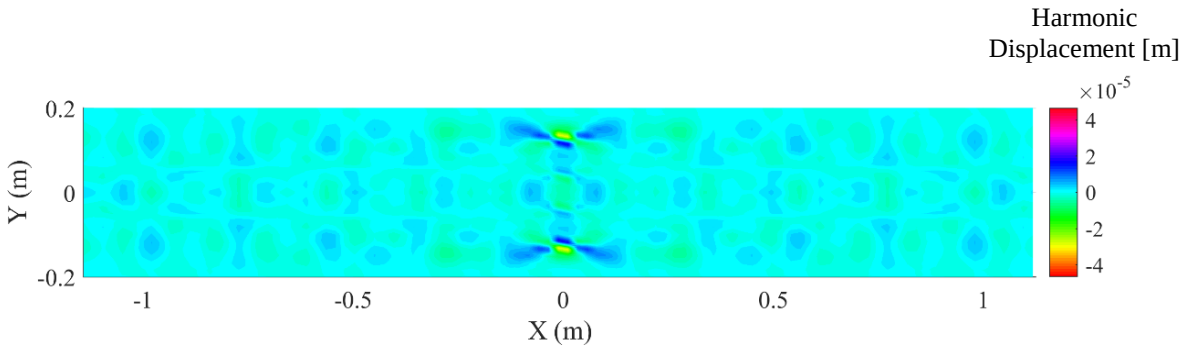

Figure 5.7. Harmonic response snapshot obtained with the cylindrical shell model for a tire of size 245/55R18.

The effects of tire rotation can also be analyzed using harmonic response simulations. Figure 5.8 shows an example of the response for a rotating tire. In this case, a harmonic response snapshot for a tire of size 225/45R17 is shown. These results were obtained using the non-uniform moving plate model presented in Chapter 2. The response has been simulated for a total of 2,800 points on its surface. The frequency is 1250 Hz and interval of wavenumbers from -2000 to 2000 [1/m] was used to perform the inverse wavenumber transform integration.

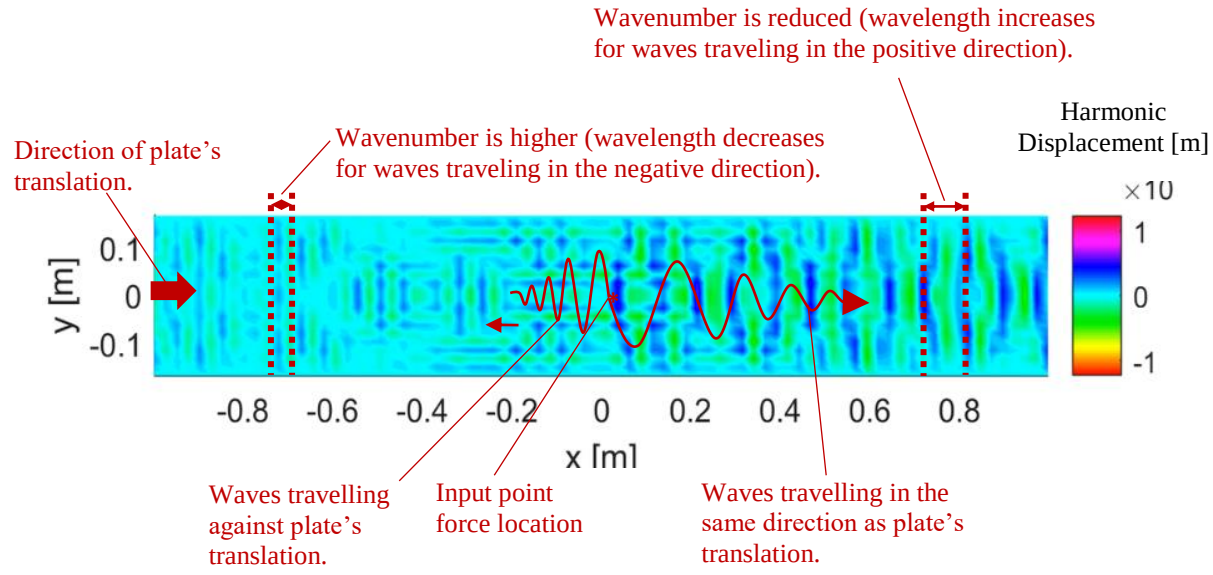

Figure 5.8. Uniform infinite plate tire model response with a traveling speed of 32 m/s for a tire of size 225/45R17. This tire is inflated at 30 psi and the response is for a frequency of 1250 Hz.

A total of 70 transversal modes were implemented for the moving plate. The velocity of the traveling plate was set to 32 m/s (equivalent to a vehicle traveling at 70 mph) and is inflated with a pressure of 30 psi. The infinite plate uniform structural properties specified in Table 2.1 were used in this case. Finally, an input point force located at the center of the with an amplitude of 0.2 N was implemented for this simulation. The moving plate results in Figure 5.8 show that waves traveling in the positive x-direction have a larger wavelength. These waves travel with higher velocities since they travel in the same direction as the rotation of the tire. On the other hand, waves traveling towards the negative x-direction have smaller wavelengths. These waves travel slower since they travel against rotation. These results were expected, as indicated dispersion analysis performed in Chapter 2.

Further comparison of the behavior of a static and a rotating tire is shown in Figure 5.9. In this case, the results for a rotating and non-rotating tire in a wrapped view i.e. the real geometry of the tire. The simulation inputs and conditions are the same as those presented for Figure 5.8. As mentioned above, the response for the rotating tire is the following. An increased wavelength size is observed for waves traveling in the same direction of rotation, while reduced wavelength size is observed for waves traveling against the rotation of the tire. For the static tire, the waves traveling in both circumferential directions are symmetric.

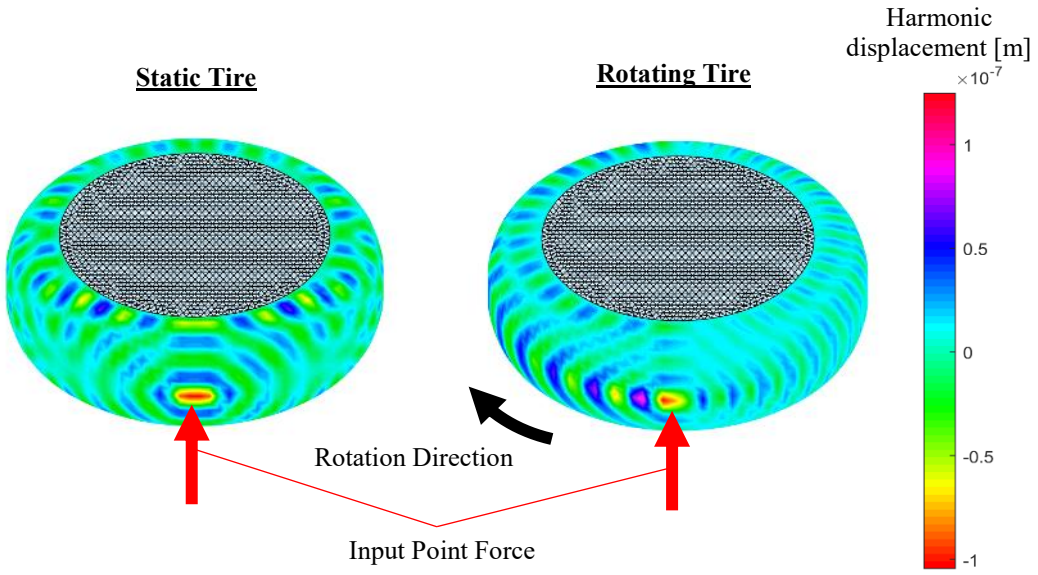

Figure 5.9. Wrapped tire view for comparison of rotating and non-rotating tire harmonic response.

Sensitive Analysis of Structural Response

In an effort to investigate how various parameters affect the behavior of the tire, several cases are analyzed using the non-uniform plate model, i.e. the structural model the shows highest accuracy. It should also be noted that all structural inputs including stiffnesses and mass per unit area are maintained unchanged for all the case below. These values are presented in Table 4.1.

First, the effect of damping is analyzed. Figure 5.10 shows simulated mobility FRFs compared to the experimental data. These mobilities are for a point located at 1 cm above the excitation location. In this case, multiple simulation cases are shown for 6 different frequency-constant loss factors. Some of the loss factors are unrealistically high e.g. >30%. For the range of 7% to 30% the model does not appear to be sensitive. Still, within the frequency range of interest (500-1500 Hz), results show that the simulation's accuracy is moderately dependent on the amount of damping used as an input to the model. Most of the work in open literature suggests that between 500 Hz and 700 Hz a loss factor below 7% should be used. Between 700 Hz and 1300 Hz, a loss factor of approximately 16% is suggested. In addition, the experimental results in Figure 5.10 show that above 1300 Hz damping increases. Techniques that accurately provide the frequency-dependent damping loss factors should be explored in the future in order to improve modeling capabilities. For the specific tire tested, a constant loss factor is chosen 16% since it shows the least error for the whole frequency range. This is the same value as suggested by Pinnington (2006a).

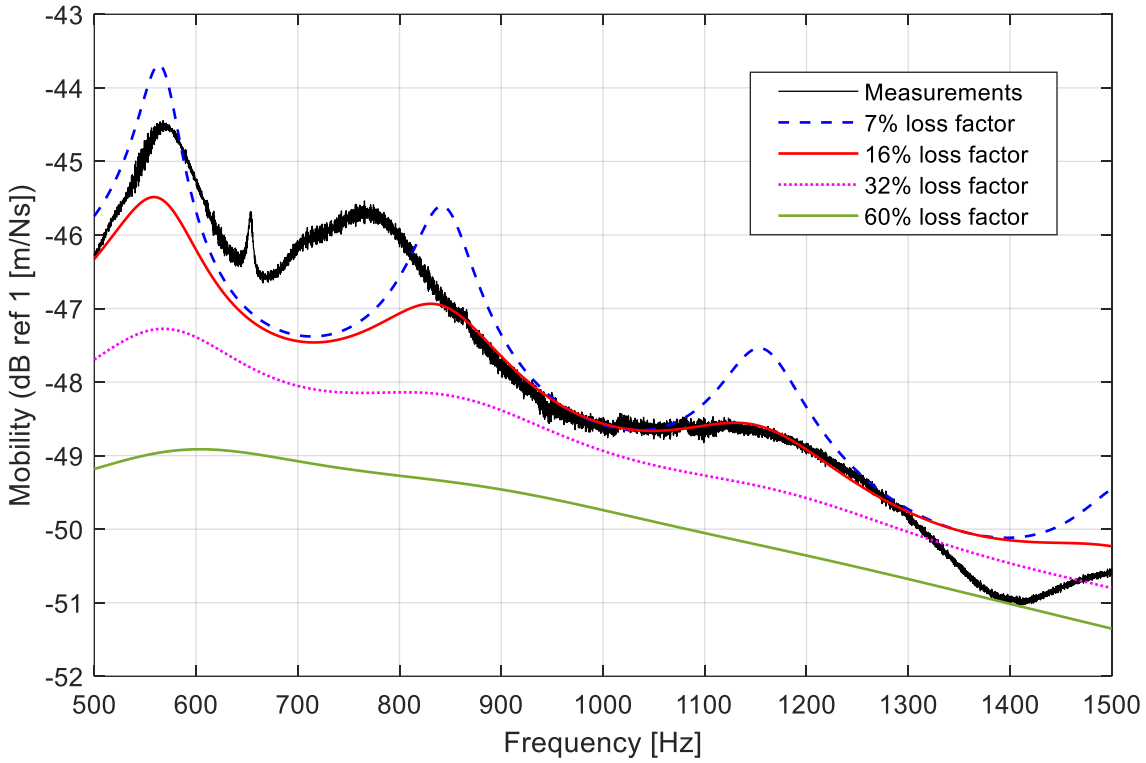

Figure 5.10. Experimental mobility FRF measured at 1 cm above the input location and compared to simulation results for various constant damping loss factor cases.

In addition to the effects of damping, the effects of inflation pressure are also analyzed. These are accounted with membrane tensions applied to the tire's structure. Figure 5.11 shows the measured (inflation pressure of 32 psi) and simulated responses for and inflation pressure of 24, 32 and 40 psi. Figure 5.11 shows that the changes in inflation pressure induce frequency shifts of the response. For example, there is a difference of approximately 150 Hz between the 24 psi and 40 psi inflation pressure response. This means that the inflation pressure terms should be included when the intention is to accurately model the tire's response. Still, the amplitudes of the response do not change much.

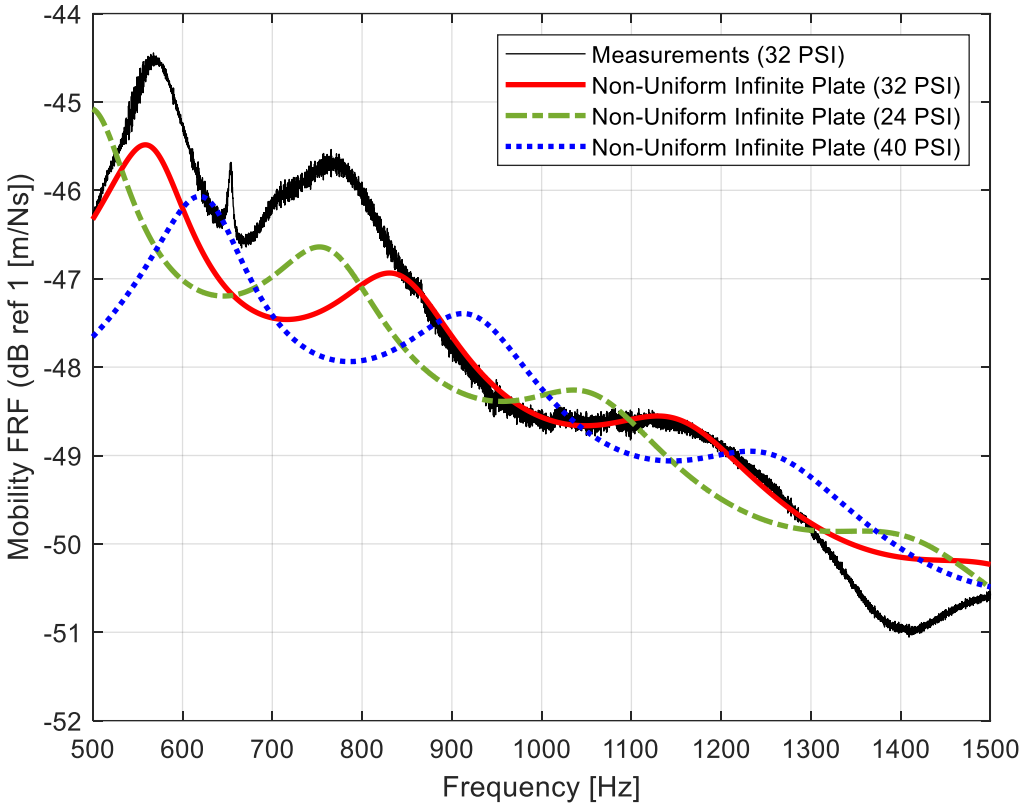

Figure 5.11. Mobility FRF for an inflated 225/45R17 tire with 24 psi, 32 psi, and 40 psi, and compared to measurements at 32 psi.

The effects on the tire's response due to changes in its geometry are also analyzed. As a reference, a tire of size 225/45R17 has been selected and its geometry changed for different study cases. The first case is shown in Figure 5.12 and consists on analyzing how aspect ratio changes affect the tire's input mobility FRF. In this case, the tire width was maintained constant at 225 mm and the rim's diameter at R17. The aspect ratio was defined between 0.35 and 0.65.

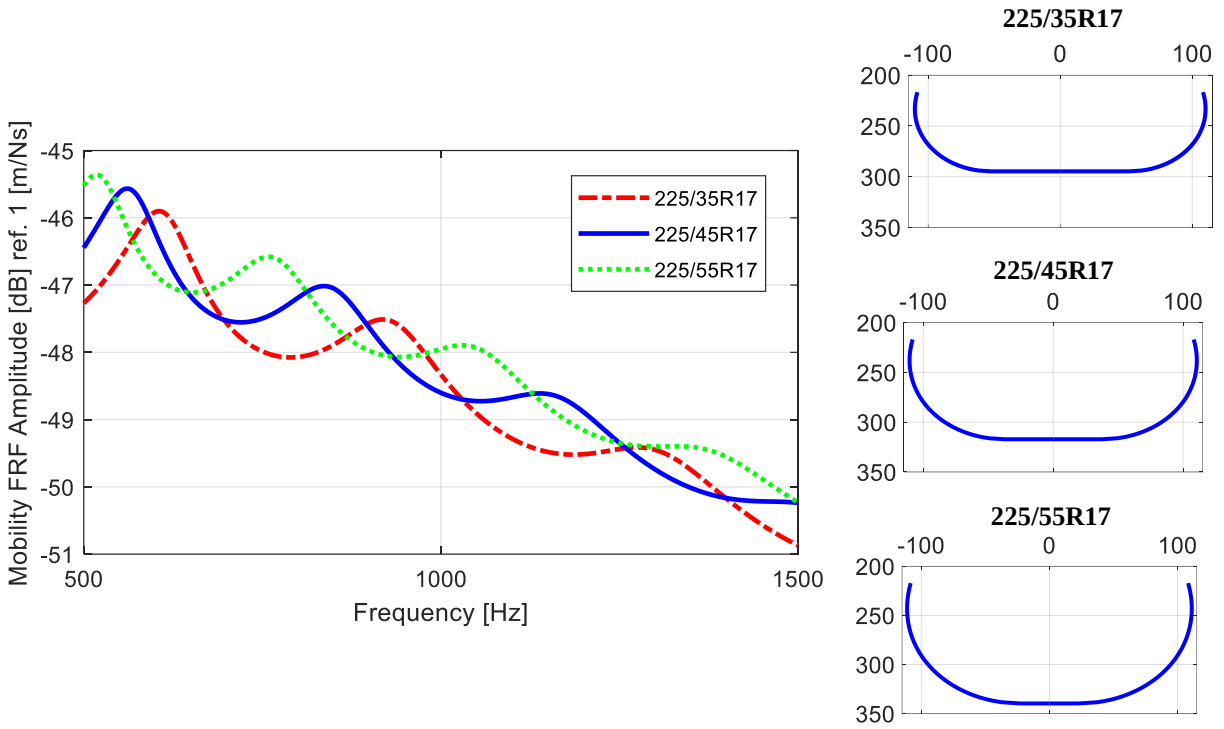

Figure 5.12. Input mobility FRF for the same tire with changing aspect ratio. Tire sizes are also shown for reference with all dimension in [mm].

Figure 5.12 shows that as the aspect ratio becomes higher, a frequency shift towards lower values is observed. In this case, a shift of 200 Hz is observed for an aspect ratio that changes between 0.35 and 0.65. Still, amplitudes do not appear to change much.

An additional case is shown in Figure 5.13. and consists in maintaining the tire's rim diameter at R17 and the aspect ratio at 0.45. The input mobility of the tire was then computed for a variation of the tire's width from 195 mm to 255 mm. In this case, the whole carcass width changes (belt width plus sidewalls length). It can be observed that the responses have similar amplitudes. However, as the width of the tire increases, a frequency shift is observed. For example, it can be observed that between a tire with a 195 mm width and a 235 mm width, the response is shifted by approximately 125 Hz. In this case, amplitude changes do not appear to be large either.

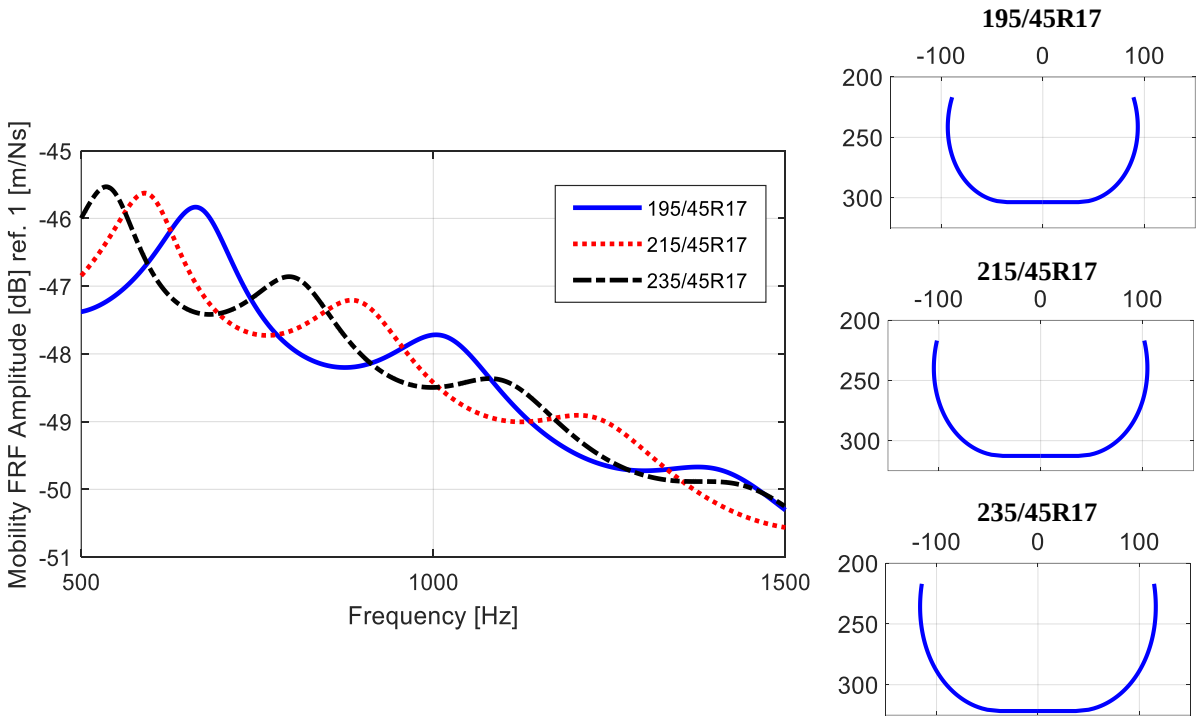

Figure 5.13. Input mobility FRF for the same tire with changing tire width. Tire sizes are also shown for reference with all dimension in [mm].

In an effort to further analyze frequency shifts and amplitude changes induced by geometry changes in the tire, the M_{MSV} of the tire according to equation (4.1) is used. As previously shown in Figure 5.12 and Figure 5.13, when the aspect ratio of the tire is changed, a frequency shift is observed in the estimated input mobility FRF. A similar behavior is observed if the M_{MSV} for different tire sizes is analyzed. Figure 5.14 shows the M_{MSV} for a tire with three different aspect ratios.

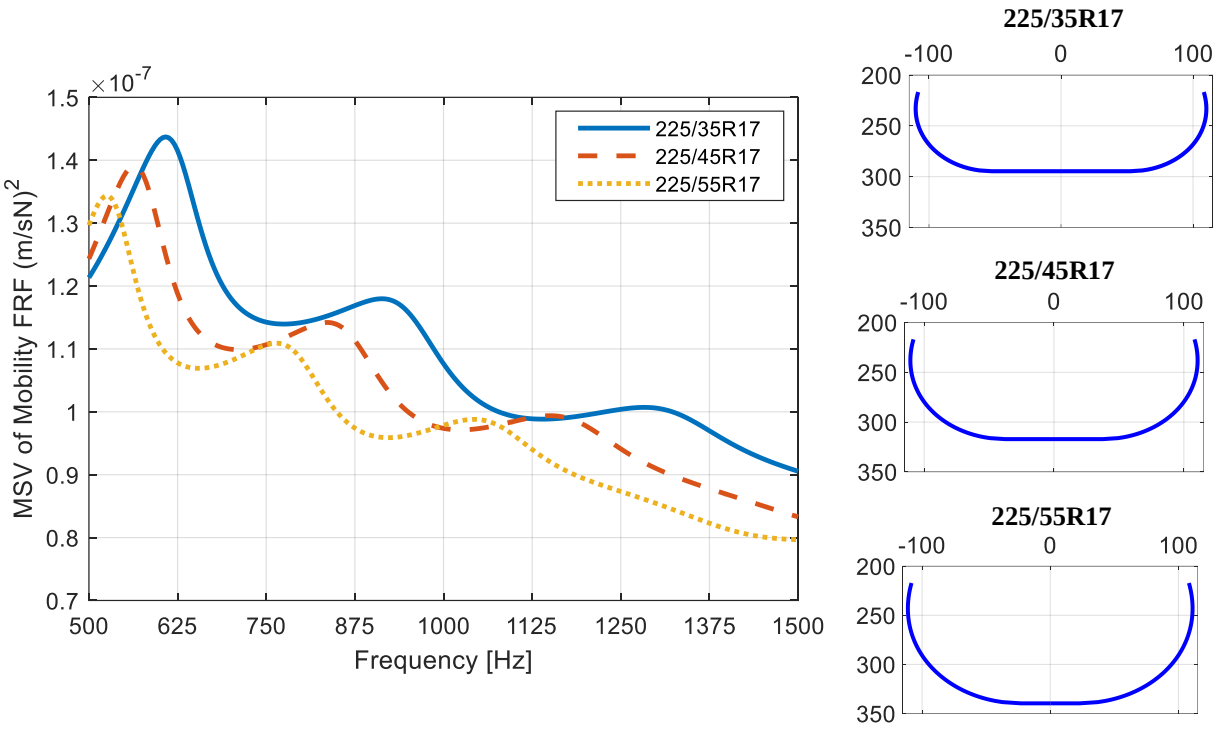

Figure 5.14. M_{MSV} vs. frequency for tires with different aspect ratio. Tire sizes are also shown for reference with all dimension in [mm].

The results in Figure 5.14 suggest that a frequency shift between two different tire sizes can be estimated with the ratio of carcass widths (defined as sidewalls length plus tire width), as follows

$$\Delta f_{shift}(f) = f\left(\frac{CW_{predict}}{CW_{ref}} - 1\right) \tag{5.6}$$

In this case, Δf_{shift} corresponds to the estimated frequency shift for a tire that has a carcass width $CW_{predict}$, with respect to a reference tire with a reference carcass width CW_{ref} for a frequency f.

Figure 5.15 shows the M_{MSV} for the same tires in Figure 5.14, plotted as a function of the normalized frequency $f\,\frac{CW_{predict}}{CW_{ref}}$[Hz]. In this case, the reference carcass width CW_{ref} was selected

for the tire of size 225/35R17, i.e. the one with the smallest aspect ratio. It can be observed that all the curves collapse very well above 1000 Hz, however for the lower frequencies still a small shift exists. Still, these results indicate the approximation in (5.6) provides a good estimate, especially for the highest frequencies. It should also be noted that by changing only the aspect ratio of the tire, no significant changes in the amplitude of the tire's response can be expected. Yet, it can be observed that tires with a smaller aspect ratio tend to have higher predicted responses.

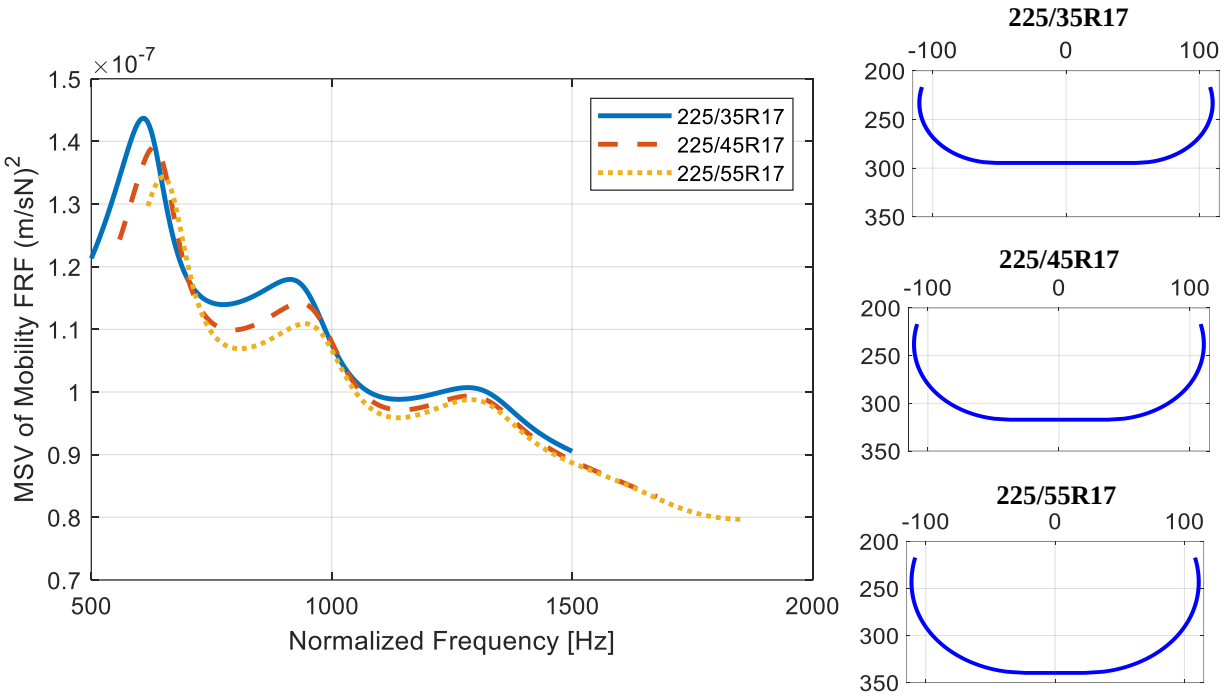

Figure 5.15. M_{MSV} vs. normalized frequency for tires with different aspect ratio. Tire sizes are also shown for reference with all dimension in [mm].

The effects of changing the whole width are also addressed by computing the tire's M_{MSV} for three different carcass widths. These results are shown in Figure 5.16. It can be observed that a frequency shift is present between each of the tires. In addition, amplitudes also changed for different tire sizes.

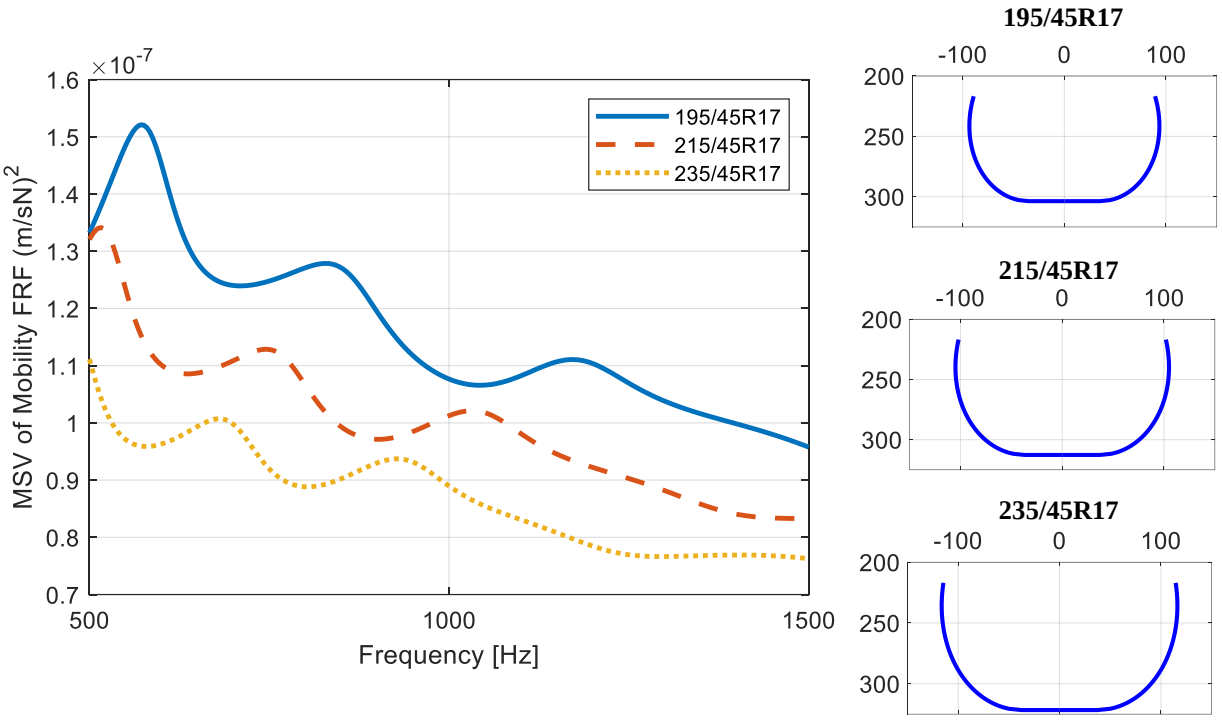

Figure 5.16. M_{MSV} vs. frequency for tires with different carcass width. Tire sizes are also shown for reference with all dimension in [mm].

If the curves in Figure 5.16 are normalized as was done for Figure 5.15, then the shift is eliminated as shown in Figure 5.17. However, it can be observed that a difference in amplitudes still exists. The amplitude shift can also be computed with the size of each of the tire's carcass width, as follows

$$\Delta\left|M_{MSV}\right|_{shift} = \left|M_{MSV}\right|_{ref}\left(\frac{CW_{predict}}{CW_{ref}} - 1\right) \tag{5.7}$$

Where, the amplitude shift is defined as $\Delta\left|M_{MSV}\right|_{shift}$ for a tire that has a carcass width defined by $CW_{predict}$, with respect to a tire that has a carcass width defined by CW_{ref} and corresponding amplitude $\left|M_{MSV}\right|_{ref}$.

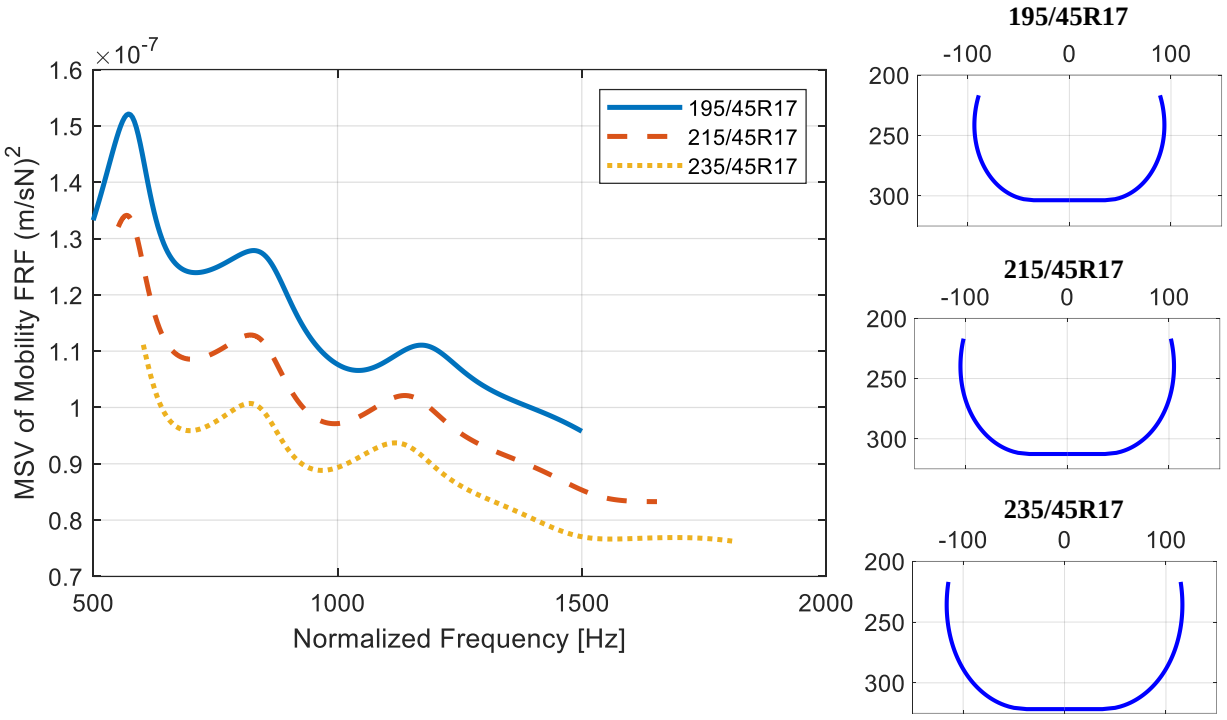

Figure 5.17. M_{MSV} vs. normalized frequency for tires with different carcass width. Tire sizes are also shown for reference with all dimension in [mm].

For example, Figure 5.18 shows the collapsed curves all the tire sizes in Figure 5.17, after multiplying the amplitudes of each by $\frac{CW_{predict}}{CW_{ref}}$. In this case, the reference tire was chosen to be the one with the smaller carcass width. These results show that the amplitudes collapse well, especially for the higher frequencies. There is still a small error for amplitudes and frequency shift. However, the carcass width ratio proves to be a good estimate of the response for different tire sizes.

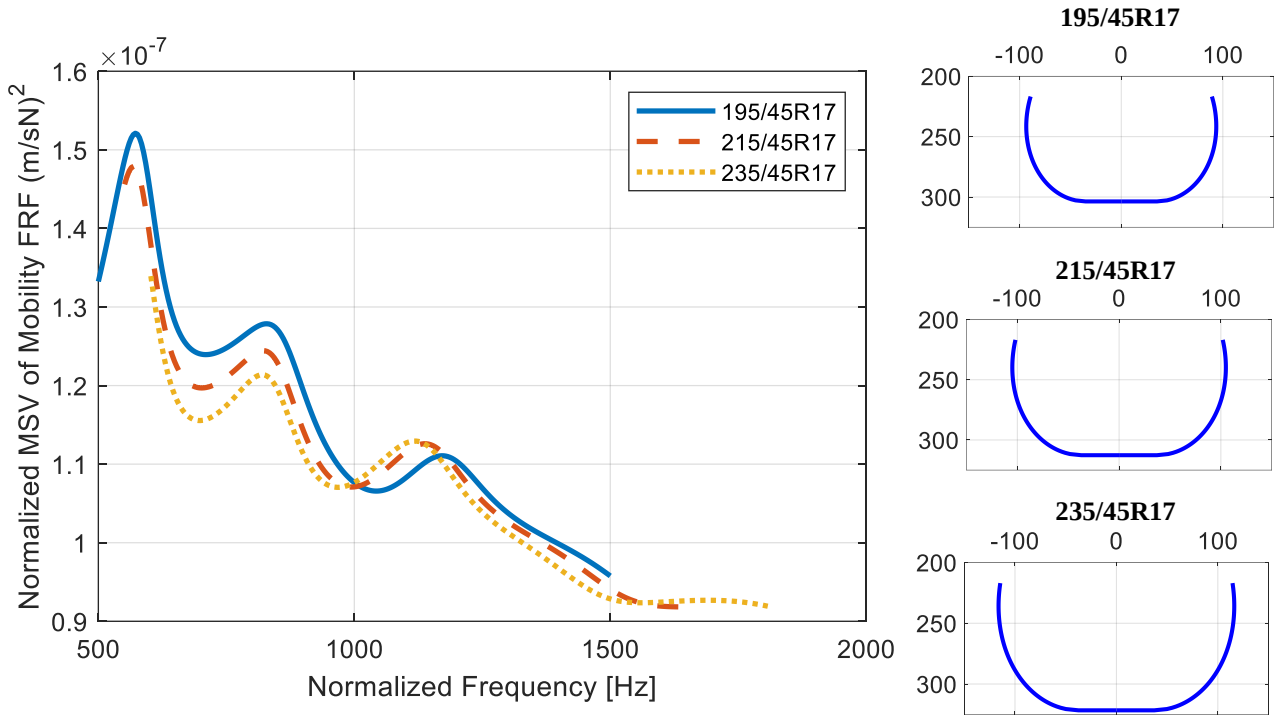

Figure 5.18. Normalized M_{MSV} vs. normalized frequency for tires with different carcass width. Tire sizes are also shown for reference with all dimension in [mm].

Finally, the effects of rotational velocity on the response of the tire are explored. In this case, the mobility FRF function has been computed along two center lines of the tire, as shown in Figure 5.19. It should be noted that in this case, it is of interest to analyze the response along the positive and negative centerlines of the tire. The reason is that non-symmetric results are expected because of the effects of rotational velocity, as previously shown in Figure 5.8.

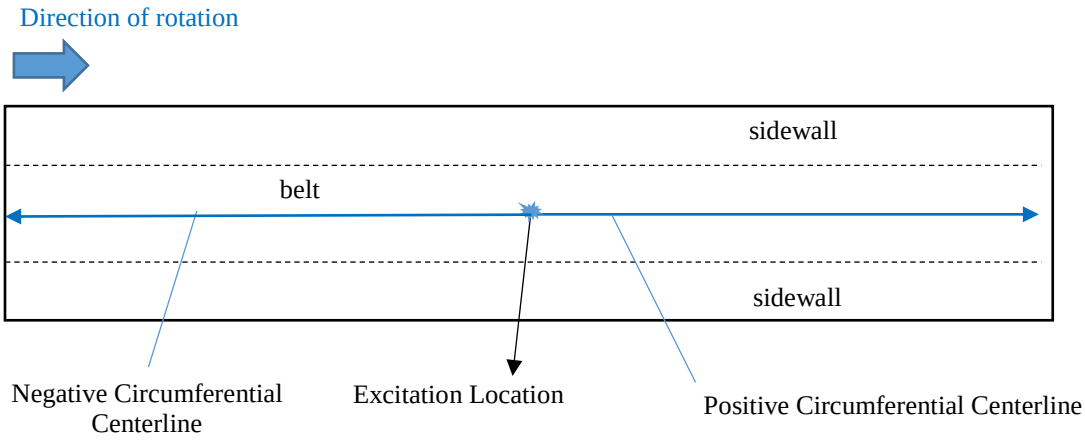

Figure 5.19. Unwrapped view of a tire showing positive and negative circumferential centerlines for a rotating tire.

The mobility along the positive circumferential direction of a tire of size 225/45R217 is shown in Figure 5.20. The tire is rotating with a rotational speed of 100 rad/s (equivalent to a vehicle traveling at 70 mph). Unlike the case where the tire is static (compare to Figure 4.8), it can be observed that decay along the same direction of rotation is less prominent, especially near 1000 Hz. On the other hand, the mobility along the negative circumferential direction i.e. along the direction contrary to the tire's rotation is shown in Figure 5.21. In this case, it can be observed that the decay is more prominent if compared to the positive circumferential direction of the tire in Figure 5.20. Still, the amplitude levels are not higher than for a non-rotating tire. This suggests that the effects of rotation on the noise produced by the tire may not be significant.

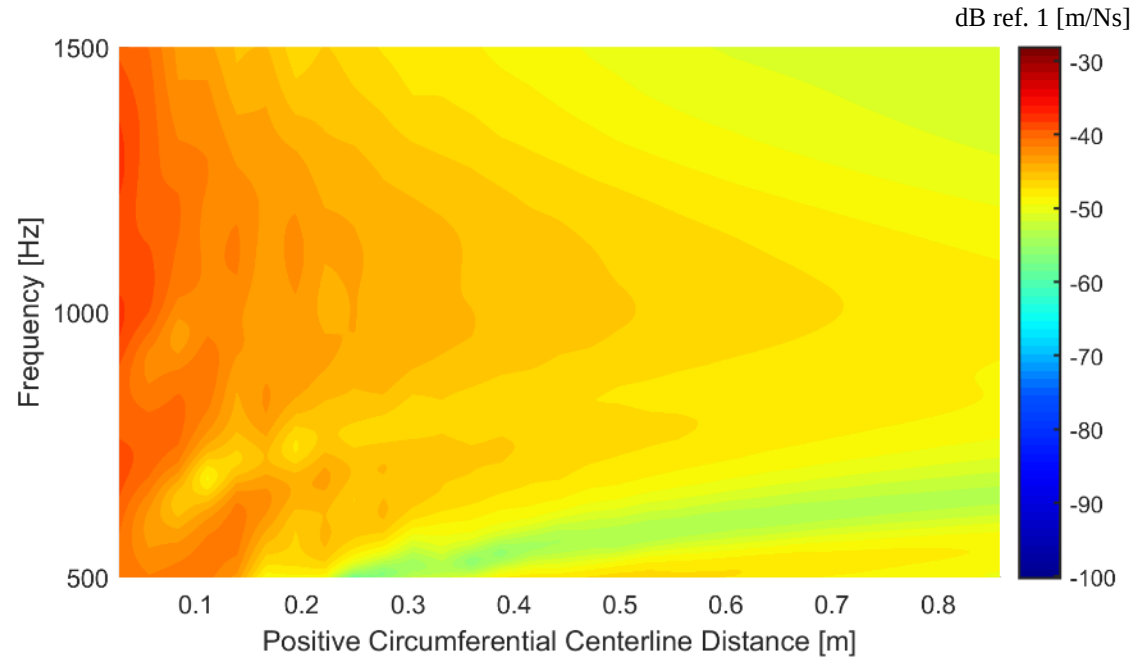

Figure 5.20. Simulated mobility FRF along the positive center circumferential line for a tire of size 225/45R17 rotating with a velocity of 100 rad/s.

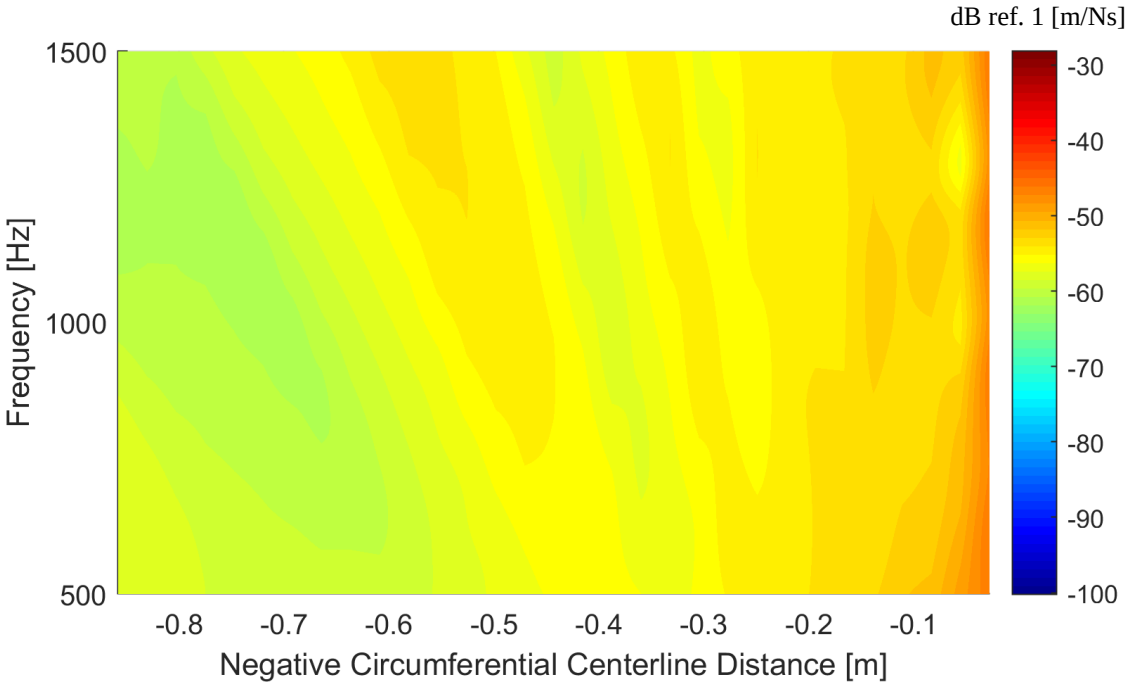

Figure 5.21. Simulated mobility FRF along the negative center circumferential line for a tire of size 225/45R17 rotating with a velocity of 100 rad/s.

Tread Pattern Noise Demonstration

In this section, a demonstration of predicted noise produced by a rotating tire with different tread patterns is presented. The intention is to demonstrate the capabilities of WavePro Tire.

Following the formulation in Chapter 3, the load distribution in the contact patch is approximated at discrete locations, as shown in schematic of an unwrapped tire in Figure 5.22. The periodic forces acting on each kth point of the rth rib due to the mth block are defined by the Fourier amplitudes at all the harmonics ($n\omega_T$) of interest, $F_{rm}^{kn}\left(x_m^r(t), y_r, n\omega_T\right)$. These harmonic terms are computed with equation (3.18). By multiplying these forces by their corresponding mobility FRF $M_s\left((x_a, y_a)\middle|((x_k, y_r)), n\omega_T\right)$, then the normal surface velocity at any location (x_a, y_a) on the tire surface is obtained. Finally, the total normal surface velocity is obtained by adding the contribution of all forces acting at the points in the contact patch. This addition is in the complex domain to account for magnitude and phase between forces and is defined in equation (3.19). In order to compute noise, the BEM previously described in this chapter is then implemented.

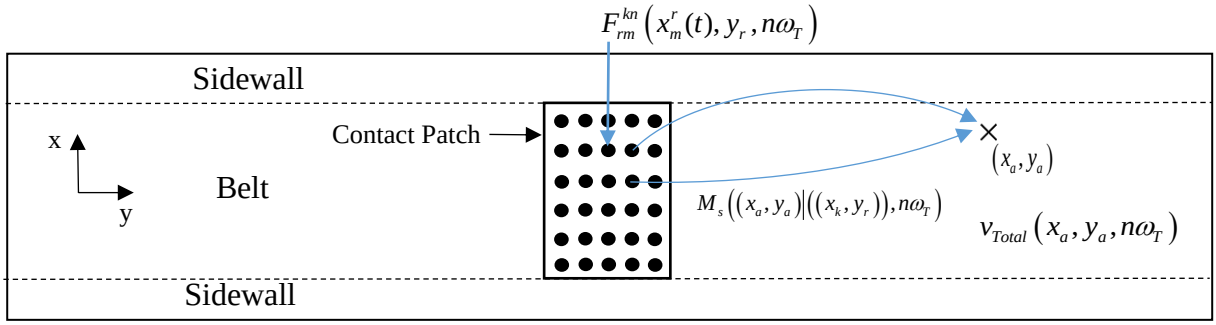

Figure 5.22. Method for computation of normal surface velocities of the tire due to excitation in tread pattern.

An initial simulation for a tire of size 225/45R17 was performed. Two different tread patterns were implemented. These are, the uniform tread pattern defined in Figure 3.14 and its corresponding randomized version, i.e. randomized spacing between blocks in each rib. The total load applied on

the tire is 2,940 N for a contact patch length of 17 cm. The selected velocity for simulations is 70 mph. Finally, an inflation pressure of 32 psi was used.

The selected structural model corresponds to the stationary non-uniform infinite plate, i.e. rotation not included in the structural model. This structural model was selected because it provides good estimates of the tire's response while maintaining a low computational burden. For example, if the predicted mobility for a stationary tire in Figure 4.7 is compared to those for a moving tire in Figure 5.20 and Figure 5.21, it can be observed that including rotation does not render significant changes in the tire's response amplitudes. Therefore, significant noise changes are not expected either. In addition, it is estimated that by including rotation in the structural model, the computational time for this simulation would increase from approximately 6 hours for a stationary tire model to 7 days for a rotating tire model, using a 4.00-GHz quad-core personal computer with 16 GB of RAM. Still, the effect of tire rotation is accounted through the periodic tread-block excitation in the contact patch formulation.

Noise has been predicted at two locations, as marked in Figure 5.23a with red. These locations are the same as the microphone locations for the OBSI, also shown in Figure 5.23a. These locations are also specified in the standard AASHTO (2015) and were selected in order to compare predicted noise with measurements. Figure 5.23b shows that the two microphones are located at 3 in (0.076 m) above the pavement surface. The tire is traveling along the positive y-axis with a velocity of 70 mph. Therefore, the microphone to the right is located at the leading edge of the rotating tire, while the other at the trailing edge. Finally, both are located at 4.125 in (0.104 m) away from the hub's center and 4 in (0.101 m) away from the tire's sidewalls, as shown in Figure 5.23c.

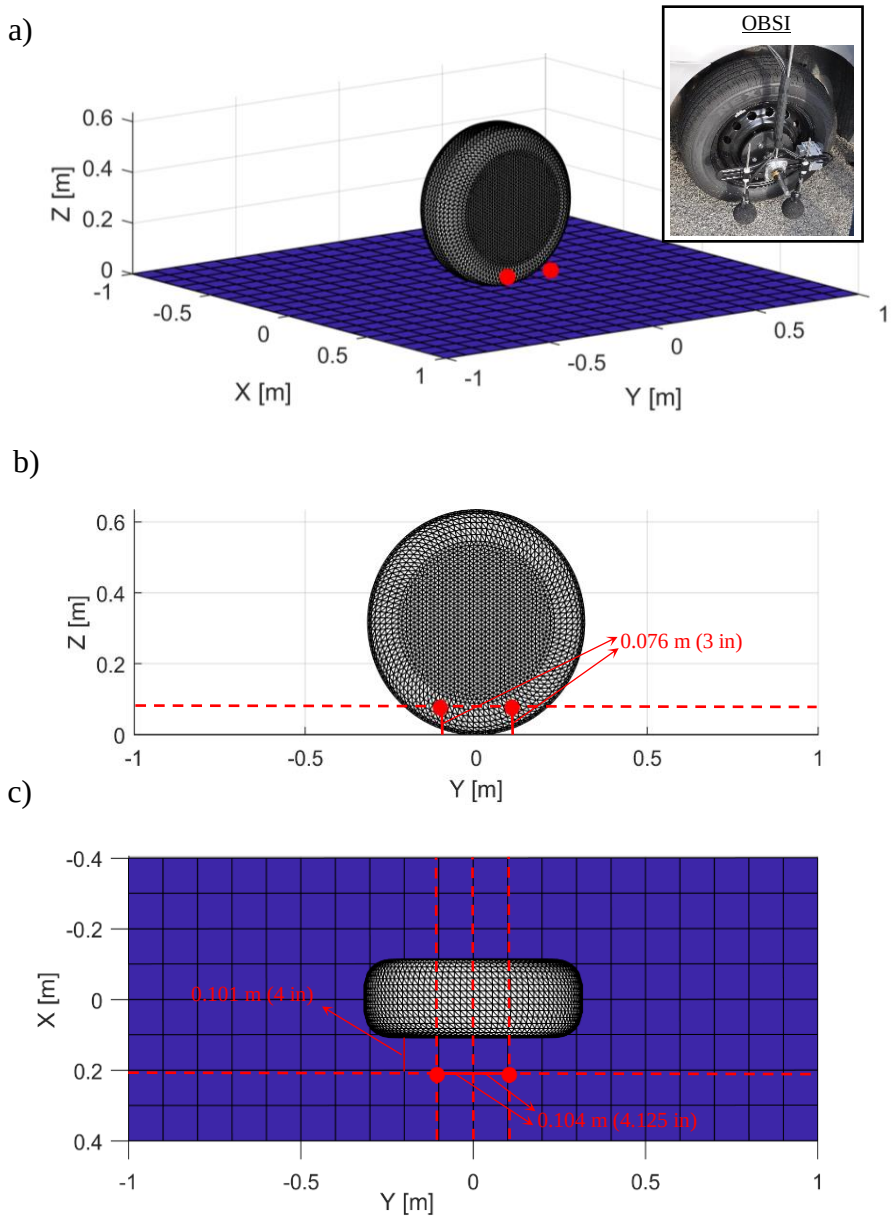

Figure 5.23. Location of field points where noise is predicted.

Figure 5.24 shows the predicted A-weighted tread pattern noise spectra at the two microphone locations in Figure 5.23. The uniform and non-uniform tread-patterns used for these simulations are also shown. The results in Figure 5.24a show that a single frequency is excited for the uniform tread pattern case. This is located at 942.1 Hz, and can be calculated as $N_B V_T / \ell_T$, where N_B is the number of blocks per rib, ℓ_T is the circumference of the tire, and V_T is the velocity of the

belt. At this frequency, the noise amplitudes are 113.5 dBA for the leading edge and 108 dBA for the trailing edge. On the other hand, Figure 5.24b shows that all frequencies are excited for the randomized tread pattern. Still, the dominant frequencies are around 1000 Hz because the tread pattern contains the same number of blocks and the distance between them cannot be modified by much. In this case, the maximum noise levels for the leading edge and trailing edge locations is 106.1 and 104.8 dBA, respectively. These results suggest that by simply randomizing the tread pattern, the maximum noise levels produced by the tread pattern can be reduced.

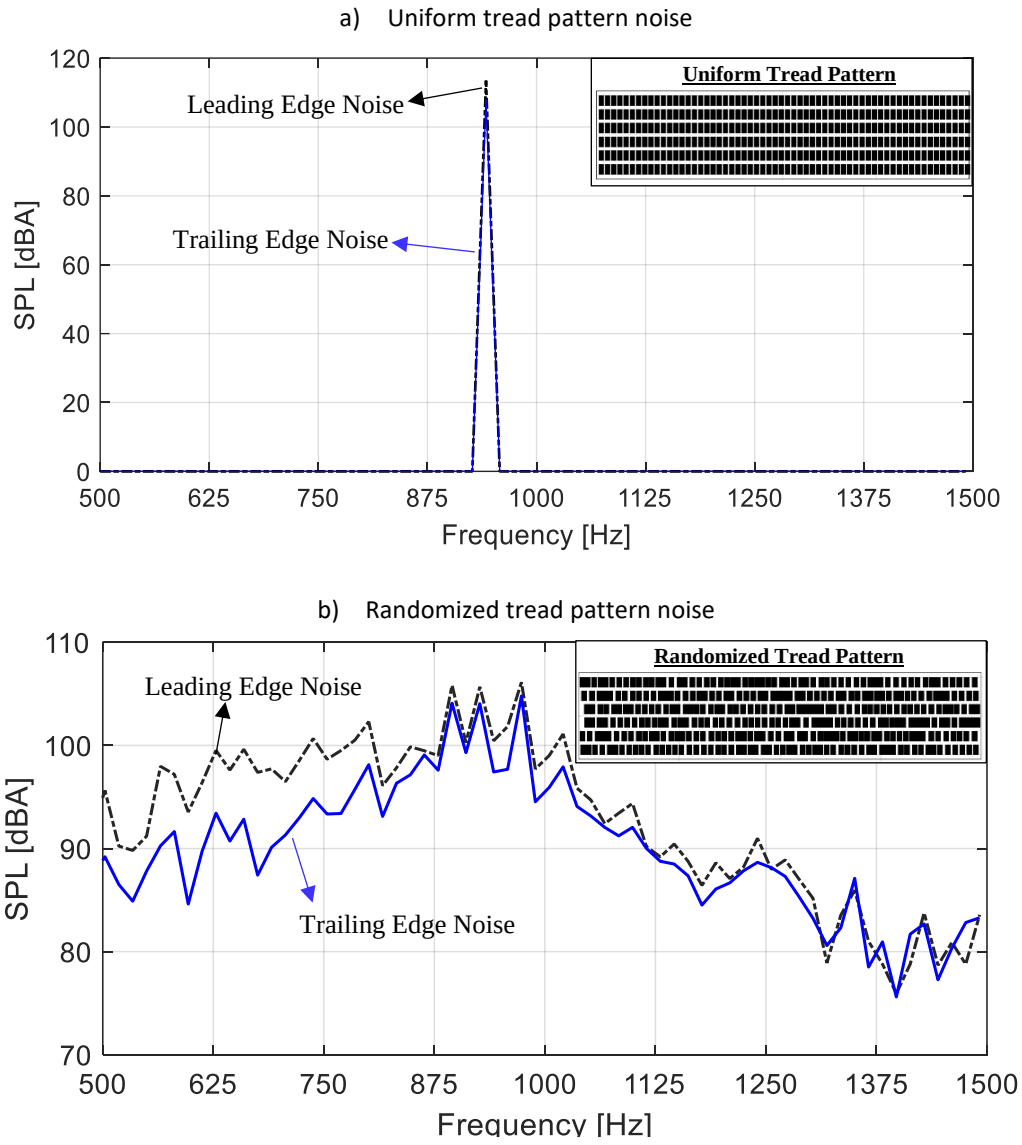

Figure 5.24. Leading and trailing edge noise produced by a) uniform tread pattern and b) randomized tread pattern (frequency resolution of 15.7 Hz).

The results in Figure 5.24 also show that the leading-edge noise levels are higher than the trailing edge noise level, especially at low frequencies. At a few high frequencies, the trailing edge noise becomes higher. This is consistent with the experimental tread-pattern noise measured with the OBSI, presented in the work by Li (2017) and Spies (2019). For example, Figure 5.25 shows the tread-pattern noise measured with the OBSI for a tire of size 215/60R16 for both the leading and trailing edges. A picture of the tire's tread pattern is also shown in Figure 5.25. These measurements were made using a 2012 Chevrolet Impala (see Figure 1.3) for a velocity of 65 mph. In this case, the leading edge noise is higher than the trailing edge noise up to a frequency of 875 Hz. However, for higher frequencies, the trailing edge noise is higher.

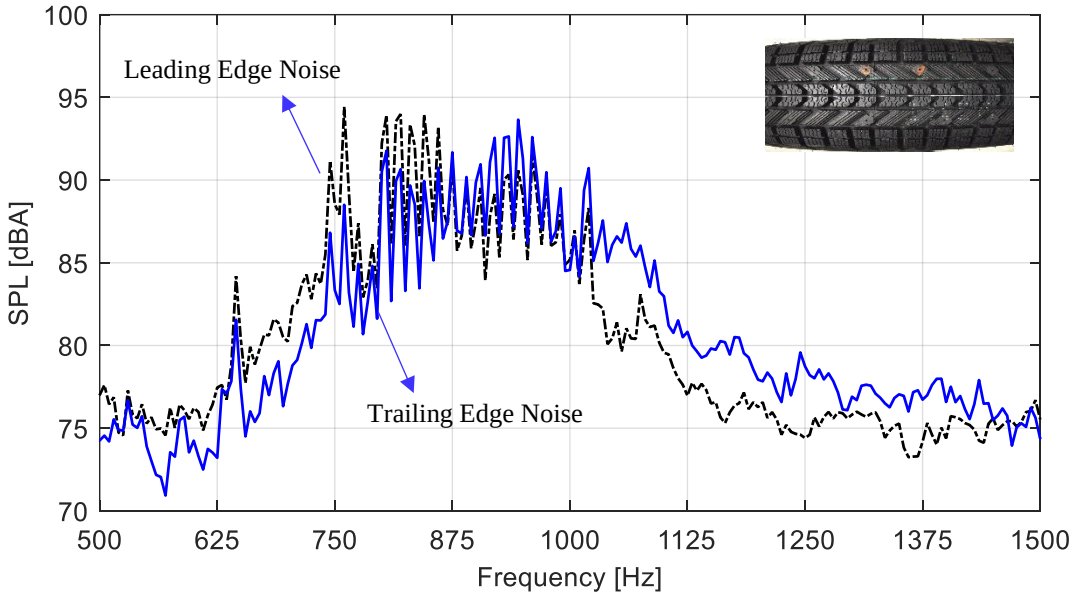

Figure 5.25. Measured leading and trailing edge noise for a tire of size 215/60R16 (frequency resolution 2.18 Hz).

The tread-pattern noise measured with the OBSI may contain noise generated by other mechanisms, such as air pumping. Therefore, a complete validation cannot be performed using simulated results and those obtained from testing. Still, an attempt to make a comparison is also presented in this section. It should be noted that this is the first time that such results are presented. In order to do so, a second simulation was performed for the tire presented in Figure 5.25.

First, the tread pattern was approximated to the real one by using the formulation presented in Chapter 3. The real and the approximated tread patterns are shown in Figure 5.26. The geometry of the real tread pattern is shown in Figure 5.26a. This was obtained by scanning the tire with a Circumferential Tread Wear Imaging System (CTWIST). On the other hand, Figure 5.26b shows the approximated tread pattern with rectangular non-skewed blocks. In this case, the total amount of blocks for all ribs is 62 (same as real tread pattern) and the size of the blocks was also approximated to those of the real tread pattern. Finally, it should be noted that the approximated tread pattern was randomized.

a) Real Tread Pattern (scanned with CTWIST)

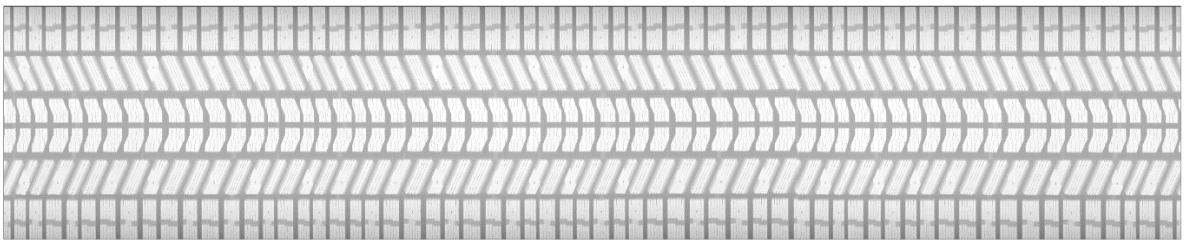

b) Approximated Tread Pattern

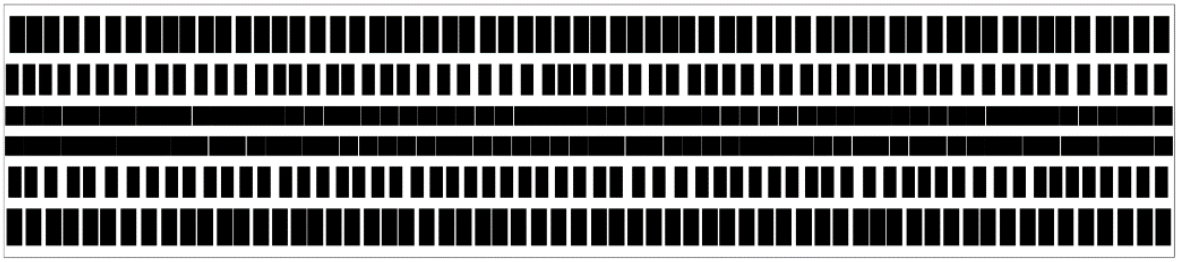

Figure 5.26. a) real and b) approximated tread patterns for a tire of size 215/60R16.

This simulation was performed using the same load and inflation pressure that was used to obtain the results in Figure 5.24. However, the selected velocity, in this case, is 65 mph, in order the experiment. Finally, noise was predicted at the same leading and trailing edge microphone locations defined in Figure 5.23.

Figure 5.27 shows the predicted and measured A-weighted noise levels at the leading and trailing edge locations. It can be observed that in both cases, the predicted noise levels are higher than

those measured for most frequencies. This could be because of the approximations made for the tread pattern. Still, the results in Figure 5.27a and Figure 5.27b show that the measured and predicted noise levels agree very well between 900 Hz and 1100 Hz. Finally, both measurements and predictions show similar spectral shapes. Their dominant frequency content is located between 800 Hz and 1100 Hz. In addition, their initial slope towards the maximum noise levels is less significant than the negative slope towards high frequencies.

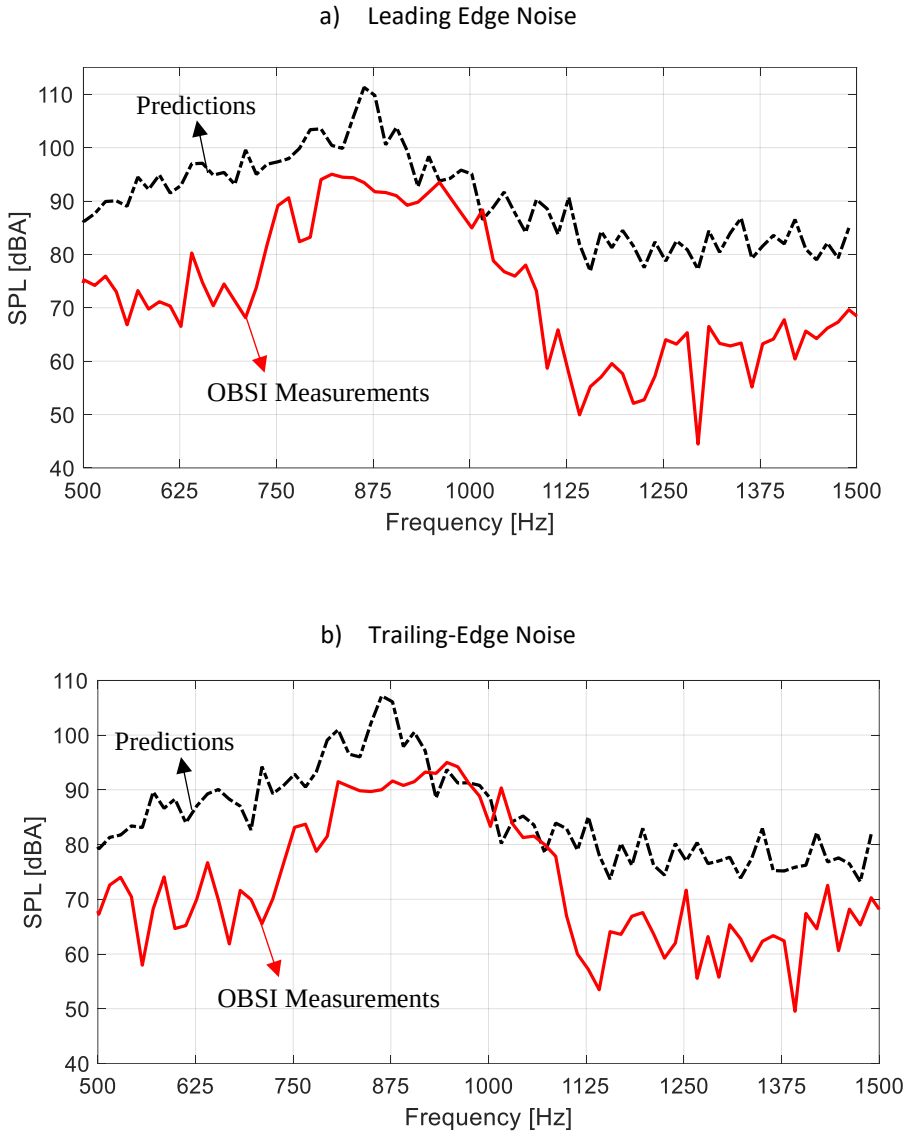

Figure 5.27. Predicted and measured tread pattern noise for a) leading edge and b) trailing edge noise for a tire of size 225/60R16 (frequency resolution 13.92 Hz).

In an effort to analyze the behavior of tread pattern noise for different vehicle speeds, additional simulations were performed. The same inputs implemented to obtain the results in Figure 5.27 were used. Tread pattern noise predicted at the leading-edge microphone location for 50 mph, 60 mph, and 70 mph, as shown in Figure 5.28. In this case, the dominant spectral content shifts in frequency, depending on the speed of the vehicle.

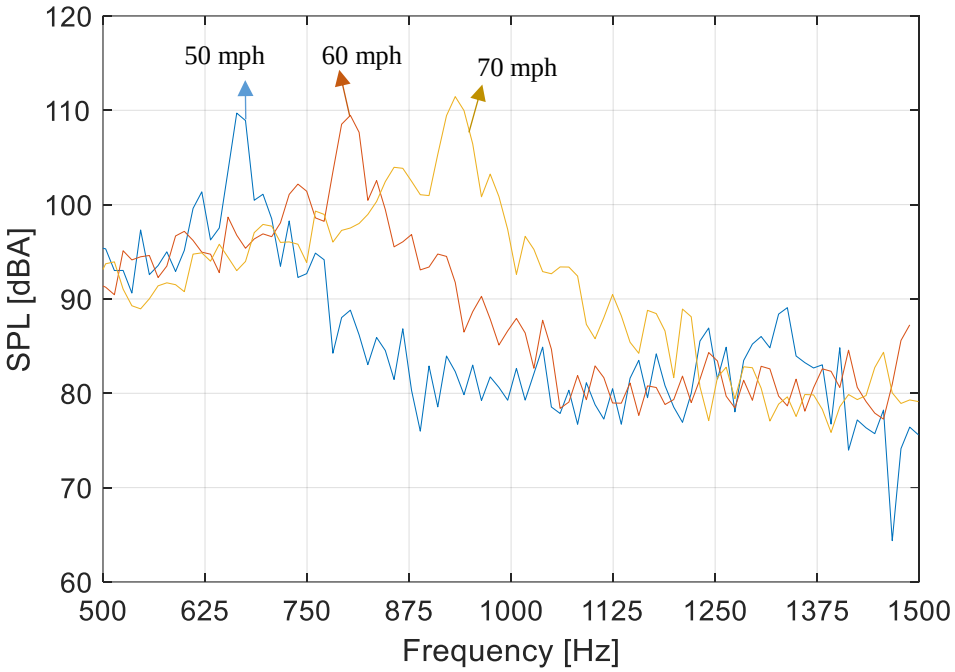

Figure 5.28. Predicted tread-pattern noise for 50 mph, 60 mph, and 70 mph (frequency resolution of 10.7 Hz).

If the frequency is then normalized using the rotational velocity of the tire, then the spectra presented in Figure 5.28 is defined in terms of the tire's order. This is calculated as follows

$$\text{Order} = \frac{Frequency[Hz]}{\Omega[Hz]} \tag{5.8}$$

where, Ω is the rotational velocity of the tire expressed in [Hz]. The resulting spectra for the three velocities, in terms of order, are shown in Figure 5.29. In this case, it can be observed that noise amplitudes depend on the rotating speed of the tire. In general, higher speeds produce higher noise

levels. The same behavior was observed on measured tread pattern noise by Li (2017). In this case, measurements showed that the amplitude of tread-pattern noise scales with speed with a scaling factor of 4.

For example, the curves in Figure 5.29 can be scaled to a velocity of 60 mph. If this is done, then the resulting curves are shown in Figure 5.30. In this case, it can be observed that up to an order of 85, all curves collapse well. This suggests that tread pattern noise predicted with *WavePro Tire* has the same scaling properties as experimentally determined.

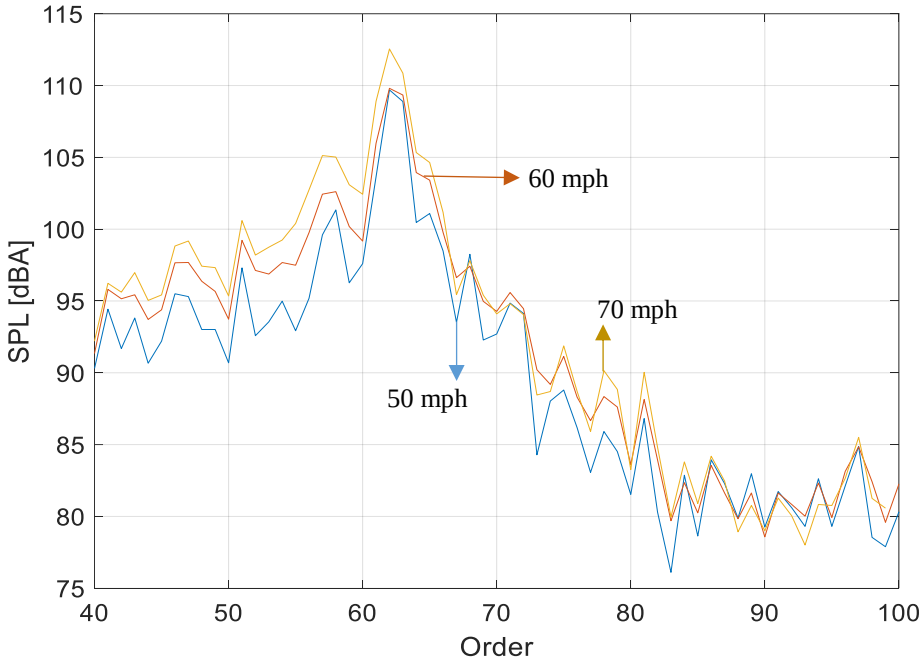

Figure 5.29. Tread pattern noise vs. order for 50 mph, 60 mph and 70 mph.

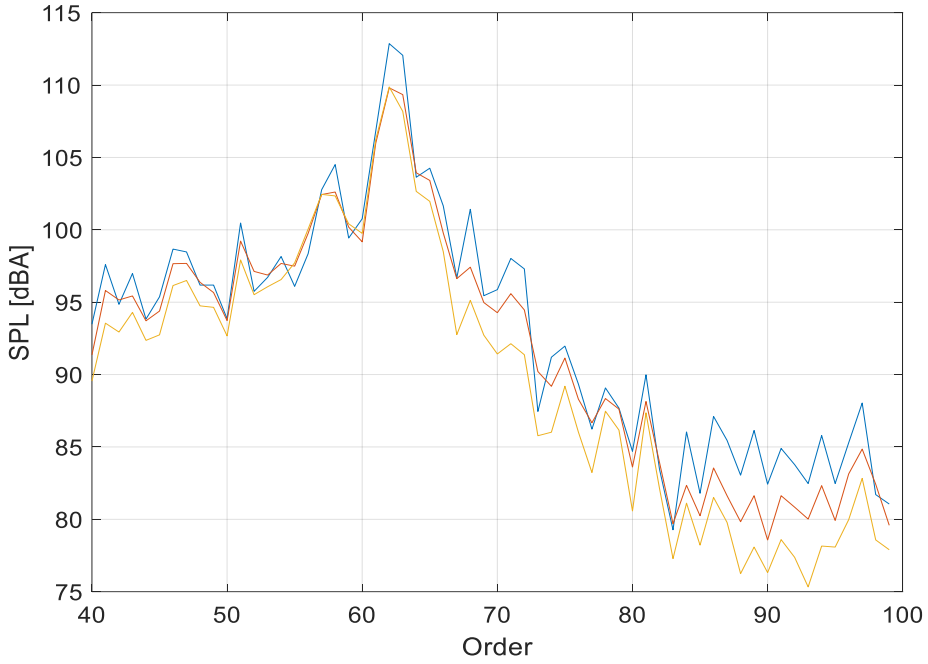

Figure 5.30. Predicted tread pattern noise curves scaled to 60 mph.

Conclusions and Future Work

The main accomplishments of the present work are the following:

In this study, a set of novel structural models of a tire are presented, including various plate and cylindrical shell models. These implement a wave propagation approach along the circumferential direction of the tire, as opposed to current prediction tools were the tire is assumed to have a full modal behavior. This is the first time a full-wave propagation model such as this is proposed. The intention is to provide a physically accurate method to predict the response of the tire within a frequency range between 500 Hz and 1500 Hz. The structural models are enhanced to include the following physical phenomena: i) Orthotropic material properties, typical of the tire's structural characteristics due to the combination of composite materials used in a tire. ii) Non-uniform properties along the transversal direction of the tire that accounts for structural differences between the tire's belt and sidewalls. iii) Inflation pressure defined by membrane tensions along the circumferential and transversal directions of the tire. iv) Effects of rotation in the tire's structural dynamic behavior.

A new contact model that accounts for the proper input to the tire's structure during rolling conditions is also presented. This is the first of its kind as it is defined in the frequency domain, unlike what is found in the open literature. This is a more efficient approach for a periodic input such as a tire's tread pattern. In addition, formulating the excitation of the tire in the frequency domain allows analyzing the excitation provided by different tread-patterns. Various tread-pattern designs were analyzed, including completely uniform and randomized designs. These were then coupled to the structural models and the produced noise was computed. This was done by implementing a boundary element algorithm. Finally, experiments were performed in order to validate the structural modeling approach and noise results.

The comparison of predicted tread-pattern noise to measurements obtained from experiments performed with an OBSI is also a new contribution. This is the first time that such comparisons

are presented within the mid-frequency range. These results show that the developed tool (WavePro Tire) has great predictive potential.

The main conclusions from the present work are the following:

1) The solution method developed to find the response of the tire is the first full wave propagation approach. Results show that by implementing this method, over-predictions made with modal approaches over the mid-frequency range (500 Hz-1500 Hz) can be avoided. Furthermore, simulations showed that the modeling approach to provide the most accurate response corresponds to the non-uniform infinite plate model, especially within 800 to 1300 Hz. This indicates, that properly capturing the transversal structural properties of the tire is very important when modeling it. In addition, this also indicates that the effects of curvature are not significant for the frequency range of interest, > 500 Hz. Furthermore, finding the appropriate input parameters for the plate models is more straightforward than for a cylindrical shell. The plate model is also computationally more efficient than the cylindrical shell, due to its lower complexity. These last two show that the plate model is more suitable for the modeling cases presented in this work. Still, the formulation for the cylindrical shell provides very good estimates of the tire's response for low-frequency responses.

2) The sensitivity analysis showed that selecting an appropriate loss factor is important, but will not significantly change the predicted response of the tire. A constant 16% modal loss factor provided a good estimate for the tire's response. On the other hand, pressure variation does not significantly affect the tire's response. In contrast, results show that the carcass width of the tire has significant effects on its response. It induces frequency shifts in the response. However, these shifts can be predicted very accurately using equations (5.6) and (5.7). Finally, including rotational velocity affects the decaying behavior along the circumference of the tire. Waves propagating contrary to the direction of rotation decay faster than those traveling in the same direction. Still, the response amplitudes for these cases did not show much variation from a static tire.

3) Results show that designing tread patterns with blocks of different sizes and randomizing of the distance between them has a great impact in distributing the total input power over multiple frequencies. This approach successfully reduces tonal excitations of the tire and thus decreases the maximum applied force to the tire.

Recommendations for Future Work:

1) In this work, the tire excitation is computed exclusively due to the impact of the tread blocks on the pavement. The tread patterns that can be implemented are limited to square, non-skewed blocks. It is recommended that new models for blocks of different geometries are developed in the future. Furthermore, the current tread pattern formulation is limited to ribs that have all blocks of the same size. Further improvements could eliminate this limitation. This would enable tread-pattern designers to be less constrained and predict tire vibrations and noise due to any new tread design.

2) Obtaining the appropriate structural parameters of a tire is no easy task, especially for a complex model such as the cylindrical shell presented in Chapter 2. A proper method that either experimentally or numerically finds them should be devised in order to overcome this problem. For example, the required parameters can be obtained directly from modal vibratory data by using optimization techniques such as genetic algorithms. Here, a methodology to do this is proposed for future work.

   The required input structural parameters are summarized in Table 6.1. A total of 6 parameters need to be estimated for the flat plate models. These are the bending stiffnesses along the circumferential, transversal and cross-directions. All for both the belt and sidewalls. These parameters in addition to two more are also required by the cylindrical shell model.

Table 6.1. Summary of structural parameters to be estimated for tire models.

Parameter	***Used Notation: Flat Plate, Cylindrical Shell***	***Tire Part***
Bending Stiffness (Circumferential Direction)	B_x , D_{11}	Belt
Bending Stiffness (Transversal Direction)	B_y , D_{22}	Belt
Bending Stiffness (Cross Direction)	B_{xy} , D_{12}	Belt
Bending Stiffness (Circumferential Direction)	B_x , D_{11}	Sidewall
Bending Stiffness (Transversal Direction)	B_y , D_{22}	Sidewall
Bending Stiffness (Cross Direction)	B_{xy} , D_{12}	Sidewall
Bending Stiffness (Due to Curvature)	*Not Required*, D_{33}	Belt
Bending Stiffness (Due to Curvature)	*Not Required*, D_{33}	Sidewall

The proposed method to obtain the required structural parameters is to first use either experimental data or FE methods to accurately compute natural frequencies of a tire. Detailed FE models used in industry that include multiple tire construction components could be used. An example can be found in the work by Brinkmeier et al. (2008). The natural frequencies of the tire are then compared to those computed with the cylindrical shell model presented in Chapter 2. If the error is too high, then new input structural parameters are selected and the process is repeated. This process is repeated iteratively until the error reaches the desired threshold, i.e. until the natural frequencies converge. This process has been summarized in the schematic in Figure 6.1. A genetic algorithm is suggested as a tool to perform this optimization.

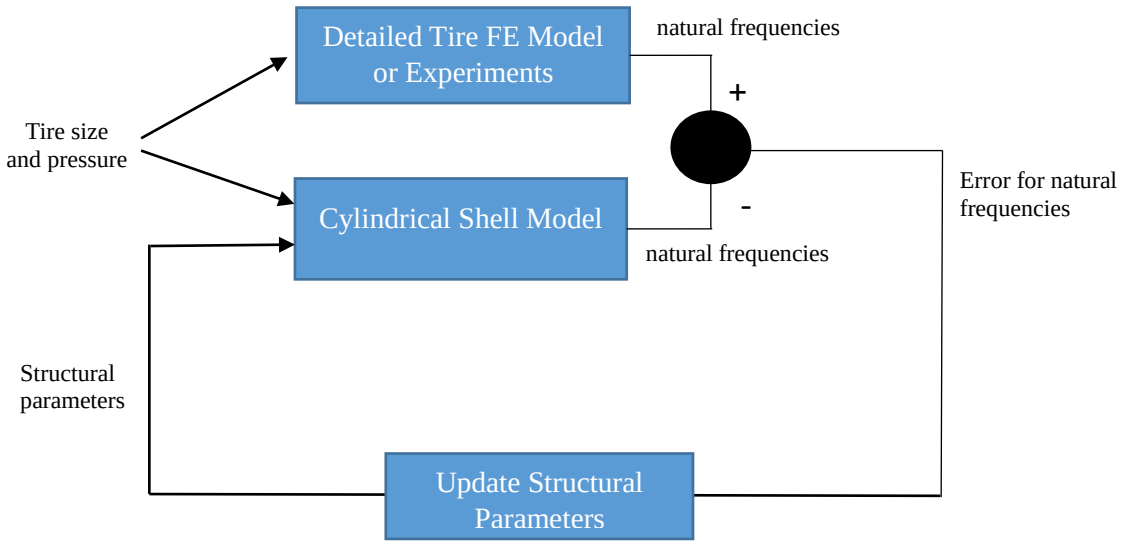

Figure 6.1. Proposed process to find structural parameters of a tire.

It should be noted that this process can be performed for one or multiple natural frequencies. Multi-objective genetic algorithms should be used for the latter. It is suggested that only up to the first 10 natural frequencies, as these are typically below 500 Hz for a tire. However, computational times should increase and convergence issues could appear as more natural frequencies are used.

Finally, the natural frequencies calculated with the cylindrical shell model presented in Chapter 2 need to be calculated as follows. First, its equation of motion needs to be equated to zero, i.e. the homogeneous version of equation (2.84) is used. In this case, a wave propagation solution is no longer assumed since the objective is to compute the natural frequencies of the tire. Therefore, modes are assumed along the circumferential direction by assigning integers to the circumferential wavenumbers of the tire. Therefore, the assumed solution in this case becomes

$$w(\theta, y, t) = \sum_{m}^{M} \sum_{n}^{N} q_n \beta_n (y) e^{-im\theta} e^{i\omega t} \tag{6.1}$$

for a total of N transversal modes and M circumferential modes. If equation (6.1) is substituted in the equation of motion (2.84), then pre-multiplied by the modes and integrated along the x-direction and y-directions, the natural frequencies can be obtained. This process is similar to that followed by Kropp's model described in section 2.1.

3) This work has focused on vibration-induced TPIN. In the future, this model could be combined with air pumping models in order to completely model TPIN and provide more insight into the general problem.

4) The models proposed in Chapter 2 implement different homogeneous equations of motion to arrive to an eigenvalue problem and compute the transversal mode shapes of the tire. These homogeneous equations for each of the models are defined in equations (2.81), (2.83) and (2.85). However, alternative methods can be implemented in order to define the transversal modes of the tire. For example, FE models or experimental data can be used instead. This approach should be explored in the future.

A final remark regarding the computational requirements for all the simulations presented in this work is made here. All simulations were performed on a 4.00-GHz quad-core personal computer with 16 GB of RAM. The computational time depends on the structural model implemented for predications, the number of elements used on the tire surface and the number of frequencies being simulated. For example, for a structural simulation where the tire is excited at a single point and predictions are made on 600 points on the tire surface, predictions take approximately 1 minute for a total of 250 different frequencies. The computational time if Kropp's model is used is approximately 30 min. The computational time for same conditions, using the moving infinite plate is approximately 9 hours. Mainly due to the computational burden of the inverse wavenumber numerical integration. Finally, the same simulation conducted with the cylindrical shell model has a computational time of approximately 15 hours. Therefore, it is clear that the infinite plate model

has a clear advantage over all other structural modeling approaches. This is attributed to the fact that all equations are solved analytically for this model.

Finally, it should be noted that noise predictions also have significant computational requirements. For example, the noise computations presented in Figure 4.13 took approximately 13 hours for 1500 frequencies and 80 field points (40 for the direct path and 40 for the image source). For this simulation, 1500 points were used on the tire surface, with an average element size of 2 cm.

References

AASHTO. (2015). TP-76: Standard Method of Test for Measurement of Tire/Pavement Noise Using the On-Board Sound Intensity (OBSI) Method. In.

Bateman, H. (1954). Exponential Fourier Transforms. In *Tables of Integral Transforms* (Vol. Volume 1, pp. 118). New York: McGraw-Hill Book Company Inc.

Berge, T., & Sandberg, U. (2017). Five years of EU tyre labelling - Success or failure? *INTER-NOISE and NOISE-CON Congress and Conference Proceedings*, *255*(7), 876-887. Retrieved from https://www.ingentaconnect.com/content/ince/incecp/2017/00000255/00000007/art00106

Bernhard, R. (2000). *Observations of the structural acoustics of automobiles*. Paper presented at the Inter-Noise Congress and Conference, Nice, France.

Bolton, J. S. H., J.S; Yoon, K.K. (1998). The Wave Number Decomposition Approach to the Analysis of Tire Vibration. *Proceedings of Noise-Con 98*, 97-102.

Brinkmeier, M., Nackenhorst, U., Petersen, S., & von Estorff, O. (2008). A finite element approach for the simulation of tire rolling noise. *Journal of Sound and Vibration, 309*(1), 20-39. Retrieved from http://www.sciencedirect.com/science/article/pii/S0022460X07001198. doi:https://doi.org/10.1016/j.jsv.2006.11.040

Cao, R. (2017). *INVESTIGATION OF NOISE AND VIBRATION IN TIRES THROUGH ANALYTICAL MODELING, TESTS AND SIMULATIONS.* (Doctor of Philosophy), Purdue University, West Lafayette, Indiana.

Cesbron, J., Anfosso-Lédée, F., Duhamel, D., Ping Yin, H., & Le Houédec, D. (2009). Experimental study of tyre/road contact forces in rolling conditions for noise prediction. *Journal of Sound and Vibration, 320*(1), 125-144. Retrieved from http://www.sciencedirect.com/science/article/pii/S0022460X08006317. doi:https://doi.org/10.1016/j.jsv.2008.07.018

Che, Y., Xiao, W. X., Chen, L. J., & Huang, Z. C. (2012). GA-BP Neural Network Based Tire Noise Prediction. *Advanced Materials Research, 443-444*, 65-70. Retrieved from https://www.scientific.net/AMR.443-444.65. doi:10.4028/www.scientific.net/AMR.443-444.65

Donavan, P. R., & Oswald, L. (1981). *Quantification of Noise Mechanisms of Blank, Rib, and Cross-Bar Tread Bias-Ply Truck Tires*.

Donavan, P. R., & Schumacher, R. (2007). Exterior Noise of Vehicles—Traffic Noise Prediction and Control. In *Handbook of Noise and Vibration Control*.

Erman, B., Mark, J. E., & Roland, M. C. (2013). Tread Design Patterns. In *Science and Technology of Rubber (4th Edition)*: Elsevier.

Fahy, F. (2007). *Sound and Structural Vibration* (Second ed.). Oxford: Academic Press.

Finnveden, S. (1994). Exact spectral finite element analysis of stationary vibrations in a rail way car structure. *Acta Acustica, 2*, 461-482. Retrieved from http://urn.kb.se/resolve?urn=urn:nbn:se:kth:diva-83554.

Finnveden, S., & Fraggstedt, M. (2008). Waveguide finite elements for curved structures. *Journal of Sound and Vibration, 312*(4), 644-671. Retrieved from

http://www.sciencedirect.com/science/article/pii/S0022460X0700898X. doi:https://doi.org/10.1016/j.jsv.2007.11.020
Fleischman, T. (1998). *Viscoelastic Material Testing for Tire Modeling*. Paper presented at the MTS Elastocmer Testing Users' Society.
Flügge, W. (1960). *Stresses in Shells* (S.-V. B. Heidelberg Ed.).
Hoever, C. (2014). *The simulation of car and truck tyre vibrations, rolling resistance and rolling noise.* (Doctor of Philosophy), Chalmers University of Technology Goteborg, Sweden.
Hofstetter, K., Grohs, C., Eberhardsteiner, J., & Mang, H. A. (2006). Sliding behaviour of simplified tire tread patterns investigated by means of FEM. *Computers & Structures, 84*(17), 1151-1163. Retrieved from http://www.sciencedirect.com/science/article/pii/S0045794906000812. doi:https://doi.org/10.1016/j.compstruc.2006.01.010
Holtschulze, J., Goertz, H., & Hüsemann, T. (2005). A simplified tyre model for intelligent tyres. *Vehicle System Dynamics, 43*(sup1), 305-316. Retrieved from https://doi.org/10.1080/00423110500140609. doi:10.1080/00423110500140609
Kim, B. S., Kim, G. J., & Lee, T. K. (2007). The identification of sound generating mechanisms of tyres. *Applied Acoustics, 68*(1), 114-133. Retrieved from http://www.sciencedirect.com/science/article/pii/S0003682X06001198. doi:https://doi.org/10.1016/j.apacoust.2006.05.019
Kim, Y. J., & Bolton, J. S. (2004). Effects of rotation on the dynamics of a circular cylindrical shell with application to tire vibration. *Journal of Sound and Vibration, 275*(3), 605-621. Retrieved from http://www.sciencedirect.com/science/article/pii/S0022460X03008575. doi:https://doi.org/10.1016/j.jsv.2003.06.003
Klein, P., Beckenbauer, T., Hamet, J.-F., & Kropp, W. (2008). *Tyre/road noise prediction: A comparison between the SPERoN and HyRoNE models - Part 2*. Paper presented at the Acoustics, Paris, France.
Klos, J., F., H., & Bernhard, R. (2002). *Response Measurement of Rolling Tires Using Laser Doppler Vibrometry*. Paper presented at the InterNoise 2002, Dearborn, MI.
Kounty, F. (2007). *Geometry and Mechanics of Pneumatic Tires*. Zlin, Czech Republic.
Kropp, W. (1999). A mathematical model of tyre noise generation. *International journal of heavy vehicle systems, 1*(1), 310. doi:10.1504/IJHVS.1999.054504
Kuijpers, A., & Blokland, G. (2001). *Tyre/road noise models in the last two decades: a critical evaluation*.
Kung, L. E., Soedel, W., & Yang, T. Y. (1986). Free vibration of a pneumatic tire-wheel unit using a ring on an elastic foundation and a finite element model. *Journal of Sound and Vibration, 107*(2), 181-194. Retrieved from http://www.sciencedirect.com/science/article/pii/0022460X86902312. doi:https://doi.org/10.1016/0022-460X(86)90231-2
Larsson, K., & Kropp, W. (2002). A HIGH-FREQUENCY THREE-DIMENSIONAL TYRE MODEL BASED ON TWO COUPLED ELASTIC LAYERS. *Journal of Sound and Vibration, 253*(4), 889-908. Retrieved from http://www.sciencedirect.com/science/article/pii/S0022460X01940738. doi:https://doi.org/10.1006/jsvi.2001.4073

Lee, U. (2009). *Spectral Element Method in Structural Dynamics*. Singapore: John Wiley & Sons (Asia) Pte Ltd.

Leissa, A. W. (1973). *Vibration of Shells*.

Li, T. (2017). *Tire-Pavement Interaction Noise (TPIN) Modeling Using Artificial Neural Network (ANN).* (PhD), Virginia Polytechnic Institute and State University, Blacksburg, VA.

Li, T. (2018). Literature review of tire-pavement interaction noise and reduction approaches. *Journal of Vibroengineering, 20*(6), 2424-2452.

Liu, F., Sutcliffe, M. P. F., & Graham, W. R. (2008). Modeling of Tread Block Contact Mechanics Using Linear Viscoelastic Theory. *Tire Science and Technology, 36*(3), 211-226. Retrieved from https://tiresciencetechnology.org/doi/abs/10.2346/1.2965832. doi:10.2346/1.2965832

Liu, F., Sutcliffe, M. P. F., & Graham, W. R. (2010). Prediction of tread block forces for a free-rolling tyre in contact with a smooth road. *Wear, 269*(9), 672-683. Retrieved from http://www.sciencedirect.com/science/article/pii/S0043164810002541. doi:https://doi.org/10.1016/j.wear.2010.07.006

Lopez Arteaga, I. (2014, 13-17 July). *Tyre/road noise and vibration: understanding their interaction and contribution to vehicle noise and fuel consumption.* Paper presented at the The 21st International Congress on Sound and Vibration (ICSV 21), Beijing, China.

Lopez, I., Blom, R. E. A., Roozen, N. B., & Nijmeijer, H. (2007). Modelling vibrations on deformed rolling tyres—a modal approach. *Journal of Sound and Vibration, 307*(3), 481-494. Retrieved from http://www.sciencedirect.com/science/article/pii/S0022460X07004816. doi:https://doi.org/10.1016/j.jsv.2007.05.056

Losa, M., Leandri, P., & Bacci, R. (2010). Empirical Rolling Noise Prediction Models Based on Pavement Surface Characteristics. *Road Materials and Pavement Design, 11*(sup1), 487-506. Retrieved from https://doi.org/10.1080/14680629.2010.9690343. doi:10.1080/14680629.2010.9690343

Nilsson, C. M. (2004). *Waveguide Finite Elements Applied on a Car Tyre.* (Doctor of Philosophy), Royal Institute of Technology, Stockholm, Sweden.

O'Boy, D. J., & Dowling, A. P. (2009a). Tyre/road interaction noise—A 3D viscoelastic multilayer model of a tyre belt. *Journal of Sound and Vibration, 322*(4), 829-850. Retrieved from http://www.sciencedirect.com/science/article/pii/S0022460X0800802X. doi:https://doi.org/10.1016/j.jsv.2008.09.021

O'Boy, D. J., & Dowling, A. P. (2009b). Tyre/road interaction noise—Numerical noise prediction of a patterned tyre on a rough road surface. *Journal of Sound and Vibration, 323*(1), 270-291. doi:10.1016/j.jsv.2008.12.024

Orrenius, U., & Finnveden, S. (1996). CALCULATION OF WAVE PROPAGATION IN RIB-STIFFENED PLATE STRUCTURES. *Journal of Sound and Vibration, 198*(2), 203-224. Retrieved from http://www.sciencedirect.com/science/article/pii/S0022460X96905659. doi:https://doi.org/10.1006/jsvi.1996.0565

Perisse, J., Clariet, J. M., & Hamet, J. F. (2000). *Modal testing of a smooth tire in low and medium frequency-estimation of structural parameters*. Paper presented at the SPIE Conferences and Exhibitions, San Antonio, Texas.

Pinnington, R. J. (2006a). A wave model of a circular tyre. Part 1: belt modelling. *Journal of Sound and Vibration, 290*(1), 101-132. Retrieved from http://www.sciencedirect.com/science/article/pii/S0022460X05002634. doi:https://doi.org/10.1016/j.jsv.2005.03.023

Pinnington, R. J. (2006b). A wave model of a circular tyre. Part 2: side-wall and force transmission modelling. *Journal of Sound and Vibration, 290*(1), 133-168. Retrieved from http://www.sciencedirect.com/science/article/pii/S0022460X05002646. doi:https://doi.org/10.1016/j.jsv.2005.03.024

Pinnington, R. J., & Briscoe, A. R. (2002). A Wave Model for a Pneumatic Tyre Belt. *Journal of Sound and Vibration, 253*(5), 941-959. Retrieved from http://www.sciencedirect.com/science/article/pii/S0022460X01939446. doi:https://doi.org/10.1006/jsvi.2001.3944

Reismann, H. (1988). *Elastic Plates*. New York.

Sanberg, U. (2003). *The Multi-Coincidence Peak around 1000 Hz in Tyre/Road Noise Spectra*. Paper presented at the Euronoise 2003, Naples, Italy.

Sanberg, U., & Ejsmont, J. A. (2002). *Tyre/road noise reference book* Harg, Sweden: INFORMEX.

Soedel, W. (1983). Simplified equations and solutions for the vibration of orthotropic cylindrical shells. *Journal of Sound and Vibration, 87*(4), 555-566. Retrieved from http://www.sciencedirect.com/science/article/pii/0022460X83905060. doi:https://doi.org/10.1016/0022-460X(83)90506-0

Soedel, W. (2005). *Vibrations of Shells and Plates* (T. a. Francis Ed. third ed.).

Spies, L. (2019). *A Machine-Learning based tool to predict Tire Noise using both Tire and Pavement Parameters.* (Master of Science), Virginia Tech, Blacksburg, VA.

Taghavifar, H., & Mardani, A. (2017). *Off-road Vehicle Dynamics* (Vol. 70): Springer International Publishing Switzerland 2017.

Ugural, A. C. (2009). *Stresses in beams, plates, and shells* (3rd ed.). Boca Raton: CRC Press.

Ugural, A. C. (2018). *Plates and Shells: Theory and Analysis* (fourth ed.). Boca Raton.

Waki, Y., Mace, B. R., & Brennan, M. J. (2009). Free and forced vibrations of a tyre using a wave/finite element approach. *Journal of Sound and Vibration, 323*(3), 737-756. Retrieved from http://www.sciencedirect.com/science/article/pii/S0022460X09000145. doi:https://doi.org/10.1016/j.jsv.2009.01.006

Wu, T. W. (2000). *Boundary Element Acoustics: Fundamentals and Computer Codes*. Southampton, UK: WIT Press.

Yum, K., Hong, K., & Bolton, J. S. (2006). Experimental relationship between tire structural wave propagation and sound radiation. *INTER-NOISE and NOISE-CON Congress and Conference Proceedings, 2006*(1), 5605-5612. Retrieved from https://www.ingentaconnect.com/content/ince/incecp/2006/00002006/00000001/art00047 .

Yum, K., Hong, K., & Bolton, J. S. (2007). Influence of Tire Size and Shape on Sound Radiation from a Tire in the Mid-Frequency Region. *SAE Transactions, 116*, 1801-1807. Retrieved from http://www.jstor.org/stable/44687949.